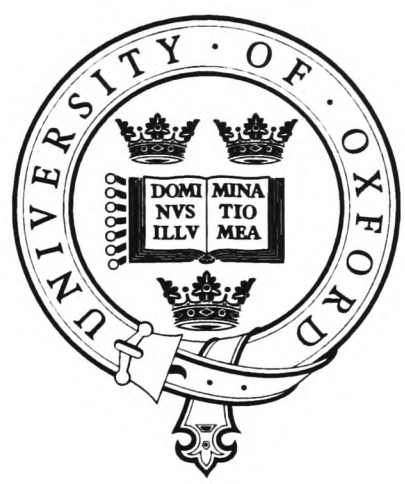


QUANTUM EFFECTS IN ARTIFICIAL ATOMS

By

Andrey Bychkov

St. John's College

SUBMITTED IN PARTIAL FULFILMENT OF THE
REQUIREMENTS FOR THE DEGREE OF
DOCTOR OF PHILOSOPHY

September 2003



To My Parents.

Contents

Acknowledgements **vi**

1 Introduction **1**

1.1 Author's contribution 3

2 Theoretical modelling of modulation-doped heterostructures **6**

2.1 Basic approximations 6

2.2 Semiconductor heterostructures and artificial atoms 9

2.3 Geometry of the system 13

2.3.1 Modulation-doped heterostructures 13

2.3.2 Surface states and Schottky barrier 16

2.4 Confinement potential 18

2.4.1 Electrostatic potential from the gate 20

2.4.2 Potential from the donor layer and surface states 21

2.5 Electron-electron interactions 23

2.5.1 Coulomb potential 24

2.5.2 Thomas-Fermi model 26

2.5.3 Thomas-Fermi-Dirac model 30

2.6 Kohn-Sham density-functional theory 33

2.6.1 Hohenberg-Kohn theorems 33

2.6.2 Kohn-Sham equations 35

2.6.3 Exchange-correlation potential 37

2.6.4 Discussion 42

2.7 Numerical scheme 44
2.7.1 Finding eigenstates 44
2.7.2 Self-consistency 48

3 Numerical simulations of spin-polarization effects in modulation-doped quantum dots 49

3.1 The role of exchange and correlation potentials in 2DEG-based quantum dots 49
3.2 Magnetic properties of modulation-doped quantum dots 53
3.2.1 Spin polarization in a single quantum dot 54
3.2.2 Spin polarization in two coupled quantum dots 65
3.3 Spin-dependent electron behaviour in quantum point contacts 72
3.3.1 0.7-anomaly 72
3.3.2 Numerical analysis 73
3.4 Applications in spintronics 79

4 Design of experiments on photon-exciton coupling in self-assembled quantum dots 82

4.1 Outline 82
4.2 Quantum-optics tools 84
4.2.1 Photons for quantum information science 84
4.2.2 Polarization-entangled photons 85
4.2.3 Photon bunching at a beamsplitter 87
4.2.4 Fabry-Perot interferometer 89
4.3 Solid-state tools 91
4.3.1 Self-assembled quantum dots for quantum information science 91
4.3.2 Optical properties and selection rules 93
4.3.3 Excitons 97
4.3.4 Exciton coherence and lifetime 100
4.3.5 QD efficiency of photon absorption and emission 102
4.4 Resonant transfer of quantum information between photons and excitons 104
4.5 Time-resolved photon-correlation experiment 108

4.5.1 Description of the proposed experiment 108
4.5.2 Visibility estimate 113
4.5.3 Optimization of the excitation source 115
4.5.4 Improvement of the sample design 119
4.6 Quantum dots in semiconductor microcavities 121
4.6.1 Purcell effect 124
4.6.2 Improved visibility estimate 127
4.7 Interference from two micropillars 129
4.7.1 Idea of the experiment 129
4.7.2 Technical requirements 131

5 Experimental results **138**
5.1 Building the experimental setup 138
5.2 QDs in square-lattice single-defect photonic crystal slab 147
5.2.1 Maxwell *vs* Schrödinger 148
5.2.2 Sample 149
5.2.3 Electromagnetic modes 150
5.2.4 Band structure calculations 153
5.2.5 Photonic bandgap 154
5.2.6 Defect modes 155
5.2.7 Observed mode properties 156
5.2.8 Mode tuning 159
5.2.9 Outlook 161
5.3 QDs in micropillars 162
5.3.1 Planar cavity 162
5.3.2 Micropillars fabricated with FIB 164
5.3.3 Micropillars with tapered oxide apertures 166
5.4 Artificial molecules 168

6 Future experiments **172**
6.1 Bell-inequality test 172
6.2 Quantum repeaters 173

6.3 Source of entangled photons 176
6.4 QED effects in the strong-coupling regime 178

7 Conclusion **181**

A Derivation of Thomas-Fermi kinetic energy functional **186**

B Papers and presentations by the author **188**

Bibliography **190**

QUANTUM EFFECTS IN ARTIFICIAL ATOMS

Andrey Bychkov

St. John's College, Oxford

D.Phil in Physics, Trinity 2003

Abstract

This thesis contains a theoretical and experimental investigation of semiconductor quantum dots (artificial atoms). The first part presents a numerical study of spin effects in GaAs/AlAs modulation-doped quantum dots containing 0 to 50 electrons. A theoretical model is developed to calculate confinement potentials and ground-state electron density distributions using the Kohn-Sham local spin-density approximation. Spin polarization, defined as the difference between the up- and down-spin electron densities, is predicted to occur spontaneously in symmetric quantum dots and in quantum point contacts in the low-density regime as a result of electron exchange interactions. This spontaneous magnetization can be controlled by an applied gate voltage, which opens up applications in spintronics and provides a possible explanation for the non-integer quantization of the quantum point contact conductance.

The second part describes experimental techniques to investigate photon-exciton coupling in InAs/GaAs self-assembled quantum dots. Two experiments on resonant excitation of a single quantum dot are proposed, whereby the quantum-dot emission is distinguished from resonant pump light by either photon bunching of collected photons with reference photons, or Michelson interferometry. The feasibility study of the proposed experiments shows that the photon-exciton coupling efficiency must be dramatically increased by putting the quantum dot inside an optical microcavity. Novel types of high-quality, low mode-volume semiconductor microcavities containing quantum dots are designed, fabricated, and studied on a newly built setup. We present the first results of photoluminescence studies of InAs quantum dots inside both GaAs single-defect square-lattice photonic-crystal slabs and GaAs/AlAs micropillars, and InAs artificial molecules formed by vertically coupled strain-assisted quantum dots. The results indicate the potential of these nanostructures for implementing resonant transfer of quantum information, developing quantum repeaters and entangled-photon sources, and studying QED effects in the strong-coupling regime.

Acknowledgements

My D.Phil course was quite an eventful story taking place in England, Sweden, Japan, and the US. What makes it an exceptional experience is the fascinating people from whom not only have I learned professionally, but who also shaped (for the better) my personality. This thesis is a direct result of their helpful influence, for which I am very grateful. In particular, my thanks go to:

Keith Burnett for accepting me to the D.Phil course at Oxford University and making it possible for me to be a member of St. John's College. As Keith had predicted, it has been a really great time for me there, probably the most interesting years in my life.

Artur Ekert for the individual approach in arranging my first interview with the Centre for Quantum Computation, Oxford, via a video-conference, and for providing me with the exciting opportunities ever since.

Dirk Bouwmeester, my supervisor, for taking care of me during these years, treating me well, as if a post-doc in many respects, introducing me to the sun of Santa Barbara and to the big science of the world. Working with Dirk, I have realised that having a broad scope of research interests is not a scary thing but, in fact, it helps generate new ideas. Also thanks for creating a truly informal atmosphere in the group.

Michiel de Dood for being extremely helpful with all aspects of my project, patiently answering my numerous questions, volunteering to read my thesis and improving it significantly. Antia Lamas Linares for ensuring my smooth transition to TeX, and helping with my thesis preparation and submission, which saved me a lot of time. Christoph Simon for the clear and to-the-point explanations of physics problems. Hagai Eisenberg for providing advice and equipment on the optics side.

William Marshall for the convincing enthusiasm and positive attitude to life, for improving my English, and for the discussions on what is true in life, often held together with Christophe Couteau, whose comments were a lot of fun. William Irvine for the very practical tips on writing and cooking, and for the selection of classical music. George Khoury for tolerating me in the lab and helping out with liquid helium. Simon Anders for systematizing work on the theory side and labelling every piece of equipment. Everyone else in the group for all the times we had together.

Our collaborators at the University of California at Santa Barbara (UCSB): Stefan

Strauf for showing me how to do the micro-PL in a proper way, putting a lot of effort in the lab, and in general for energizing our collaboration. Kevin Hennessy for the photonic-crystal sample, for sharing the data and being so supportive. Brian Gerardot and Antonio Badolato for the quantum dots. Dan Lofgren for the MATLAB codes. Pierre Petroff for the expert advice and discussions. Evelyn Hu for the expert advice and clean-room course.

My Swedish collaborators Irina Yakimenko and Karl-Fredrik Berggren for inviting me to Linköping University. Their very gentle and attentive supervision has guided me through the jungle of electron-electron interactions in semiconductors and resulted in three publications, a very rewarding experience. Anton Starikov and Almas Sadreev for improving considerably my numerical coding in MATLAB. Ingegärd Andersson for the impeccable administrative support.

Simon Benjamin for helping with my application to Oxford University. Neil Johnson for fruitful theoretical discussions. Edouard Alfandery for helping out with the first PL setup. Mark Hopkinson for growing our first samples at Oxford. Workshop and administrative staff at Oxford University and at the UCSB.

My D.Phil course would not be possible without the financial support of St. John's College, the Physics Department of Oxford University, the British Council, and the UCSB, which I very much appreciate. My research at Linköping University was supported by the Swedish Natural Science Research Council.

I would also like to thank the people who have extended my horizons, both personally and research-wise. Toshio Ohshima for kindly inviting me to Fujitsu Labs, showing how research is done in Japan, and for the general supervision of my stay in their beautiful country. Bernard Pannetier for my first experience to the clean-room and nanofabrication during an exchange program at CNRS in Grenoble. Vasili Semenov who invited me for a summer internship at the State University of New York at Stony Brook. He defined my choice of applying for a Ph.D., which turned out to be a D.Phil.

I am very grateful to the people who had originally turned me to physics and to international research. Leonid Openov, the supervisor of my Bachelor and Master degrees at the Moscow State Engineering Physics Institute, for teaching me the basics of research work and being such a generous person. Svetlana Koretskaya, editor-in-chief of the PersT magazine where I wrote my first news-in-science reports, for initiating my first internship abroad and involving me in a collaboration with the Europhysics News. Serguei Andreev for being a brilliant professor of quantum mechanics, whose lecture notes still appear on my desk from time to time.

I am indebted to my relatives and friends, to the people who are close and special to me, for bearing with me during my D.Phil.

Finally, I would like to thank my parents, whose support, motivation, wisdom and belief keep me up at all times. You deserve this thesis more than I do.

Chapter 1

Introduction

The need for fast computing appeared in the second half of the twentieth century as a result of the revolutionary progress in science and technology. A faster computer must contain more transistors, the size of which must inevitably shrink. Moore's law, which states that the number of transistors on a chip doubles every eighteen months, has indeed proved to be quite accurate in recent decades. This is a result of a major effort on the part of the electronics and optoelectronics industries to drive research into the properties of semiconductor micro- and nanostructures. Extrapolated into the future, Moore's prediction of ever decreasing feature size of the commercial transistor shall reach the quantum limit by year 2015. At that time, the 'classical' principle of operation of conventional electronic devices will be confronted with the indeterministic features of quantum physics.

In terms of research, the quantum limit has long been passed and new computational paradigms based on *quantum effects* – including the quantum information science – have emerged and been carefully developed, if mostly in theory. Originally conceived in a myriad of physical systems, many quantum information proposals are

converging to semiconductor nanostructures, in particular to quantum dots, or *artificial atoms*, because of their potential scalability and the well-established nanofabrication technology.

The experimental requirements to build a quantum computer are difficult and, in fact, it remains to be seen whether a quantum computer will be our next-generation computer at all. But at the moment, nanostructures provide a new playground to study quantum physics at a yet unexplored level of detail, with a great potential for scientific breakthroughs and applications. This has attracted a lot of attention in the physics community, raised significant public and private funding and even received extensive coverage in non-scientific media and fiction.

It is somewhat surprising that all physical phenomena occurring in nanostructures, no matter how different they may seem, have the same nature at the quantum level. Essentially, it is the dynamics of electrons occupying the states – as allowed by the quantum confinement of the nanostructure and electron-electron interactions – under the influence of the applied electromagnetic fields. This simple rationale gives rise to an amazing variety of quantum effects in artificial atoms, including the Coulomb blockade used in the single-electron transistor, photon anti-bunching that leads to the single-photon source, Kondo effect, which is promising for spintronics, Rabi oscillations indicating the presence of quantum coherence and so many yet undiscovered effects!

In this thesis, I shall first present theoretical results predicting the *spontaneous magnetization* in modulation-doped quantum dots and its potential applications in spintronics. This work has been performed in collaboration with the theoretical physics group of Professor Karl-Fredrik Berggren at Linköping University in Sweden. Second, I shall describe an experimental study of the *photon-exciton coupling* in self-assembled quantum dots, with possible applications in quantum information science.

The experimental part of my D.Phil research has been performed in the quantum optics and quantum information group of Professor Dirk Bouwmeester. The group moved from Oxford University to the University of California at Santa Barbara in the second year of my D.Phil. Although this transfer implied an interruption of my experimental work, it enabled me to perform and publish theoretical work as well as establish collaborations with world-leading experts in nanofabrication. I have been the first D.Phil student in the quantum optics group that ventured into solid-state physics. As such I have been involved in identifying promising research directions, proposing, designing, and building new experiments, and performing optical studies of novel semiconductor samples. Given the new setting and direction of our research, I am very pleased to be able to report the first experimental results on several recent ideas, including photon emission from quantum dots in photonic crystals and photon emission from a single quantum-dot molecule. It goes without saying that this type of research is heavily based on a collaborative effort, in particular with the Materials, Engineering, and Physics Departments of the University of California at Santa Barbara.

1.1 Author's contribution

This thesis consists of two blocks, one theoretical and the other experimental.

The first part (Chapters 2 and 3) describes the computer modelling of the spin properties of GaAs/AlGaAs modulation-doped quantum dots. This project started in September 1999 at Linköping University, Sweden, where I worked from August 1999 till September 2000 as a postgraduate research assistant at the Department of Physics and Measurement Technology. I continued working on ths project after coming to Oxford University in October 2000 to do a D.Phil course. The theoretical nature of

this work, which involved the developing of complex simulation software, allowed for a certain degree of independence in my research. Hence, most of theoretical work presented here was done by me under the supervision of my Swedish collaborators Dr. Irina Yakimenko and Professor Karl-Fredrik Berggren.

I wrote computer codes based on the theoretical model developed by I.Y. and K.F.B., which included calculation of the realistic confinement potential and ground-state electron density distributions (Chapter 2). I also participated in improving the model by simplifying the form of the electron exchange-correlation potential (Sections 2.6 and 3.1), performed extensive computer simulations of spin behaviour in single and double quantum dots (Section 3.2), and applied these findings to investigating the 0.7-anomaly in conductance of quantum point contacts (Section 3.3). In the three papers that we have published, I wrote a major part of the manuscripts, made the figures showing my numerical results, and participated in replying to referees' comments.

The second part of the thesis (Chapters 4 to 6) covers the experimental realisation of a new research direction. The project, supervised by Professor Dirk Bouwmeester, was conceived and started at Oxford University, and from May 2002, continued at the University of California at Santa Barbara (UCSB) in the US.

My activities included information analysis in identifying the research direction of new projects, setting up a new laboratory, finding and ordering scientific equipment, machining necessary parts in the workshop, writing grant proposals, designing samples, building the micro-PL setup, and carrying out optical measurements (see Section 4.1).

Being experimental research on sophisticated nanodevices, this project can only be implemented in a collaboration. Consequently, the work described in the second part is largely a result of our collaboration, which I helped to establish, with groups at

the Departments of Materials (Professor Pierre Petroff) and Engineering (Professors Evelyn Hu and Larry Coldren) at UCSB. To be concrete, let me specify which parts of the project have had an input from our collaborators:

- Experimental proposals (Sections 4.5 and 4.7) were developed together with Simon Anders (D.B. group).
- Micro-PL setup (Section 5.1) was built with the help and advice from Dr. Michiel de Dood (D.B. group) and Dr. Stefan Strauf (P.P. group). Some equipment from the P.P. lab was also used.
- The S1 photonic-crystal QD sample (Section 5.2) was grown by Antonio Badolato (P.P. group) and nanofabricated by Kevin Hennessy (E.H. group). Michiel de Dood performed the band structure calculations. Stefan Strauf helped with optical measurements, and Kevin Hennessy also provided his optical pre-characterization results.
- The planar-cavity QD sample (Section 5.3) was grown by Brian Gerardot (P.P. group) and designed together with Dan Lofgren (L.C. group), who also provided the MATLAB codes to calculate the cavity modes. Michiel de Dood fabricated the micropillars using the focussed ion beam.
- The artificial-molecule sample (Section 5.4) was grown by Brian Gerardot, and the first measurements were performed by Brian Gerardot and Stefan Strauf.

My main experimental contribution has been to build the optical setup needed for the characterization of the various samples, and to perform and support the optical measurements.

Chapter 2

Theoretical modelling of modulation-doped heterostructures

2.1 Basic approximations

Impressive progress in materials science and nanotechnology over the last twenty years has enabled to grow artificial semiconductor compounds with the properties controlled on the atomic scale and further shape them into repeatable sub-micron features, which provided a base for the state-of-the-art electronic devices. To understand and very often predict their physical properties, one should address the two fundamental questions [89]:

1. What is the ground state of a given system?

2. How does the system behave under external influences?

Answering these questions, however, remains one of the most challenging problems of modern physics, mainly due to the many-body nature of nanostructures composed of $N = 10^4$ and more atoms, each having $Z \sim 10$–100 electrons (Z is the atomic number). Analytic theory usually fails at this level of complexity, and therefore numerical modelling of the microscopic quantum effects in nanostructures has become utterly

important. Even still, solving numerically the Shrödinger equation that accounts for the interactions between all the many particles in the system is a formidable task hardly approachable with currently available computational resources.

A traditional way to tackle this problem is to assume a series of approximations, which the theoretical description of this Chapter will be based upon. Note that most approximations mentioned below are commonly used in solid-state physics and a more rigorous discussion and justification of their use can be found elsewhere [89, 4]. However, the approximations specific to our theoretical model will receive a comprehensive description in the following.

First of all, we will be dealing with idealized defect-free *semiconductor crystals* where ions are arranged in a regular periodic array.[i] Secondly, any crystal is comprised of two groups of electrons – *valence electrons* which contribute to chemical bonding and *core electrons* which are tightly bound in the core shells of the ions. In semiconductors, valence electrons fill in the valence band. Core electrons scarcely influence the properties of the crystal, and for that reason are usually not considered.

An important role is played by the *adiabatic approximation.* It is based on the fact that ions are much heavier than electrons. Therefore, the ions move so slowly on the scale of velocities of electrons, that at any moment the electrons will be in their ground state for that particular instantaneous ionic arrangement. In other words, the ions can respond only slowly to a change in the electron configuration, while the electrons respond adiabatically to a change in the positions of the ions. Thus, the motion of the ions can be effectively decoupled from the motion of the electrons and, in the following, left behind.

[i]Even the smallest nanostructures – quantum dots of less than 2 nm in size – are big enough to develop the crystalline structure of the bulk material [151].

A key assumption is the *one-particle approximation*, whereby the many-particle problem is reduced to the motion of an electron in the potential created both by the periodic ion lattice and all electrons in the system including itself. It enormously simplifies the problem of many interacting electrons by effectively removing pair potentials, and thus allowing to describe it with a single-particle Schrödinger equation. Note that this one-particle point of view does not completely neglect electron-electron interactions, but rather summarizes their effects by an average global contribution to the potential. In this way, the single-particle Schrödinger equation does not treat an electron independently of all the others, since the wave functions of the other electrons are present through the form of that average contribution. A clever choice of the electron-electron interaction energy is the subject of the theoretical schemes described in Sections 2.5 and 2.6.

Finally, we will make use of the *effective mass approximation*. It can be shown [89] that the interaction of electrons with the periodic potential due to the ion lattice can be taken account of in many cases by introducing an effective mass tensor $m^*_{\alpha\beta}(\mathbf{r})$. The problem of an electron moving under the simultaneous influence of external forces and the lattice potential can then be simplified to an equivalent problem where 'quasi-electrons', distinguishable from free electrons only by their different mass, move only under the influence of the external forces. This approximation is valid in semiconductors where the concentrations of the electrons are mostly low, hence the electrons occupy the states near the bottom of the conduction band. In this case, the band energy $E(\mathbf{k})$, where $\mathbf{k}$ is the wave vector in a crystal, can be expanded about the minimum. The linear term of the expansion is zero at the minimum, and the energy dependance will have a familiar quadratic law, to which the effective mass tensor can be assigned. Furthermore, assuming that the semiconductor region occupied by the electrons is uniform and isotropic, the effective mass tensor can be replaced by a

constant m^*.

As a result of the given approximations, the Schrödinger equation of the system becomes

$$\left[-\frac{\hbar^2}{2m^*}\nabla^2 + U_{ext} + U_{e-e}\right]\psi(\mathbf{r},\sigma) = E_\sigma\psi(\mathbf{r},\sigma). \tag{2.1}$$

Here, $\psi(\mathbf{r},\sigma)$ is the electron wavefunction that depends on its position $\mathbf{r}$ in space and $\sigma = \pm\frac{1}{2}$ projection of its spin on the axis of quantization. The first term in the brackets is the operator of electron kinetic energy. U_{ext} is the confinement potential due to external forces, such as potential of the impurities embedded in the crystal and/or applied electric fields. It will be discussed in Section 2.4 when defining the system geometry. U_{e-e} is the Coulomb potential describing interactions between the electrons. It will be the main focus of Sections 2.5 and 2.6. E_σ represents the spin-dependent spectrum of energy eigenstates obtained by solving Eq. (2.1) self-consistently. The self-consistent procedure and its numerical implementation will be described in Section 2.7.

2.2 Semiconductor heterostructures and artificial atoms

The energy spectrum of a bulk semiconductor consists of energy bands separated by gaps where electronic states are forbidden. This is illustrated in Figure 2.1a, which shows the band diagram of GaAs, a III-V semiconductor commonly used in opto-electronics. The allowed energy states vary as a function of the electron wave vector $\mathbf{k}$, however, we are mostly interested in what the spectrum looks like at the Γ-point ($\mathbf{k} = 0$) around the Fermi level ($E = 0$), as shown in more detail in Figure 2.1b, which corresponds to the experimental conditions (see Section 4.3.2 below).

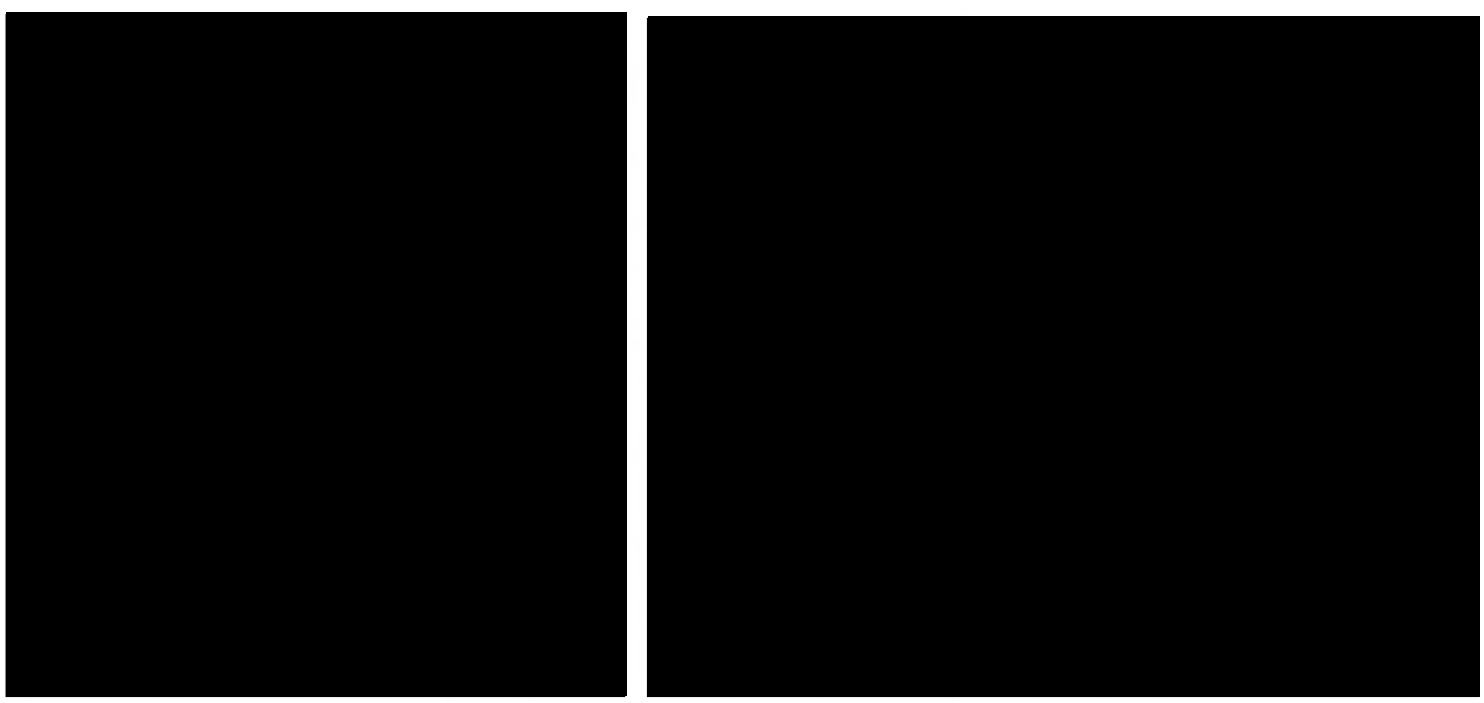


Figure 2.1: *(a) Band diagram of GaAs. The points on the horizontal axis correspond to different crystallographic directions. Figure from Ref. [28]. (b) A blow-up of the circled region in (a) with energy values given at room temperature, note the inverted horizontal axis. Figure from Ref. [165].*

In the ground state of an undoped semiconductor, the lower band called the *valence band* (VB) is completely filled with electrons, whereas the upper band called the *conduction band* (CB) is empty. If the semiconductor is excited with energy greater than the bandgap E_g (typically, a few electron-volts) electrons are promoted from VB to CB leaving behind positively charged vacancies called *holes*. It is also possible to introduce delocalised electrons into the CB and holes into the VB by doping the semiconductor with impurity atoms that have more (*donors*) or fewer (*acceptors*) electrons in the external orbitals than the atoms of the lattice. In this case, no excitation is involved, and the semiconductor remains in its ground state. Electrons and holes are quasiparticles that carry electric charge, they are responsible for all interesting phenomena occurring in semiconductors.

The semiconductor era is considered to begin with the discovery of the transistor effect in 1947 by Bardeen, Brattain, and Shockley (Nobel Prize in Physics 1956).

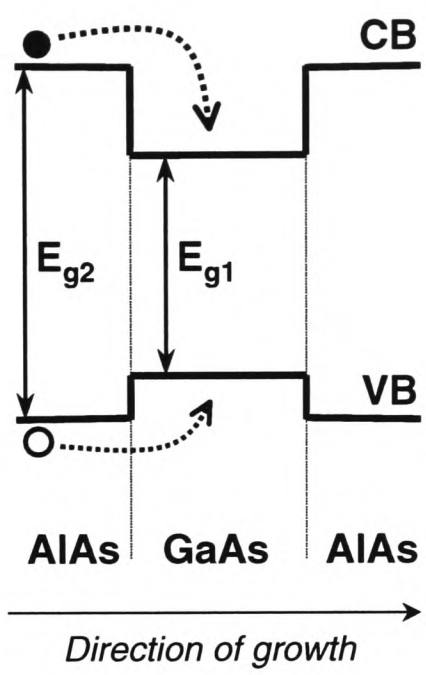


Figure 2.2: *Schematic band alignment in double-barrier GaAs/AlAs heterostructure. Black and white circles depict electrons and holes, respectively.*

An important breakthrough was the development of novel growth techniques, such as molecular beam epitaxy (MBE) and metal-organic chemical vapour deposition (MOCVD), in the early 1970-s. Application of these techniques made it possible to fabricate *heterostructures* – artificial crystals composed of layers of different semiconductors [15]. The thickness of the layers along the growth axis can be controlled with atomic precision, thus enabling to create unique new materials and devices with predefined properties. The art of this modern alchemy is known as 'band structure engineering'.

Consider a heterostructure (Figure 2.2) where a layer of lower-bandgap material (GaAs, $E_{g1} = 1.42$ eV) is sandwiched between two layers of higher-bandgap material (AlAs, $E_{g2} = 2.16$ eV). Thus, the modulated band structure is formed containing a potential well and two barriers. The carriers, i.e., electrons in CB and holes in VB, will travel to the region of lower potential (GaAs layer) where they will remain. If the layer has thickness of only a few lattice constants, the carriers will be effectively

confined in two dimensions, in the structure called a *quantum well* (QW).

If one further restricts motion of the carriers inside the QW, e.g. by etching a narrow mesa across the QW, the carriers in the mesa will be allowed to move in only one dimension, and the resulting structure is called a *quantum wire.*

Cutting the quantum wire into islands with a size comparable to the de Broglie wavelength of confined electrons (from a few to a hundred nanometers in semiconductors) will result in a quasi zero-dimensional structure, or *quantum dot* (QD) [15, 65, 109, 103]. Although QDs are crystals made up of 10^3–10^6 atoms, they are often called *'artificial atoms'* because of the carrier confinement in all directions giving rise to a discrete spectrum of energy levels of electrons and holes, similar to electron levels in an atom.

QDs can be fabricated by various techniques, including electron-beam lithography and etching [15], colloidal growth [1], cleaved-edge overgrowth [124], strain-induced confinement [86], and others. In what follows, we will be mostly concerned with the modulation-doped QDs formed by electrostatic depletion of the two-dimensional electron gas (2DEG), whose detailed description will be given in Chapter 2, and self-assembled quantum dots, which will be described in Chapter 4.

Properties of QDs, e.g. size, shape, number of confined electrons, and structure of energy levels strongly depend on the fabrication conditions such as the amount and composition of deposited materials, temperature, pressure (vacuum), rate of growth, and can be further controlled by applying external electric and magnetic fields. It is possible, in principle, to obtain the whole 'periodic table of elements' at hand by tailoring the growth process. On the other hand, QDs have proved to be flexible structures for various device applications.

2.3 Geometry of the system

2.3.1 Modulation-doped heterostructures

The systems we will be dealing with in Chapters 2 and 3 rely on *free carriers*, electrons in the conduction band (CB) or holes in the valence band (VB) that propagate in delocalized states all over the crystal [30]. The obvious way of introducing carriers is to dope the regions where electrons or holes are needed. Unfortunately, charged donors or acceptors are left behind when electrons or holes are released, and scatter the carriers via the Coulomb interaction (*ionized-impurity scattering*). This spoils the propagation of the carriers within the structure, blurs energy levels and disrupts the coherence of the electron and hole wavefunctions needed to see the desired quantum effects.

The solution is *modulation doping*, whereby the doping is grown in one region but the carriers subsequently migrate to another, as shown in Figure 2.3 for a heterojunction between negatively doped AlGaAs and undoped GaAs. The two materials have different energy gaps, with the discontinuity ΔE_c of the CB. The electrons in the CB travel around the structure and some cross into GaAs lowering their energy (Figure 2.3a). This motion separates negatively charged electrons from their positively charged donors, which sets up an electrostatic potential that tends to drive the electrons back into the AlGaAs. As a result, the edge of the CB has a slope (Figure 2.3b). Since electrons cannot climb the barrier ΔE_c, they become trapped at the heterointerface in a potential well.

A detailed analysis in Ref. [30] shows that the potential well is roughly triangular and spreads over 10 nm along the growth direction at typical energy of the electrons E_1 in GaAs. The energy levels for motion along z are quantized similarly to those

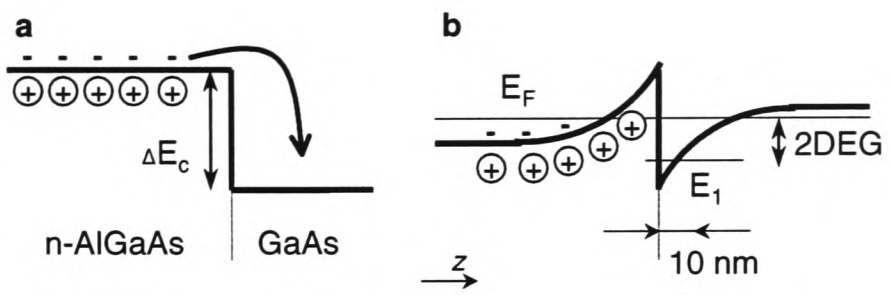


Figure 2.3: *Conduction band around a heterojunction between negatively doped AlGaAs and undoped GaAs. Electrons are separated from their donors to form the two-dimensional electron gas.*

in a square potential well. Often electrons occupy only the lowest quantized state along z while remaining free in the other two dimensions x and y. This forms the *two-dimensional electron gas* (2DEG), the basis of many electronic devices.

Thus, modulation doping has achieved two benefits: it has separated electrons from their donors to reduce scattering by ionized impurities, and confined electrons to two dimensions. Coherent motion of such electrons is analogous to electromagnetic waves in a waveguide. A refinement is made by leaving a *spacer* layer of undoped AlGaAs between the n-AlGaAs and GaAs to increase the separation between electrons and donors. This reduces further the scattering (achieving record high electron mobilities of 1.5×10^7 cm^{2}V^{-1}s^{-1} at 1.5 K [91]) but decreases the density of electrons in the 2DEG.

The system of interest is schematically depicted in Figure 2.4. The layers are grown epitaxially on the GaAs substrate: the AlGaAs spacer of thickness $s = 10$ nm separates electrons from the donors located in the negatively doped with the density $\rho_d = 6 \times 10^{17}$ cm^{-3} AlGaAs donor layer of thickness $d = 36$ nm. To prevent the oxidation of the aluminium content in the ambient atmosphere, the heterostructure is covered with the GaAs cap layer of thickness $c = 24$ nm. Parameters c, d and s are chosen here to correspond to realistic experimentally grown devices, and they can be

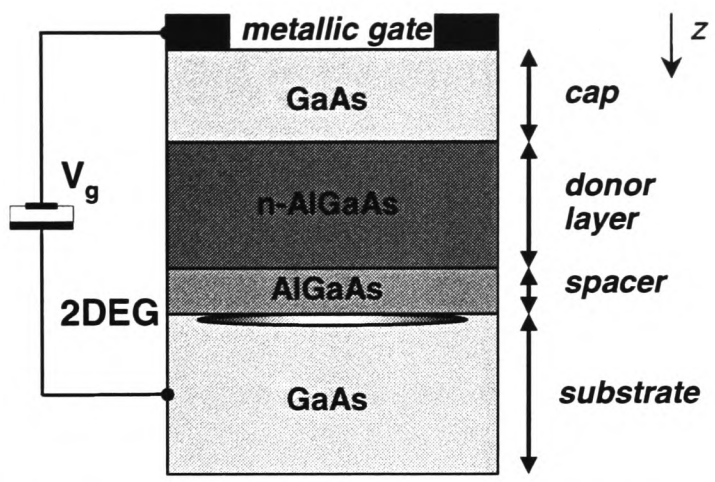


Figure 2.4: *Heterostructure of interest in the vertical cross-section. The 2DEG is localized in the substrate near the interface with the spacer. Bias voltage V_g is applied between the gate and the substrate. Device parameters are described in the text.*

tuned to change the electron density, mobility, and other properties of the system. Since the substrate is much thicker than the grown layers, it is safely assumed to have an infinite thickness in our modelling.

A metallic gate is deposited on top of the heterostructure in order to control the density of the 2DEG (by forming a capacitor between the gate and the 2DEG). If a positive or negative bias voltage is applied to the gate, the heterointerface region underneath it will be populated or depleted with the 2DEG, respectively.

A new degree of control over the 2DEG is obtained by patterning the planar gate lithographically into a *split gate*, which only partially covers the heterostructure (see Figure 2.5). At negative gate voltages, the 2DEG is electrostatically squeezed from underneath the gate into the regions under the uncovered openings. As a result, the conduction band electrons will be confined in the x–y plane, in addition to the vertical confinement at the heterointerface. By changing the lithography of the split gate, one can reduce the 2DEG to 1D forming *quantum wires* and 0D forming *quantum dots.*

Figure 2.5 shows the gate geometry (left column) and the calculated confinement

potential in the 2DEG plane (right column) of the modelled devices: (a, b) symmetric and (c, d) asymmetric quantum dots; (e, f) a pair of dots; (g, h) *quantum point contact* (QPC). The latter is formed by a short quantum wire between two large pads. In the right column of the figure, the electron Fermi energy is set to zero, and we can see how the regions with a negative potential are occupied with electrons following the lithographic patterns of the gate. The calculation method of the confinement potential is described in Section 2.4.

2.3.2 Surface states and Schottky barrier

Submicron devices inevitably have a large surface-to-volume ratio, which means that surfaces have a greater effect on their properties. Layers of GaAs have a high density of *surface states* both on a free surface and at the interface with the metallic gate, which occupy a narrow band of energies near the middle of the bandgap [31, 32]. The Fermi level of an ungated layer always lies within this narrow band – *pinned* by the surface states – because it is practically impossible to put enough charge into the surface states to fill or empty the band and allow the Fermi level to leave it. It turns out that most of the donors contribute electrons to the surface states; only a small fraction of them (less than two percent estimated for our devices) goes to the 2DEG.

There is little change when a metal is deposited on the surface to form a gate. The bandgap of GaAs at $T = 0$ K is $E_g = 1.52$ eV. Hence, there is always a *Schottky barrier* of typically 0.8 eV that separates electrons in the semiconductor from those in the metal. The barrier must be made thin if the contact is intended to be *ohmic*, to allow tunnelling through such a barrier. In our system, on the other hand, the barrier must be thick to prevent the gate from leaking.

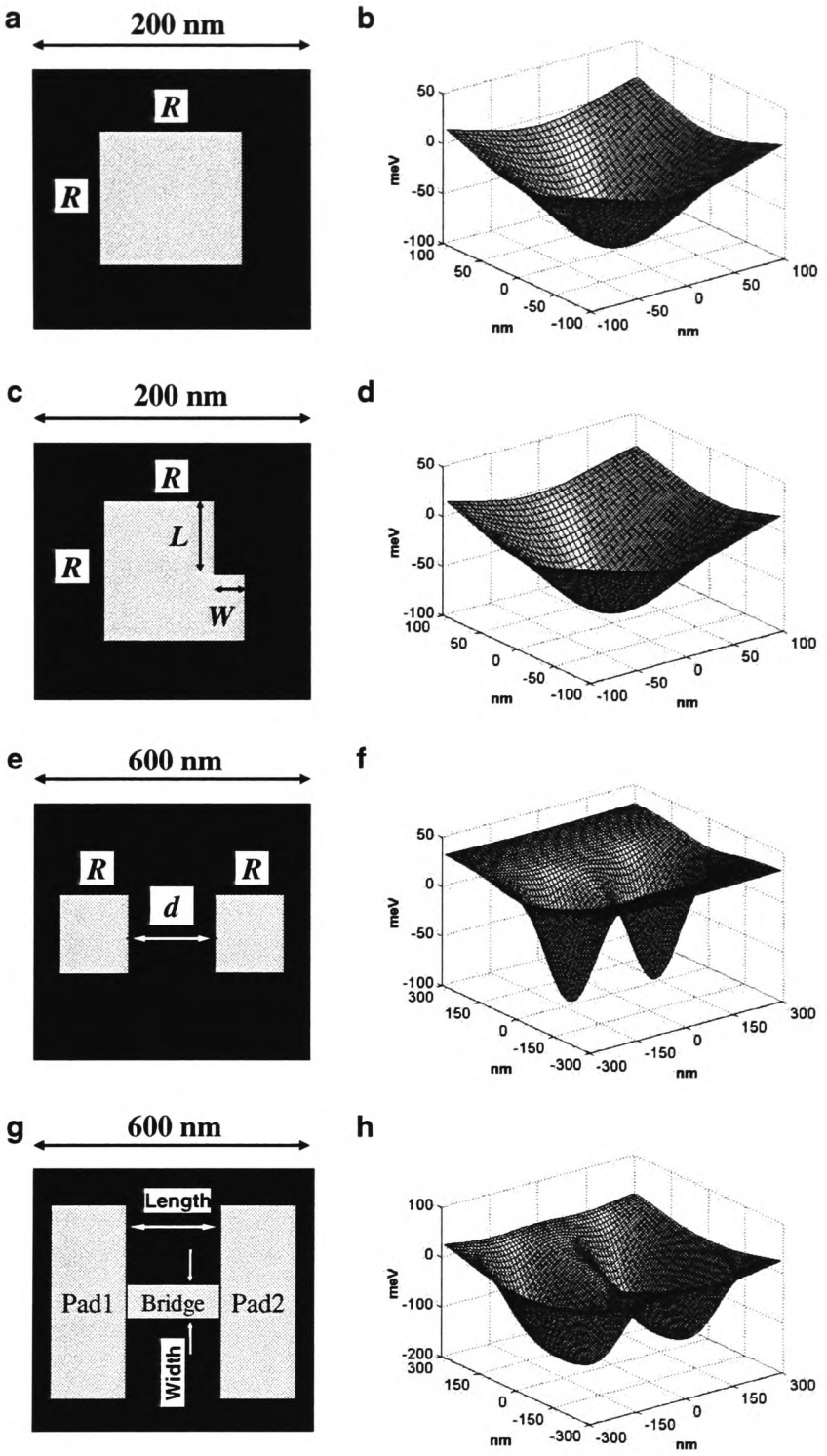


Figure 2.5: *Top-view schematics of the metallic gate (left column) and the lateral confinement potential for: (a, b) Circular symmetric quantum dot. The size of the gate opening is* $R = 110$ *nm. (c, d) Asymmetric quantum dot. The gate is modified by a structure in the top right corner, which has width* $W = 20$ *nm and length varied from* $L = 0$ *nm (circular dot) to* $L = 110$ *nm (ellipsoidal dot). (e, f) Two coupled symmetric quantum dots. The gate openings are squares of* $R = 110$ *nm separated by* $d = 0$ *to 200 nm. (g, h) Quantum point contact. The two pads are* 100×400 nm^2 *rectangles connected by a bridge (*200×10 nm^2*), whose length and width can be varied. All confinement potentials are shown at the applied gate voltage* $V_g = -0.505\,V$.

2.4 Confinement potential

The *confinement potential* entering the Schrödinger equation (2.1) determines the electrostatic environment of the 2DEG and in general contains the information about the heterostructure. In a sense, the confinement potential provides a sensitive knob, which can be tuned to control the electronic properties of the system. Because of this sensitivity, it is crucial to model the confinement potential as closely as possible to the experimental situation. To proceed with calculations, we have to make several important assumptions specific for our model:

1) Electrons in the 2DEG are degenerate and occupy only the first subband (the ground state of motion along z). This requires low temperatures and low densities of electrons (roughly $n_e < 6 \times 10^{15}$ m^{-2}), the conditions that are usually satisfied in the experiment. In the following, we neglect the thermal occupation of excited states by formally setting the temperature zero. This is a valid assumption, since a typical energy splitting between the subbands exceed by an order of magnitude the working temperature in liquid helium of $T = 4.2$ K ≈ 0.36 meV.

2) The electron gas (2DEG) is strictly two-dimensional and totally confined in the plane of the heterojunction in the GaAs substrate. This is a reasonable assumption, since for typical densities of the 2DEG ($n_e \sim 10^{15}$ m^{-2}) the *Fermi energy* in GaAs $E_F = \pi\hbar^2 n_e/m^* \sim 10$ meV corresponds to the electron *de Broglie wavelength* $\lambda_{DB} = h/\sqrt{2m^* E_F} \sim 50$ nm, which is five times the vertical spread of the 2DEG in the ground state. As a result, we can treat the problem purely in 2D, which will greatly facilitate the calculations.

3) The charge density of the donor layer is constant and does not depend on the gate voltage. This implies that the donor layer is fully ionized.

4) The structure is in the thermal equilibrium at $T = 0$, so that the chemical

potential μ is constant throughout the structure, and we set $\mu = E_F = 0$ as the reference energy.

We also assume two *boundary conditions*, which give a simplified electrostatics: a) The system is electrically neutral, i.e. the electric field vanishes at $|z| \to \infty$. b) The surface of the device is pinned to $E_F = 0$, and the Schottky barrier has the same height everywhere at the interface with the metallic gate, i.e. the surface is a zero equipotential.

The above assumptions enable us to apply the results of Davies *et al.* [31, 32] for the gate potential to obtain a simple analytic expression for the confinement potential. First of all, it consists of the following terms:

$$U_{ext}(\mathbf{r}) = eV_g(\mathbf{r}, z) + eV_d + eV_s. \tag{2.2}$$

Here, $e = -|e|$ is the electron charge, $eV_g(\mathbf{r}, z)$ is the electrostatic potential of the gate at the point $\mathbf{r} = (x, y)$ in the 2DEG plane at depth $z = c + d + s$ nm from the gate, eV_d and eV_s are contributions from the donors and surface states. Each of the terms in Eq. (2.2) will be calculated in the following paragraphs, using the following values of the parameters: doping density of the donor layer $\rho_d = 6 \times 10^{17}$ cm^{-3}, height of the Schottky barrier $eV_s = 0.8$, layer thicknesses of the device $c = 24$ nm, $d = 36$ nm, $s = 10$ nm. The values of the dielectric constant $\epsilon = 12.9$ and electron effective mass $m^* = 0.067m$ (where m is the free electron mass) are taken to be the same in GaAs and AlGaAs.

Note that the confinement potential has the dimensionality of energy and in fact means the confinement potential energy. It is traditionally called a 'potential', which may sometimes be delusive.

2.4.1 Electrostatic potential from the gate

The potential caused by the gate at the point $\mathbf{r} = (x, y)$ in the 2DEG plane at depth z from the gate was derived in Ref. [32]. Solving Laplace's equation $\nabla^2 V_g(\mathbf{r}, z) = 0$ with the boundary conditions defined above and taking the two-dimensional inverse Fourier transform leads to an explicit form of the *electrostatic potential from the gate*:

$$eV_g(\mathbf{r}, z) = \frac{1}{2\pi} \int d\mathbf{r}' eV_g(\mathbf{r}', 0) \frac{|z|}{(z^2 + |\mathbf{r} - \mathbf{r}'|^2)^{3/2}}, \tag{2.3}$$

where $eV_g(\mathbf{r}', 0)$ is the distribution of the potential along the surface of the gate. This expression can be directly calculated numerically. However, the integration can be done analytically for certain gate patterns. E.g. for a gate defined by a finite rectangle $L < x < R$, $B < y < T$ with an applied voltage V_g, Davies *et al.* [32] obtained

$$\frac{eV_g(\mathbf{r}, z)}{e\ V_g} = g(x-L, y-B) + g(x-L, T-y) + g(R-x, y-B) + g(R-x, T-y) \tag{2.4}$$

where

$$g(u, v) = \frac{1}{2\pi} \arctan \frac{uv}{zR}\ ; \quad R = (u^2 + v^2 + z^2)^{1/2}. \tag{2.5}$$

We use this result to construct the gates shown in Figure 2.5 by superposing rectangular gates of the size defined by the openings (light regions) with applied voltages $-V_g$ on the plane gate biased at voltage $+V_g$. We consider in the following that the gate is infinite in the x–y plane, which enables to perform the integration of Eq. (2.3) in the semi-space $z > 0$ below the gate:

$$eV_g(\mathbf{r}, z) = \frac{1}{2\pi} \int_{-\infty}^{+\infty} dx' \int_{-\infty}^{+\infty} dy' \frac{eV_g z}{[(y - y')^2 + a^2]^{3/2}}$$

where $a^2 = z^2 + (x - x')^2$. Then integration can be done as follows:

$$\int_{-\infty}^{+\infty} \frac{dy'}{(y'^2 + a^2)^{3/2}} = -\frac{1}{a}\frac{\partial}{\partial a} \int_{-\infty}^{+\infty} \frac{dy'}{(y'^2 + a^2)^{1/2}} = -\frac{1}{a}\frac{\partial}{\partial a} \ln(y + \sqrt{y^2 + a^2}) \Big|_{-\infty}^{+\infty} = \frac{2}{a^2}$$

and the gate potential

$$eV_g(\mathbf{r},z)=\frac{eV_g z}{\pi}\int_{-\infty}^{+\infty}\frac{dx'}{x'^2+z^2}=\frac{eV_g}{\pi}\arctan\frac{x'}{z}\Big|_{-\infty}^{+\infty}=eV_g \tag{2.6}$$

becomes constant in the semi-space including the 2DEG plane. The simplification of the infinite gate may be justified by the fact that the 2DEG occupies the central region of the x–y plane and is less sensitive to the boundary effects. Furthermore, the integrated function decreases as $|\mathbf{r}-\mathbf{r}'|^{-3}$, so the contribution from the peripheral background will not be significant and in principle can be compensated by adjusting an appropriate voltage V_g.

2.4.2 Potential from the donor layer and surface states

The negatively doped donor layer is fully ionised with a uniform density ρ_d, as depicted in Figure 2.6. It is modelled as a slab of thickness d infinite in the x–y plane, as well as the gate, in order to satisfy the electro-neutrality condition.

The electrostatic field and potential of the donor layer matched at its vertical boundaries can be derived from Gauss's theorem as

$$\begin{aligned}\mathbf{E}&=-\frac{e\rho_d\, d}{2\epsilon\epsilon_0}\cdot\frac{\mathbf{z}'}{z'}\\ \phi(z')&=\frac{e\rho_d\, d}{2\epsilon\epsilon_0}(z'^2+\frac{d^2}{4}),\end{aligned} \tag{2.7}$$

where $z'=z-c-d/2$. In order to be zero at the plane of the metallic gate $z=0$, the electrostatic potential should include a contribution from the *mirror charges* [92]. The latter contribution is expressed by the same Eqs. (2.7) after substituting an oppositely charged density $+e\rho_d$ and a shifted coordinate $z'=z+c+d/2$, as shown in Figure 2.6. One can check that the electrostatic potentials from two layers indeed cancel out at $z=0$, and the potential at the gate surface is determined as before by its

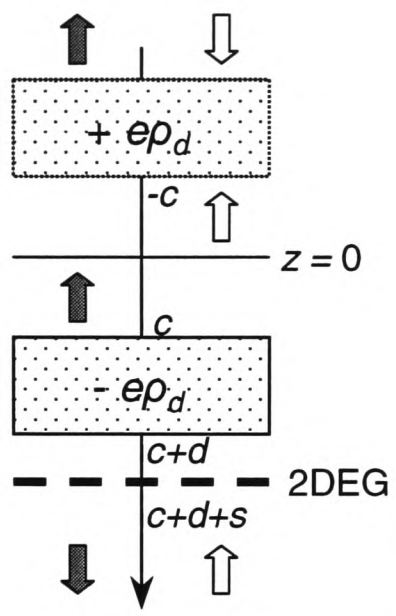


Figure 2.6: *Electrostatic diagram showing the donor layer charged with density* $-e\rho_d$ *(note* $e < 0$*) and a layer of its mirror charges. The plane of the gate is at* $z = 0$*. Dark and light arrows indicate the electric fields from the donor layer and its mirror charges, respectively. The two fields cancel out in the semi-space under the donor layer, which contains the 2DEG.*

own distribution $eV_g(\mathbf{r}, 0)$. At the same time, the electric field is zero at $|z| > (c+d)$, so that electro-neutrality is satisfied too.

Superposing the fields from the two layers in the semi-space of interest $z > c+d$, one obtains:

$$\mathbf{E} = 0; \qquad \phi(z) = -\frac{e\rho_d\, d}{\epsilon\epsilon_0}(c + \frac{d}{2}), \tag{2.8}$$

which gives the *potential from the donor layer*

$$eV_d = e\phi(z) = -\frac{e^2}{\epsilon\epsilon_0}\rho_d\, d(c + d/2). \tag{2.9}$$

Interestingly enough, it is constant and thus does not depend on the depth of the spacer, as a result of the mirror charges. For our system parameters $eV_d = -1.27$ eV.

The last term in Eq. (2.2) describes the *potential from the surface states.* It was already given above as the Schottky barrier $eV_s = 0.8$ eV. Thus, the donors and

surface states provide a constant background to the confinement potential, whereas its spatial profile is determined by the electrostatic potential from the gate.

Figure 2.5 shows the confinement potential of four devices (at $V_g = -0.505$ V), as calculated according to the described model. A quantum dot formed by a symmetric square gate (Figure 2.5b), has a nearly parabolic confinement that flattens out near the boundaries. Importantly, it shows that the realistic confinement potential of the quantum dot is not exactly parabolic, as opposed to what is commonly assumed [65], which may e.g. give rise to novel effects in the electron shell-filling [83, 93]. On the other hand, the realistic confinement derived in our model is also based on certain assumptions.

The confinement potential of an asymmetric dot (Figure 2.5d) looks very similar to the previous case. Barely seen in the figure, it is slightly higher than that of the symmetric dot due to a positive contribution from the cut-corner opening in the gate. However, such a tiny distortion of the symmetry of the confinement gives rise to a considerable variation of the electronic properties, namely, the spin polarization of the confined 2DEG, as will be shown in Chapter 3.

Figure 2.5f shows the confinement potential of two uncoupled quantum dots, which repeats for each of the dots the confinement in Figure 2.5b. If the two dots are coupled, e.g. by a narrow channel (Figure 2.5h), the confinement potential in the centre has a saddle-point form characteristic of a *quantum point contact* also discussed in Chapter 3.

2.5 Electron-electron interactions

Electron-electron interactions play a crucial role in the behaviour of any solid-sate system but at the same time they present the most challenging task for any theoretical

model, including ours. We will first consider a simple example of a two-electron system in order to introduce the necessary physical quantities.

2.5.1 Coulomb potential

The wavefunction of a system of two electrons can be described by an antisymmetrized product of two single-electron orbitals to allow for its fermionic nature:

$$\Psi(\mathbf{x_1}, \mathbf{x_2}) = \frac{1}{\sqrt{2}}\big[\psi_1(\mathbf{x_1})\psi_2(\mathbf{x_2}) - \psi_1(\mathbf{x_2})\psi_2(\mathbf{x_1})\big]. \tag{2.10}$$

Here, orbitals $\psi_1(\mathbf{x})$ and $\psi_2(\mathbf{x})$ are orthonormal, each of them is a product of a spatial orbital and a spin function, and $\mathbf{x} = (\mathbf{r}, \sigma)$ is a composite variable. The Coulomb interaction of the two electrons is described by

$$U_{e-e} \propto \int\int d\mathbf{x_1} d\mathbf{x_2}\ \Psi^* \frac{1}{|\mathbf{r_1} - \mathbf{r_2}|}\Psi, \tag{2.11}$$

where integration over the spatial coordinates and summation over the spin coordinates are implied. Substituting expression (2.10) for Ψ into (2.11) we obtain:

$$\begin{aligned} U_{e-e} \ &\propto \ \int\int d\mathbf{x_1} d\mathbf{x_2}\ \psi_1^*(\mathbf{x_1})\psi_2^*(\mathbf{x_2}) \frac{1}{|\mathbf{r_1} - \mathbf{r_2}|}\psi_1(\mathbf{x_1})\psi_2(\mathbf{x_2}) \\ &- \ \int\int d\mathbf{x_1} d\mathbf{x_2}\ \psi_1^*(\mathbf{x_1})\psi_2^*(\mathbf{x_2}) \frac{1}{|\mathbf{r_1} - \mathbf{r_2}|}\psi_1(\mathbf{x_2})\psi_2(\mathbf{x_1}) \\ &= \ U_e + U_x. \end{aligned} \tag{2.12}$$

The first integral in (2.12) represents the classical Coulomb energy between the two elements of the charge density distribution proportional to $|\psi_i(\mathbf{x_i})|^2$. It is called the *direct* or *Hartree* term. The second integral has the two electrons at $\mathbf{x_1}$ and $\mathbf{x_2}$ "swap" their states; it is called the *exchange* or *Fock* term. Since the single-particle wavefunctions localized one around $\mathbf{r_1}$ and the other around $\mathbf{r_2}$ overlap less than if they were localized at the same coordinate, then $|U_x| < |U_e|$. The exchange term

arises from the antisymmetric character of the fermionic state and thus constitutes a quantum correction to the classical Coulomb interaction between the electrons. Note that both U_e and $-U_x$ are real and non-negative.

In the case of N electrons, the total state of the system is described by the *Slater determinant*

$$\Psi = \frac{1}{\sqrt{N!}} \begin{vmatrix} \psi_1(\mathbf{x_1}) & \psi_2(\mathbf{x_1}) & \cdots & \psi_N(\mathbf{x_1}) \\ \psi_1(\mathbf{x_2}) & \psi_2(\mathbf{x_2}) & \cdots & \psi_N(\mathbf{x_2}) \\ \vdots & \vdots & & \vdots \\ \psi_1(\mathbf{x_N}) & \psi_2(\mathbf{x_N}) & \cdots & \psi_N(\mathbf{x_N}) \end{vmatrix} = \frac{1}{\sqrt{N!}} \det[\psi_1 \psi_2 \cdots \psi_N] \tag{2.13}$$

Here, the antisymmetry is satisfied by the mathematical property of the determinant (2.13) to change the sign under the permutation of any two columns or rows. The Coulomb integrals in the N-electron case will read:

$$U_e^{ij} \propto \int\int d\mathbf{x_1} d\mathbf{x_2}\ \psi_i^*(\mathbf{x_1}) \psi_j^*(\mathbf{x_2}) \frac{1}{|\mathbf{r_1} - \mathbf{r_2}|} \psi_i(\mathbf{x_1}) \psi_j(\mathbf{x_2}), \tag{2.14}$$

$$U_x^{ij} \propto -\int\int d\mathbf{x_1} d\mathbf{x_2}\ \psi_i^*(\mathbf{x_1}) \psi_j^*(\mathbf{x_2}) \frac{1}{|\mathbf{r_1} - \mathbf{r_2}|} \psi_i(\mathbf{x_2}) \psi_j(\mathbf{x_1}). \tag{2.15}$$

In reality, however, the actual wavefunction of a system is never a single determinant [108], which means the Coulomb interaction can not be fully described by the direct and exchange potentials alone. Rather, these correspond only to zeroth and first order terms in the expansion of the electron-electron interactions. The higher-order corrections are accounted for by the *correlation potential*

$$U_{corr} = U_{e-e} - U_e - U_x, \tag{2.16}$$

which is defined to be negative, and still smaller in the absolute value than the exchange potential. By introducing the correlation potential, we have singled out the major expressible components of the unknown Coulomb interaction and reduced the problem to the calculation of the minor correction, for which there is no explicit

analytical expression. Much effort has been devoted to calculating the correlation potential [94]. On the other hand, electron correlation can be neglected in special circumstances. This result, that we have obtained for semiconductor quantum dots, will be described in Chapter 3.

In the previous section, we defined the confinement potential U_{ext} that enters the Schrödinger equation (2.1). Here, we take account of the remaining term U_{e-e} representing the Coulomb interactions between the electrons forming the 2DEG, and then develop mechanisms to solve the Schrödinger equation in the remainder of this chapter.

The fundamental difficulty is that the potential U_{e-e} and electron wavefunctions are intertwined, hence a self-consistent calculation process has to be applied, which requires an initial assumption on the form of the potential. Section 2.5.2 describes the basic Thomas-Fermi model of the 2DEG that provides such an approximated form of U_{e-e}. A more elaborate Thomas-Fermi-Dirac model is presented in Section 2.5.3, and a comparison between the two models is given. The approximated solutions for the electron density and resulting potentials are then supplied to launch the self-consistent process in the framework of the Kohn-Sham density-functional theory in Section 2.6. Finally, we present the details of our numerical scheme in Section 2.7.

2.5.2 Thomas-Fermi model

The original idea of this model comes from the works of Thomas and Fermi in the 1920 on approximating the distribution of electrons in an atom (see e.g. Ref. [108]). The assumptions stated by Thomas that "electrons are distributed uniformly in the six-dimensional phase space for the motion of an electron at the rate of two for each h^3 of volume," and that there is an effective potential field that "is itself determined

by the nuclear charge and this distribution of electrons" were used to derive the Thomas-Fermi equation:

$$\frac{1}{2}[3\pi^2\rho(\mathbf{r})]^{2/3} - \frac{Z}{r} + \int \frac{\rho(\mathbf{r}')}{|\mathbf{r}-\mathbf{r}'|}d\mathbf{r}' = \mu_{TF}. \tag{2.17}$$

Here, $\rho(\mathbf{r})$ is the electron density, μ_{TF} is the chemical potential, Z is the atomic number, and atomic units are assumed. The terms in the equation are, respectively, the approximated electron kinetic energy, the potential energy of an electron in the field of the nucleus, and the classical part of electron-electron interactions. The Thomas-Fermi model neglects the exchange and correlation parts of the Coulomb potential.

We apply this model to the semiconductor heterostructure to obtain first-order approximation for the potentials and electron density of the 2DEG. A derivation of the Thomas-Fermi kinetic energy functional given in Appendix A is used to obtain a 2D analogue of the Thomas-Fermi equation for our system of interest. An important idea employed in the derivation is the so-called *local density approximation* (LDA). In this approximation, electronic properties are determined as functionals of the electron density by applying locally relations appropriate for a homogeneous electronic system [108]. LDA is the basis of the density-functional theory to be described in Section 2.6.

As a result, the total energy functional of the system of the 2DEG comprising N electrons can be written in terms of the electron density alone [145]:

$$E_{TF}[\rho(\mathbf{r})] = \frac{\pi\hbar^2}{2m}\int \rho^2(\mathbf{r})d\mathbf{r} + \int \rho(\mathbf{r})U_{ext}(\mathbf{r})d\mathbf{r} + \frac{1}{2}\,\frac{e^2}{4\pi\epsilon\epsilon_0}\int\int \frac{\rho(\mathbf{r})\rho(\mathbf{r}')}{|\mathbf{r}-\mathbf{r}'|}d\mathbf{r}d\mathbf{r}', \tag{2.18}$$

where the first term is the kinetic energy functional derived in the appendix, and the confinement and electron-electron energy functionals are written explicitly. Note, that the confinement potential U_{ext} is put in place of the potential of the nuclei.

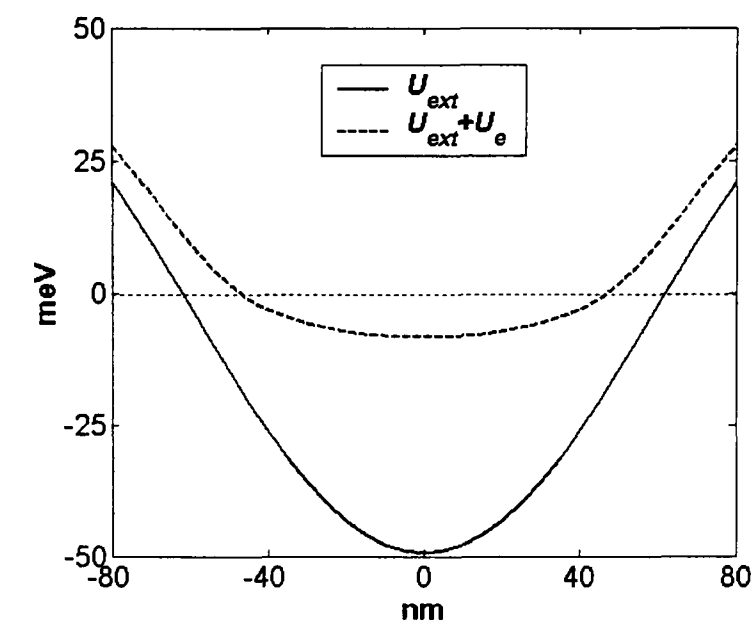


Figure 2.7: *Middle cross-section of the calculated potentials in a quantum dot at the applied gate voltage* $V_g = -0.553\,V$. *The solid line indicates the confinement potential, and the dashed line corresponds to the total Thomas-Fermi potential. The Fermi level is set at zero and is shown for reference by the dotted line.*

The electron density in the ground state should minimize the total energy of the system $E_{TF}[\rho(\mathbf{r})]$ under the normalization condition

$$N = \int \rho(\mathbf{r}) d\mathbf{r}. \tag{2.19}$$

Thus, the ground-state electron density must satisfy the variational principle

$$\delta\Big\{ E_{TF}[\rho] - \mu_{TF} \left[\int \rho(\mathbf{r}) d\mathbf{r} - N \right] \Big\} = 0, \tag{2.20}$$

where μ_{TF} is a Lagrange multiplier. We have used here elements of the functional analysis, which can be found in Ref. [108]. This yields the Euler-Lagrange equation, which after applying the SI units and the effective mass approximation ($m^* = 0.067m$ in GaAs) reads:

$$\mu_{TF} = \frac{\pi\hbar^2}{m^*}\rho(\mathbf{r}) + U_{ext}(\mathbf{r}) + \frac{e^2}{4\pi\epsilon\epsilon_0}\int \frac{\rho(\mathbf{r}')d\mathbf{r}'}{|\mathbf{r}-\mathbf{r}'|}. \tag{2.21}$$

To compensate the mirror charges of the donor layer and satisfy the boundary conditions, one has to introduce the mirror charges for the 2DEG. This is done by

locating an infinite plane charged with density $-e\rho(\mathbf{r}')$ at distance $z = c+d+s$ above the plane of the gate. The *direct Coulomb potential* now has contributions from the two oppositely charged planes with the distance of $2z$ between them:

$$U_e(\mathbf{r}) = \frac{e^2}{4\pi\epsilon\epsilon_0}\int d\mathbf{r}'\rho(\mathbf{r}')\left[\frac{1}{|\mathbf{r}-\mathbf{r}'|} - \frac{1}{\sqrt{|\mathbf{r}-\mathbf{r}'|^2+4z^2}}\right]. \tag{2.22}$$

Setting $\mu_{TF} = 0$ as the reference energy, one obtains the *2D Thomas-Fermi equation* for the electron density $\rho(\mathbf{r})$ becomes:

$$\rho(\mathbf{r}) = -\frac{m^*}{\pi\hbar^2}\big[U_{ext}(\mathbf{r}) + U_e(\mathbf{r})\big], \tag{2.23}$$

where U_{ext} is given by Eq. (2.2) and U_e by Eq. (2.22).

Since the electron density enters into the Coulomb integral, it is reasonable to solve it self-consistently. Initially, we neglect the Coulomb term and find from Eq. (2.23) the electron density determined by the confinement potential only. Next, the density is substituted into integral (2.22) to calculate the Coulomb term, which is fed back to the Thomas-Fermi equation to find a new distribution of the electron density for the next iteration (see Section 2.7).

Figure 2.7 shows the total potential $(U_{ext} + U_e)$ of a single quantum dot obtained in the Thomas-Fermi model, as compared to the bare confinement potential. One can see how the total potential is significantly raised due to the positive contribution from the electron-electron interactions. As a consequence, the electron content of the dot will decrease. Secondly, the Coulomb potential is proportional to the electron density and thus it is strong in the center of the QD and fades away at the edges. As a result, the total potential has a shape of a bowl with a flat bottom and is no longer parabolic.

2.5.3 Thomas-Fermi-Dirac model

Based on straightforward assumptions, the Thomas-Fermi model provides a fairly good and simple approximation for a variety of systems. Its main disadvantage is that being a semiclassical model it fails to predict the the quantum behaviour of a system. In particular, the Thomas-Fermi model completely ignores the spin component of the electron wavefunction, as seen in Eq. (2.23).

The main motivation for the Thomas-Fermi-Dirac model is to incorporate the electron spin effects in the simplest form. The idea is to include in the Thomas-Fermi equation the exchange potential U_x (2.15) for a uniform electron gas, despite the fact the confined 2DEG is obviously not uniform. The famous exchange-energy formula of Dirac [33] for a uniform electron gas becomes in 2D [145]:

$$K_D[\rho] = -\frac{\sqrt{2}e^2}{3\epsilon\epsilon_0\pi^{3/2}}\int \rho^{3/2}(\mathbf{r})d\mathbf{r}. \tag{2.24}$$

Substituting it into Eq. (2.18) for the total energy and similarly applying the variational principle (2.20), one obtains the *2D Thomas-Fermi-Dirac equation* for the electron density

$$\rho(\mathbf{r}) = -\frac{m^*}{\pi\hbar^2}\left[U_{ext}(\mathbf{r}) + U_e(\mathbf{r}) - \frac{e^2}{\sqrt{2}\epsilon\epsilon_0\pi^{3/2}}\rho^{1/2}(\mathbf{r})\right], \tag{2.25}$$

where the last term is the contribution from the exchange potential.[ii] To include the spin degree of freedom, the electron density is written as the sum of the densities of up- and down-spin electrons $\rho(\mathbf{r}) = \rho_\uparrow(\mathbf{r}) + \rho_\downarrow(\mathbf{r})$ and the Thomas-Fermi-Dirac equation is rewritten as a system of two equations (for $\sigma = \pm\frac{1}{2}$):

$$\rho_\sigma(\mathbf{r}) = -\frac{m^*}{2\pi\hbar^2}\left[U_{ext}(\mathbf{r}) + U_e(\mathbf{r}) + U_x^\sigma(\mathbf{r})\right]. \tag{2.26}$$

[ii] A complete derivation of the Thomas-Fermi-Dirac equation can also be found in § 6.1 of Ref. [108].

Here, the exchange term is also split into spin-dependent parts

$$U_x^\sigma(\mathbf{r}) = -\frac{e^2}{\epsilon\epsilon_0\pi^{3/2}}\sqrt{\rho_\sigma(\mathbf{r})}. \tag{2.27}$$

As a simple check, one can see that summing up the two equations (2.26) for $\sigma = +\frac{1}{2}$ and $-\frac{1}{2}$ and considering an unpolarized electron gas $\rho_\uparrow(\mathbf{r}) = \rho_\downarrow(\mathbf{r}) = \frac{1}{2}\rho(\mathbf{r})$ leads to the Thomas-Fermi-Dirac equation (2.25).

The spin up and down equations (2.26) are interdependent via the classical Hartree term $U_e(\mathbf{r})$ proportional to the total electron density and thereby have to be solved together. The computational scheme here is analogous to the Thomas-Fermi model. One subtle point is, the densities for spin up and down electrons are by default identical and will evolve in the same way during the iterative process. In this way, the 2DEG will remain unpolarized even in a situation where spin effects are expected. To avoid this scenario, we deliberately push the system out of the spin-degenerate equilibrium by applying a weak external magnetic field of 1000 Gs, or equivalently Zeeman splitting of ~ 0.01 meV. The magnetic field is chosen to favour the up ($\uparrow$) direction of the spin and may be turned off after a few iterations. As a result, the exchange potentials U_x^σ will be different for the opposite spins, and they will determine the evolution of the system to a new equilibrium state characterized by a non-zero *spin polarization*

$$p(\mathbf{r}) = \rho_\uparrow(\mathbf{r}) - \rho_\downarrow(\mathbf{r}) \tag{2.28}$$

Figure 2.8 shows the calculated electronic potentials in the Thomas-Fermi-Dirac model. The exchange term is about five times smaller in magnitude than the direct term and has an opposite sign. Even that the exchange potential is a higher-order correction to the direct term, it becomes dominant in the total potential because the direct term is for the most part cancelled out with the confinement potential. Therefore, electron exchange largely determines the 2DEG behaviour, and especially

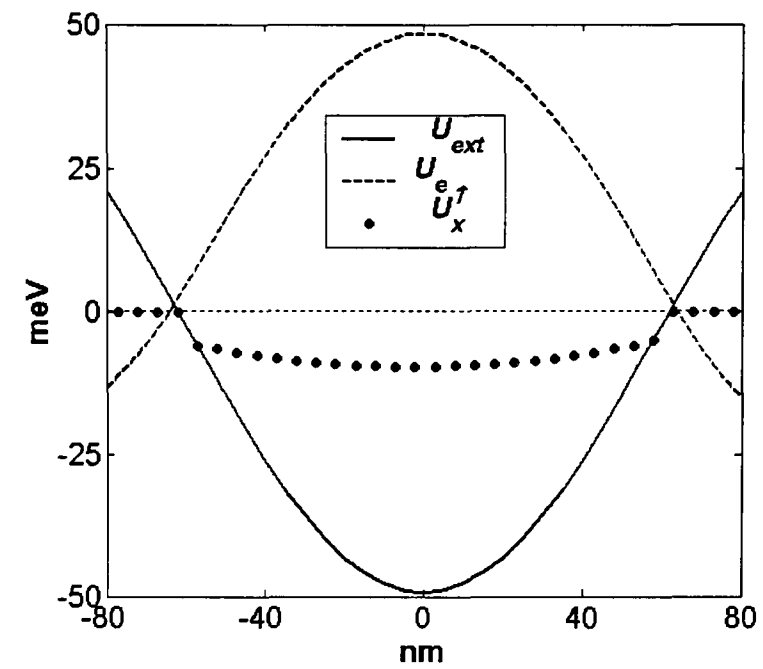


Figure 2.8: *Middle cross-section of the calculated Thomas-Fermi-Dirac potentials in a quantum dot at the applied gate voltage* $V_g = -0.553\,V$*: confinement potential (solid line), direct (dashed line) and spin-up exchange (filled circles) Coulomb potentials. The exchange term for spin-down is degenerate with the spin-up and is not shown.*

the spin configuration of the system because of its inherent spin dependance.

Note in Figure 2.8 the visible jumps in the exchange potential at $x = -60$ and 60 nm. This is due to the deliberate truncation of the electron density in the regions where the total potential is above the Fermi level. The truncation has to be done to prevent the electron density from being negative, which would formally give rise to a complex part of the exchange potential in this semi-classical model. This problem does not exist in a proper quantum description provided by the density-functional theory, as we will see in the next section.

Another question is the spin-dependent splitting of the total potential. It is determined by the difference between the up-spin and down-spin exchange terms (the remaining part of the total potential does not depend on the spin), which varies in the above example from 0.2 meV in the center of the dot to 1.6 meV at its periphery.

While the splitting does exceed the initial Zeeman splitting of 0.01 meV introduced in the model, it is not sufficient to induce any spin effects; our calculations have shown that the spin polarization of the 2DEG is negligible. The failure of the Thomas-Fermi-Dirac model to incorporate the spin-dependent behaviour of the system is in fact not surprising, because it does not describe the discrete energy spectrum and shell-filling of the artificial atoms. For that purpose, a purely quantum model is needed. When choosing the best model for an initial approximation, the Thomas-Fermi-Dirac model does not constitute any conceptual improvement over the Thomas-Fermi model,[iii] so the latter is advantageous merely because it is more simple.

However, the most useful for us result of the Thomas-Fermi-Dirac model is that it showed, if approximately, the structure of the Coulomb interaction (as the sum of the direct and exchange terms) and introduced the spin degree of freedom. Both procedures will be needed in the Kohn-Sham density-functional theory, which we are now ready to go to.

2.6 Kohn-Sham density-functional theory

2.6.1 Hohenberg-Kohn theorems

The confinement potential $U_{ext}(\mathbf{r})$ entering the Shrödinger equation (2.1) completely fixes the Hamiltonian of an N-electron system and therefore determines the electronic properties of the system's ground state. In 1964, Hohenberg and Kohn laid the foundations of the *density-functional theory* [59] by proposing to use the electron

[iii] In fact, sometimes the Thomas-Fermi model gives quantitatively better results than the Thomas-Fermi-Dirac model, e.g., in providing an estimate of the total energy of the closed-shell (noble-gas) atoms [108].

density $\rho(\mathbf{r})$ as the basic variable, in place of N and $U_{ext}(\mathbf{r})$. The *first Hohenberg–Kohn theorem* states: the external potential is determined, within a trivial additive constant, by the electron density.

The proof of this theorem is so simple that we will give it here right away. Suppose there are two external potentials $U_{ext}(\mathbf{r})$ and $U'_{ext}(\mathbf{r})$ differing by more than a constant and each giving the same $\rho(\mathbf{r})$ for the ground state. We would then have two Hamiltonians $\hat{H}$ and $\hat{H}'$ whose ground state densities are the same, although the ground state wavefunctions Ψ and Ψ' would be different. Applying the variational principle to finding the ground-state energy of $\hat{H}$ with Ψ' as a trial function, one has

$$\begin{aligned} E_0 < \langle \Psi' | \hat{H} | \Psi' \rangle &= \langle \Psi' | \hat{H}' | \Psi' \rangle + \langle \Psi' | \hat{H} - \hat{H}' | \Psi' \rangle \\ &= E'_0 + \int \rho(\mathbf{r}) [U_{ext}(\mathbf{r}) - U'_{ext}(\mathbf{r})] d\mathbf{r}, \end{aligned} \tag{2.29}$$

where E_0 and E'_0 are the ground-state energies for $\hat{H}$ and $\hat{H}'$, respectively. Similarly, taking Ψ as a trial function for the $\hat{H}'$ problem,

$$\begin{aligned} E'_0 < \langle \Psi | \hat{H}' | \Psi \rangle &= \langle \Psi | \hat{H} | \Psi \rangle + \langle \Psi | \hat{H}' - \hat{H} | \Psi \rangle \\ &= E_0 - \int \rho(\mathbf{r}) [U_{ext}(\mathbf{r}) - U'_{ext}(\mathbf{r})] d\mathbf{r}. \end{aligned} \tag{2.30}$$

Adding (2.29) and (2.30), we obtain a contradictory relation $E_0 + E'_0 < E'_0 + E_0$. Therefore the external potential – and all properties of the ground state – are uniquely determined by the electron density $\rho(\mathbf{r})$.

The *second Hohenberg–Kohn theorem* states that the ground-state electron density minimizes the total energy of the system. The latter can be written as

$$E[\rho] = \int \rho(\mathbf{r}) U_{ext}(\mathbf{r}) d\mathbf{r} + F[\rho], \tag{2.31}$$

where

$$F[\rho] = T[\rho] + V_{ee}[\rho] \tag{2.32}$$

is the functional consisting of the kinetic energy and the energy of electron-electron interactions. According to the energy variational principle, the ground-state electron density has to satisfy the condition:

$$\delta\Big\{E[\rho] - \mu\left[\int \rho(\mathbf{r})d\mathbf{r} - N\right]\Big\} = 0 \tag{2.33}$$

in the same way as described for the Thomas-Fermi model (c.f. (2.20)). This leads to the Euler-Lagrange equation:

$$\mu = U_{ext}(\mathbf{r}) + \frac{\delta F[\rho]}{\delta\rho(\mathbf{r})}. \tag{2.34}$$

$F[\rho]$ is defined independently of the external potential, which means that it is a universal functional of $\rho(\mathbf{r})$. If we knew it exactly, then Eq. (2.34) would be an exact equation for the ground-state density of any system. Unfortunately, the functional $F[\rho]$ is hard to come by, and the challenge is to find the best approximate form for it, while not making it too complex. For that reason, we have chosen the *local spin-density approximation* (LSDA) based on the Kohn-Sham equations.

2.6.2 Kohn-Sham equations

In a trade of simplicity for accuracy, Kohn and Sham invented an indirect approach to the kinetic-energy functional $T[\rho]$. They proposed introducing orbitals into the problem in such a way that the kinetic energy can be calculated simply to good accuracy leaving a small residual correction that is handled separately.

The exact formula for the ground-state kinetic energy is

$$T = \sum_i n_i \langle\psi_i| -\frac{1}{2}\nabla^2|\psi_i\rangle, \tag{2.35}$$

where ψ_i and n_i are electron orbitals and their occupation numbers, $0 \leq n_i \leq 1$ due

to the Pauli principle. The total electron density is given by

$$\rho(\mathbf{r}) = \sum_i n_i \sum_\sigma |\psi_i(\mathbf{r},\sigma)|^2. \tag{2.36}$$

For any interacting system, each of N electrons can in principle occupy any state with a corresponding occupation number, so expressions (2.35) and (2.36) would contain an infinite number of terms. The basic idea of the Kohn-Sham theory is to replace an interacting system with a noninteracting reference system of N electrons, which has exactly the same ground-state electron density ρ. The Hamiltonian of the new system

$$\hat{H}_{ref} = \sum_{i=1}^{N}(-\frac{1}{2}\nabla_i^2) + \sum_{i=1}^{N} U_{ref}(\mathbf{r}_i), \tag{2.37}$$

does not contain electron-electron interactions and can be decomposed into N independent one-electron Hamiltonians, all of which are equivalent. In this special case $n_i = 1$ for N orbitals and $n_i = 0$ for the rest, and the Kohn-Sham kinetic energy of the new system is described by a simplified formula

$$T_{ref} = \sum_{i=1}^{N} \langle\psi_i| -\frac{1}{2}\nabla^2|\psi_i\rangle, \tag{2.38}$$

where ψ_i are the N lowest eigenstates of the one-electron Hamiltonian:

$$\big[-\frac{1}{2}\nabla^2 + U_{ref}(\mathbf{r})\big]\psi_i = \varepsilon_i\psi_i. \tag{2.39}$$

Note that the quantity T_{ref} is not equal to the kinetic-energy functional $T[\rho]$, but plays the same role for the non-interacting reference system and can be accurately calculated exactly. The major simplification of the resultant theory is its independent-particle form. To produce the desired separation, rewrite Eq. (2.32) as

$$F[\rho] = T_{ref}[\rho] + J[\rho] + E_{xc}[\rho],$$

where $J[\rho]$ is the classical Coulomb energy and

$$E_{xc}[\rho] = T[\rho] - T_{ref}[\rho] + V_{ee}[\rho] - J[\rho], \tag{2.40}$$

is the *exchange-correlation energy.* Note that in the Kohn-Sham approximation, it contains not only the non-classical part of electron-electron interactions (c.f. Eq. (2.16)) but also the difference between T and T_{ref}, presumably fairly small. The Euler-Lagrange equation (2.34) now becomes

$$\mu = U_{eff}(\mathbf{r}) + \frac{\delta T_{ref}[\rho]}{\delta \rho(\mathbf{r})}, \tag{2.41}$$

where the *Kohn-Sham effective potential* is defined by

$$\begin{aligned} U_{eff}(\mathbf{r}) &= U_{ext}(\mathbf{r}) + \frac{\delta J[\rho]}{\delta \rho(\mathbf{r})} + \frac{\delta E_{xc}[\rho]}{\delta \rho(\mathbf{r})} \\ &= U_{ext}(\mathbf{r}) + U_e(\mathbf{r}) + U_{xc}(\mathbf{r}) \end{aligned} \tag{2.42}$$

with the *exchange-correlation potential*

$$U_{xc}(\mathbf{r}) = \frac{\delta E_{xc}[\rho]}{\delta \rho(\mathbf{r})}. \tag{2.43}$$

Finally, the ground-state *Kohn-Sham electron density* that satisfies Eq. (2.41) for a given potential $U_{eff}(\mathbf{r})$ can be obtained by solving the one-electron equations

$$\Big[-\frac{1}{2}\nabla^2 + U_{eff}(\mathbf{r}) \Big] \psi_i = \varepsilon_i \psi_i. \tag{2.44}$$

and setting

$$\rho(\mathbf{r}) = \sum_{\varepsilon_i \leq \mu} \sum_{\sigma} |\psi_i(\mathbf{r}, \sigma)|^2. \tag{2.45}$$

Once the solution for the ground-state density is found, every other property of the system can be formally obtained, as verified by the first Hohenberg–Kohn theorem. Eqs. (2.42)–(2.45) are called the *Kohn-Sham equations.*

2.6.3 Exchange-correlation potential

The Kohn-Sham equations have provided an exact treatment of the kinetic energy, and the only remaining question is to calculate the exchange-correlation energy $E_{xc}[\rho]$.

The search for an accurate form of $E_{xc}[\rho]$, however, continues to be the greatest challenge of the density-functional theory [94]. In this section, we address the problem by applying the local density approximation (LDA) that we already used to derive the kinetic energy of the Thomas-Fermi model. According to the LDA, we assume that the exchange-correlation energy for a nonuniform system can be obtained by applying locally the uniform-gas results to infinitesimal portions of the electron distribution, each having $\rho(\mathbf{r})d\mathbf{r}$ electrons, and then summing over all space the individual contributions:

$$E_{xc}[\rho] = \int \rho(\mathbf{r})\varepsilon_{xc}(\rho)d\mathbf{r}. \tag{2.46}$$

Here ε_{xc} indicates the exchange-correlation energy per particle of a uniform electron gas of density $\rho(\mathbf{r})$.

To explicitly include the spin degree of freedom into the Kohn-Sham equations, we proceed in the same spirit as in the Thomas-Fermi-Dirac model described in Section 2.5.3. Such an extension of the LDA constitutes the *local spin-density approximation* (LSDA).

The Kohn-Sham equation (2.44) splits up in two spin components[iv] for $\sigma = \pm\frac{1}{2}$

$$\Big[-\frac{1}{2}\nabla^2 + U_{ext}(\mathbf{r}) + U_e(\mathbf{r}) + U^\sigma_{xc}(\mathbf{r})\Big]\psi^\sigma_i(\mathbf{r}) = E^\sigma_i\psi^\sigma_i(\mathbf{r}). \tag{2.47}$$

Since the exchange-correlation energy can be divided into the exchange and correlation contributions, $\varepsilon_{xc}(\rho) = \varepsilon_x(\rho) + \varepsilon_c(\rho)$, one can rewrite the corresponding potential as

$$U^\sigma_{xc} = U^\sigma_x + U^\sigma_c, \tag{2.48}$$

where the exchange part U^σ_x can be locally represented by Dirac's formula (2.27) for a uniform electron gas, a reasonable approximation within the LDA. Unfortunately, there is no closed analytical form for the electron correlation potential U^σ_c. In the

[iv] For more details, see § 8 in Ref. [108].

	$\zeta = 0$	$\zeta = 1$
$a_{0\zeta}$	-0.3568	-0.0515
$a_{1\zeta}$	1.1300	340.5813
$a_{2\zeta}$	0.9052	75.2293
$a_{3\zeta}$	0.4165	37.017

Table 2.1: *Fitting coefficients of the correlation energy $\varepsilon_c(\rho)$ for the fully polarized ($\zeta = 1$) and non-polarized ($\zeta = 0$) 2DEG obtained from the quantum Monte Carlo calculations, from Ref. [135].*

following, we develop formalism to obtain a parameterized form of the correlation potential using the accurate values of $\varepsilon_c(\rho)$ obtained by the quantum Monte Carlo calculations for a spin-polarized and unpolarized 2DEG [135].

The main parameter, the normalized spin polarization of the 2DEG, is defined as

$$\zeta = \frac{\rho_\uparrow - \rho_\downarrow}{\rho_\uparrow + \rho_\downarrow}, \tag{2.49}$$

and we assume for the moment the effective atomic units $Ry^* = m^* e^4 / 2\hbar^2 (4\pi\varepsilon\varepsilon_0)^2$ and $a_B^* = \hbar^2 (4\pi\varepsilon\varepsilon_0)/m^* e^2$. In the two limiting cases of the fully polarized ($\zeta = 1$) and non-polarized ($\zeta = 0$) 2DEG, the corresponding correlation energies $\varepsilon_{c\zeta}$ can be fitted [135] as

$$\varepsilon_{c\zeta} = a_{0\zeta} \frac{1 + a_{1\zeta} x}{1 + a_{1\zeta} x + a_{2\zeta} x^2 + a_{3\zeta} x^3}, \tag{2.50}$$

where $x = \sqrt{r_s} = (a_B^* \sqrt{\pi\rho})^{-1/2}$ is the density parameter, and the coefficients $a_{i\zeta}$ are given in Table 2.1. For the general case, $0 < \zeta < 1$, the following interpolation has been used [88, 79]

$$\varepsilon_c(\rho, \zeta) = \varepsilon_c(\rho, 1) + [\varepsilon_c(\rho, 0) - \varepsilon_c(\rho, 1)] f(\zeta),$$

$$f(\zeta) = \frac{(1+\zeta)^{3/2} + (1-\zeta)^{3/2} - 2\sqrt{2}}{2 - 2\sqrt{2}}. \tag{2.51}$$

Since there are two components of the electron density, $\rho_\uparrow$ and $\rho_\downarrow$, the spin-dependent correlation potential becomes

$$U_c^\sigma(\mathbf{r}) = \frac{\delta E_c[\rho_\uparrow, \rho_\downarrow]}{\delta \rho(\mathbf{r})} = \frac{\partial(\rho\varepsilon_c)}{\partial \rho_\sigma} \tag{2.52}$$

which after a transformation from $\{\rho_\uparrow, \rho_\downarrow\}$ to a new set of independent variables $\{\rho = \rho_\uparrow + \rho_\downarrow, \zeta = (\rho_\uparrow - \rho_\downarrow)/\rho\}$ leads to the equations

$$\begin{aligned} U_c^\uparrow(\mathbf{r}) &= \frac{\partial}{\partial\rho}(\rho\varepsilon_c) + (1-\zeta)\frac{\partial\varepsilon_c}{\partial\zeta} \\ U_c^\downarrow(\mathbf{r}) &= \frac{\partial}{\partial\rho}(\rho\varepsilon_c) - (1+\zeta)\frac{\partial\varepsilon_c}{\partial\zeta}. \end{aligned} \tag{2.53}$$

After taking the partial derivatives in Eq. (2.53) and putting Eqs. (2.50)–(2.53) together, one obtains an explicit parameterized form of the spin-dependent electron correlation potentials:

$$\begin{aligned} U_c^\uparrow &= Ry^*\Big\{\varepsilon_{c1} - \frac{x}{4}\big[(1-f)\frac{d\varepsilon_{c1}}{dx} + f\frac{d\varepsilon_{c0}}{dx}\big] \\ &+ (\varepsilon_{c0} - \varepsilon_{c1})\frac{(5-\zeta)(1+\zeta)^{1/2} - (1-\zeta)^{3/2} - 4\sqrt{2}}{4-4\sqrt{2}}\Big\} \end{aligned}$$

$$\begin{aligned} U_c^\downarrow &= Ry^*\Big\{\varepsilon_{c1} - \frac{x}{4}\big[(1-f)\frac{d\varepsilon_{c1}}{dx} + f\frac{d\varepsilon_{c0}}{dx}\big] \\ &+ (\varepsilon_{c0} - \varepsilon_{c1})\frac{(5+\zeta)(1-\zeta)^{1/2} - (1+\zeta)^{3/2} - 4\sqrt{2}}{4-4\sqrt{2}}\Big\} \end{aligned} \tag{2.54}$$

Now we can rewrite Eq. (2.44) to obtain the *2D Kohn-Sham equations* for $\sigma = \pm\frac{1}{2}$ electrons in the final form:

$$-\frac{\hbar^2}{2m^*}\left(\frac{\partial^2}{\partial x^2} + \frac{\partial^2}{\partial y^2}\right)\psi_i^\sigma(x,y) + [U_{ext} + U_e + U_x^\sigma + U_c^\sigma + g^*\mu_B H\sigma]\psi_i^\sigma(x,y) = E_i^\sigma\psi_i^\sigma(x,y), \tag{2.55}$$

where the confinement potential U_{ext} is given by (2.2), the direct term U_e including the mirror charges is given by (2.22), the exchange term U_x^σ by (2.27), and the correlation

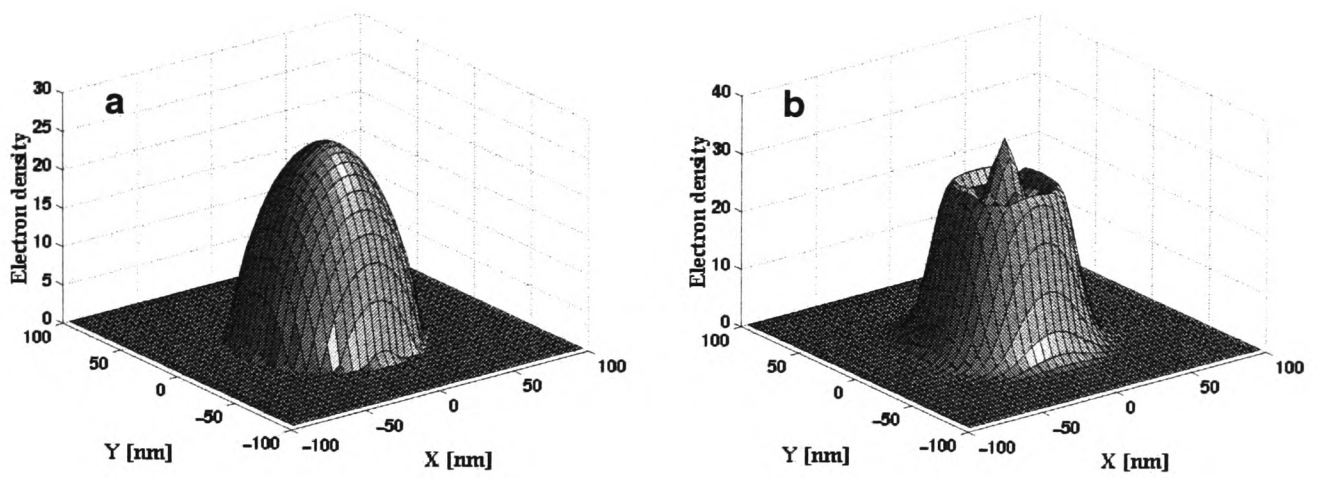


Figure 2.9: *Calculated total electron density of a single symmetric quantum dot at gate voltage* $V_g = -0.553$ *V [in units of* 10^{-4} nm^{-2}*]: (a) in the Thomas-Fermi approximation, where the dot is occupied with* 12 *electrons; (b) in the Kohn-Sham LSDA, where the dot is occupied with* $N^{\uparrow} = 8$ *and* $N^{\downarrow} = 6$ *electrons.*

potential U_c^{σ} by (2.54). The last term in the brackets is the weak magnetic field (0.01 meV or roughly 1000 Gs) introduced to trigger the spontaneous spin polarization (see the discussion in Section 2.5.3).

The Kohn-Sham equations (2.55) are solved together with the spin-dependent electron density (2.45) numerically for our specific devices by applying a self-consistent process. The results of our numerical simulations will be presented in Chapter 3.

As an example, Figure 2.9 shows the total electron density of a single quantum dot at $V_g = -0.553$ V, calculated in the Kohn-Sham LSDA as compared to the result of the Thomas-Fermi model. In both cases, the shape of the electron density has a rotational symmetry provided by the symmetric confinement potential. However, the Kohn-Sham density (on the right) shows radial oscillations, which are to a large extent determined by the structure of the energy levels and by the profile of the exchange-correlation potential.

Another main distinction is that the electron distribution in the LSDA shows a non-zero spin polarization of the dot ($N^{\uparrow} \neq N^{\downarrow}$) and a higher density than in

the Thomas-Fermi approximation (the dot is occupied by 14 and 12 electrons, respectively). The latter effect can be explained by the negative contribution of the exchange-correlation potential, which favours higher occupation numbers.

2.6.4 Discussion

A few important comments should be made about the developed theoretical model before we proceed with aspects of the numerical simulations.

Mirror charges

The contribution of the mirror charges, although accurately accounted for the confinement and direct Coulomb potentials, has been left out for the exchange-correlation potential. While including this term would obviously improve the model, the way to do that is currently unknown. In fact, this remains an open theoretical question [94] in the physics community that has not been solved within the scope of this thesis.

Spin-orbit interaction

Another term omitted in the model is the spin-orbit interaction (SOI). It is known that the SOI potential is responsible for the splitting of the hole states (the split-off subband with the total angular momentum $J = \frac{1}{2}$ from the heavy-hole and light-hole subbands with $J = \frac{3}{2}$) in the valence band of semiconductors [151]. On the other hand, it is considered to be less significant for the conduction band electrons in GaAs [64]. Here we estimate the effects of the SOI on our system by applying the formalism of Refs. [65, 66].

The SOI potential is defined as $U_{SOI} = \alpha\, \mathbf{l} \cdot \sigma$, where $\mathbf{l}$ and σ are the orbital and spin angular momenta of an electron. The coupling constant α can be obtained in

zeroth order as

$$\alpha = \frac{1}{3}\beta\hbar\Omega_0\sqrt{N}, \tag{2.56}$$

where $\beta = 0.5$ is a dimensionless fitting parameter for a quasi-2D GaAs quantum dot, N is the number of conduction band electrons in the dot, and $\Omega_0 = \omega_0(100a_B^*/27\pi R_0)^{1/2}$ is the effective frequency of the confinement potential. We take $\hbar\omega_0 = 5$ meV as the confinement energy and $a_B^* = 10$ nm as the effective Bohr radius, whereas the radius of the dot R_0 is approximated as

$$R_0 = \left(\frac{3\pi N e^2}{4\epsilon m^* \omega_0^2}\right)^{1/3} = \left[\frac{3\pi N e^4 a_B^*}{8\epsilon(\hbar\omega_0)^2}\right]^{1/3}.$$

As a result, we obtain for a GaAs quantum dot that $\alpha = 0.44N^{1/3}$ meV, where N is the electron occupation number of the quantum dot.

For a typical multi-electron quantum dot occupied with $N = 36$ electrons and having an average angular momentum $\langle l \rangle \approx 3$, the SOI potential is estimated as ~ 2.2 meV. At the same time, the exchange-correlation potential as calculated by our model reaches ~ 11 meV in absolute value at the center of the dot and goes to zero at the edges. Hence, a factor of five difference in magnitudes of the two potentials allows us to neglect the effects of the SOI. This assumption works the better, the fewer electrons occupy the QD.

Justification of DFT

Formally, the local spin-density approximation as a part of the density-functional theory is applicable only to systems with slowly-varying electron densities, which may not be the case for highly inhomogeneous systems such as atoms, molecules, and to a lesser extent semiconductor nanostructures. However, in the situation where an exact analytical solution is impossible, the ultimate criterion of validity of a certain

model is its comparison with the experimental results and, perhaps, with the results of other models.

In this respect, the DFT is doing well predicting lattice constants, atomic positions, elastic properties and phonon frequencies with errors smaller than a few percent [14]. It provided a better estimate than the Hartree–Fock model for the binding energies of N_2 and CO molecules [108]. The DFT-based quantum molecular dynamics simulations of the C_{60} molecules agreed almost perfectly with the neutron scattering data and were, in fact, used for the initial calibration of the experimental setup [161, 27]. The overall success of the DFT was acknowledged by the 1998 Nobel Prize in chemistry that Walter Kohn shared with John Pople.

An advantage of the local spin-density approximation is the accurate and relatively simple treatment of systems containing many (up to 10^3) electrons, for which the exact diagonalization methods no longer work and semiclassical models like Thomas-Fermi and Thomas-Fermi-Dirac are oversimplified. The only comparable method, the Hartree–Fock model, does not account for the correlation potential and also is more complex in the implementation.

To summarize, successful numerical calculations together with the simplicity in describing many-electron systems provide an essential justification for the use of the DFT.

2.7 Numerical scheme

2.7.1 Finding eigenstates

We solve the differential Kohn-Sham equations (2.55) by the *discretization method*, which has been long used in first-principles calculations because of its simplicity [100].

We discretize the x–y plane into a grid of $N_i \times N_j$ elements. The second derivatives of the wavefunctions in the equations are replaced by the finite differences in the following way:

$$D_i\psi = \psi^\sigma_{i-1,j} - 2\psi^\sigma_{i,j} + \psi^\sigma_{i+1,j} \; ; \quad \delta_i = x_{i+1} - x_i$$
$$D_j\psi = \psi^\sigma_{i,j-1} - 2\psi^\sigma_{i,j} + \psi^\sigma_{i,j+1} \; ; \quad \delta_j = y_{j+1} - y_j$$

$$-\frac{\hbar^2}{2m^*}\left(\frac{D_i\psi^\sigma}{\delta_i^2} + \frac{D_j\psi^\sigma}{\delta_j^2}\right) + U^\sigma_{ij}\ \psi^\sigma_{i,j} = E^\sigma\psi^\sigma_{i,j}, \tag{2.57}$$

where i, j denote the discretization indices along x and y, and δ_i and δ_j are the corresponding spacings between the adjacent nodes. $\psi^\sigma_{i,j}$ and U^σ_{ij} are the values of the spin-dependent wavefunction and total potential for $\sigma \pm \frac{1}{2}$ at a point (x_i, y_j) of the 2DEG plane, and E^σ is an energy eigenstate.

In the following, we consider a square grid, such that $N_i = N_j = 2N_0$. It is convenient to perform an index transformation to convert a 2D grid into a 1D string by defining $n = 2N_0(i-1) + j$, which gives a system of equations

$$-\frac{\hbar^2}{2m^*}\left(\frac{\psi^\sigma_{n-2N_0} + \psi^\sigma_{n+2N_0}}{\delta_i^2} + \frac{\psi^\sigma_{n-1} + \psi^\sigma_{n+1}}{\delta_j^2}\right) + \left[\frac{2}{\delta_i^2} + \frac{2}{\delta_j^2} + U^\sigma_n\right]\psi^\sigma_n = E^\sigma\psi^\sigma_n \tag{2.58}$$

for $n = 1, 2, ..., 4N_0^2$ with the zero conditions on the wavefunction at the boundaries of the grid

$$\psi^\sigma_n = 0 \quad \begin{cases} 1 \le n \le N_0, \\ 4N_0^2 - 2N_0 - 1 \le n \le 4N_0^2, \\ n = 2N_0k \ \text{ for } \ 1 < k < 2N_0. \end{cases} \tag{2.59}$$

To satisfy this boundary condition, we define the region covered with the grid to be bigger than the area occupied by the confined 2DEG. Of course, by increasing the voltage on the gate and introducing more electrons into the 2DEG, new quantum states will be occupied that spread out in space, ultimately reaching the grid boundaries. In the quantum dot case, electrons in the low-lying states will be confined by

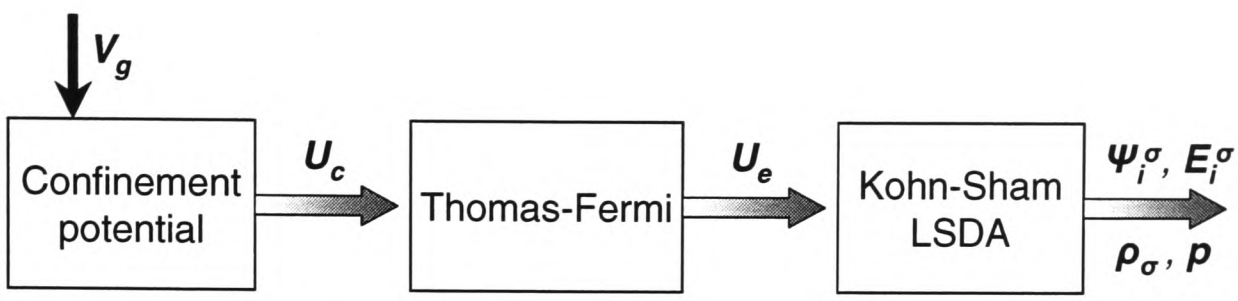


Figure 2.10: *Modelling algorithm consists of three blocks. Separate codes were written for each block and data passed on as shown by the horizontal arrows. The variable device parameters, including the gate voltage V_g, were supplied (vertical arrow) to calculate the corresponding confinement potential. The calculated potential distributions were communicated between the blocks to obtain at the output the eigenstates ψ_i^σ, E_i^σ, electron densities $\rho_\sigma(\mathbf{r})$, and spin polarization $p(\mathbf{r})$.*

a roughly parabolic total potential, whereas electrons in the high-lying, less localized states may be bouncing against an infinite potential barrier imposed by the boundary condition (2.59). The spectrum of the energy eigenstates will reflect this change of the potential by going from a nearly linear (in the parabolic well) to quadratic (in the hard-wall potential) form. Having this as a check, it is always possible to define the grid region big enough that the energy states below the Fermi level are well confined within the boundaries.

Another consequence of discretizing on a grid is that the calculated spectrum consists of $4N_0^2$ states, whereas the original energy spectrum of the system is discrete but infinite. However, this does not present a problem, since the we are interested in the lowest N levels below the Fermi energy, but not in the whole spectrum. One should only choose the grid spacings δ_i and δ_j small enough to make sure that $N \ll 4N_0^2$. In the modelling we have used the spacings of 5 and 10 nm, which satisfy the above condition, and on the other hand do not exceed the effective Bohr radius in GaAs ($\sim$ 10 nm) providing a reasonable discretization.

The Hamiltonian is now given by a five-diagonal matrix:

$$H_{n,n} = \frac{\hbar^2}{m^*}\left(\frac{1}{\delta_i^2} + \frac{1}{\delta_j^2}\right) + U_n$$
$$H_{n,n-2N_0} = H_{n-2N_0,n} = -\frac{\hbar^2}{2m^*} \tag{2.60}$$
$$H_{n,n+1} = H_{n+1,n} = \begin{cases} 0 & \text{if } n = 2N_0k \text{ and } 1 \leq k \leq 2N_0 \\ -\frac{\hbar^2}{2m^*} & \text{otherwise} \end{cases}$$

All the other elements of the matrix are zero. For our device geometries, the typical grids cover regions of 600×600 nm^2 with the 10 nm spacing, and 200×200 nm^2 with the 5 nm spacing, which leads to the Hamiltonian matrix sizes of $2N_0 = 3600$ and 1600. Since the complexity of the problem increases as N_0^2 to N_0^3, the computational overhead becomes a major challenge.

Fortunately, there are two circumstances that greatly facilitate finding the eigenstates: 1) The Hamiltonian is a sparse matrix. 2) We only need to solve for the N lowest eigenstates. Making use of these two issues has enabled us to find self-consistent solutions typically in less than an hour on a Pentium-IV computer with 1 Gb RAM.

The simulation code was written using the MATLAB 5.2 software package [164] useful here because of the built-in advanced matrix calculus, extensive math function library, and good visualization tools. The modelling was implemented in the way shown in Figure 2.10. Separate codes were written for each block of the graph to calculate the confinement potential for the input parameters of the device, the total Thomas-Fermi potential serving as an initial approximation for the Kohn-Sham LSDA equations, and finally to obtain the self-consistent solutions for the energy eigenstates and eigenvectors, electron densities and spin polarization. The core routine used for finding the energy spectrum and wavefunctions of the system of the Kohn-Sham equations (2.57) is `sptarn` from the partial differential equation toolbox, which solves

a generalized sparse eigenvalue problem in a specified interval of energies. The codes are available from the author upon request.

2.7.2 Self-consistency

As was mentioned before, a self-consistent process has to be developed to solve the Kohn-Sham LSDA equations. Usually one chooses an initial approximated form of the total potential, which is inserted into Eq. (2.57), whose solution yields the first-iteration wavefunctions and eigenenergies. It is desirable that the initial total potential has a 'realistic' shape, in order to accelerate the convergence of the iteration process. For that reason, we used the Thomas-Fermi model, which itself was solved self-consistently (with the total potential initially approximated by the bare confinement potential).

The electron density is calculated according to formula (2.45) from the eigenstates obtained at the same iteration and substituted to calculate the total potential at the next iteration. The procedure is repeated until self-consistency is reached. In our case, the process stops when the calculated eigenenergies in successive iterations are identical to an accuracy of 10^{-5} eV.

In practice, the iterative scheme tends to be unstable unless the newly calculated potential at each iteration is mixed with its value at the previous step

$$U^{i+1} = \alpha U^{i-1} + (1-\alpha)U^{i} \tag{2.62}$$

before further going into equations. The mixing parameter α lies in the interval (0,1), its purpose being to dampen the iterative oscillations of the Coulomb integrals. Decreasing the value of α, in principle, reduces the number of iterations but increases the risk of oscillations. In our calculations $\alpha = 0.95$, which typically requires ~ 300 iterations to achieve the desired numerical accuracy.

Chapter 3

Numerical simulations of spin-polarization effects in modulation-doped quantum dots

3.1 The role of exchange and correlation potentials in 2DEG-based quantum dots

Published in: I. I. Yakimenko, A. M. Bychkov, and K.-F. Berggren, *On the role of electron exchange and correlation in semiconductor quantum dots*, Nanotechnology 12, 529 (2001).

Having developed the analytical expressions for the exchange and correlation potentials in the previous chapter, we were able to evaluate their relative effects on the spin properties of the artificial atoms based on the modulation-doped heterostructures. The results of these calculations are presented in this section.

We have simulated a single symmetric quantum dot (formed by a split gate shown in Figure 2.5a) at different applied gate voltages, which changed the size and electron content of the confined 2DEG. Analysis of the electron density distributions for up and down-spin electrons shows a rich variety of spin polarizations $p(\mathbf{r}) = \rho_{\uparrow}(\mathbf{r}) - \rho_{\downarrow}(\mathbf{r})$

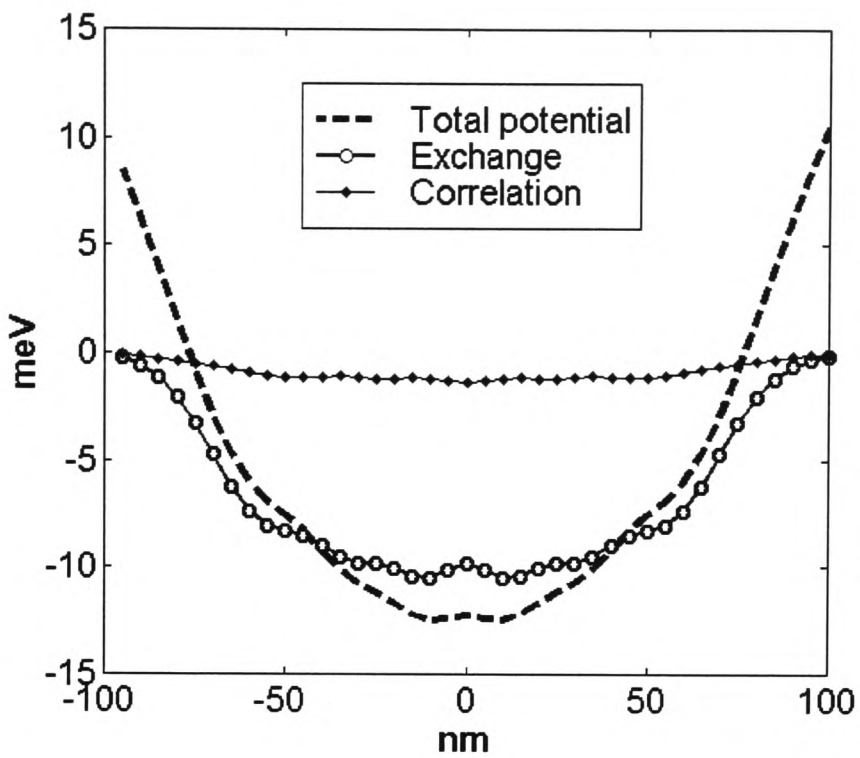


Figure 3.1: *Electronic potentials in the quantum dot (middle cross-section): exchange (white circles) and correlation (black diamonds); the total Kohn-Sham potential (dashed line) is also shown for reference.*

at no applied magnetic fields, which depend on the number of electrons occupying the dot, as will be discussed in Section 3.2.

Here, our goal is to look more closely into the nature of the spontaneous spin polarization due to the exchange-correlation potential. It is known that exchange favours the ferromagnetic alignment of the electron spins making, e.g., up-spin states have lower energy as compared to the down-spin states. Intuitively, this can be understood from Dirac formula (2.27), where the exchange potential is proportional to $-\sqrt{\rho^{\sigma}(\mathbf{r})}$ thereby favouring an increase in the electron density with the same direction of the spin. The effect of correlation is the opposite.

The contributions of the two terms are, however, not equal. Figure 3.1 presents the potentials for up-spin electrons across the quantum dot (the results for down-spin are similar). In the center of the dot where electron density is maximal, the exchange

potential is about an order of magnitude larger than the correlation one. Although both potentials are negative, the peaks (local maxima) of exchange correspond spatially to the dips (local minima) of correlation. Thus, indeed the two terms counteract each other, but on a different scale.

To confirm this finding, we have calculated the energy spectra in the case of the total potential and in the case where correlation was neglected, see Figure 3.2. The applied gate voltage corresponds to a quantum dot containing 21 up-spin electrons and 15 down-spin electrons. Symmetric two-dimensional confinement gives rise to the atomic-like *shell structure* of the quantum dot energy spectrum, whereby successive shells are formed by degenerate energy levels of up and down spins (2, 4, 6, etc.) The steps between the shells are determined by the strength of the confinement potential. Furthermore, the exchange–correlation interaction splits the levels for up and down-spin electrons. In the polarized case shown here the splitting is large enough that the uppermost shell is filled only with up-spin electrons. As a result, the quantum dot is occupied with electrons of the preferred spin orientation, or in other words, is spontaneously magnetized.

The splitting of the levels on the left (Figure 3.2a) is reduced compared to the exchange-only case (Figure 3.2b), but the effect of correlation is not strong enough to bring the states of opposite spins together, nor to change the total magnetization of the dot. The negative sign of the correlation potential also results in a small downshift of the levels of both spins, which gives rise to the spatial redistribution of the electron densities, see Figure 3.3. One can see that the spin polarization is more uniform in the presence of electron correlation, but the total spin (magnetic moment) and shell-filling of the dot remains the same in this case.

For other gate voltages one may find slight variations in the electron content. In order to preserve the number of electrons in the dot one would therefore have to

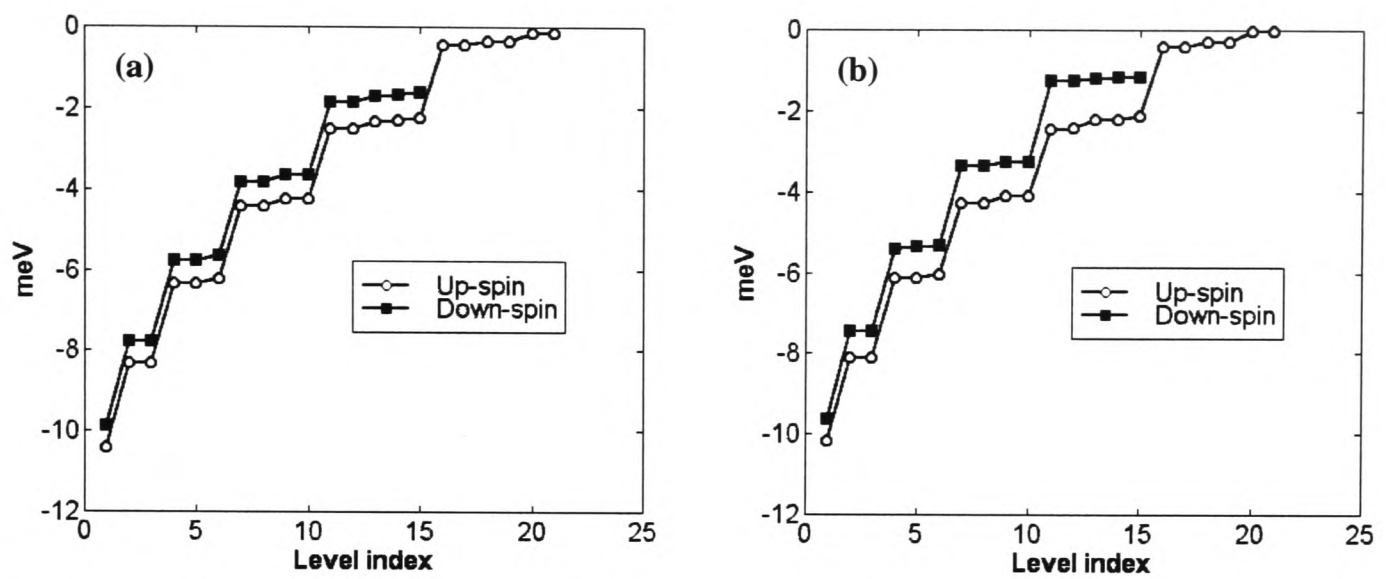


Figure 3.2: *Spin-split energy levels of a magnetized quantum dot. At a given gate voltage, the dot is occupied with 21 up-spin and 15 down-spin electrons. (a) The total Kohn-Sham potential includes both electron exchange and correlation terms; (b) simplified model with neglected correlation.*

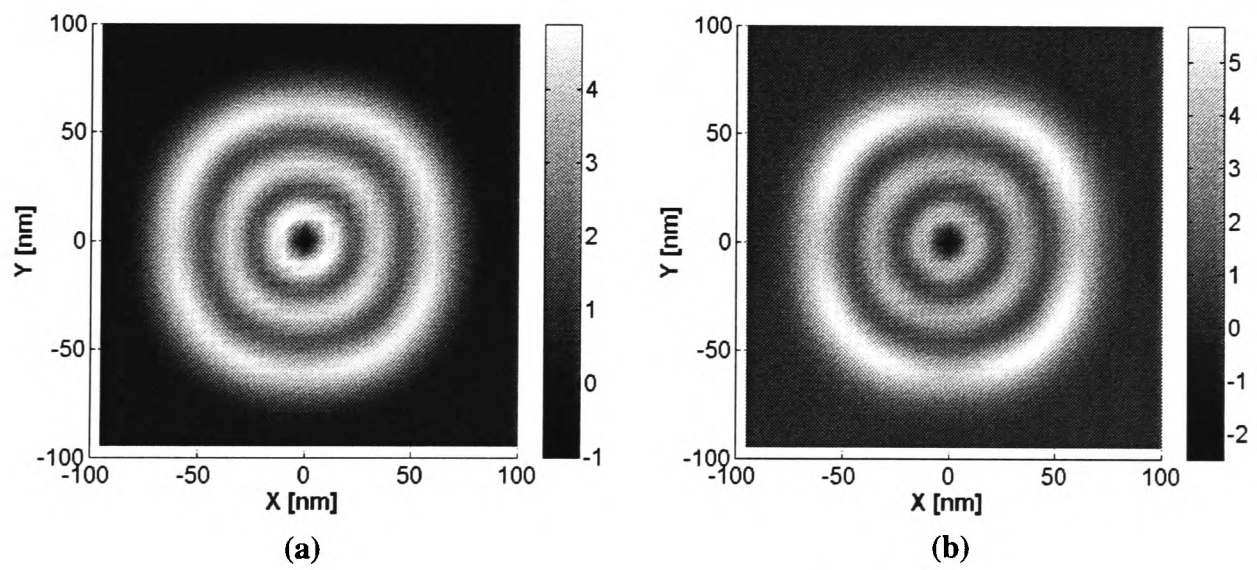


Figure 3.3: *Spin polarization of the quantum dot, top view in the 2DEG plane: (a) modelling includes exchange and correlation, (b) correlation is neglected. The bars on the right show the scale [in units of* 10^{-4} nm^{-2}*].*

make a small readjustment of the gate voltage. At gate voltages corresponding to an unpolarized case, or to spin-density wave state (oscillations in spin-density but no net magnetization, see Section 3.2), the splitting of up and down-spin electrons is initially suppressed and correlation only shifts the degenerate states downwards. As above our calculations suggest that this effect be compensated for by a slight adjustment of the gate voltage.

In conclusion, we have demonstrated that the exchange potential in the Kohn-Sham equations provides the dominant mechanism that drives spontaneous magnetization in the kind of symmetric quantum dots we consider here, while the correlation part turns out to play a minor role in the spin related behavior. Hence one may omit the correlation term in the Kohn-Sham potential in many calculations of the electronic structure of $GaAs/Al_xGa_{1-x}As$ quantum dots, which would simplify the theoretical model conceptually and reduce the amount of the computational burden.

In the following sections of this chapter, we apply this result to perform numerical studies of the spin-related properties of quantum-dot systems according to a simplified, exchange-only model.

3.2 Magnetic properties of modulation-doped quantum dots

Published in: I. I. Yakimenko, A. M. Bychkov, and K.-F. Berggren, *Symmetry and spin polarization in single and coupled quantum dots*, Physical Review B 63, 165309 (2001).

Here, we study the effect of the spontaneous spin polarization of the 2DEG in

single and double quantum dots, and ways to control it by external means. In particular, we investigate atomic-like shell structures and spin-polarized states in symmetric quantum dots that obey *Hund's rule*. The latter states that every orbital in a shell is singly occupied with one electron before any one orbital is doubly occupied, and all electrons in singly occupied orbitals have the same spin. We show how Hund's rule is violated when the dots are coupled or the symmetry in an isolated dot is broken, and how spin polarization (magnetization) of the dots can be changed by electric fields from the gate. The work continues previous experimental [136, 137, 104] and theoretical [79, 83, 98, 99, 58, 117] studies to the case of many electrons in realistic device structures.

3.2.1 Spin polarization in a single quantum dot

A. Symmetric quantum dot

We have modelled a symmetric square quantum dot in a large gate voltage region yielding 0 to 50 electrons in the dot. Every number of confined electrons gives rise to its own spin configuration. However, all the observed configurations can be attributed to one of the three main cases, as illustrated in Figures 3.4–3.6:

-*polarized* – total spin polarization of the confined electrons is non-zero, the quantum dot is magnetized;

-*non-polarized* – the number of up and down-spin electrons is the same, spin polarization is equal to zero all over the dot region;

-*spin-density wave* – the number of up and down-spin electrons is again the same, but spin polarization experiences spatial oscillations accompanied by changes in sign.

In Figure 3.4, the dot is occupied with $N^{\uparrow} = 21$ and $N^{\downarrow} = 15$ electrons. It has a pronounced shell structure (Figure 3.4a) where the first five shells are filled with

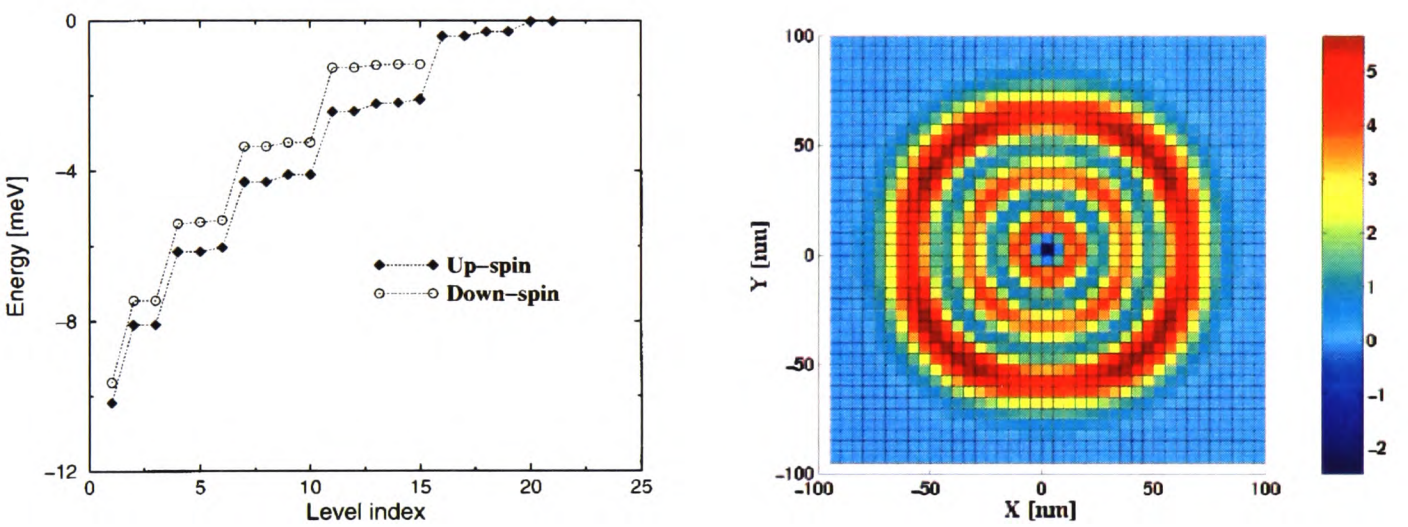


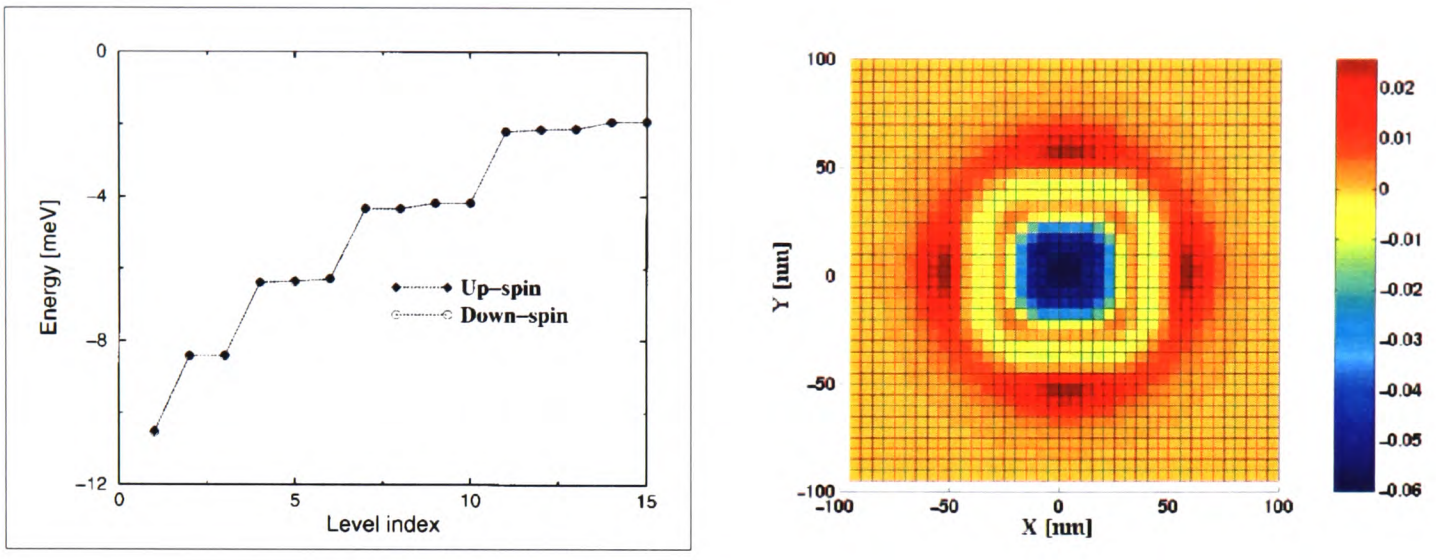
Figure 3.4: *(a) Energy spectrum of the single square quantum dot for ↑ (black diamonds) and ↓ (white circles) electrons in the polarized case of half-filled shell. Fermi level has a zero energy. Level index increases with energy starting from 1, which corresponds to the lowest state of the electronic spectrum. Dotted lines are shown to guide the eye. (b) Spin polarization of the dot [in units of* 10^{-4} nm^{-2}*] in the 2DEG plane. At* $V_g = -0.505$ V *the dot is occupied by* $N^{\uparrow} = 21$ *and* $N^{\downarrow} = 15$ *electrons.*

both up and down-spin electrons while the sixth shell is only half-filled with up-spin electrons – the corresponding states for down-spin electrons are above the Fermi level.

The shell structure without inclusion of electron-electron interactions can be qualitatively understood in the approximation of the 2D harmonic oscillator. In this case, the energy spectrum is given by $E_{n,l} = \hbar\omega(2n + |l| + 1)$ where $n = 0, 1, 2, ...$ and $l = 0, \pm 1, \pm 2, ...$ are the radial and angular momentum quantum numbers. Some energy states are degenerate and thus cluster shell-wise, the shells being successively formed by a total *'magic' number* of states (2, 6, 12, 20, 30, 42,...). Pairs of states with the same n and $|l|$ have the highest degeneracy and wavefunctions differing just by a $\pi/2$ symmetry rotation [98].

When electron-electron interactions are included, two major changes take place. First, the up- and down-spin branches of the spectrum split because of the exchange interactions. Note that the splitting between up- and down-spin sub-shells of each shell in Figure 3.4a has the order of 0.5–1 meV, which greatly exceeds the introduced Zeeman splitting of 0.01 meV (see Section 2.5.3), and remains when the magnetic field is switched off during the iterative process. Second, the degeneracy within sub-shells is slightly lifted as well due to non-parabolicity of the total potential caused by both electron-electron interactions and a slightly non-parabolic shape of the realistic confinement potential [98, 83]). Still, the states with the same n and $|l|$ remain degenerate which is seen from the pairwise structure of the sub-shells.

We also notice that, due to the shell structure and the exchange splitting, the distance between the neighboring sub-shells is much bigger than the level separation within each sub-shell, which makes filling of the state next to a closed sub-shell relatively unfavourable. This gives rise to the peaks in the addition spectrum of the dot not only at full ($N_{tot} = 2, 6, 12, ...$) but also at half-full ($N_{tot} = 4, 9, 16, ...$) shell filling, which has been reported elsewhere [136, 6, 117].



(a) **(b)**

Figure 3.5: *(a) Energy spectrum of the single square quantum dot in the unpolarized (closed-shell) case. At $V_g = -0.513$ V the dot is occupied by $N^{\uparrow} = N^{\downarrow} = 15$ electrons. The two branches of the spectrum for $\uparrow$ and $\downarrow$ electrons are not discernible because of the degeneracy. (b) Spin polarization of the dot [in units of 10^{-4} nm^{-2}] in the 2DEG plane. The colour bar on the right shows that the spin polarization is suppressed, as compared to Figure 3.4b.*

Figure 3.4b presents the spin polarization over the dot region in the case of half-filled shell. Here spin polarization is not distributed uniformly over the dot but has a circular pattern. Since the first five shells in the dot are fully occupied with up- and down-spin electrons and cancel, the behavior of spin polarization is determined by the contribution from the half-filled sixth shell. As long as up-spin sub-shell of the sixth shell is filled it possesses rotational symmetry, and the superposition of the peaks and dips of the radial part of the wavefunction may result in the radial oscillations of the spin polarization.

On further decrease of the gate voltage we arrive at an opposite situation that corresponds to the closed-shell dot in Figure 3.5. Here, the dot is occupied with $N^{\uparrow} = N^{\downarrow} = 15$ electrons. As Figure 3.5a depicts, the first five shells are completely filled and the sub-shells are degenerate, so the contributions from both spin directions

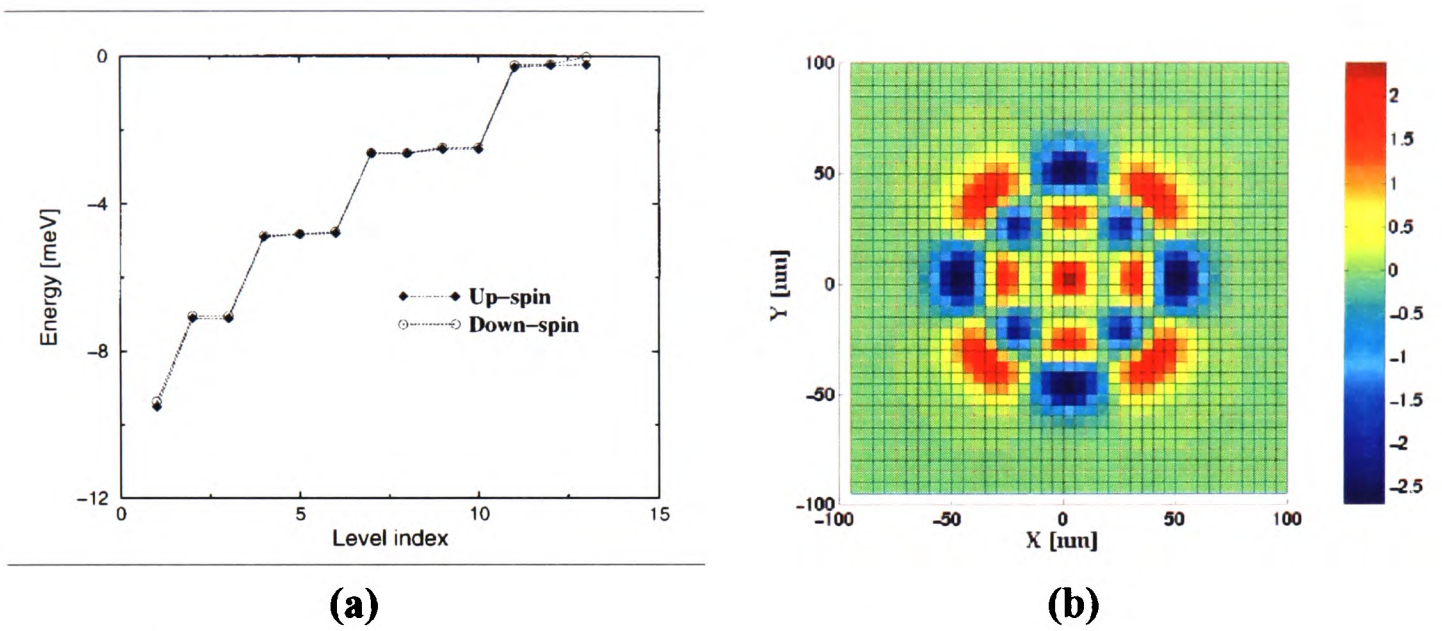


Figure 3.6: *(a) Energy spectrum and (b) spin polarization of the single square quantum dot in the spin-density wave case. At* $V_g = -0.523$ *V the dot is occupied by* $N^{\uparrow} = N^{\downarrow} = 13$ *electrons.*

are equal and cancel out, as seen in Figure 3.5b. The spin polarization reaches its maximum of about 2.5×10^{-6} nm^{-2} which is at least two orders of magnitude less than in the previous case. Given that the electron density in both cases has a maximum at 4×10^{-3} nm^{-2}, one can conclude that spin polarization practically vanishes in a closed-shell dot.

So far, all situations are manifestations of Hund's rule stating that the total spin takes the maximum value allowed by the exclusion principle and becomes zero for closed shells, due to an interplay between kinetic energy and exchange potential. Depending on which term dominates, two limiting cases take place, as shown in Figures 3.4 and 3.5, while filling of the shells at intermediate gate voltages should proceed according to these lines. However, if we further decrease the gate voltage, another situation occurs that violates Hund's rule. Figure 3.6a shows the dot's energy spectrum where the same number of up- and down-spin electrons occupy the energy states, $N^{\uparrow} = N^{\downarrow} = 13$, thus precluding the total spin polarization of the dot. The

splitting between the sub-shells is strongly suppressed, for instance, only about 5×10^{-5} eV for the second shell, which is however more than the Zeeman splitting. Surprisingly, the spatial distribution of the spin polarization, Figure 3.6b, does not drop to zero but instead oscillates in radial and angular directions with an amplitude comparable to that for a half-filled shell. This is a feature of the *spin-density wave* (SDW) (or anti-ferromagnetic state) that was pointed out in 2DEG quantum dots by Koskinen *et al.* [79] and has been discussed further [6, 58, 117, 158].

The SDW state should in the case of a finite system not be taken literally. Obviously, our SDW state is degenerate. For example, by turning spin $\uparrow$ into spin $\downarrow$, and vice versa we obtain an equally acceptable solution. The spatial variation of the spin density is therefore an artefact due to the approximation with a single determinant. Obviously, we may restore proper symmetry by taking a linear combination of Slater determinants. As a consequence, such a generalized state would not predict the naive SDW state in Figure 3.6b. It would, however, predict two-particle correlations which are consistent with the SDW concept, i.e., LSD reveals subtle correlations inherent in the true ground state. Keeping this interpretation of the SDW state in mind we will stay with LSD and a single Slater determinant.

The overall results for a square symmetric quantum dot are presented in Figure 3.7. A Coulomb staircase is shown in Figure 3.7a that reflects the filling of the dot with electrons as a function of the gate voltage. The total number of electrons varies from 0 at a pinch-off voltage of -0.62 V and up to 50 electrons. Some of the steps along the vertical axis experience a jump of two electrons (such as from 12 to 14 and in the region from 30 to 42 electrons). In those cases the step of the gate voltage $\Delta V_g = 1$ mV has not been sufficiently small to distinguish between a pair of highly degenerate energy states, and a double filling has occurred. The curve has a parabolic form which gives rise to the following consideration. The capacitance of a quantum dot is defined

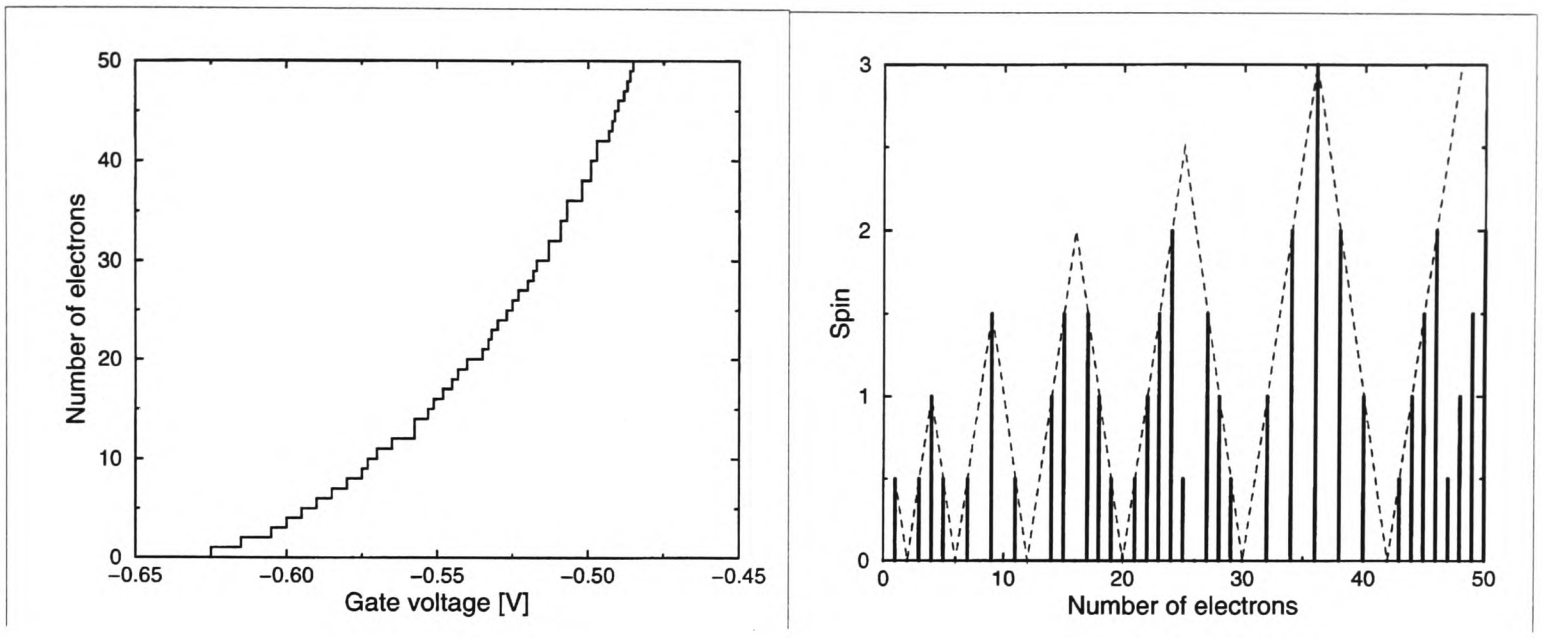


Figure 3.7: *(a) Coulomb staircase diagram for a single square quantum dot. (b) Variation of the total spin polarization in the square quantum dot containing N_{tot} electrons. Solid bars represent the results of the modelling. The dashed line indicates the spin configuration when Hund's rule is satisfied.*

as the first derivative of the total electron charge with respect to the applied gate voltage. Therefore by putting aside the charge-quantized steps and differentiating the curve in Figure 3.7a one obtains the capacitance as a linear function of the gate voltage. On the other hand, the classical capacitance of a uniformly charged disk is proportional to its radius r. Provided that the radius of the dot is proportional to the applied gate voltage (which is consistent with what we have seen in our modelling), one may consider the 2DEG region of the dot as a disk whose average electron density remains constant and size increases linearly with the gate voltage. From Figure 3.7a we have estimated r for a given gate voltage and found it in agreement with the size of the 2DEG region observed explicitly in the electron density plot. Thus, the electronic filling of the quantum dot can be qualitatively understood in classical terms while the steps in Figure 3.7a manifest discreteness of the dot's charge. The unevenness in

the steps is a quantum effect.

Figure 3.7b plots the total spin polarization S_z of the dot as a function of its electron content. The peak $S_z = 3$ at $N_{tot} = 36$ electrons corresponds to the case in Figure 3.4, this is a maximum total spin polarization observed in our modelling. Other situations are found in Figure 3.7b as well. In general, by external variations in the gate voltage one can vary the spin polarization (magnetization) of a single symmetric quantum dot in a range limited by Hund's rule. Our results are in good agreement with those obtained by Koskinen *et al.* (see Table 1 in [79]).

B. Asymmetric quantum dot

Now let us consider a single asymmetric quantum dot. The asymmetry is achieved by having a metallic gate deposited in the top-right corner of the square gate opening (Figure 2.5c) and thus deforming the confinement potential. The corner gate has a fixed width and a variable length L, therefore by changing L we investigate the influence of the asymmetry on the total potential as well as on the spin polarization. We start out from a non-deformed symmetric square dot at the gate voltage corresponding to the half-filled shell case (Figure 3.4). As mentioned in the previous paragraph, in this case the dot has a maximum total spin polarization $S_z = 3$. Having fixed the gate voltage we gradually increase L from 20 nm to 110 nm when it reaches the size of the gate opening and the dot becomes rectangular. At the same time, the 2DEG experiences a transformation of its shape from circular to elliptical.

The results for the energy spectrum of the asymmetric dot are presented in Figures 3.8 and 3.9. Two main trends can be noted. First, as the asymmetry grows the spin polarization decreases dropping to zero at $L = 55$ nm which equals to half-size of the gate opening. At that moment, the exchange splitting between up- and down-spin

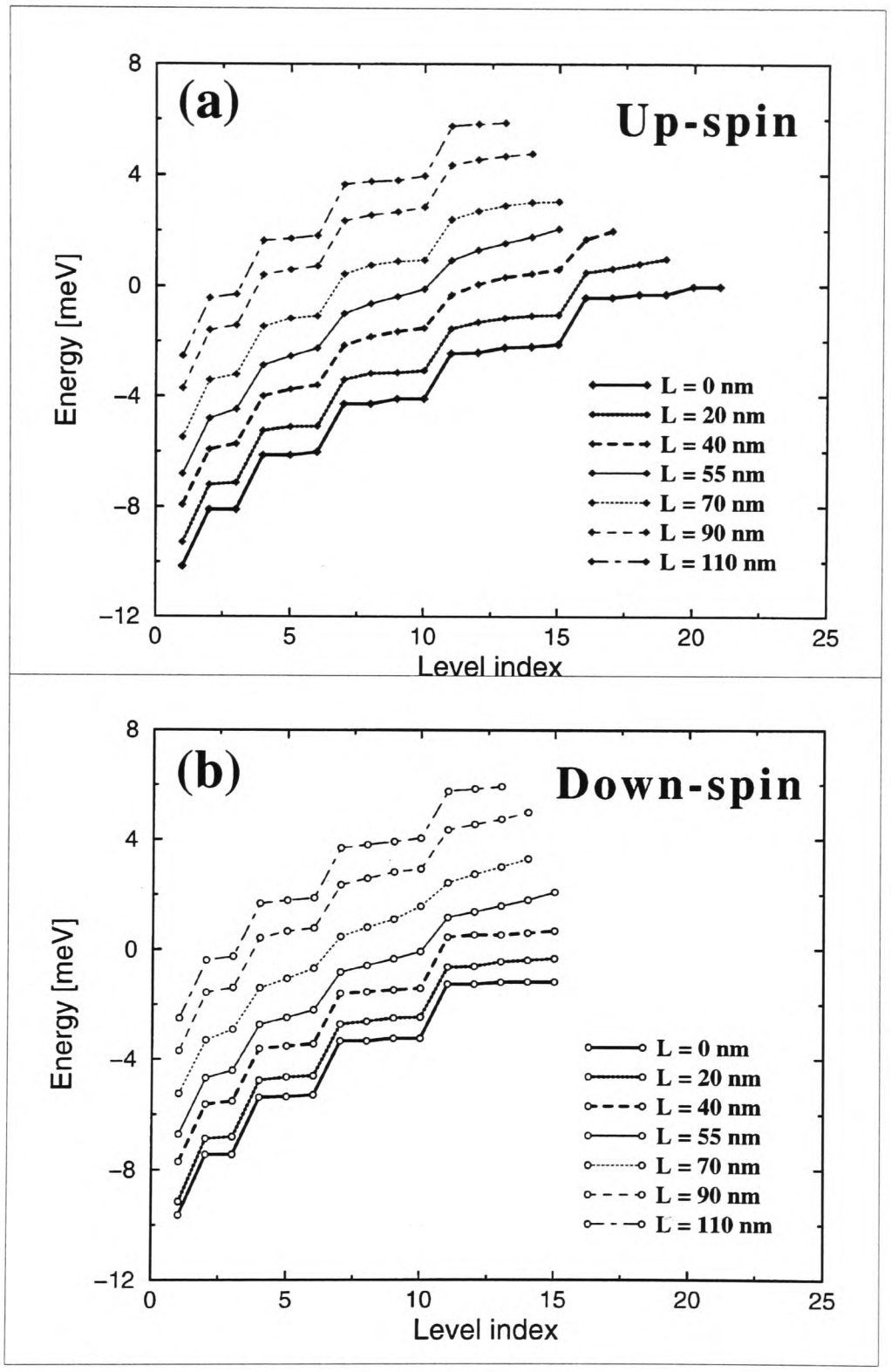


Figure 3.8: *Energy spectra of the asymmetric square quantum dot (depicted in Figure 2.5c) at different gate geometries for (a) up-spin and (b) down-spin electrons. Energy levels for distorted cases (where the deformation length $L > 0$) have been vertically offset by 1 meV for clarity.*

branches of the spectrum is suppressed, and further symmetry-breaking makes electrons of both spin directions leave the dot at the same rate, since the total metallic area of the gate is getting effectively enhanced. Second, the asymmetry of the dot potential splits the shells. At $L = 55$ nm sub-shells of both spins undergo a similar splitting. However, when L deviates from that value in either direction, $L = 40$ or 70 nm, one of the spectral branches (for up- or down-spin) experiences more pronounced splitting than the other. Spatial distribution of the spin polarization of an asymmetric dot at $L = 55$ and 110 nm is shown in Figure 3.9(a,b). One can see how the spin polarization is suppressed, as compared to the non-deformed case, and its rotational symmetry is broken due to the distortion of the confinement potential. In general, breaking the symmetry of the dot destroys its magnetization, see Figure 3.9c, which is the consequence of lifting degeneracies. This is an expected result [6, 83, 58]. Figure 3.9b also shows the oscillations in spin polarization indicating the SDW behavior for the rectangular quantum dot. Thus, the SDW states remain, or even become more prevalent [6], in asymmetric quantum dots, as opposed to the highly polarized states (Figure 3.4) which are characteristic for non-deformed symmetric dots alone. We emphasize, however, that for the case shown in Figure 3.9b the deformation of the dot is weak, the gate opening has the size of 110×90 nm^{-2} and the shell structure is still well pronounced, as seen in Figure 3.8. Therefore, the SDW states cannot be produced by lifting the degeneracy of the energy levels only, but rather are the effect of the suppressed exchange splitting between up- and down-spin branches of the spectrum.

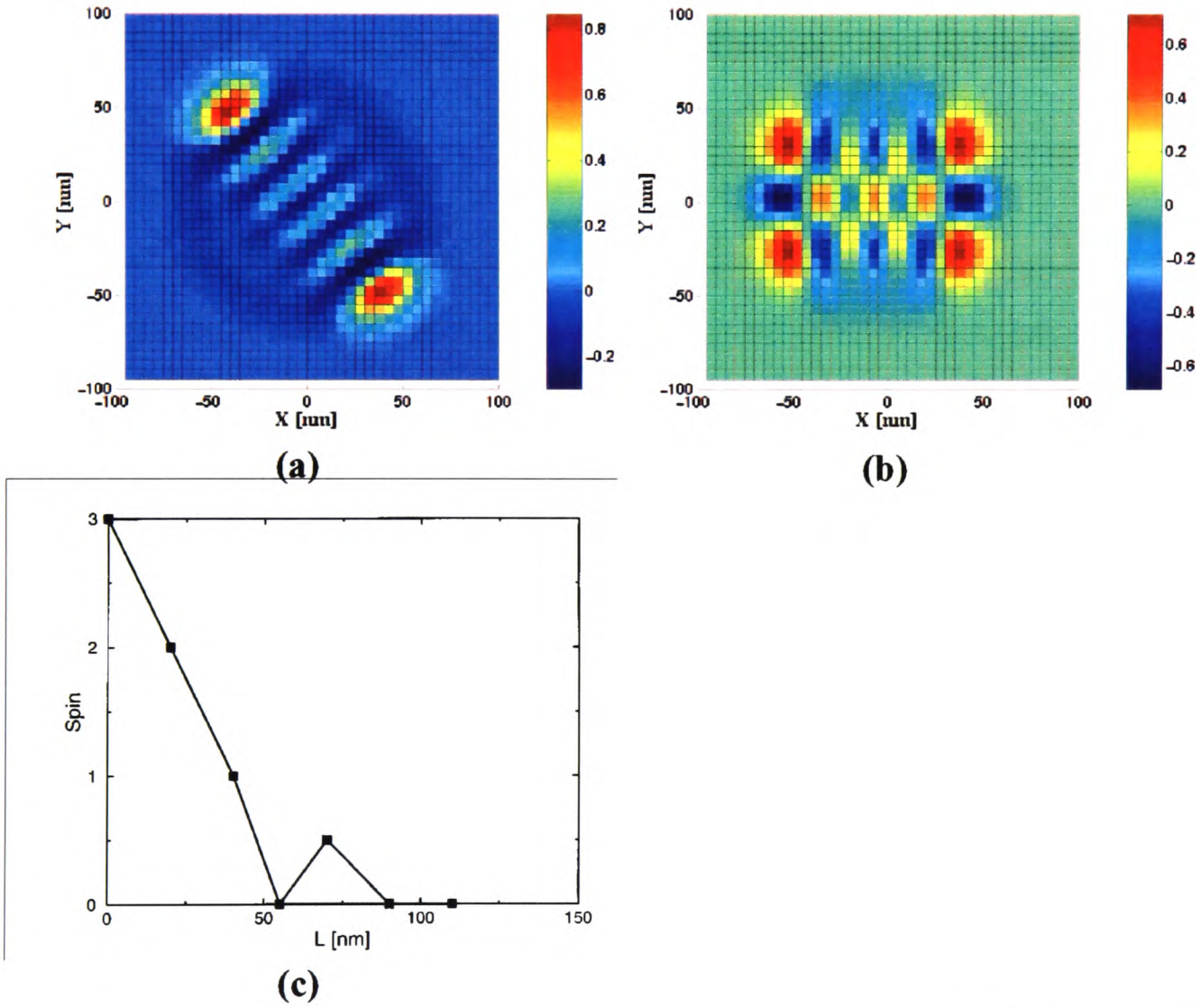


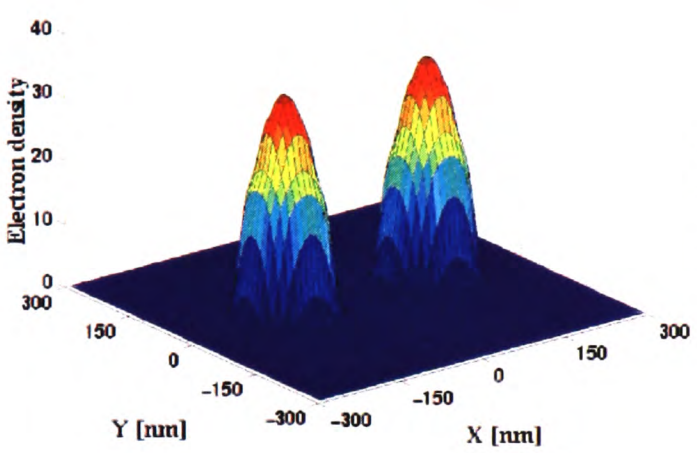
Figure 3.9: *Spin polarization [in units of* 10^{-4} nm^{-2}*] of the asymmetric quantum dot at (a)* $L = 55$ *nm and (b)* $L = 110$ *nm. In case (b) of the rectangular dot oscillations in spin polarization are reminiscent of the spin-density wave. (c) Total spin polarization* S_z *of the asymmetric quantum dot as a function of the deformation length* L*.*

3.2.2 Spin polarization in two coupled quantum dots

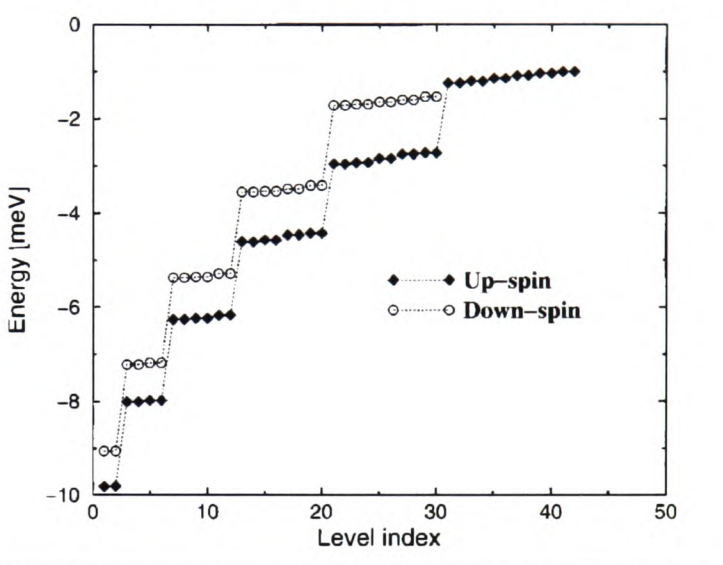
Here, we study a system of two coupled square dots which models an *artificial diatomic molecule.* The corresponding gate geometry is shown in Figure 2.5d. Here, the coupling strength between the constituent 'atoms' can be varied by changing the distance between the quantum dots, and different applied gate voltages determine the electron content of such a molecule. A similar system has been implemented and measured experimentally by Oosterkamp *et al.* [104]. It consists of two lateral dots of different size containing about 60 and 35 electrons respectively, which can be interpreted as a molecule composed of atoms of two different elements. A system of two identical quantum dots has been modelled by Nagaraja *et al.* [99]. They have studied low-electron cases corresponding to light molecules, such as H-H or Be-Be.

In this section, we investigate massive dots with a high-electron content. Initially, the system parameters (gate voltage $V_g = -0.505$ V and inter-dot distance $d = 200$ nm) are set in such a way that the quantum dots are well separated and contain $N^{\uparrow} = 21$ and $N^{\downarrow} = 15$ electrons each, which corresponds to a highly polarized half-filled shell state described above (Figure 3.4). Having fixed the gate voltage, we increase the coupling between the dots by gradually reducing the inter-dot distance d. The aim is to see how the introduced coupling changes the symmetry of the confinement potential and, ultimately, what happens to the spin polarization of the double dot.

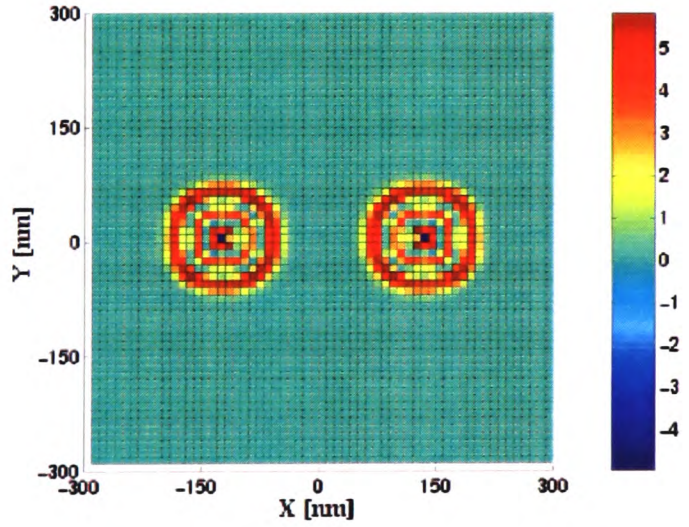
The results for the double dot in different coupling regimes are shown in Figures 3.10–3.12. As long as the inter-dot distance exceeds 150 nm the quantum dots remain uncoupled, see Figure 3.10. The electron density of the system (Figure 3.10a) is split into two separate 2DEG droplets and the total number of electrons, $N^{\uparrow} = 42$ and $N^{\downarrow} = 30$, is just two times the electron content of a single isolated dot at the same



(a)



(b)



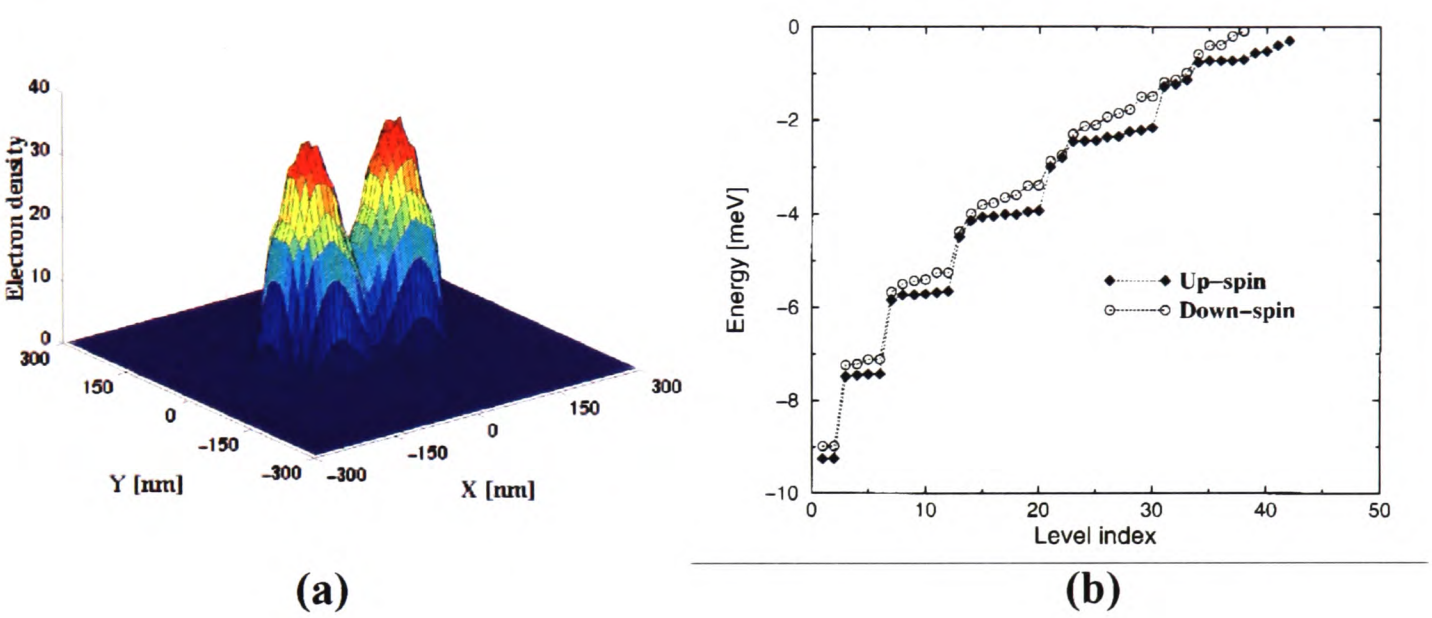
(c)

Figure 3.10: *Double dot in the weak-coupling regime: (a) electron density of the double dot [in units of* 10^{-4} nm^{-2}*]. At* $V_g = -0.505$ V *and inter-dot distance* $d = 150$ nm *the system is occupied by* $N^{\uparrow} = 42$ *and* $N^{\downarrow} = 30$ *electrons; (b) energy spectrum; (c) spin polarization [in units of* 10^{-4} nm^{-2}*].*

gate voltage. This implies the charging of both dots is carried out independently, and the situation is similar to the double charging effect observed by Nagaraja *et al.* for the first two electrons filling the lowest localized states of the double dot [99]. The energy spectrum of the system (Figure 3.10b) shows a pronounced shell structure, the shells being 'doubled' because of the degeneracy of the levels of the two identical quantum dots. The sixth shell is only half filled due to exchange splitting and spin polarization (Figure 3.10c) is clearly seen in the dot regions, in accordance with Hund's rule. The shape and value of the spin polarization for each dot is exactly the same as in Figure 3.4b.

The situation changes when the dots are brought closer to each other into an intermediate coupling regime, see Figure 3.11. Here, the inter-dot distance is as short as $d = 50$ nm. As one can see in Figure 3.11a the 2DEG droplets merge into one, although two single-dot humps of the electron density are still easily distinguished. The shell structure (Figure 3.11b) has experienced two significant transformations. First, the shells corresponding to high-lying delocalized states start to split because of the partially lifted degeneracy, and energy levels shift as the dots approach each other. Second, the exchange gap between up- and down-spin branches of the spectrum is diminished considerably as compared to the previous case, which brings in new available energy states for down-spin electrons from above the Fermi level. Thus, additional charging takes place, up to $N^{\uparrow} = 42$ and $N^{\downarrow} = 38$, and spin polarization is reduced. The light area in Figure 3.11c (positive spin polarization) shrinks and dark (zero and negative spin polarization) extends compared to Figure 3.10c.

Finally, when the separation between the dots is zero the coupling reaches its maximum value and the two-dot system transforms into a single asymmetric quantum dot, see Figure 3.12. The electron density of the system (Figure 3.12a) is confined to one island and two single-dot humps can no longer be distinguished. Shell structure



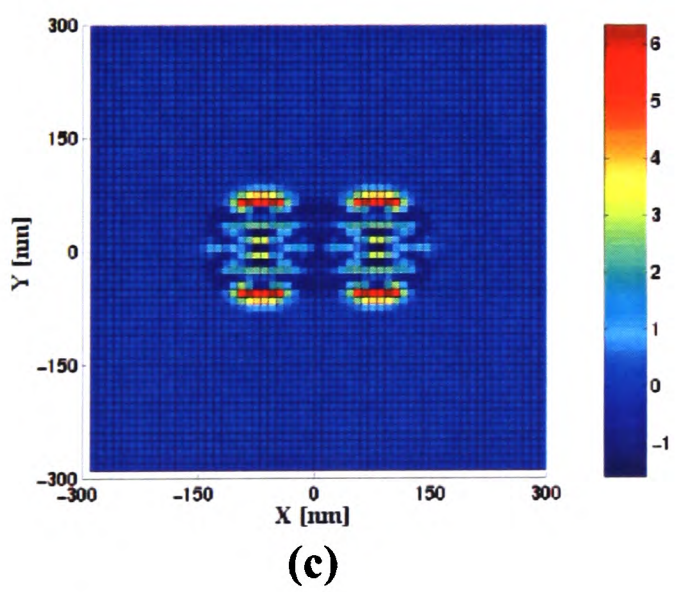
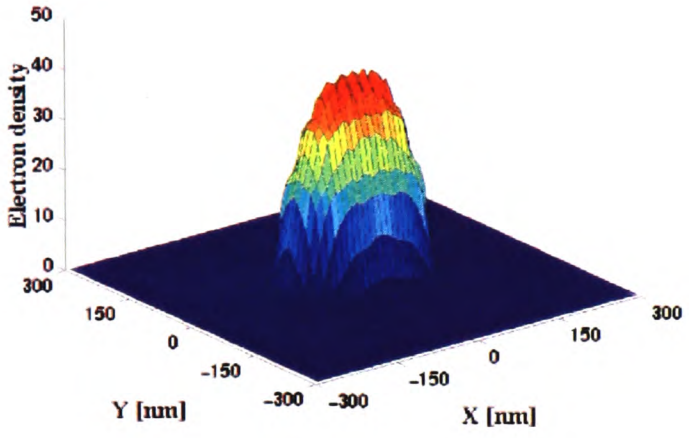


Figure 3.11: *Double dot in the intermediate-coupling regime: (a) electron density of the double dot [in units of* 10^{-4} nm^{-2}*]. At* $V_g = -0.505$ V *and* $d = 50$ nm *the system is occupied by* $N^{\uparrow} = 42$ *and* $N^{\downarrow} = 38$ *electrons; (b) energy spectrum; (c) spin polarization [in units of* 10^{-4} nm^{-2}*].*

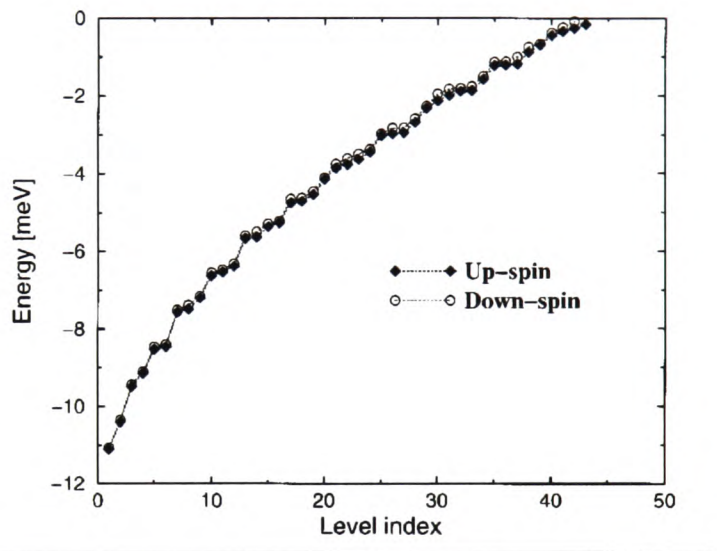
smears out but close inspection of Figure 3.12b enables one to trace remains of two single-dot shell structures with corresponding shells shifted relative to each other. This partial conservation of the level degeneracy can also be explained from the ellipticity of the formed dot confinement potential. The resulting gate opening is a rectangle of the length being twice its width. Thus, neglecting electron-electron interactions one can roughly estimate the energy spectrum of the system as that of a 2D harmonic oscillator with energy of the confinement $\hbar\omega_0$ along the y-axis two times larger than along the x-axis (though it is not absolutely true [6]). This will give the energy spectrum in the form $E_{n_x,n_y} = \hbar\omega_0(n_x + 2n_y) + \text{const}$, where $n_x, n_y = 0, 1, 2, ...$ and therefore a half reduced degeneracy of the levels.

The exchange gap between up and down-spin branches of the spectrum is strongly reduced being only about 0.1 meV which is nearly an order of magnitude less than in the case of weak coupling. Furthermore, energy levels experience a drop of about 1–2 meV as compared to previous cases of separated dots, which is likely to be an effect of the molecular binding of the constituent artificial atoms [99]. These two properties result in a considerable increase in the number of occupying electrons, $N^{\uparrow} = 43$ and $N^{\downarrow} = 42$, and almost complete suppression of the total spin polarization of the system. The spatial distribution of the spin polarization (Figure 3.12c) is, however, not zero-flat but shows oscillations all over the two-dot region with an amplitude of the same order as in the highly polarized weak-coupling regime. This is a feature of the SDW that is typical for elliptical dots, as discussed in the previous section.

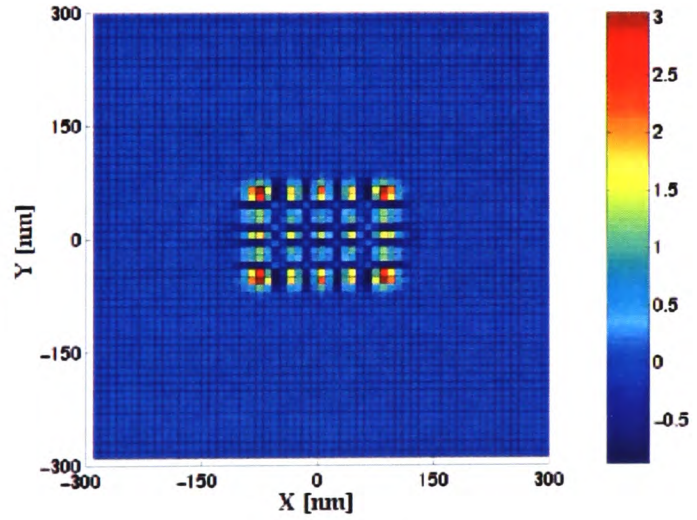
Overall results for a double dot are presented in Figure 3.13 showing two major trends. Firstly, as the inter-dot distance decreases, formation of an artificial diatomic molecule provides an energy boost for new states to be filled and thus increases electron content of the system. Secondly, the coupling between the dots deforms the symmetry of the confinement potential, which destroys spin polarization of the double



(a)



(b)



(c)

Figure 3.12: *Double dot in the strong-coupling regime: (a) electron density of the double dot [in units of* 10^{-4} nm^{-2}*]. At* $V_g = -0.505$ V *and* $d = 50$ nm *the system is occupied by* $N^{\uparrow} = 43$ *and* $N^{\downarrow} = 42$ *electrons; (b) energy spectrum, the levels drop due to molecular binding; (c) spin polarization [in units of* 10^{-4} nm^{-2}*].*

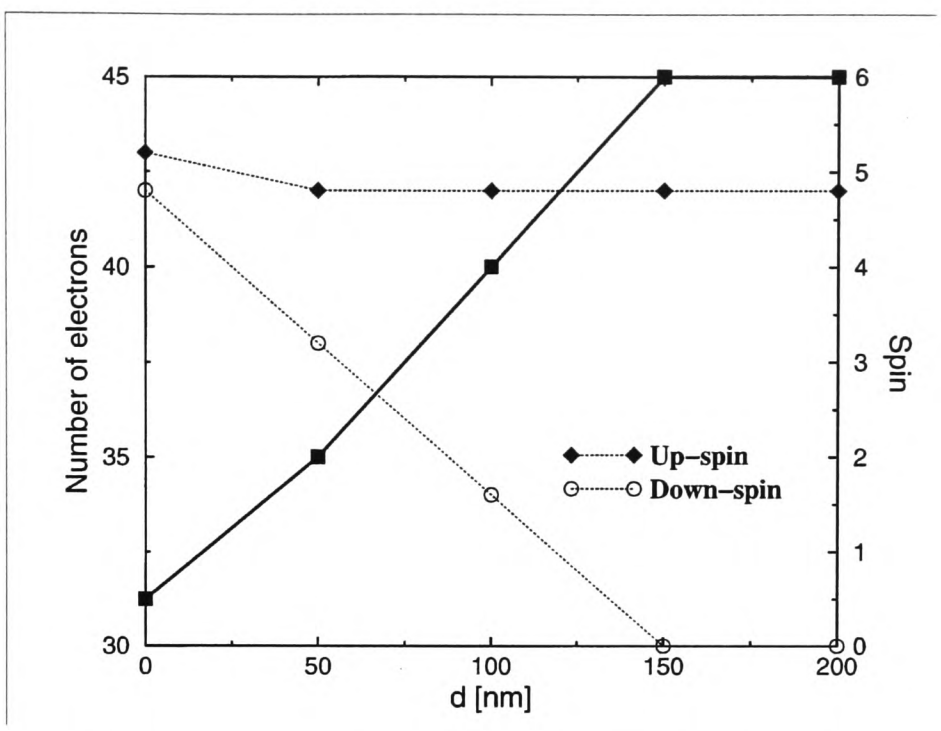


Figure 3.13: *Total electron content (dotted lines, left scale) and total spin polarization (solid line, right scale) of the double dot as a function of the inter-dot distance d.*

dot.

In the description above, we have analyzed the quantum-mechanical coupling of two quantum dots as a means to control the spin polarization of the whole double-dot systems. Another interesting problem is to investigate the spin behaviour exactly in the region of quantum-mechanical contact between the two dots. Such a system represents a quantum point contact. Our study of this problem showed its direct relation with the '0.7-anomaly' in the conductance of the short quantum wires, and it became our separate research topic. The next section presents our findings.

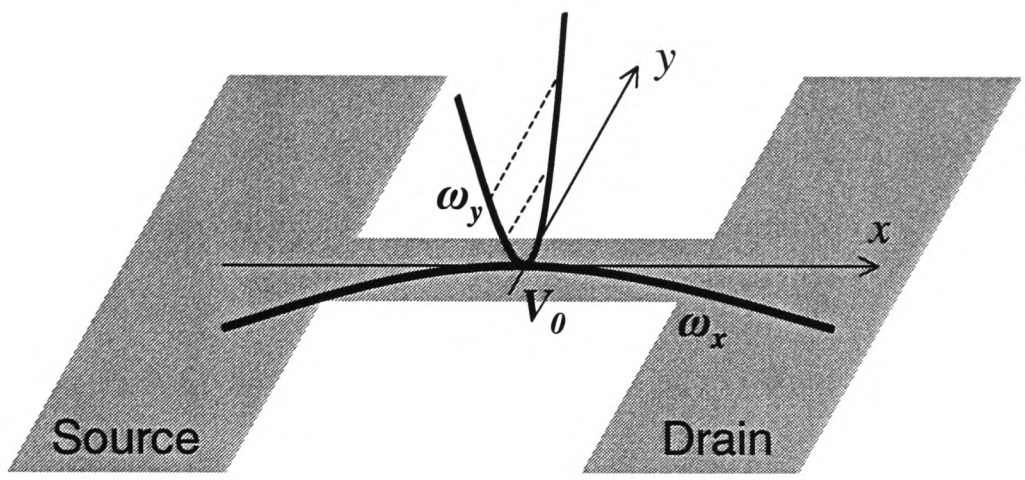


Figure 3.14: *Schematic of the saddle-point potential of a quantum point contact in the 2DEG plane.* V_0 *is the potential at the saddle point, and* ω_x *and* ω_y *are characteristic curvatures of the longitudinal and lateral potential profiles. The parabolic confinement along y gives rise to the energy subbands (dashed lines). The number of subbands below the Fermi level corresponds to the number of open channels in the quantized conductance of the electron source-drain current.*

3.3 Spin-dependent electron behaviour in quantum point contacts

Published in: A. M. Bychkov, I. I. Yakimenko, and K.-F. Berggren, *Spin-dependent electron behaviour in quantum point contacts*, Nanotechnology 11, 318 (2000).

3.3.1 0.7-anomaly

The total electrostatic potential of a short quantum wire, or quantum point contact (QPC), can be described with the *saddle-point model* [24] as a quadratic function of the coordinates

$$V(x,y) = V_0 - \frac{1}{2}m\omega_x^2 x^2 + \frac{1}{2}m\omega_y^2 y^2, \tag{3.1}$$

where V_0 is the potential in the middle, and ω_x, ω_y characterise the (inverted) parabolic confinement in the plane of 2DEG, as schematically depicted in Figure 3.14. Such a simple analytic form of the potential is sufficient to account for the quantization of conductance in units of $G_0 = 2e^2/h$ discovered experimentally in 2DEG constrictions as early as in 1988 [149, 150].

However, the saddle-point model fails to explain the deviations from the integer quantization, e.g. the anomalous shoulder-like structure ('smeared plateau') observed in various QPC geometries at $0.7G_0$ [140, 23], in addition to the quantized plateaus at multiples of G_0. The so-called *0.7-anomaly* has received much attention in the recent years, both experimentally and theoretically [146, 147, 141, 142, 128, 42, 23], but has not yet been thoroughly understood. One important finding (see Figure 3.15) is that the structure gradually transfers from $0.7G_0$ to $0.5G_0$ as a function of the applied magnetic field. The latter value represents the case of a usual Zeeman splitting of conductance channels for up and down-spin electrons. This implies that the 0.7-anomaly may have a spin-related origin, and a more accurate description of the total potential experienced by electrons in realistic QPCs is needed.

3.3.2 Numerical analysis

In our modelling, the QPC is formed electrostatically with a split-gate (shown in Figure 2.5g), which consists of two 100×400 nm^2 rectangular openings (contact pads) connected by a narrow bridge of 200 nm in length and 10 nm in width. Once a negative voltage is applied to the gate, the 2DEG at the heterojunction shrinks to a quasi-1D constriction connecting two reservoirs (source and drain).

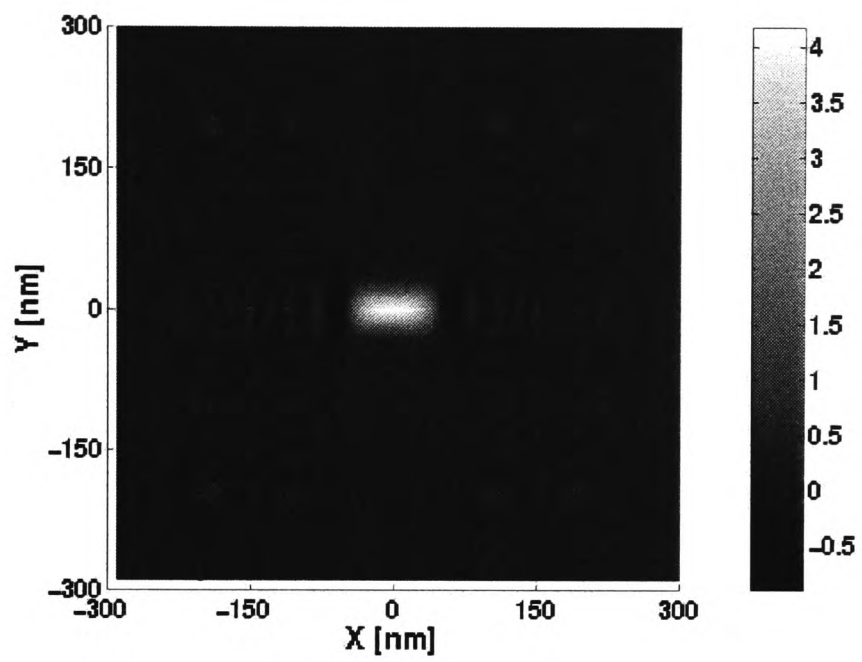
In Section 3.2 we have shown that spin polarization occurs spontaneously in a symmetric confinement potential, e.g. in that of an isolated quantum dot. Here, the



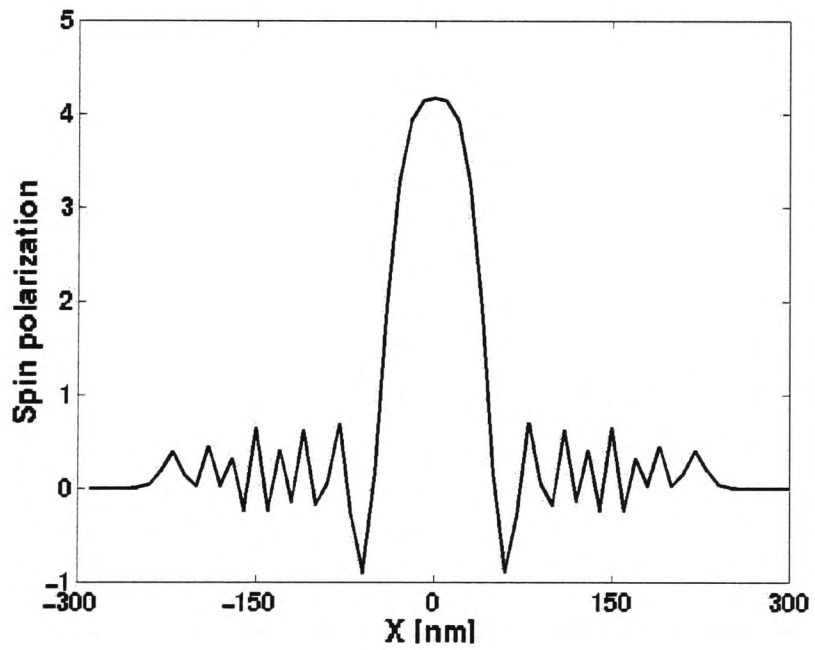
Figure 3.15: *Magnetic field dependance of the anomalous 0.7-structure in the conductance of a quantum point contact. Figure from Ref. [140].*

QPC geometry is determined by a narrow gate opening, and the symmetry of the confinement potential is reduced. Therefore the level degeneracy is precluded and spin polarization is expected to disappear or to form a spin-density wave.

Surprisingly, this is not the case when the QPC is in the low-density regime (when the maximum number of open subbands is less than one). By decreasing the gate voltage one effectively reduces the density of electrons occupying the channel area. The electron kinetic energy that favours double occupancy decreases linearly with the electron density while the exchange term that makes electron spins align ferromagnetically has a square root dependence and a negative sign. Thus at a certain gate voltage when the density is low the exchange term becomes prevalent over the kinetic energy and the spin polarization occurs in the channel. Figure 3.16 shows the spin polarization of the QPC in the 2DEG plane. A highly pronounced peak is seen in the area of the channel while some minor peaks and valleys are present in the pad regions. Note that at $V_G = -0.5$ V (the case shown in Figure 3.16) very few



(a)



(b)

Figure 3.16: *Spin polarization of the quantum point contact at* $V_G = -0.5$ *V in the plane of the 2DEG: (a) top view, the color bar on the right shows the scale in units of* 10^{-4} nm^{-2}*; (b) middle cross-section in the longitudinal direction.*

electrons occupy the channel of the QPC, only about five electrons according to our estimations. A similar ferromagnetic alignment of the electron gas has been found earlier [146, 147] for a long quantum wire with a constriction as the electron density was decreased.

The oscillations in the pads are to a large extent caused by the constrains on size of our model system. The condition that the wavefunctions vanish at the boundaries gives rise to the standing waves along the x and y axes. These standing waves give rise to the oscillations in the spin polarization. In the experimental QPC devices the contact pads have infinite length on the mesoscopic scale, so the boundaries along the x-axis are open and longitudinal standing waves are precluded. Therefore, by increasing the system size we expect the spin polarization in the pads to oscillate with a smaller spatial period and amplitude and asymptotically average to zero, whereas the spin polarization in the channel which has a different origin (as discussed further) will be sustained. However, modelling of a full-scale device is not practical for the reason of increased computational complexity of the problem.

The total potentials for $\uparrow$ and $\downarrow$ electrons in the channel region for the spin-polarized case at $V_G = -0.5$ V are presented in longitudinal (Figure 3.17a) and lateral (Figure 3.17b) middle cross-sections. The effective potential barriers experienced by electrons of different spins split compared to the non-polarized case at $V_G = -0.499$ V (Figure 3.17 and 3.17d). When the barrier for the unfavorable spin direction (which we have chosen to be $\downarrow$ by an appropriate orientation of the weak magnetic field) rises above the Fermi level, i.e. becomes positive, the electrons cannot occupy the corresponding region in the channel but are allowed just to tunnel through the barrier. Hence the $\downarrow$ electron density is pulled away from the region and the spin polarization becomes non-zero. In fact, taking into account the discreteness of the energy spectrum in the potential well along the y-axis spin polarization occurs even if the potential

for $\downarrow$ electrons is negative but remains above the lowest eigenstate. This is seen in Figure 3.17b where the region of positive spin polarization extends from $x = -60$ nm to $x = 60$ nm while the potential barrier for $\downarrow$ electrons (Figure 3.17a) is positive only over the region of about 50 nm along the x-axis. When we slightly increase the gate voltage to $V_G = -0.499$ V (Figure 3.17c) the $\downarrow$ electron potential drops below zero and has almost the same value as the one for $\uparrow$ electrons. The lowest eigenstates in the lateral potentials (Figure 3.17d) are now equally occupied with electrons of both spins and the corresponding electron densities cancel out resulting in the suppression of the spin polarization.

It also follows from Figure 3.17 that the shape of the potential barriers deviates from the saddle-point model in the spin-polarized case. Instead, the total $\uparrow$ electron potential in the longitudinal cross-section (Figure 3.17a) exhibits a 'cut-parabolic' form, whereas in the lateral cross-section, the $\downarrow$ electron potential (Figure 3.17b) flattens out. Such a dramatic shape distortion of the total potentials in the spin-polarized case not only results in the rearrangement of the energy spectra but must also have a deep effect on the transport properties of the QPC.

For instance, our findings may be related to the 0.7-anomaly in the following way. The 0.7-structure is realised in the low-density regime when only the first subband is open for conduction. In this case, the expression for the QPC conductance at zero temperature [24] can then be written as $G = \frac{e^2}{h}(T^{\uparrow} + T^{\downarrow})$ where $T^{\uparrow}$ and $T^{\downarrow}$ are the σ-spin transmission coefficients through the barrier in the channel region. At a certain gate voltage when spontaneous spin polarization sets up in the channel the barriers for $\uparrow$ and $\downarrow$ electrons suddenly become different in value, as we have shown before. At that moment, $\uparrow$ electrons continue conducting current through the lowest eigenstate that propagates all over the QPC, whereas the $\downarrow$ electrons having the same energy now have to tunnel from source to drain.

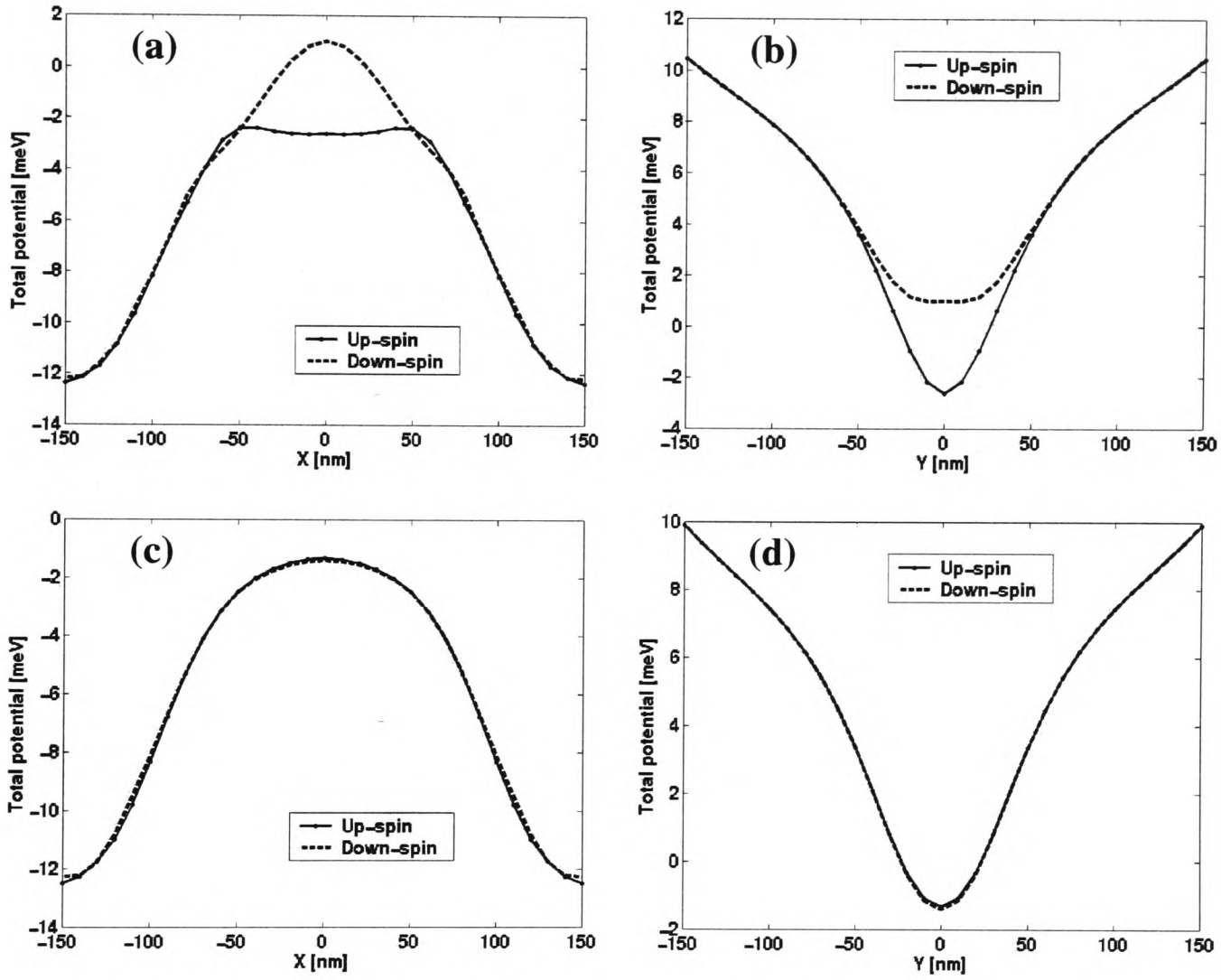


Figure 3.17: *Total potentials for up-spin (solid line) and down-spin (dashed line) electrons in the quantum point contact in the longitudinal (a, c) and lateral (b, d) direction. (a, b) at* $V_G = -0.5$ *V the potentials for up-spin and down-spin electrons split and the channel is in the spin-polarized state (see also Figure 3.16); (c, d) at an increased gate voltage* $V_G = -0.499$ *V the potentials coincide and the spin polarization in the channel disappears.*

Note that if the potential barriers were only different in height, the transmission coefficients $T^{\uparrow}$ and $T^{\downarrow}$ would always have the same step-like dependence on the gate voltage, and their fronts would shift relative to each other in the amount equal to the difference in barrier heights. In this case, an extra plateau in conductance would always appear at $0.5(2e^2/h)$. It is the shape distortion of the potentials that changes this value. The 'cut-parabolic' barrier for $\uparrow$ electrons (Figure 3.17a) is effectively wider than the parabolic one for $\downarrow$ electrons and is more difficult to penetrate. As a result, the transmission coefficient $T^{\uparrow}$ is much steeper than $T^{\downarrow}$, and such a difference in slope of the $\uparrow$ and $\downarrow$ fronts will offset the extra plateau from $0.5(2e^2/h)$. The value of $0.7(2e^2/h)$ can be readily achieved in this case.

Of course, a more accurate quantitative verification is needed involving numerical analysis of the energy spectrums, calculation of the transmission coefficients, and ultimately inclusion of the finite temperature in our model. These studies are under way [131] and beyond the scope of this thesis. However, the above considerations allow us to suggest that the concept of the spin-polarized electron gas may be essential in the understanding of the 0.7-structure.

3.4 Applications in spintronics

Back in 1959, Richard Feynman has challenged scientific community to build "computers with wires no wider than 100 atoms, a microscope that could view individual atoms, machines that could manipulate atoms one by one, and circuits involving quantized energy levels or the interactions of quantized spins" [39]. These revolutionary ideas are now becoming real. In particular, the latter idea has been the basis of the emerging field of spin electronics, or *spintronics*, that exploits the spin of the

electron rather than its charge and has the potential advantages of nonvolatility, increased data processing speed, decreased electric power consumption, and increased integration densities compared with conventional electronics [152].

Semiconductor quantum dots are very promising as building blocks of spintronic devices, since their electronic properties can be readily engineered and spin coherence can be sustained long enough to be monitored and transported within the device [106, 74]. Specifically for the GaAs/AlGaAs modulation-doped quantum dots considered above, we have shown that local magnetic moments can be generated in these structures solely by applying appropriate gate voltages, with no external magnetic fields. Hence, these systems can be easily integrated on a chip with other spintronic devices, providing an all-semiconductor approach to spintronics. This is a significant advantage of the modulation-doped quantum dots compared to their magnetic impurity counterparts, which will face a challenging fabrication task of position-controlled implantation in a circuit.

Of course, the magnetic moments of a few Bohr magnetons, which we have calculated in the quantum dots containing up to 50 electrons, are still too small to be reliably measured. While there is on-going research on improving the magnetometer sensitivity using nano-SQUIDs or optical techniques, it is also worth investigating whether one can obtain larger magnetic moments in the modulation-doped quantum dots. In this respect, it is interesting to perform a simulation of quantum dots containing a larger number of confined electrons and see whether Hund's rule can still be followed in higher shells. This may be a topic of future research.

Another important issue of spintronics is spin injection. Clearly, any spin mechanism can work only if spin-polarized electrons can be injected into a working domain. Some successful attempts have been already made in this direction, based on the use of ferromagnetic metal or combined magnetic and non-magnetic semiconductor

contacts [152, 101]. Nevertheless, in general this problem remains unsolved from an experimental point of view.

The effect of spontaneous spin polarization, which we have found in quantum point contacts and presented in Section 3.3, is an attractive candidate for implementing an all-semiconductor mechanism for spin-injection. The situation shown in Figure 3.17 corresponds to the case where only electrons of $\uparrow$ spin are present in the channel region. When passing electron current through such a QPC at an appropriate gate voltage (one-subband conduction mode), the $\uparrow$ electrons will propagate through the barrier while the $\downarrow$ electrons will be blocked. The challenge is perhaps to make electrons of the right spin (say, $\uparrow$ but not $\downarrow$) to be injected. In our modelling, such symmetry breaking is introduced by a weak magnetic field of about 0.1 T, which can be generated experimentally, e.g. by depositing a ferromagnetic particle in the channel vicinity or by means of an STM. Certainly, some other sources of the spin anisotropy may be found as well, which is evident from the fact that the 0.7-structure is observed experimentally at zero magnetic fields. Obviously, this concept is not free from a number of open questions but the basic idea appears promising and deserves further exploration.

Chapter 4

Design of experiments on photon-exciton coupling in self-assembled quantum dots

4.1 Outline

This project began three years ago when I came to Oxford. My supervisor Dirk Bouwmeester had expertise in quantum optics experiments, and was interested in the coherent coupling of light to solid-state structures. Such a coupling is expected to be of crucial importance for future developments of quantum information science. I wanted to complement my theoretical background in semiconductor nanostructures with experimental skills in the field of QD-based quantum computation. That was the start of a brand new project on quantum information transfer between single photons and excitons in semiconductor QDs.

In parallel to my theoretical research (Chapters 2 and 3), during the three years of my D.Phil course I have made major contributions to following:

1) Identifying interesting and challenging new research topics combining quantum optics and solid-state physics.

2) Initiating collaborations with world-leading experts on semiconductor materials growth and nanofabrication. In particular, we established collaborations with the groups of Professors Pierre Petroff (MBE growth of self-assembled quantum dots), Evelyn Hu (nanofabrication of microcavities and photonic crystals), and Larry Coldren (fibre-optics, fabrication of micropillar lasers and LEDs) at the University of California at Santa Barbara (UCSB).

3) Designing and building experimental setups.

4) Installing a new research laboratory at UCSB.

5) Writing research proposals to secure long-term funding.

6) Guiding the MBE growth to produce samples. To obtain the necessary practical background, I followed a cleanroom course in semiconductor device processing at the Materials Department, UCSB (Sep–Dec 2002).

7) Carrying out photoluminescence studies of the samples.

As indicated in 4), in May 2002, Dirk Bouwmeester accepted a position at UCSB, and our research group moved along. The project which started in Oxford had to be restarted from scratch, this time including the construction of the lab space itself. The project has been through all stages of development, see Figure 4.1, up to the stage of a running experiment and first results. As a consequence of 5), in June 2003 we were awarded a four-year research grant. We are now in the position to perform state-of-the-art research in the field of semiconductor nanostructures for quantum information science.

Usually, the scheme in Figure 4.1 is reiterated many times in different order during the project. However, each of the four stages has to be dealt with, and I will describe below how they were implemented in our project.

First of all, since this project is aimed at combining the ideas of quantum optics with the properties of solid-state nanodevices, we will review the quantum-optics

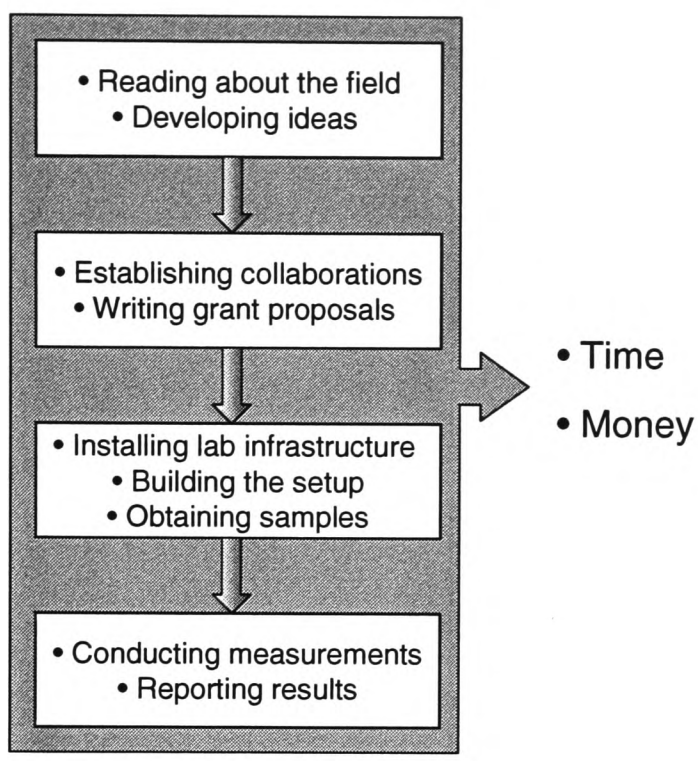


Figure 4.1: *Organisational scheme of a research project.*

and solid-state tools in Sections 4.2 and 4.3, respectively. Armed with these tools, we propose two experiments on the resonant excitation in Sections 4.5 and 4.7. We describe our on-going work towards realisations of the proposed photon-exciton coupling, including the first experimental results on quantum dots in novel microcavities, in Chapter 5. Finally, we present our ideas for future experiments in Chapter 6.

4.2 Quantum-optics tools

4.2.1 Photons for quantum information science

Single photons are very suitable carriers of quantum information. In particular, their polarization degree of freedom can be used to produce a *qubit* $\alpha|V\rangle + \beta|H\rangle$, where the vertical and horizontal polarization states $|V\rangle$ and $|H\rangle$ form a complete basis in the two-dimensional Hilbert space, and α and β are complex amplitudes. The

main advantage of photons is that they are largely decoupled from the environment what allows for transport and manipulations of the qubits. As a result, photons have proven to be instrumental in creating entanglement and in demonstrating elementary schemes in quantum information science, such as quantum cryptography [20], quantum teleportation [21], and quantum cloning [82].

Current technology limits the transmission of single-photon quantum states to some 100 kilometers because of optical losses and/or dispersion effects in the optical fibers [5, 77]. It has been shown theoretically that it is, however, possible to go beyond that limit using the *quantum repeaters*. This approach requires a short-distance photon transmission via optical fibres or in free space, as well as local storage and manipulation of photon quantum states. The quantum repeater scheme is one of the motivations to study the combination of quantum optics and solid-state physics and will be described in Section 6.2.

4.2.2 Polarization-entangled photons

The refraction index n of *non-linear optical crystals* (NLOC), such as β-barium borate (BBO) [36] can be expressed as a function of the electric field $\mathbf{E}$ of the light wave inside the crystal:

$$n(\mathbf{E}) = n_0 + n_1|\mathbf{E}| + n_2\mathbf{E}^2 + ..., \tag{4.1}$$

where n_0 is the conventional refractive index used in linear optics, and n_i describe the non-linear response. The dielectric polarization inside a NLOC can be expanded according to the matter equation as

$$\mathbf{P}(\mathbf{E}) = \kappa(\mathbf{E})\mathbf{E} = \kappa_0\mathbf{E} + \chi^{(2)}\mathbf{E}^2 + ..., \tag{4.2}$$

where κ_0 is the linear dielectric susceptibility, and $\chi^{(2)} = \frac{1}{2\pi}n_0n_1$ is the *square non-linear coefficient.*



Figure 4.2: *Schematics of the type-II non-collinear parametric down-conversion. Figure taken from Ref. [20].*

It is the non-zero $\chi^{(2)}$ that gives rise to the spontaneous *parametric down-conversion* (PDC), the lowest order non-linear process whereby a photon of the *pump field* at frequency ω_p interacts with the material in such a way that two photons called *signal* and *idler* are spontaneously created in the two other fields at frequencies ω_1 and ω_2. Energy conservation implies that $\omega_p = \omega_1 + \omega_2$, and in the following we assume a degenerate case $\omega_1 = \omega_2 = \omega_p/2$. In order to observe significant non-linear effects, contributions from the whole interaction volume of the crystal need to interfere constructively, which leads to the *phase-matching conditions* $\mathbf{k}_p = \mathbf{k}_1 + \mathbf{k}_2$.

There are two possible types of phase matching [20]: *type I* where the two down-converted photons have parallel polarizations, and *type II* where they have orthogonal polarizations. Geometrically, the phase-matching conditions can be *collinear*, where all the wavevectors are parallel, and *non-collinear*.

The non-collinear type-II PDC is shown in Figure 4.2. The phase-matching conditions are such that the signal and the idler photons come out of the crystal along the two cones. The upper cone emits vertically polarized idler photons, while the lower cone emits horizontally polarized signal photons. At the points of intersection of the

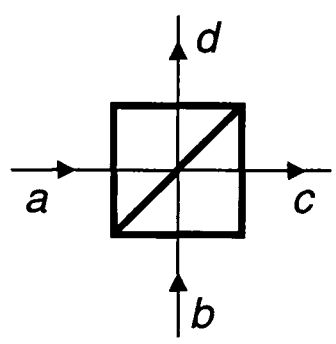


Figure 4.3: *Beamsplitter with quantum fields at the input and output.*

two cones, photons can emerge in a *maximally-entangled polarization state*

$$|\Psi\rangle = \frac{1}{\sqrt{2}}\big(|H\rangle_1|V\rangle_2 + e^{i\varphi}|V\rangle_1|H\rangle_2\big), \tag{4.3}$$

where the phase φ can be changed by using additional optical elements (see section 3.4.4 of [20]).

Entanglement is a crucial resource in quantum information science (see e.g. [138]), and we will address the possibility of entangling photons with solid-state nanodevices in Section 6.1.

4.2.3 Photon bunching at a beamsplitter

It is surprising how important the role of the *beamsplitter* (BS) is in modern quantum optics experiments, given its relative simplicity.

Figure 4.3 depicts a BS in action. Incident light in either mode a or b is split into two beams coming out via modes c and d. If t and r are the transmission and reflection coefficients of the BS, the following mode relations apply

$$\begin{aligned} c &= t\,a + i r\,b \\ d &= i r\,a + t\,b \\ r^2 + t^2 &= 1, \end{aligned} \tag{4.4}$$

where the complex numbers appear due to the $\pi/2$ phase shift acquired upon reflection, and t and r are assumed to be real, in order to satisfy the unitarity requirement of the BS transformation. In the case of a 50:50 BS, $t = r = \frac{1}{\sqrt{2}}$ and formulas (4.4) correspond to the Hadamard transformation.

Suppose that two photons, one in mode a and one in mode b, are simultaneously incident on the BS. The input state is given by $|\Psi_{in}\rangle = a^\dagger b^\dagger |vac\rangle = |1_a, 1_b\rangle$, where $a^\dagger, a$ are the usual bosonic creation and annihilation operators: $a^\dagger|N\rangle = \sqrt{N+1}|N+1\rangle$, $a|N\rangle = \sqrt{N}|N-1\rangle$. Applying the operator transformations (4.4) to the input state, one gets the output state of the field:

$$|\Psi_{out}\rangle = (R-T)|1_c, 1_d\rangle + i\sqrt{2RT}\,|2_c, 0_d\rangle + i\sqrt{2RT}\,|0_c, 2_d\rangle, \tag{4.5}$$

where $R = r^2$ and $T = t^2$ are reflectivity and transmissivity of the BS, correspondingly. For a perfect 50:50 BS $R = T$ and the first term in Eq. (4.5) disappears. The remaining terms indicate that the two photons will always leave the BS together either in arm c or d. In the following sections, we will refer to this effect as *photon coalescence* [52] or *photon bunching*, which was first demonstrated in the Hong-Ou-Mandel experiment [60] with a PDC source of photon pairs.

Experimentally, photon bunching is observed as a dip (called the *Hong-Ou-Mandel dip*) in the number of two-photon coincidences in arms c and d as a function of the time delay. Here, the background level is given by the average number of photons registered by the detectors in two arms within a time-resolution interval of the coincidence counter. The *full-width at half-maximum* (FWHM) of the dip is determined by the coherence time of the interfering photons. We will use this information in formulating our proposed experiment in Section 4.5.

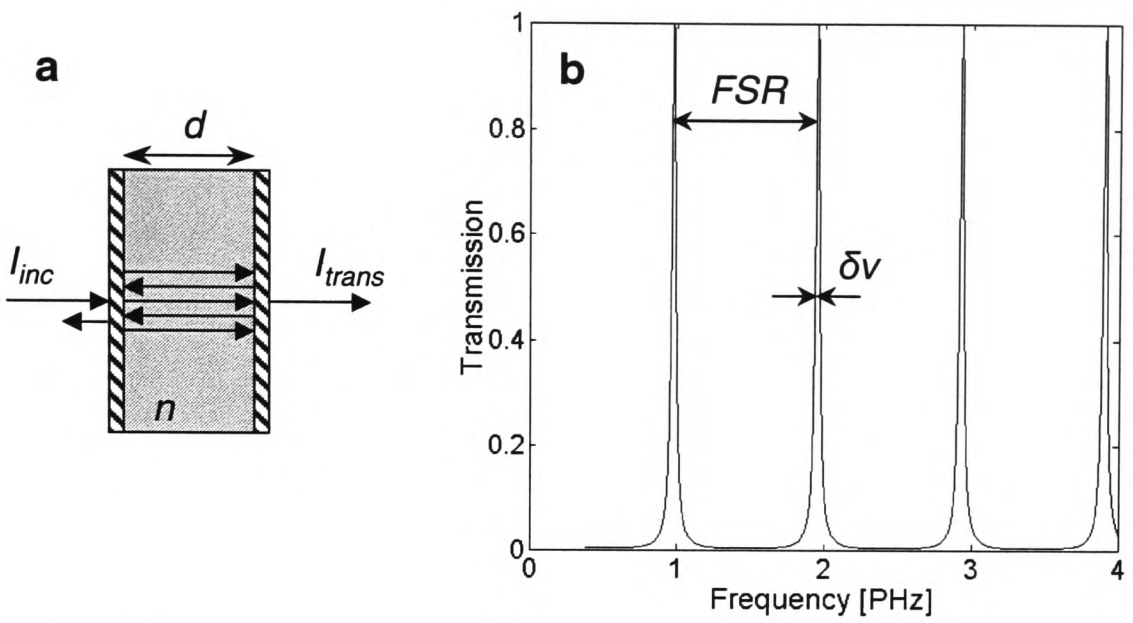


Figure 4.4: *(a) Schematic of the Fabry-Perot interferometer, and (b) the calculated transmission according to Eq. (4.6) through the system for parameters given in the text as a function of frequency shown in units of* 10^{15} *Hz.*

4.2.4 Fabry-Perot interferometer

Many concepts of semiconductor microcavities discussed below can be conveniently illustrated in the example of the *Fabry-Perot interferometer* (FPI), shown schematically in Figure 4.4a. Strictly speaking, this is a quantum-optics tool, which will be implemented in solid-state nanostructures.

It consists of two parallel flat mirrors with high reflectivities R_1 and R_2 separated by a gap of thickness d filled with a medium having refractive index n. Assume a plane-wave of electromagnetic field is incident on the system from the left with intensity I_{inc}. Part of it will be reflected by the first mirror, and the rest, assuming no absorption in the mirror material, will be transmitted into the FPI where it will in turn be partly reflected by the second mirror. Thus, light will be bouncing back and forth between the two high-reflectance mirrors gradually leaking outside.

Only resonant frequencies can be confined, which correspond to the usual interference condition that a plane-wave should acquire a phase of 2π (i.e. constructively interfere with itself) after each round-trip $\Delta\phi = \frac{2\pi\nu}{c} 2nd = 2\pi m$. Here, ν is the frequency of the incident light, c is the speed of light, and m is an integer. The *cavity resonant modes* are $\nu_m = \frac{mc}{2nd}$, or $\lambda_m = \frac{2nd}{m}$. The case of $m = 1$ defines the *fundamental mode.* It corresponds to the largest wavelength – equal to the round-trip distance – that can be confined in the cavity.

It can be shown[i] that the transmission of the FPI in the plane-wave approximation is given by:

$$T = \frac{I_{trans}}{I_{inc}} = \frac{T_1 T_2}{1 + R_1 R_2 - 2\sqrt{R_1 R_2}\cos(\frac{4\pi\nu nd}{c})}, \tag{4.6}$$

where $T_i = 1 - R_i$ are the individual transmissivities of the mirrors. The calculated transmission through a cavity with $R_1 = R_2 = 0.9$, $d = 280$ nm, and refractive index $n = 3.45$ equal to that of GaAs at 5K is plotted in Figure 4.4b.[ii] One can see that a symmetric cavity with $R_1 = R_2$ is transparent only at the frequencies of the resonant modes.

The interval between two consecutive resonant modes is called the *free spectral range* (FSR):

$$\text{FSR} = \nu_{m+1} - \nu_m = \frac{\nu_m}{m} = \frac{c}{2nd}. \tag{4.7}$$

The linewidth of each mode $\delta\nu$ is given by the FWHM of the transmission peaks in Figure 4.4b and indicates the lifetime of the cavity, which is directly dependent on the mirror reflectivities. A figure of merit used to describe a cavity is the *finesse*

$$\mathcal{F} \approx \frac{\pi}{1 - \sqrt{R_1 R_2}}, \tag{4.8}$$

[i]The derivation includes a careful summation over amplitudes of the reflected and transmitted waves with corresponding phase shifts, see Ref. [78].

[ii]Here we have chosen the typical parameters of a semiconductor microcavity but reduced reflectivities of the mirrors in order to make the transmission linewidths clearly seen in the figure.

where the approximation is valid when R_1 and R_2 are close to unity [78]. The finesse is related to the linewidth of the resonant modes as $\mathcal{F} = \frac{\text{FSR}}{\delta\nu}$, and it can be roughly understood as the number of times a photon bounces back and forth inside the cavity before its amplitude decays by a factor of $1/e$.

As a result of the constructive interference, the intensity inside the symmetric cavity with $R_1 = R_2$ increases by a factor of $\mathcal{F}$. Of course, this does not mean there are more photons in the cavity, but that the probability of a photon to be in the given cavity mode is increased. Sometimes it is also referred to as the *vacuum field enhancement.*

An alternative to the finesse measure often used in the experimental literature on semiconductor microcavities is the cavity *quality factor*

$$Q = \frac{\nu_m}{\delta\nu} = \frac{\lambda_m}{\delta\lambda}, \tag{4.9}$$

which is related to the finesse as $Q = m\mathcal{F}$. Here m is the mode number, although we will be mostly dealing with the fundamental mode of the cavity, where quantitatively $Q = \mathcal{F}$.

4.3 Solid-state tools

4.3.1 Self-assembled quantum dots for quantum information science

Semiconductor self-assembled quantum dots (SAQDs) are fabricated by a technique called the *Stranski-Krastanow mode growth*, which has been routinely used with III-V materials, e.g. InAs/GaAs.

When one material is deposited on top of another with a different lattice constant (e.g. 7% lattice mismatch for InAs and GaAs) the growth involves a few steps. The



Figure 4.5: *(a) Transmission electron microscope cross-sectional image of a single InAs self-assembled quantum dot grown on the GaAs substrate (from Ref. [166]). (b)Scanning tunnelling microscope image of InAs self-assembled quantum dots (from Ref. [167]).*

first deposited monolayers form an epitaxial *wetting layer* having the same lattice constant (but not the same type of atoms) as the material underneath. As growing proceeds, strain increases in the deposited layer. When a critical thickness of the wetting layer is reached, a spontaneous formation of 3D coherent islands takes place, see Figure 4.5a. The islands have a perfect crystalline structure and are free from edge defects. It is now possible to fabricate arrays of QDs (see Figure 4.5b) as small as 10 nm in base diameter and a few nm in height with an area density of 10^8 to 10^{11} cm^{-2}.

SAQDs are promising candidates for the local operations and, ultimately, storage and retrieval of the photon quantum states. Their discrete energy spectrum allows one, just like in atoms, to single out two levels for encoding $|0\rangle$ and $|1\rangle$, such as e.g. the double-degenerate excitonic state created by optical transitions σ^+ and σ^-

between the heavy-hole and electron spin states (see Section 4.3.2 and Figure 4.7 below). QDs couple rather efficiently to light due to the large dipole moments of the optical transitions (50–100 times larger than those of atoms [44]). Furthermore, recent demonstrations of excitonic Rabi oscillations [72, 61, 133] and an all-optical two-bit conditional quantum gate [84] clearly indicate that individual QDs are reliable two-level quantum systems. Last but not least, properties of the QDs can be changed fairly accurately by virtue of well-established nanofabrication means.

There are, however, two main disadvantages of the SAQDs with respect to atoms. First, because of the spontaneous process of self-assembly, the QDs are inhomogeneously broadened: their optical and electronic properties vary due to the variation in size of 10–30%. This inhomogeneous broadening is detrimental for conducting coherent excitations of the QD ensembles because of the charge transfer from smaller to bigger dots involving phonon generation and decoherence. Second, the QDs are surrounded by the material, e.g. InAs SAQDs are grown in the GaAs matrix, what gives rise to the inevitable coupling to the environment (the crystal lattice) and phonon-related decoherence, described in Section 4.3.4. The current experimental estimate of dephasing in InAs SAQDs is 630 ps [18].

In order to use SAQDs for quantum information processing, both problems have to be addressed. In this chapter we will focus on single-QD experiments, what will largely eliminate the first problem, and present proposals on how to increase the QD coherence time.

4.3.2 Optical properties and selection rules

Let's consider optical excitation of the semiconductor nanostructure in the case when the CB minimum and VB maximum have the same coordinate in the reciprocal space,

as seen in Figure 2.1b[iii]

An electron absorbs a photon of energy $E > E_g$ implementing a *direct* transition from the VB to the CB. Since the wavelength of the excitation light (0.5–1.5 μm) is several orders of magnitude greater than the lattice constant, the light wavevector is negligible compared to the dimensions of the Brillouin zone, $\mathbf{K} = 0$. Thus, the conservation of momentum and energy during the transition implies [76]:

$$\mathbf{k} = \mathbf{k}' \tag{4.10}$$

$$E_{VB}(\mathbf{k}) + \hbar\omega = E_{CB}(\mathbf{k}') \tag{4.11}$$

Another possibility is excitation through an *indirect* transition, involving a photon and a phonon. The conservation laws in this case read

$$\mathbf{k} \pm \mathbf{q} = \mathbf{k}' \tag{4.12}$$

$$E_{VB}(\mathbf{k}) + \hbar\omega \pm \hbar\Omega = E_{CB}(\mathbf{k}') \tag{4.13}$$

where the two signs correspond to absorption and emission of a phonon. Indirect transitions are two-step processes and therefore are less probable. In order to specify E_{CB} and E_{VB}, we consider the energy spectrum of the QD heterostructure in more detail.

In reality, for semiconductors like GaAs, the CB is formed from s-orbitals of the Ga ions, whereas the VB develops from p-orbitals of the As [151]. The orbital momentum of the s-states is zero, so the CB has only two-fold spin degeneracy at $\mathbf{k} = 0$ (the Γ-point of the Brillouin zone). However, due to the p-type character of the atomic orbitals the orbital momentum is $L = 1$, and the VB consists of a larger number of subbands. Those can be classified by the total angular momentum $\mathbf{J} = \mathbf{L} + \mathbf{S}$, representing the sum of the orbital angular momentum and the spin, into a four-fold degenerate band with $J = 3/2$ and a two-fold degenerate band with $J = 1/2$.

[iii] True for direct-bandgap semiconductors, such as GaAs and InAs.



Figure 4.6: *Band structure of the semiconductor around the* Γ*-point : (a) in the absence of strain, (b) under compression, (c) under tension (from Ref. [10]).*

At $\mathbf{k} = 0$, the latter is separated in energy from the former due to the spin-orbit interaction (see also Section 2.6.4); it is called the *spin-orbit split-off band* (SO), and it does not participate in the optical transitions of interest to us.

As a result of the accumulated strain in the structure, the remaining four-fold degenerate VB splits at the Γ-point into the *heavy-hole band* (HH) and the *light-hole band* (LH), see Figure 4.6. Both the HH and the LH bands near the Γ-point have a parabolic dispersion, see Figure 4.6a, which is proportional to the inverse hole effective mass:

$$\frac{1}{m^*} = \frac{1}{\hbar^2}\frac{d^2E}{dk^2}. \tag{4.14}$$

Since the curvature of the LH subband is steeper than that of HH, the HH have a bigger effective mass, i.e. they are 'heavier', than the LH, hence the origin of the name. QDs are usually formed of the material with a bigger lattice constant, giving

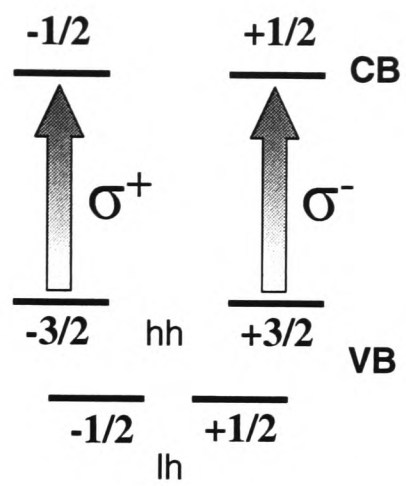


Figure 4.7: *Ground state transitions in semiconductor heterostructures. The two electron states in the conduction band are represented by the up- and down-spin projections on the quantization axis, whereas the four hole states in the valence band are labelled by the projections of the total angular momentum.*

rise to the compressive strain. As a result, the situation in Figure 4.6b takes place: the HH subband is shifted above the LH subband.

In addition to the inherent z-confinement of the carriers in quantum wells, QDs provide lateral confinement along the x and y directions, which forms additional potential minima in the CB and maxima in the VB, in which the energy spectrum is quantized. As a result, each subband in the QD is reduced to a discrete subset of localized energy states.

Figure 4.7 shows the lowest CB and highest VB states corresponding to the *lowest excitonic transition*, at $\mathbf{k} = 0$. As just mentioned, the CB electron ground state has a zero orbital angular momentum $L = 0$ and it can be occupied with spin up ($S_z = +\frac{1}{2}$) and down ($S_z = -\frac{1}{2}$) electrons, i.e., it is two-fold degenerate in the absence of the magnetic field. The VB hole ground state has $L = 1$, and its total angular momentum has two quantised values $\frac{3}{2}$ and $\frac{1}{2}$, of which we are interested in the case of $J = \frac{3}{2}$. It has four projections $J_z = \pm\frac{3}{2}, \pm\frac{1}{2}$ corresponding to the HH and LH, respectively.

Consider inter-band absorption of a resonant photon. Since a photon has spin

$S = 1$ ($S_z = 0, \pm 1$), this leads to the *optical selection rules in semiconductors*: only transitions that obey conservation of the total angular momentum, expressed by $\Delta J_z = 0, \pm 1$ are allowed [40, 106]. The two transitions from the HH states to the CB depicted in Figure 4.7 by σ^+ and σ^- have the maximum probability. They correspond to $\Delta J_z = \pm 1$ and proceed with absorption of a photon with right- and left-handed circular polarization, respectively. Transitions with $\Delta J_z = 0$ from the LH states to the CB are also possible, although they are less probable (e.g. having the transition matrix element a factor of 3 smaller in the GaAs quantum wells [40]) and also detuned in energy. The transitions with $\Delta J_z = 2$ between the HH states and the CB electron states are *dark transitions*; they are not allowed by the selection rules.

In general, the probability of an optical transition in a nanostructure can be evaluated in the dipole approximation as $\alpha(\omega) \sim p_{cv}^2 |\langle \phi_i | \phi_f \rangle|^2$, where p_{cv} is the size-independent interband dipole matrix element of the bulk semiconductor, and $\phi_i(\mathrm{r})$, $\phi_f(\mathrm{r})$ the envelope wavefunctions of the initial and final states [151]. It follows that the optical transitions mostly occur between the electron and hole levels with identical quantum numbers, i.e. $0s_e \rightarrow 0s_h$, $1s_e \rightarrow 1s_h$, $1p_e \rightarrow 1p_h$, since the corresponding wavefunctions have the same symmetry and maximum overlap.

4.3.3 Excitons

Suppose we have a semiconductor in its ground state, i.e. with the filled VB and empty CB. Exciting the structure with an incident photon of the energy $E > E_g$, one creates a negatively charged electron in the CB and a positively charged hole in the VB. As a result, attractive Coulomb interaction between the excited electron and hole binds them together to form a neutral system similar in some respects to a hydrogen atom. Such an "electron-hole pair with mutual interaction" is called an

exciton [89, 126]. The typical size of the system is given by the exciton radius, which in GaAs is on the order of 10 nm [15].

The exciton energy can be obtained by solving the modified hydrogen problem. The result for bulk semiconductor is given by

$$E_n = E_g - E_{ex} + \frac{\hbar^2 K^2}{2M}. \tag{4.15}$$

It consists of the energy difference E_g between the two bands less the binding energy E_{ex}, and the kinetic energy of the centre of gravity of the exciton, $M = m_e + m_h$ and $\mathbf{K}$ being its total effective mass and wave vector, respectively. The binding energy is obtained as

$$E_{ex} = \frac{\mu e^4}{32\pi^2 \varepsilon_0^2 \varepsilon^2 \hbar^2 n^2} \tag{4.16}$$

where $n = 1, 2, ...$ is the level number, $\mu^{-1} = m_e^{-1} + m_h^{-1}$ is the exciton reduced mass and ε is the dielectric function [89].

For small $\mathbf{K}$, the exciton energy levels are located below the CB edge (Figure 4.8). The values of the binding energy for bulk III-V semiconductors are on the order of several meV (e.g. about 1 meV for InAs, 4.2 meV for GaAs), whereas in low-dimensional structures these values are enhanced. In InAs/GaAs cone-shaped QDs the binding energy increases from 25 meV to 32 meV as the dot base size is decreased from 15 nm to 7 nm [15].

Excitons are the simplest of the possible optical excitations of the semiconductors. Consider a sample of InAs SAQD layer embedded in the GaAs matrix, which is pumped by a laser source at energy above the GaAs bandgap. At low pump intensities, there is one or no excitons created in each QD. If the pump power is increased, two photons are absorbed by a QD to create a *biexciton*, a system of two excitons coupled by Coulomb forces. If the pump energy is increased further, more excitons

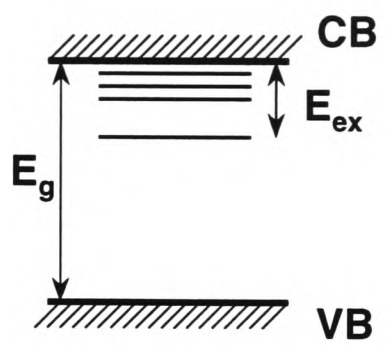


Figure 4.8: *Schematic of the exciton energy levels in a semiconductor.*

occupy the QD, forming multiexciton complexes. Up to six excitons occupying a single InAs QD have been observed [11].

Another type of optical excitations is *charged excitons.* These can be formed if the QD had originally an extra hole or electron due to doping, or if an electron or a hole that belong to the excitons generated in the GaAs matrix or in the wetting layer get subsequently trapped in the QD. In either way, an electron-hole pair in the QD interacts electrostatically with the trapped unpaired carrier forming a *trion.* Charged complexes containing one hole and up to six electrons were observed by controlling an applied gate voltage [148].

These optical excitations become especially pronounced at the increased pump powers and their energies are typically a few meV off on either side of the exciton energy, which provides a rich structure in the photoluminescence spectrum [48].

Despite the apparent similarity between an exciton and a hydrogen atom, which we used to calculate the exciton energy spectrum, it is important to point out the fundamental difference between the two. Excitons by their nature are "quasiparticles of the lowest electronic excitations in semiconductors" [71], i.e., they are always representative of the system in an excited state. On the contrary, the hydrogen atom that consists of an electron and a proton does exist in the ground state. In this way,

it would be more appropriate to draw an analogy between an exciton and an atom of positronium, where the proton is replaced with a positron. Now, both systems are unstable and have a finite lifetime, after which they recombine. The exciton recombination is further described in the next section.

4.3.4 Exciton coherence and lifetime

One of the crucial requirements for quantum information processing is the ability to maintain coherence of qubits in a controlled way. The present knowledge of the decoherence mechanisms in heterostructures is far from complete. It is, therefore, very important to investigate the effects that determine dynamics of excitons in semiconductors. Those are the following [71]:

1) *Dephasing* is loss of coherence of an exciton caused by elastic and inelastic scattering with other carriers, phonons, impurities and disorder. The timescales vary from a few femtoseconds (for electron-electron scattering in bulk GaAs) to nanoseconds (for localised excitons in mixed crystals). For the QDs, the typical dephasing times are on the order of tens to hundreds of picoseconds, e.g. 39 ps in GaAs/AlGaAs QDs formed by surface fluctuations [17], and up to 630 ps measured in InAs/GaAs SAQDs at 7 K by the four-wave mixing technique [18].

2) *Thermalisation* is a redistribution of the optically generated carriers towards a thermal quasi-equilibrium. It includes the establishment of a thermal distribution (Fermi-Dirac or Boltzmann), relaxation of electrons to the minima and holes to the maxima of the band structure, carrier cooling or heating. The timescales are similar to those of the dephasing processes, and both depend strongly on the experimental conditions, such as carrier density and temperature.

3) *Recombination* is a process of transfer of the excited electrons from the CB

down to the VB back to the equilibrium. Usually we are interested in the optical recombination that is accompanied with the spontaneous emission of the photon. Non-radiative recombination, however, also has to be taken into account in some specific cases, for example, at the surface of the heterostructure that has a lot of unoccupied states due to the dangling bonds.

Typical recombination times in heterostructures are on the order of a few hundred ps to a few ns for direct transitions, and much longer (up to 10^{-3} s) for indirect transitions involving an additional phonon. E.g. the recombination time in a single InAs SAQD was obtained from photon anti-bunching measurements to be 2.2–3.4 ns, whereas in the GaAs barrier and wetting layer it was only 100–200 fs [95].

Recombination time increases with the strength of the confinement, thus small size QDs with large confinement values would favour longer exciton lifetimes. However, the reasonably long timescale of optical recombination makes it a rather unimportant source of decoherence in comparison to the first two processes.

All of the above processes are mostly related to the *charge degree of freedom* of the exciton, i.e., the presence of the optically generated carriers in the CB and VB. A promising, though less studied, alternative in respect to the extension of coherence times is provided by considering the *spin degree of freedom*, i.e., spins of the electrons and holes forming excitons. Awschalom *et al.* have developed the time-resolved Faraday rotation technique to study *spin coherence* in bulk as well as low-dimensional semiconductors [7, 74]. Their findings of 100 ns spin coherence time in n-doped bulk GaAs at $T = 5$K and nanosecond-scale spin lifetimes in CdSe QDs at room temperature are very encouraging. Recently, Paillard *et al.* have observed long coherence times of 20 ns at 4K in InAs/GaAs SAQDs [106]. *Resonant excitation* of QDs (according to the σ^+ and σ^- transitions in Figure 4.7) was found essential to extend the spin coherence time well beyond the exciton lifetime.

It is important to emphasize that many of the decoherence effects of the excitons in QDs are believed to be caused by the carriers excited in the neighbouring materials (e.g. adjacent QDs, wetting layer, substrate, etc.). They include carrier-carrier and spin-spin scattering, as well as Auger processes – non-radiative energy transfer between the carriers resulting in the ejection of the electron or hole, or separation of the exciton. These effects become significant when a large number of carriers is present. The main effort of our project will therefore be to study individual excitons created by low-intensity (and ultimately by single-photon) pulses.

4.3.5 QD efficiency of photon absorption and emission

Since our project aims to implement the photon-exciton coupling in QDs, it is important to estimate the efficiency of the photon coupling to a QD. The absorption efficiency of an InAs SAQD can be estimated from e.g. the transmission experiment by Dürr *et al.* [38]. A sample containing InAs QDs (surface density $\rho_{QD} = 5 \times 10^9$ cm^{-2}) embedded in the field-effect device was resonantly excited with a cw pump, and transmission through the sample was measured. A reference spectrum was also taken at an applied positive gate voltage, such that all CB states in the QDs are occupied and no interband absorption could occur. Comparing the two spectra, the QD contribution could be extracted, and its absorption was found to be on the order of $\xi = 10^{-4}$. Let's rewrite it as $\xi = \frac{\Sigma_{abs}}{S}$, where Σ_{abs} is the total absorption cross-section of all QDs in the illuminated area S. Since $\Sigma_{abs} = \sigma_{abs}\rho_{QD}S$, this gives the expression for the average absorption cross-section of a single QD:

$$\sigma_{abs} = \frac{\xi}{\rho_{QD}} = 2 \times 10^{-14} \text{ cm}^2. \tag{4.17}$$

This value is in agreement with the absorption cross-section of InAs QDs 2.3×10^{-14} cm^2 obtained from a mid-infrared spectroscopy experiment [123].

The minimum spot size on which we can focus the excitation laser beam is given by the diffraction limit [102] of the microscope objective (MO)[iv] as

$$A_F = \left(\frac{0.61\lambda}{\mathrm{NA}}\right)^2, \tag{4.18}$$

which for the operating wavelength $\lambda \approx 950$ nm and numerical aperture NA $= 0.55$ is on the order of $A_F \approx 1\ \mu\mathrm{m}^2$. The probability that a cw photon excites the QD is then

$$p_{cw} = \frac{\sigma_{abs}}{A_F} = 2 \times 10^{-6}.$$

However, we will be mainly interested in a resonant pulsed excitation (100 fs to 60 ps with our laser systems), in order to apply time-resolved measurement techniques. Since a pulse has a finite bandwidth, only the frequency components that fit in the linewidth of the QD excitonic state will be absorbed, and the rest will be transmitted or reflected. The probability p_{cw} thus should be multiplied by the bandwidth ratio, or equivalently, the ratio of the photon coherence time and the excitonic lifetime

$$f_{freq} = \frac{\tau_{ph}}{\tau} \tag{4.19}$$

to give the overall probability of QD absorption for a pulsed excitation source

$$p_{abs} = p_{cw} f_{freq}. \tag{4.20}$$

Once a photon is absorbed by the QD, another photon will be spontaneously emitted as a result of the exciton recombination. Spontaneous emission occurs isotropically in all directions, but only the photons emitted in a finite solid angle, determined by the numerical aperture of the MO, will be collected by the objective for further use in the experiment, as seen in Figure 4.9. Assuming that the QD layer is capped with GaAs,[v] it follows from the definition of the NA and Snell's law that

[iv] See Section 5.1 for the specification of our MO.

[v] To prevent the QDs from oxidation and mechanical damage.

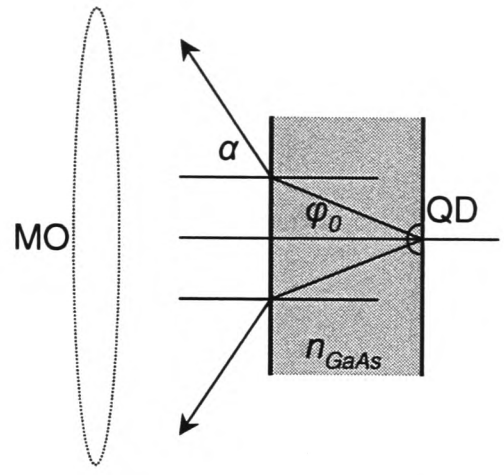


Figure 4.9: *Schematic of propagation of light emitted by the QD and collected by the microscope objective.*

$\mathrm{NA} = \sin\alpha = n_{GaAs}\sin\varphi_0$. Thus $\varphi_0 = \arcsin(\mathrm{NA}/n_{GaAs})$ and the emission efficiency is given by

$$p_{em} = \frac{\Omega}{4\pi} = \frac{1}{2}\int_0^{\varphi_0} d\varphi \sin\varphi = \frac{1}{2}\left[1 - \sqrt{1 - \left(\frac{\mathrm{NA}}{n_{GaAs}}\right)^2}\right], \tag{4.21}$$

For $\mathrm{NA} = 0.55$ and $n_{GaAs} = 3.45$, one finds that $p_{em} = 0.006$. This value can be improved by an order of magnitude if a micro-lens with an intermediate refractive index ($1 < n_{lens} < n_{GaAs}$) is attached on top of the sample [162]. In this case the emission efficiency $p_{em} = 0.08$ will be limited only by the NA of the MO.

4.4 Resonant transfer of quantum information between photons and excitons

In most photoluminescence (PL) experiments on a single QD, the dot is excited above the resonance, i.e., the excitons are created in the wetting layer (sometimes in the high-lying excited states of the QD) and subsequently relax to the QD lowest excited state before they recombine by emitting a photon of a characteristic frequency. The

exciton relaxation to the lowest excited QD state typically involves phonon emission and scattering. Hence, the quantum phase of the relaxed exciton will be random and in no relation to the initial phase of the absorbed photon that created the exciton.

For quantum information science applications one wishes to transfer the polarization and phase information from a photon to an exciton. To avoid the above-mentioned dephasing mechanism, we propose to consider *résonant* coupling of individual photons and QDs.

Another major source of decoherence in semiconductors, inherent in a typical PL experiment, is the Coulomb scattering between an exciton in a QD and additional excitons in the same QD or in adjacent regions. We propose to suppress the Coulomb scattering by exciting the QD at the level of single photons, so that only one exciton of interest is optically generated each time.

As discussed in Section 4.3.2, a resonant photon in the left- or right-handed circular polarization state creates in a symmetric QD an exciton in one of the two degenerate spin states according to the σ^+ or σ^- transitions. The resonant optical excitation process can be formally written as following:

$$\begin{aligned} \hat{A}\big(|Left\rangle|0_{\sigma^+}, 0_{\sigma^-}\rangle\big) &= |vac\rangle|1_{\sigma^+}, 0_{\sigma^-}\rangle, \\ \hat{A}\big(|Right\rangle|0_{\sigma^+}, 0_{\sigma^-}\rangle\big) &= |vac\rangle|0_{\sigma^+}, 1_{\sigma^-}\rangle, \end{aligned} \tag{4.22}$$

where $\hat{A}$ is the light-matter interaction operator, and the kets on the left and on the right are the quantum states of the system 'photon-QD' before and after the excitation. $|Left\rangle$ and $|Right\rangle$ are polarization states of the photon, and $n_{\sigma^+}, m_{\sigma^-} = 0, 1$ are the occupation numbers of excitons created in the two spin states.

What happens if the photon irradiating the QD is itself in a superposition state $|\psi\rangle = \alpha|Left\rangle + \beta|Right\rangle$ and its energy is resonant with the excitonic transition? Due to the energy conservation, exactly one exciton will be created, and from Eq. (4.22)

it follows that the exciton will be created in the superposition of its two degenerate spin states with the same amplitudes α and β:

$$\hat{A}\Big[\big(\alpha|Left\rangle + \beta|Right\rangle\big)|0_{\sigma^+}, 0_{\sigma^-}\rangle\Big] = |vac\rangle\big(\alpha|1_{\sigma^+}, 0_{\sigma^-}\rangle + \beta|0_{\sigma^+}, 1_{\sigma^-}\rangle\big). \qquad (4.23)$$

Note that we made the crucial assumption that the σ^+ and σ^- transitions are degenerate in energy. In general, the epitaxially grown self-assembled QDs are not symmetric, and it is important to develop ideas and techniques to tune the σ^+ and σ^- transitions into degeneracy. This issue will be addressed in Section 6.3, and for the moment we assume that the energy degeneracy holds.

If the exciton decoherence time is longer than the recombination time, then the exciton will remain in the initial superposition state until it spontaneously emits a photon. Since the exciton was created resonantly in its lowest energy state, no phonons will be involved in the recombination, and the emitted photon will be resonant with the exciton energy state. A process reverse to (4.23) will take place, and as a result, the polarization state of the emitted photon will be $|\psi\rangle = \alpha|Left\rangle + \beta|Right\rangle$.

Thus, information encoded in the polarization quantum state of a photon will be coherently transferred to an exciton in a QD, stored there for the time determined by the exciton recombination time, and then transferred back by spontaneous emission of a photon in the same polarization state. Retrieving the photon states afterwards will be a test of the coherent transfer of quantum information between photons and excitons and can be used as a method to study exciton decoherence processes.

There is a significant technical difficulty in studying resonant excitation. Resonant condition obviously implies that the pump frequency and emission frequency are the same. Hence, one has to use the time information to distinguish the emitted photons from the scattered pump light. Exciton recombination lifetimes τ in, e.g., InAs/GaAs SAQDs are on the order of a nanosecond. If a QD is excited with laser pulses on the

order of tens of picoseconds, the reflected photons will be described by a high and narrow time-dependent peak, whereas the re-emitted photons wavepackets will be spread over time with a much weaker amplitude. Moreover, since most reflections are coming from the surface of the sample, cryostat windows, microscope objective lenses, and other optics surfaces located in our setup within $\Delta l \sim 6$ cm from the QDs, the reflected pulses will all occur within the first $\Delta t = \Delta l/c \approx 200$ ps leaving the longer delay times entirely for the QD emission.

Effectively, the problem is reduced to finding a way of detecting light in a specified time-delay window $\Delta t \leq t \leq \tau$. A possible solution is to use a streak camera which provides a picosecond resolution. A complication is that a streak camera has a relatively small dynamic range (typically 1000:1) what makes it difficult to detect a small signal (the QD emission) shortly after detecting a bright signal (scattered light).

We have designed two setups that avoid using an expensive streak camera[vi] but still can resolve temporally the two signals. Our proposed solution is to employ techniques of quantum optics, namely *quantum interference of photons*, in combination with the two-photon coincidence detection. In our design, a time resolution of the order of 50 ps, determined by the pump pulse duration, can be obtained despite using conventional single-photon detectors that only have a time resolution ~ 400 ps and a coincidence unit with the time window of 2 ns.

[vi] E.g. Hamamatsu C7700 model quotes for USD 150,000.

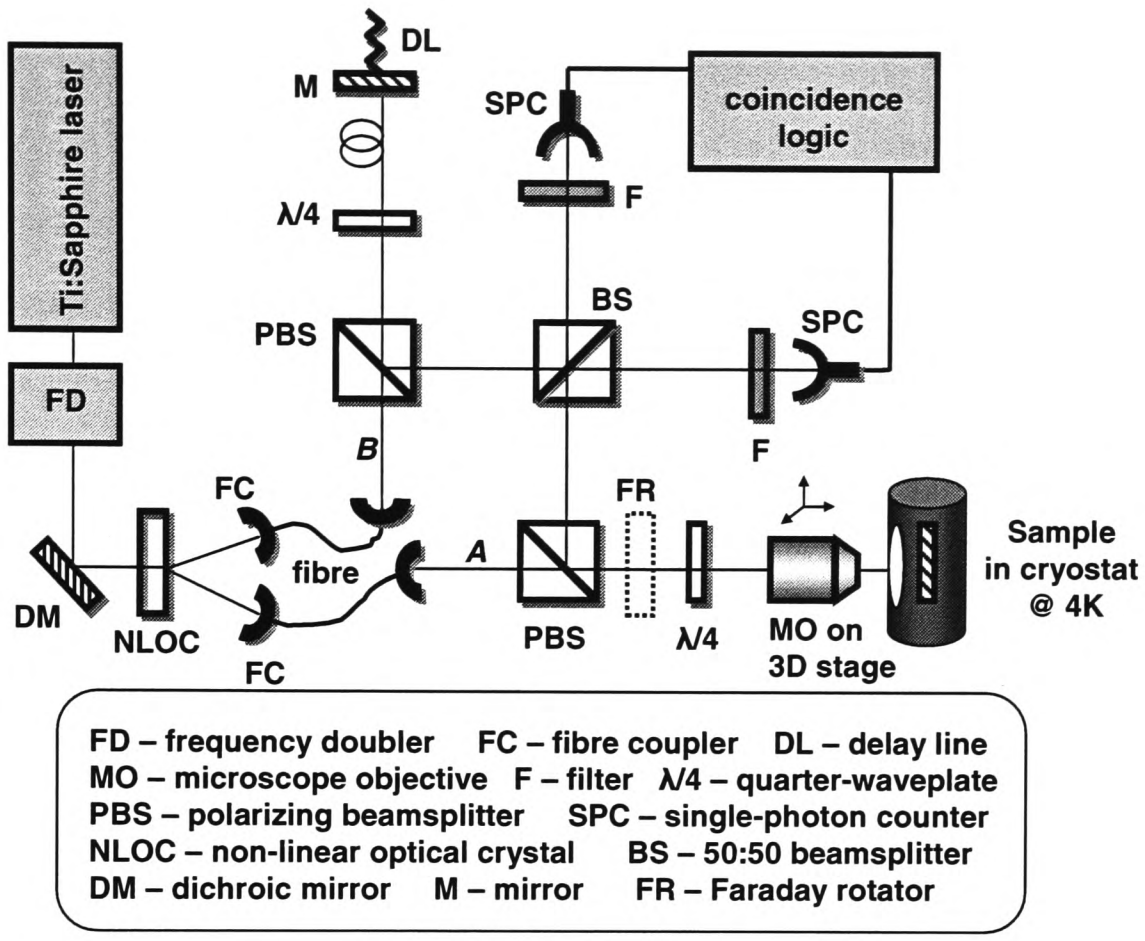


Figure 4.10: *Schematics of the time-resolved photon-correlation experiment. Faraday rotator (FR) can be inserted in arm A for the polarization analysis of the sample, as discussed in the text.*

4.5 Time-resolved photon-correlation experiment

4.5.1 Description of the proposed experiment

This experiment makes use of single-photon pulses and the Hong-Ou-Mandel dip described in Section 4.2.3, the outline of the setup is shown in Figure 4.10. Light from a mode-locked Ti:Sapphire laser is frequency-doubled and then down-converted in a non-linear crystal to produce (by type-I non-collinear parametric down-conversion) pairs of photons prepared in the state $|H_A, H_B\rangle$, where H denotes the horizontal polarization state of a photon in mode A or B.

The two photons are coupled through *single-mode* (SM) fibres to a free-space interferometer, where they fall onto two *polarizing beamsplitters* (PBS). A PBS transmits the horizontal and reflects the vertical polarization state. Thus, both incoming photons are transmitted. After the PBS each photon passes through a $\lambda/4$ plate at 45° that transforms the $|H\rangle$ state into $\frac{1}{\sqrt{2}}|H + iV\rangle$ corresponding to the right-hand circular polarization state.

Photon in arm A is focussed by a microscope objective (MO) on the QD sample in the cryostat. Note that the sample should be first pre-characterized to find both spatially and spectrally a single QD transition[vii] and then the photon energy should be tuned on-resonance with that transition. This can be done with the standard μ-PL technique. After the resonant absorption and exciton recombination, the emitted photon should in principle have the same energy and polarization as the absorbed photon. Passing back through the MO and $\lambda/4$ plate, its polarization is now transformed to vertical $|V\rangle$,[viii] and the PBS will reflect the photon towards the 50:50 BS.

The photon in arm B is reflected by a mirror mounted on the delay line and sent by the same combination of the PBS and $\lambda/4$ plate to the second input of the 50:50 BS. At the outcome of the BS, photons are detected by *single-photon counters* (SPC), and two-photon coincidences are registered.

Note that the resonant photon is prepared in the right-hand circular polarization state to excite the σ^+ transition. This can be changed to any other polarization using a combination of waveplates and a Faraday rotator.

[vii] It is preferable to choose a QD transition in the low-energy part of the QD spectrum, in order to avoid generation or transfer of excitons to adjacent QDs.

[viii] As a simple check of the polarization transformations, the photon passes twice through the $\lambda/4$ plate, which is equivalent to passing once through the $\lambda/2$ plate. The latter rotates the polarization by 90 degrees, thus $|H\rangle$ becomes $|V\rangle$.

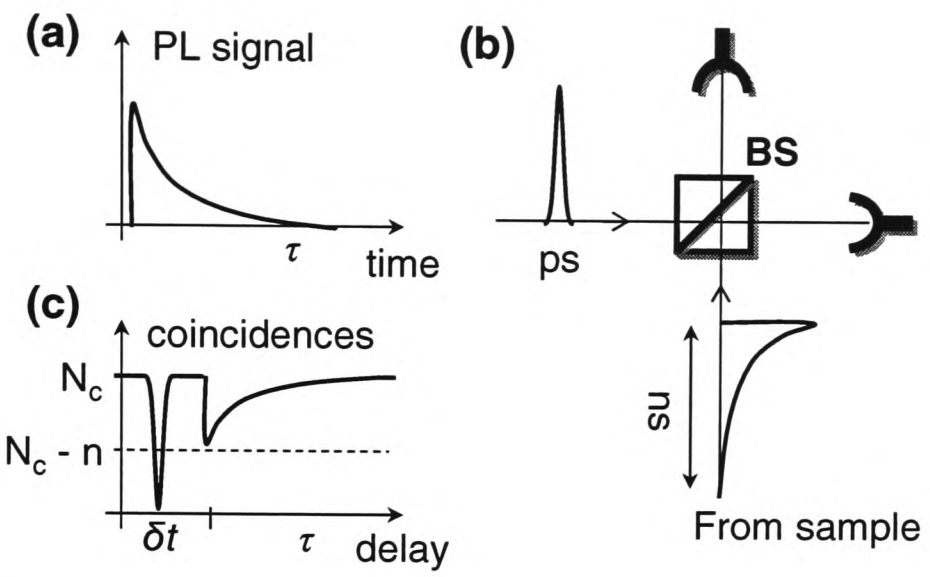


Figure 4.11: *Operation principle of the setup. (a) Time-dependent profile of the photons emitted by a quantum dot. (b) Schematics of the two-photon interference and detection: the photon emitted by the QD has a nanosecond coherence time (shown in (a)), whereas the reference photon has a typical width of the order of picoseconds. (c) The detected signal reproduces the inverted shape of the QD emission as well as reflections from the optics on the way (drawn not to scale.)*

If the polarization of the photon is preserved during the QD absorption and emission, then at the input of the BS, the two photons will have the same energy and polarization but different time-dependent profiles. The photon emitted by a QD in arm A is described by an exponent with a typical width of $\tau \approx 1$ ns, whereas the profile of the photon in arm B is determined by the down-conversion conditions (and optional narrow-band filters, see below) and is much shorter, as illustrated in Figure 4.11. Controlling the delay in arm B it is possible to achieve a maximum overlap of the two photons on the BS, which corresponds to zero delay time. However, because of the different time-dependent shape of the photon pulses, the temporal overlap will be only partial, and unlike in the Hong-Ou-Mandel experiment mentioned in Section 4.2.3, the two-photon coincidences count shall never reach zero at its minimum. On the contrary, the dip for the reflected photons at time delay δt

(Figure 4.11c) should go down to zero since their time-dependent shape is the same as of the reference photons.

The main point of concern is the *visibility* of the dip defined as

$$\nu = \frac{I_{max} - I_{min}}{I_{max} + I_{min}}, \tag{4.24}$$

where I_{max} and I_{min} correspond to an average uncorrelated number of photon coincidences per measurement time, and the minimum number of coincidences at zero delay time, respectively.

The visibility of the dip ν will be quantitatively analyzed below in this section. Nonetheless, even at this stage it is possible to see that it is proportional to the amplitudes of the overlapping single-photon pulses at a given delay time. Hence, by changing the delay of the photon in arm B, it should be possible to sweep over the whole duration of the QD emission signal, so that its time-dependent profile will be reflected as an inverted function of the visibility ν over the delay time.

This time resolution is indeed determined by the width of the reference photons in arm B, which we choose to be about 50 ps to provide enough measurement points of the QD emission with a nanosecond lifetime. Clearly, the time resolution can be further decreased by taking shorter pulses if required. E.g. intervals on the scale of 100 fs were measured in the Hong-Ou-Mandel experiment [60]. Hence the above technique should prove extremely useful to overcome the limited and insufficient temporal resolution of the available single-photon detectors.

An additional benefit is that the two-photon coincidence counting is not sensitive to the uncorrelated background noise. Indeed, at typical dark counts not exceeding 500 photons per second, the probability of the second 'dark' photon being registered by a single-photon detector within 2 ns, given that the first photon has been registered by the other detector, is less than 10^{-6}.

Polarization analysis

The experimental design in Figure 4.10 allows for the time-resolved measurement of the resonant excitation. We now have to improve the setup to be able to analyze the polarization characteristics of the emitted photons. This analysis will give us information on the possible spin dephasing of the resonant excitons optically generated in the QD.

For the sake of clarity, let's consider two limiting cases. In the first case, an exciton created via the σ^+ transition preserves its spin coherence until it recombines. The emitted photon is collected by the MO, and after passing through the $\lambda/4$ plate it ends up vertical $|V_A\rangle$, which is fully reflected by the PBS. This case was considered above.

Putting a Faraday rotator after the PBS, as shown in Figure 4.10, we can design optics in arm A such that the emitted photon ends up in the state $|H_A\rangle$, which is fully transmitted by the PBS. Indeed, one can apply a 45° Faraday rotation of the initial horizontal state of the pump photon and further transform it to right-hand circular by the $\lambda/4$ plate.[ix] On the way back, if no spin dephasing occurs, the emitted photon has a right-hand circular polarization, which is transformed to the $-45°$ linear by the $\lambda/4$ plate, and then another 45° Faraday rotation transforms it back to $|H_A\rangle$. In this case, no photons will be reflected to the 50:50 BS.

The second limiting case assumes complete spin dephasing of the exciton in the QD. After exciton recombination, the emitted photon is randomly polarized, and after passing the $\lambda/4$ plate it will be in an equal mixture of states $|H_A\rangle$ and $|V_A\rangle$. In this case, the PBS will only reflect the vertical component, and the signal arriving at the 50:50 BS will be characterised by a half-decreased intensity, which does not depend

[ix] In this case, the $\lambda/4$ plate has to be rotated by the same 45° as was chosen for the Faraday rotation.

on the presence of the Faraday rotator in arm A.

Thus, by detecting the intensity of the signal on the 50:50 BS with and without the Faraday rotator, one can get the information on the spin-dephasing of the resonantly created excitons in QDs. We should mention that in reality, the QD sample can have a preferential polarization of the optical emission. In this case, it will be useful to probe not only the σ^+ transition, but also the σ^-. This can be done by preparing the pump photon in the vertical state $|V_A\rangle$, e.g., by choosing a 135° Faraday rotation instead of 45°, while leaving the $\lambda/4$ plate unchanged.

4.5.2 Visibility estimate

How feasible is the proposed experiment? To answer this question we have to estimate the visibility ν of the correlation dip. Figure 4.11c shows schematically how the number of coincidences per measurement time is decreased from the average level of N_c by n at the minimum of the dip. Recall that the dip is the result of photon bunching. (The first dip comes from the pump photons reflected by the cryostat window.)

According to formula (4.24), visibility becomes

$$\nu = \frac{N_c - (N_c - n)}{N_c + (N_c - n)} = \frac{n}{2N_c - n}. \tag{4.25}$$

To calculate this fraction, we should take into account the following factors.

1. Natural width of the Hong-Ou-Mandel dip

As mentioned previously in Section 4.2.3, the phase-matching conditions of the crystal determine the pulse shape of the down-converted photons. The shape of the dip, in turn, is given by the convolution of the two photon pulses. For type-I PDC, the

natural width of the correlation dip is approximately

$$\tau_{dip} = \sqrt{DL}, \tag{4.26}$$

where $D = \frac{d^2k}{d\omega^2}$ is the dispersion of light in the non-linear crystal at frequency $\omega_c = \omega_p/2$, and L is the crystal length [73]. For a typical type-I lithium triborate (LBO) crystal $D \approx 1.2 \times 10^{-25}$ s^2/m at 950 nm (derived from dispersion data in the Handbook of Nonlinear Optical Crystals [36]) and $L = 4$ mm, one obtains $\tau_{dip} \approx 20$ fs. The width of the dip does not change, although the magnitude of the dip decreases, with the bandwidth of the pump.

2. Temporal overlap of photons on the BS

Photon wavepackets emitted by the QD spread out over the time interval from zero to τ (the recombination time), whereas the reference photons reflected from the mirror in the other arm are localised within a time interval determined by their coherence time $\tau_{ph} = \tau_{dip}$. As a result of the bunching, the two-photon coincidence detection rate will be modulated by a factor

$$f_{coinc} = \frac{\tau_{dip}}{\tau} \tag{4.27}$$

Given that a typical recombination time in e.g. InAs SAQDs is on the order of 1 ns, one obtains $f_{coinc} = 2 \times 10^{-5}$.

3. Emitted vs reflected photons

If C is the count-rate of correlated photon pairs produced in the PDC, then $n = Cp_{abs}p_{em}f_{coinc}$, where p_{abs} and p_{em} are the probabilities to absorb and re-emit a single photon from the optical mode coupled to the QD. The photons that are directly reflected from the surface of the sample with the probability p_{refl} will determine the background number of two-photon coincidences $N_c = Cp_{refl}$.

Putting those factors into Eq. (4.25) gives an *estimate for the visibility*:

$$\nu = \frac{p_{abs} p_{em} f_{coinc}}{2 p_{refl}}, \tag{4.28}$$

To increase the visibility, the probability of photon reflection from the sample p_{refl} should be minimised, e.g. by depositing anti-reflection (AR) coatings on the surfaces of the sample and cryostat windows. It may be reduced to $p_{refl} = 2.5 \times 10^{-4}$ with commercially available AR coatings [163]. If we substitute $\tau_{ph} = \tau_{dip} \approx 20$ fs to get $p_{abs} \approx 4 \times 10^{-11}$ and take $p_{em} = 0.08$ (Section 4.3.5), we obtain

$$\nu \approx 10^{-13}. \tag{4.29}$$

This is a painfully small number! Fortunately, there are ways to dramatically improve ν. For this purpose we will describe ways to increase p_{abs}, p_{em}, and f_{coinc} as well as increase the photon count-rate C, which will reduce the measurement time of the experiment.

4.5.3 Optimization of the excitation source

First of all, we should look into the source of excitation. The main drawbacks of the PDC photon pairs for our experiment are their ultra-short coherence time (on the order of 20 fs) and low count rate (currently not exceeding 10^5 s^{-1}). An ideal pulse duration of the excitation photons would be on the order of 50 ps, so that they are highly monochromatic to increase the QD absorption efficiency while maintaining sufficient time resolution to probe the shape of the signal on the nanosecond scale.

Filtering

The down-converted photons can be stretched in time by narrow-band interference filters, which will determine the shape and width of the correlated dip. The additional

filtering will decrease the count-rate of photon pairs by a factor of τ_f/τ_{ph}, where

$$\tau_f = \frac{2\pi}{\delta\omega_f} = \frac{\lambda^2}{c\delta\lambda_f} \tag{4.30}$$

is the coherence time of the filter. However, the effective repetition rate of photons in arm A will not be affected, since the most significant filtering occurs at the stage of photon absorption by the narrow QD resonance. On the other hand, stretching of the reference photons in arm B will improve the temporal overlap on the BS f_{coinc} and therefore the visibility (4.28).

At the moment, commercially available filters are limited in bandwidth to $\delta\lambda_f = 1$ nm [49], which for the operational wavelength $\lambda = 950$ nm gives the coherence time of $\tau_f = 3$ ps. This would improve the visibility by more than four orders of magnitude, $\nu = 2 \cdot 10^{-9}$.

Attenuated laser source

Although our research group has expertise in PDC, what guided the initial ideas, this process might not be the best way to create pairs of correlated photons for this experiment. A major improvement is to replace the PDC part of the setup with a single 50:50 BS and generate light directly by the 50-ps mode-locked laser whose output is attenuated with neutral-density filters and/or high-energy dielectric attenuators, as shown in Figure 4.12. The idea is to attenuate the generated pulses such that on average each of them contains two photons, which with the 50% probability will be split by the BS into two perfectly correlated single-photon pulses. Both PDC drawbacks are readily overcome here too, since e.g. our mode-locked Ti:Sapphire laser generates relatively long 60 ps pulses at the repetition rate of 82 MHz. Furthermore, the laser can be easily tuned in a wide wavelength range to a specific QD transition.

However, this option suffers from the fact that a laser is a Poissonian source of

light, which means that the probability of generating N photons in the pulse is

$$P(N) = \frac{N_0^N}{N!} e^{-N_0}, \tag{4.31}$$

where N_0 is the average number of photons per pulse. Attenuating the pulses such that $N_0 = 2$, we will actually obtain almost twice as many pulses containing one or three photons as with two, which will contribute to the noise background. And if we attenuate further to get $N_0 = 1$, then from Eq. (4.31) we get $P(0) = P(1) = 2P(2)$, and in addition to noise, the effective repetition rate will be reduced due to the significant number of pulses containing no photons.

Overall this technique can improve the visibility by four to five orders of magnitude, and increase the photon rate by two orders of magnitude.

Single-photon source

Another possible generator of time-correlated photon pairs recently become available [95, 120, 162, 97, 160], whereby the problem of the photon-number fluctuations is effectively removed. It is based on a *single-photon source* (SPS); an individual InAs QD is excited above the optical transition energy, and the pump power is high enough to generate one or many excitons in the QD. Single-photon emission is due to the fact that multi-excition transitions have different transition energies than the one-exciton. Thus, detecting only the recombined photons in the narrow frequency range that corresponds to the one-exciton transition gives rise to the generation of 'single photons on demand'.

If an SPS (Box 2 in Figure 4.12) is used instead of the attenuated laser source, then an emitted single photon in one half of the cases will go into arm B with the delay line, whereas the following emitted photon may go into arm A with the sample, also in one half of the cases (making the total probability of the event to be 25%).

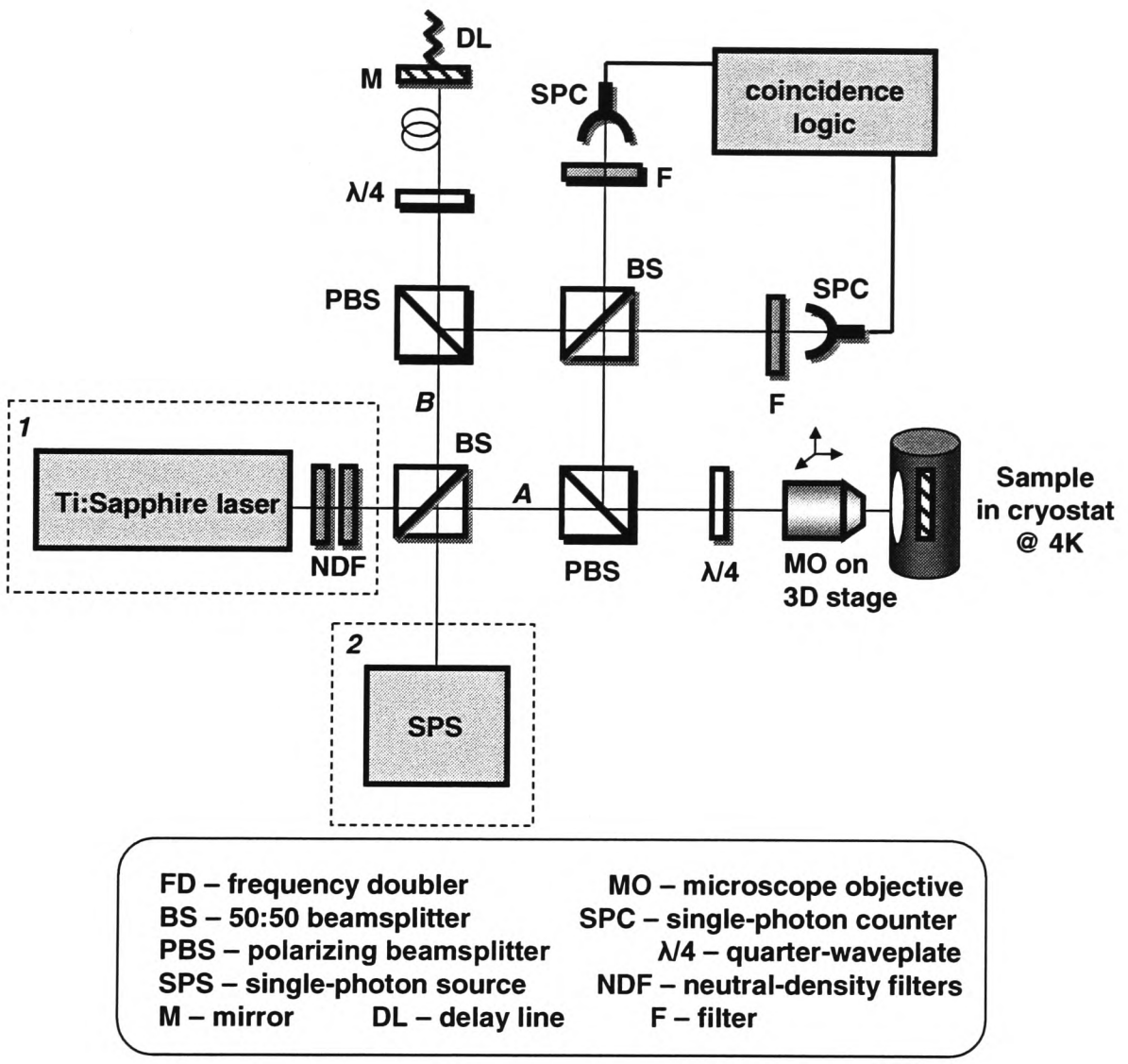


Figure 4.12: *A possible modification of the time-resolved photon-correlation experimental setup depicted in Figure 4.10. Dashed boxes 1 and 2 represent two excitation sources alternative to the PDC and further described in the text.*

The advantages of this excitation source are the following. First, an SPS is a non-classical photon emitter, which obeys the sub-Poissonian statistics; the number of two or more photons per pulse is strongly suppressed. Second, the width of the emitted single-photon wavepackets is a few hundred picoseconds and holds the promise of becoming shorter.[x] On the one hand, it would provide enough data points for tracking the decoherence phenomena on the order of nanoseconds. On the other hand, it is much longer than the PDC pulse width, thus increasing the absorption probability of the QD. Third, the generation rate of an SPS is in theory limited by the exciton recombination time divided by the Purcell factor and thus can go up to 10^9 photons/s. In fact, splitting the pump beam into parts and directing them on the QD sample with relative delays, it is possible to provide the photon generation rate higher than the repetition rate of the mode-locked pump laser. Finally, it has been shown recently by the Yamamoto group [121] that consecutive photons produced by the SPS are independent and indistinguishable.

The drawbacks include the low count rates (currently less than 10^5 photons/s due to the low collection/detection efficiency), lack of tunability in wavelength, and finally the complicated installation, since an SPS requires a separate μ-PL setup. Basically, these drawbacks originate from the fact that SPS technology is still at the stage of experimental development.

4.5.4 Improvement of the sample design

Another important way to improve the visibility is by increasing p_{abs} and p_{em}. This can be achieved by improving the coupling between the optical mode and the single QD. As discussed in Section 4.3.5, the coupling efficiency is limited by the angle of

[x]Due to the Purcell effect, which will be discussed in the next section.

the total reflection of GaAs. Placing a microlens [162] with an intermediate refractive index ($1 < n_{lens} < n_{GaAs}$) on top of the sample, it is possible to increase the opening angle of the emission cone of light. This leads to an improvement of the collection efficiency by a factor of 5 to 10.

In Section 4.3.5, the probabilities p_{abs} and p_{em} were calculated using the cross-section of focussed light passing the sample. A large improvement in the coupling efficiency can be achieved by placing the QD inside an optical cavity. Basically, the cavity allows the light to interact many times with the QD, provided the cavity can be tuned on resonance with the QD, and the pump light is resonant with the cavity. The cavity acts as a bandwidth interference filter for the pump light. As explained in Section 4.5.3, an effective pump coherence length of around 50 ps would be ideal for the proposed experiment, and this can be achieved with high-quality microcavities. Another advantage of a cavity is that the spontaneous emission rate can be changed, the so-called Purcell effect. This is a QED effect in the 'weak-coupling' regime. This means that the cavity lifetime and mode volume are such that a photon emitted by an excited QD has a small chance to be re-absorbed by the QD. Re-absorption would imply the 'strong coupling' leading to the vacuum Rabi splitting and other QED effects. To date, the 'strong-coupling' regime has not yet been achieved for a single QD but the Purcell effect has been demonstrated.

The next section gives an overview of QDs in various microcavities, and explains the Purcell effect in more detail. In Chapter 5, we will concentrate on micropillars and square-lattice photonic crystal slabs, and present our first experimental results. A brief discussion of the 'strong-coupling' regime is included in Chapter 6.

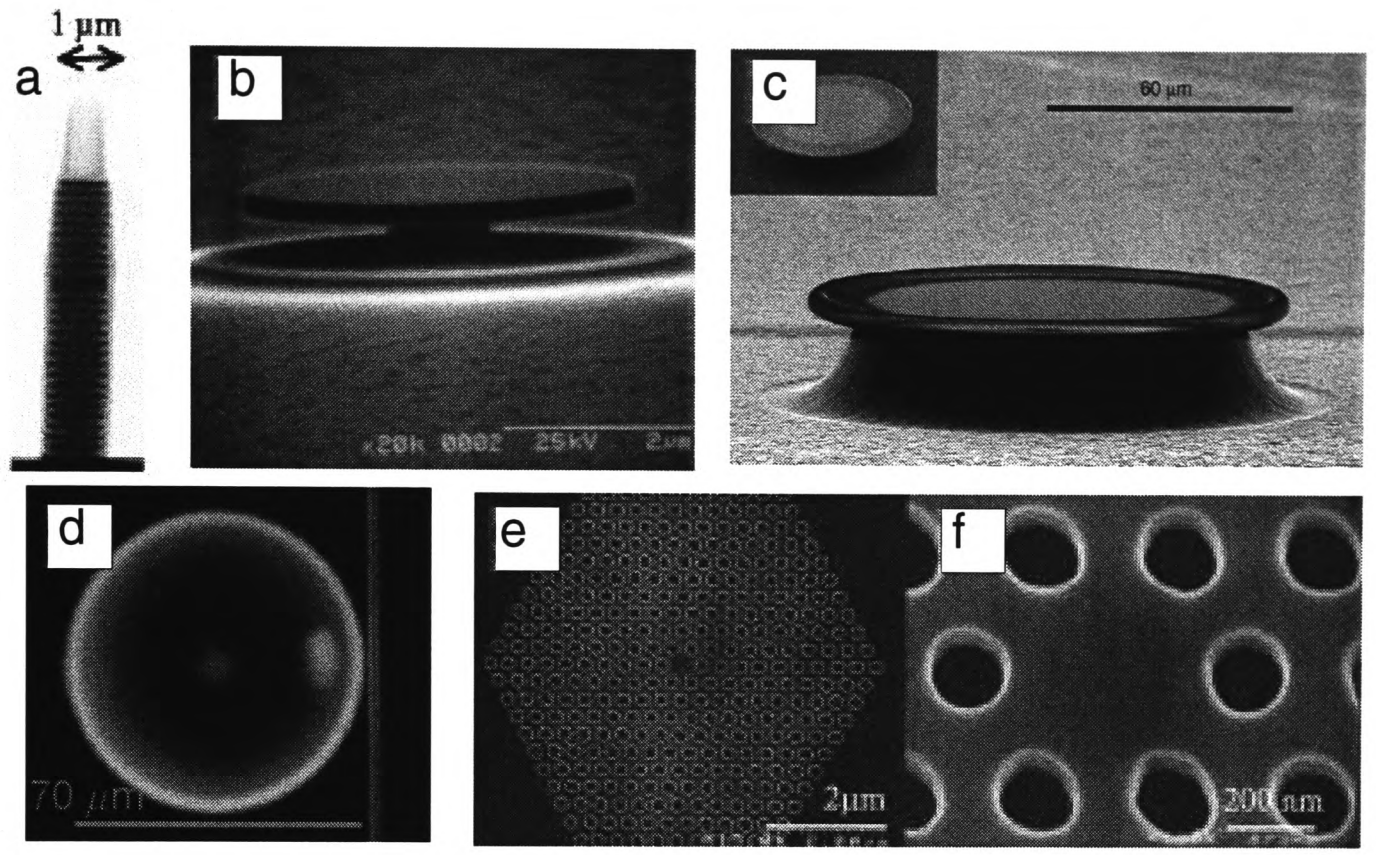


Figure 4.13: *Semiconductor microcavity zoo: SEM images of (a) GaAs/AlAs micropillar (from Ref. [97]), (b) GaAs microdisk (from Ref. [95]), (c) SiO_2 toroid, the inset shows the cavity prior to laser treatment (from Ref. [3]), (d) SiO_2 microsphere (adapted from Ref. [128]), (e) GaAs hexagonal lattice photonic-crystal slab single-defect cavity, and (f) zoom of the single-defect region in the structure shown in (e) (from Ref. [159]). Relevant sizes are given by the scale bars in the images.*

4.6 Quantum dots in semiconductor microcavities

Impressive nanofabrication research has lead to a variety of available *semiconductor microcavities*, see Figure 4.13. Operation of the shown structures is based on the same principle as that of the FPI described in Section 4.2.4, i.e. on the constructive interference of reflected light inside the cavity.

The main distinction here is the *3D confinement of light* defined by the size and structure of the microcavity, as compared to the 1D confinement of the FPI described in the plane-wave approximation. Additional confinement usually arises due to the

Cavity	Q	V_{eff}	γ_0/γ	Ref.
Micropillar	2250	5	5	[47]
	1300	1	5	[127]
Microdisk	6500	-	6	[75]
	10000	5	12	[46]
Toroid	$> 10^8$	-	-	[3]
Microsphere	$> 10^8$	-	-	[128]
Photonic crystal slab	400	0.5	-	[159]

Table 4.1: *Experimental parameters of the semiconductor microcavities studied to date: quality factor Q, effective mode volume V_{eff} in units of $(\lambda/n)^3$, and the enhancement of the QD spontaneous emission rate due to the Purcell effect described further in the text.*

waveguiding effect caused by the refractive-index difference between the microcavity material and air. As a result, another important parameter characterising a microcavity, in addition to the Q-factor, is the *effective mode volume* V_{eff}. It describes the size of the region occupied by the standing waves of confined light in a given cavity mode and is defined as

$$V_{eff} = \frac{\int \varepsilon(r)|\mathbf{E}(\mathbf{r})|^2 d\mathbf{r}}{\max[\varepsilon(\mathbf{r})|\mathbf{E}(\mathbf{r})|^2]}, \tag{4.32}$$

where $\varepsilon(\mathbf{r})$ is a position-dependent dielectric constant. Experimentally reported values of Q and V_{eff} for the microcavities in Figure 4.13 are summarized in Table 4.1.

Figure 4.13a shows a *micropillar*, which consists of the two *distributed Bragg reflectors* (DBR) with an active GaAs layer sandwiched between them. InAs SAQDs can be embedded in the active layer during the epitaxial growth. Each DBR is a stack of of epitaxially grown GaAs and AlAs pairs of layers, each of thickness $\lambda/4n_i$, where λ is the resonant-mode wavelength and n_i are the refractive indices of GaAs and AlAs, respectively. The thickness of the active layer is often equal to λ/n_{GaAs} (the 'λ-cavity') to allow for the fundamental mode.[xi] Lithography and ion etching

[xi]The minimum distance between the two DBRs is equal to λ/n_{GaAs} and not $\lambda/(2n_{GaAs})$ because

are used to pattern the cavity into a micropillar with variable diameter on the order of a few micrometers. The cavity mode spectrum consists of the longitudinal modes confined vertically by the DBRs and transversely by the pillar waveguide. Photons in the modes leak out through the DBRs with a good degree of directionality[xii], which is advantageous for their collection. In addition, there are undesired leaky modes that spread out perpendicularly to the pillar. We will come back to this type of microcavity in Section 5.3.

Microdisks studied in Refs. [75, 95] were processed by a two-step wet etching of the sample consisting of the layer of GaAs (the disk itself) grown on top of AlGaAs (the post layer). The diameter of the disk in Figure 4.13b is 500 nm and thickness 200 nm. InAs QDs were grown in the middle of the disk layer. The cavity modes here are formed by the total internal reflection of light along the circumference of the disk thus making a closed loop. They are called *whispering-gallery modes.*[xiii] While these modes are beneficial for obtaining high Q-factors (see Table 4.1) the photons in the modes leak out in the horizontal plane, which makes their collection difficult.

The silica *toroid* and *microsphere* shown in Figures 4.13b and 4.13c, respectively, are given for comparison. The recently reported toroid [3] was fabricated by photolithography, dry etching, and laser-induced selective reflow, whereas the microsphere was made by laser melting the tip of a single-mode fibre. The modes (WGM) spread out along the periphery of the disk, or along the equator of the sphere, respectively, and have the highest to date $Q \approx 10^8$–10^9. However, the mode volumes are very large and it is not yet clear how efficiently such cavities can be coupled to the QDs.

---

the vertical distribution of the field in the cavity mode has anti-nodes at the edges of the DBRs [125].

[xii] The solid angle of emission from the vertical cavity mode is on the order of 10 degrees [96].

[xiii] The name comes from the historical analogy with the acoustic modes in St. Paul's cathedral in London.

Finally, the *photonic-crystal (PC) slab cavity*, an example of which is shown in Figures 4.13e and 4.13f represents a novel type of microcavity that has a promise of combining high Q and very low V_{eff}. It is made of GaAs/AlAs, which undergoes e-beam lithography and reactive ion etching (RIE) to form an ordered lattice (triangular in this case) of holes in the material, except for a defect consisting of one or several removed holes in the center. The sample is further chemically etched to selectively remove the AlAs layer and leaving a free-standing 2D GaAs membrane. The in-plane periodic modulation of refractive index, similar to that used in the DBR, gives rise to an energy gap (*photonic bandgap*), which forbids light from propagating in 2D, whereas the vertical confinement is due to the waveguiding effect. Together, these provide a 3D confinement with $V_{eff} < (\lambda/n)^3$. The SAQD layer can be embedded in the GaAs membrane at the stage of epitaxial growth. Active experimental research into this type of cavities is going on at the moment, and we will present our results in Section 5.2.

4.6.1 Purcell effect

Back in 1946, Edward Purcell proposed that the spontaneous emission rate of a quasi-monochromatic dipole can be modified by controlling the surrounding electromagnetic fields with a cavity [112]. This idea has been successfully verified in a series of experiments on solid-state optical microcavities with individual QDs being the emitters [47, 127].

The FWHM of a cavity mode can be estimated from Eq. (4.9) for typical $Q = 2000$ and $\lambda = 950$ nm to be $\delta\lambda_c \approx 0.5$ nm, whereas the QD transitions have a linewidth of 2–5 μeV [18], equivalent to $\delta\lambda_e \approx 0.002$ nm. This leads to

$$\frac{\delta\lambda_c}{\delta\lambda_e} \gg 1,$$

which is a signature of the *weak-coupling regime*: the spontaneously emitted photons escape from the cavity well before they can be re-absorbed by the QD.

In the weak-coupling regime, the spontaneous emission rate is expressed by Fermi's golden rule [47, 127]:

$$\gamma = \frac{1}{\tau} = \frac{2\pi}{\hbar}\rho_c(\lambda)|\langle f|\mathcal{H}|i\rangle|^2, \tag{4.33}$$

i.e. it is proportional to the photon density of states in the cavity $\rho_c(\lambda)$ at the QD transition wavelength, as well as to the matrix element of the optical transition from the excited state of the emitter $|i\rangle$ to its ground state $|f\rangle$. Here, $\mathcal{H} \propto \mathbf{d} \cdot \mathbf{E}(\mathbf{r})$ is the interaction Hamiltonian between the optical dipole $\mathbf{d}$ of the emitter and the amplitude of the electromagnetic field $\mathbf{E}(\mathbf{r})$ in the cavity mode.

An optical cavity in general reduces the number of allowed modes for the spontaneous emission and thereby increases the vacuum field intensity in these modes. By modifying $\rho_c(\lambda)$, i.e. shifting the cavity modes in and out of resonance with the QD transition, the spontaneous emission can be enhanced or inhibited, according to the following equation [47, 127]

$$\eta = \frac{\gamma_0}{\gamma} = \frac{2}{3}\,\frac{3Q\lambda_c^3}{4\pi^2 n^3 V_{eff}}\,\frac{\delta\lambda_c^2}{\delta\lambda_c^2 + 4(\lambda_e - \lambda_c)^2}\,\frac{|\mathbf{E}(\mathbf{r})|^2}{|\mathbf{E}|^2_{max}} + f. \tag{4.34}$$

Here, γ_0 and γ are the emission rates of a QD with and without a cavity, and $f\gamma$ is the decay rate into the leaky modes.[xiv] The value of

$$F_p = \frac{3Q\lambda_c^3}{4\pi^2 n^3 V_{eff}} \tag{4.35}$$

is called the *Purcell factor*, which describes the enhancement of the spontaneous emission of an ideal emitter into the cavity mode. 'Ideal' here means that:

- The emission transition is resonant with the cavity mode, $\lambda_e = \lambda_c$.

[xiv] For micropillars with diameters from 20 to 2 μm, f was found to increase from 0.3 to 0.9 [127].

- The emitter is located at the anti-node of the cavity mode, where the amplitude of the electromagnetic field is the highest $\mathbf{E}(\mathbf{r}) = \mathbf{E}_{max}$.

- The optical dipole is parallel to the electromagnetic field.

For such an ideal emitter, the maximum enhancement of the emission rate into the cavity mode (and maximum reduction of the radiative lifetime) was calculated to reach $F_p = 32$ for a typical micropillar device [47].

In practice, however, the spontaneous emission ratio η is reduced. First, QD optical dipoles $\mathbf{d}$ are randomly oriented [47], which gives rise to the factor of $\frac{2}{3}$ in (4.34) as a result of the angular averaging. Second, any non-zero detuning from the resonance condition decreases the factor $\frac{\delta\lambda_c^2}{\delta\lambda_c^2+4(\lambda_e-\lambda_c)^2}$ from 1 to zero in the limit of $(\lambda_e - \lambda_c) \gg \delta\lambda_c^2$. Obviously, a displacement of the emitter from the anti-node will also reduce η by the factor of $\frac{|\mathbf{E}(\mathbf{r})|^2}{|\mathbf{E}|^2_{max}}$. Indeed, the reported values of $\eta = \gamma_0/\gamma = 5$ for micropillars [47, 127] are considerably smaller than the theoretically predicted F_p. Still, they suggest that the observed enhancement of the spontaneous mode is largely due to the Purcell effect, and not because of the emission into the leaky modes $f\gamma$.

The Purcell effect can be used to increase the photon absorption and collection efficiency for two reasons: it decreases the radiative lifetime of the QD, and increases the coupling efficiency of the QD transition to the highly directional cavity mode. As follows from Eq. (4.34), to take full advantage of the Purcell effect, it is desirable to be able to control the spatial and spectral positioning of the emitters inside the microcavity, as well as improve the key figure of merit of the microcavity, the ratio of Q/V_{eff}.

On the other hand, by tuning the cavity mode out of resonance and suppressing the coupling f to the leaky modes, it should also be possible to inhibit the radiative emission of the QD by times exceeding its natural recombination lifetime. This idea

could be further used in the realisation of the quantum memory device, which we propose in Section 6.2.

4.6.2 Improved visibility estimate

Let's estimate how much it would change the visibility of the time-resolved photon-correlation experiment if we put the QDs inside a semiconductor microcavity. First, for a QD placed in the anti-node of the cavity, the absorbtion probability will be enhanced by a factor of Q due to the constructive interference of the field amplitudes, as described in Section 4.2.4. Second, the field in the microcavity is concentrated inside a mode volume. Assuming the geometry of a symmetric λ-cavity whose fundamental mode is resonant with the QD transition, the mode volume can be rewritten as

$$V_{eff} = \frac{\lambda}{n} A_{cav},$$

where n is the refractive index of the microcavity medium and A_{cav} is the mode cross-section. The probability of a QD in the microcavity to absorb a photon is modified, accordingly, from Eq. (4.20) to

$$p_{abs}^{cav} = \frac{Q\sigma_{abs} f_{freq}^{cav}}{A_{cav}} = \frac{Q\lambda\sigma_{abs} f_{freq}}{nV_{eff}}. \tag{4.36}$$

Here, the frequency overlap

$$f_{freq}^{cav} = \frac{\tau_{ph}}{\tau_{cav}} \cdot \frac{\tau_{cav}}{\tau_0}$$

is formally left unchanged (c.f. Eq. (4.19)), since to first order the symmetric cavity acts as a narrow-band filter before the main filtering at the QD.[xv] An important change is that of the QD spontaneous emission time τ_0, which is reduced due to the Purcell effect by a factor of η from Eq. (4.34), which was found to be around 5 for

[xv] A more accurate analysis of coupling of the photons to a microcavity is given in Section 4.7.2.

micropillars (see Table 4.1). In the same way, the QD lifetime reduction will affect

$$f_{coinc}^{cav} = \frac{\tau_{ph}\eta}{\tau} = f_{freq}^{cav}. \tag{4.37}$$

Another consequence of the microcavity is that the emitted photons are coupled into the resonant cavity mode and in the case of micropillars are efficiently collected because of the high vertical directionality of the mode emission. Thus, we can take a conservative estimate of $p_{em}^{cav} = 0.4$, which is mainly limited by the leaking of the emitted photons through the bottom mirror.

Substituting the new values in Eq. (4.28), we obtain the expression for the improved visibility accounting for the cavity-induced effects:

$$\nu = \frac{1}{2}\frac{p_{em}^{cav}}{p_{refl}}\frac{\lambda}{n}\frac{Q}{V_{eff}}\sigma_{abs}\left(\frac{\tau_f\eta}{\tau}\right)^2. \tag{4.38}$$

For $Q = 1300$ and $V_{eff} = (\lambda/n)^3$ from Table 4.1, as well as for the improved photon coherence time $\tau_f = 3$ ps after the narrow-band filters (see Section 4.5.3), Eq. (4.38) gives

$$\nu = 6 \cdot 10^{-3}.$$

We have shown how technical improvements on the basic idea result in a visibility increase from $\nu = 10^{-13}$ to $\nu = 6 \cdot 10^{-3}$. We now estimate how long a measurement would take given an improved visibility.

If T is the measurement time, then the noise level is given by

$$\text{Noise} = \sqrt{N_c T}.$$

The signal accumulated per time T is given by the height of the time-correlated dip nT, and from Eq. (4.25) it follows that

$$\text{Signal} \approx 2N_c\nu T.$$

Assuming a signal-to-noise ratio ρ = Signal/Noise of at least $\rho = 3$, we obtain for the measurement time

$$T = \frac{\rho^2}{4\nu^2 C p_{refl}}. \tag{4.39}$$

Substituting $\nu = 6 \cdot 10^{-3}$ value into Eq. (4.39) and taking into account the reduced count-rate due to the filtering $\tilde{C} = C\tau_{ph}/\tau_f$, we obtain the estimate for the measurement time

$$T = 4 \cdot 10^5 \text{ s} \sim 100 \text{ hours}.$$

This relatively long measurement time poses a major challenge, especially since cryogenic equipment is notorious for vibration and long-term stability problems. The general conclusion is that it is highly desirable for this experiment to employ cavities with high ratios of Q/V_{eff}, that will give rise to the pronounced Purcell effect. Photonic crystals that provide a genuinely three-dimensional optical confinement are very promising in this respect; our study of these structures will be presented in Section 5.2.

In the meantime, we conceived a different experiment that employs the photon-interference effects to achieve a higher visibility. It is described in the next section.

4.7 Interference from two micropillars

4.7.1 Idea of the experiment

The second experimental proposal pursues the same goal as the first designed experiment, i.e. an investigation of the ultimate limit of excitonic decoherence in QDs for optical transfer of quantum information. It is based on *Michelson interferometry* to suppress scattered light at the resonant frequency of the QD transition.

Figure 4.14 shows the schematic of the experimental setup. A mode-locked laser

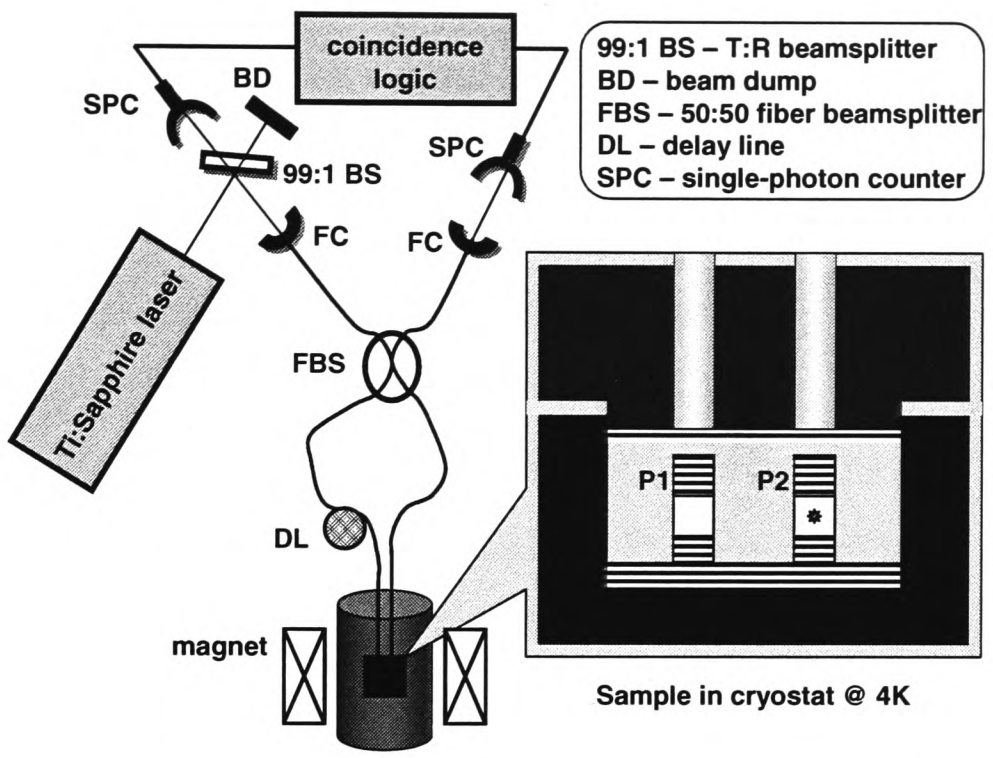


Figure 4.14: *Schematic of the interference experiment with two micropilars. The inset shows a blow-up of the sample with the fibre plug discussed in the text.*

sends a pulse of which 1% is reflected into a single-mode (SM) fibre. The pulse is then split in two equal parts by the 50:50 fibre beamsplitter (FBS) and sent on to the sample in the cryostat. The inset shows in more detail the nano-assembly of the sample, which constitutes the main part of the interferometer.

The sample is fabricated such that it contains two micropillars $P1$ and $P2$ with identical geometry and thus identical optical properties, except that only one of the micropillars has a QD whose lowest excitonic transition is on resonance with the cavity mode. The idea is to implement a classical Michelson-Morley interferometer [54] with the micropillars instead of the two end-mirrors. Tuning the relative optical path difference between the two arms with a fine-delay line (DL), one can achieve that most of the photons reflected from $P1$ and $P2$ will destructively interfere on the FBS before reaching the single-photon counters (SPC). Thus the huge background

in the number of coincidences – which was making the main trouble in the previous experiment – will be suppressed, and the tiny differential signal caused by the QD emission will come into play unobscured.

To calibrate the optical path lengths, we may first tune the excitation energy of the laser pump below the QD resonance, so that no photons will be absorbed by QDs. If the two micropillars are indeed identical to a high degree (to be estimated below), then the photons reflected from the top DBR of $P1$ will destructively interfere with their counterparts reflected from the top DBR of $P2$, those from the bottom DBR of $P1$ with the ones from the bottom DBR of $P2$, etc. The coarse pre-adjustment of the two paths can be done electronically when registering the coincidences, whereas the fine adjustment (on the order of λ) can be done with a piezo DL till all reflections are suppressed as indicated by the minimum coincidence count-rate on the two SPCs.

Now that the interferometer is adjusted, we shift the laser excitation energy back to the QD resonance and detect the signal, which is the difference between the light fields of the two cavities. Namely, it is the difference between the photons that were absorbed and re-emitted by the resonant QD in pillar $P2$, and the photons that were reflected by the bottom DBR of pillar $P1$. While the latter are defined by the excitation source and known *a priori*, the former constitute the desired response of the QD to resonant single-photon excitation, which can be deduced by analyzing the registered coincidence data.

4.7.2 Technical requirements

We now estimate whether this second experiment is feasible with the available technology. It is of course impossible to predict all potential experimental hurdles, but the most obvious ones are listed in the following, together with our proposed solutions.

Coupling photons and micropillars

To implement an efficient suppression of reflected light, the two paths of the interferometer should be as identical as possible. The main technical difficulty is that the two arms end up on the same sample, where the micropillars have diameter of a few μm and the distance between them on the order of tens to hundreds of μm. Besides, the sample should be in the cryostat operated at 4 K to avoid thermal effects.

The easiest way would be to couple light in and collect the signal back with two separate microscope objectives. Unfortunately, it is not possible to have two standard microscope objectives to be exactly the same on the microscopic scale and position them in the same way at two pillars. Both issues will give rise to uncompensated reflections.

As an alternative, two SM fibres can be drawn to the sample surface to couple light directly into the micropillars. To minimize the coupling losses, the size of the optical mode in the fibre should be the same as that in the pillar. The standard available SM fibres have a minimum core diameter of 3–4 μm, which can be taken as a guideline in the etching of the micropillar. In principle, smaller diameters should also be possible by tapering the fibres, although this may result in internal fibre losses.

To position the fibres directly on top of the pillars, it would be necessary to have two independent x-y-z high-resolution translation stages. However, these need to be operated in vacuum at low-temperatures, which is a non-trivial engineering task. A simplified fibre access is proposed, shown in the inset of Figure 4.14. It consists of a plug with holes drilled or etched for the SM fibres. The fibres are fixed in the holes and the surface of the structure is polished. The layout of the fibres in the plug is then reproduced on a mask for a pattern transfer on the sample, so that the fabricated micropillars match exactly the fibres' positions. The plug is then fixed

on the sample using additional markers. The thermal expansion/contraction can be reduced by making the plug of the same material as the sample substrate, e.g. GaAs.

To avoid spurious cavities between the surfaces of the fibres and the pillars, AR coatings should be deposited on the surfaces of the plug and sample. Moreover, the width and frequency of the photon pulses should be chosen to minimize their reflection from the micropillar. We can estimate that taking a Fabry-Perot cavity with symmetric mirrors and parameters typical for the semiconductor micropillars: $d = 280$ nm is the λ-thickness of the active layer, refractive index of GaAs at 4 K $n = 3.45$, and $Q \approx 1300$. The cavity has a resonant mode at $\lambda_0 = nd = 966$ nm and a lifetime

$$\tau_{cav} = \frac{Qnd}{c} \tag{4.40}$$

of about 4 ps. Assume that the cavity is excited with $\tau_{ph} = 60$ ps pulses (corresponding to the specification of our mode-locked laser), which have a Gaussian spectrum

$$S_{ph}(\omega) = \frac{1}{\sqrt{2\pi}\delta\omega_{ph}} \exp\left[-\frac{(\omega - \omega_0 - \Delta\omega)^2}{2(\delta\omega_{ph})^2}\right], \tag{4.41}$$

where $\omega_0 = 2\pi c/\lambda_0$ is the resonant frequency, $\delta\omega_{ph} = 2\pi/\tau_{ph}$ is the pulse width, and $\Delta\omega$ is the frequency detuning of the laser.

For such a pulse, the intensity of its reflected part is obtained from

$$I_{refl} = \int_0^\infty d\omega \big[1 - T(\omega)\big] S_{ph}(\omega), \tag{4.42}$$

where T is given by Eq. (4.6). Performing the numerical integration of (4.42) for the resonant case $\Delta\omega = 0$, we get

$$I_{refl}^{on} = 0.017,$$

whereas $I_{inc} = \int_0^\infty d\omega S_{ph}(\omega) = 1$. These numbers will be used to estimate the signal intensity.

Another issue is the coupling loss due to a possible position and/or size mismatch. While it is difficult to estimate this number without a proper modelling of the mode profile at the exit of the micropillar, we may take a factor of $p_{coupl} = 0.85$ (as a rough estimate assuming a Gaussian mode distribution), which should be squared to describe the combined in/out coupling loss.

Nanofabrication

Two questions arise immediately:

- how to have exactly one QD on resonance in one of the pillars?

- how to make two identical micropillars?

The answer to the first question is complicated by the fact that InAs SAQDs form spontaneously with the optical transition energy specified in the range of about 50 meV. The thickness of the layers for the micropillar should be chosen beforehand such that the resonant cavity mode is in the red part of the QD spectrum, in order to avoid excitation of the near-lying QDs with transition energies below the resonance.

It is possible to grow a low-density QD layer having 10^8 dots per cm^2, so that a pillar with diameter 3 μm will contain about $\sim$ 30 QDs. A low-intensity PL pre-characterisation should be done in order to find the resonance between the cavity mode and the lowest in energy optical transition of a QD. A certain degree of control of the resonance is provided by varying the temperature of the sample. It has been shown for the microdisks [75] that changing the temperature from 5 to 60 K shifts the cavity mode to the red by about 1 meV, whereas the exciton transition shifted by more than 3 meV.

Assuming that $\sim$ 30 QDs inside the pillar cover on average the whole PL range of 50 meV, the separation between individual QD peaks will be less than the temperature-induced relative shift of about 2 meV. On the other hand the QD density is low enough



Figure 4.15: *Measured and calculated energy shifts of the fundamental cavity mode vs micropillar diameter at 4K (from Ref. [127]).*

that the chance of having two QDs with overlapping PL peaks indistinguishable with the spectrometer is negligible. Hence, it should be possible to resonantly couple a micropillar with a single QD.

Since there are at least two micropillars processed in the sample, we simply increase the temperature until we reach the lowest QD resonance in the two pillars. This will make sure that only one micropillar has a single QD on resonance.

The second question is more difficult, since the high device reproducibility is a big technical challenge at the nanoscale. The electron-beam lithography with e.g. the poly-methyl methacrylate (PMMA) resist commonly used to pattern the mask for etching micropillars has a typical resolution of 20–30 nm, which is a reasonable estimate of the difference in the micropillars' diameter. From the experimental findings of the Yamamoto group in Figure 4.15, one can roughly estimate that for a pillar diameter of 3 μm, the 20-nm variation in size leads to a cavity-mode shift of $\Delta E \sim 30$ μeV. Thus, one of the two micropillars will in general be detuned from exact resonance with the excitation pulse by the amount of ΔE. Figure 4.16 shows

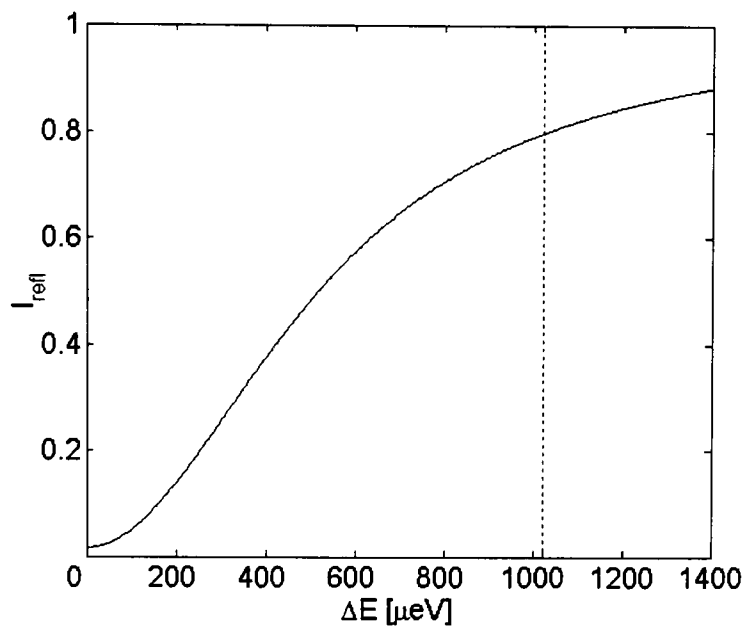


Figure 4.16: *Calculated normalised intensity of 60-ps photon pulses reflected from a micropillar ($Q = 1300$, $FWHM \sim 1\ meV$, $\tau_{cav} = 4\ ps$) as a function of the energy detuning with the cavity resonance. The dashed line shows the FWHM of the cavity mode.*

the reflected part of the incoming light intensity calculated according to Eq. (4.42) as a function of the energy detuning. In our case of 60-ps excitation pulses and realistic micropillar parameters $Q = 1300$, FWHM $= \lambda/Q = 0.73$ nm ~ 1 meV, $\tau_{cav} = 4$ ps, it gives $I_{refl}^{off} = 0.020$. As a result, the fraction of reflected light uncompensated by the destructive interference is

$$\frac{I_{refl}^{off} - I_{refl}^{on}}{I_{inc}} = \frac{0.020 - 0.017}{1} = 3 \times 10^{-3}. \tag{4.43}$$

To further minimise this number, a possible solution would be to achieve a higher resolution in making the etching mask, e.g. using an array of scanning-probe microscopes. A more conventional way is to fabricate an array of micropillars and look for a pair of the most 'identical' ones where the reflection is the least. This approach requires the ability to position the fibres freely on the sample, as well as collecting statistics on many micropillars.

Signal intensity

We can now estimate how much signal is expected to come from the QD. Let's take the experimental parameters $Q = 1300$, $V_{eff} = (\lambda/n)^3$, and $\eta = 5$ of a micropillar from Table 4.1, as well as $\tau_{ph} = 60$ ps for our excitation source and $\tau = 1$ ns as the QD recombination time without a cavity.

The normalized intensity of the signal is given by

$$\frac{I_{signal}}{I_{inc}} = p_{coupl}^2 \frac{I_{inc} - I_{refl}^{on}}{I_{inc}} p_{abs}^{cav} p_{em}^{cav}, \tag{4.44}$$

where p_{abs}^{cav} is given by Eqs. (4.36), (4.37), and $p_{em}^{cav} = 0.4$ is taken from Section 4.6. Substituting the numbers in Eq. (4.44), we obtain

$$\frac{I_{signal}}{I_{inc}} \sim 3 \times 10^{-3},$$

which is comparable with the intensity of the uncompensated reflections (4.43).

Detection

The above finding brings about the issue of detection, which should separate the signal photons from the reflected photons, which are separated by sub-nanosecond time intervals. The HOM-like interference here might not be applicable, since it is not possible to change the optical path length independently in one of the arms without lifting the destructive interference condition. Hence, schemes of ultrafast optical gating of the SPCs using time-to-amplitude cards have to be explored.

Another way to further improve the sample design is by integrating QDs into microcavities with higher ratios of Q/V_{eff}. The collaborations that we have established with the materials and engineering groups at UCSB have provided us with this opportunity. The results on the optical studies of the first devices are presented in Chapter 5.

Chapter 5

Experimental results

5.1 Building the experimental setup

To implement any of the proposed ideas, we need to address optically individual QDs in microcavities. This can be done with a *micro-photoluminescence (μ-PL) setup*, the working horse of the single-QD-spectroscopy research. This section describes our experimental setup, which we have designed from scratch in order to meet the stringent technical requirements imposed by our project. Building the high-resolution, high-efficiency μ-PL setup with good stability has been a significant part of my experimental work.

The schematic of the setup is depicted in Figure 5.1. The mode-locked Ti:Sapphire laser, pumped by the cw solid-state laser, generates multi-photon pulses, which are attenuated by 50:50 beamsplitters, neutral-density filters in the filter wheel (FW), and partially transmitting dichroic beamsplitter (DBS), and are further focussed on the sample in the liquid-helium cryostat with a microscope objective (MO) on a 3D translation stage. The signal from the sample is collected with the same MO and reflected on the way back by the DBS into the spectrometer to be detected with the liquid-nitrogen-cooled CCD camera (LN CCD) or through an optical fibre with the

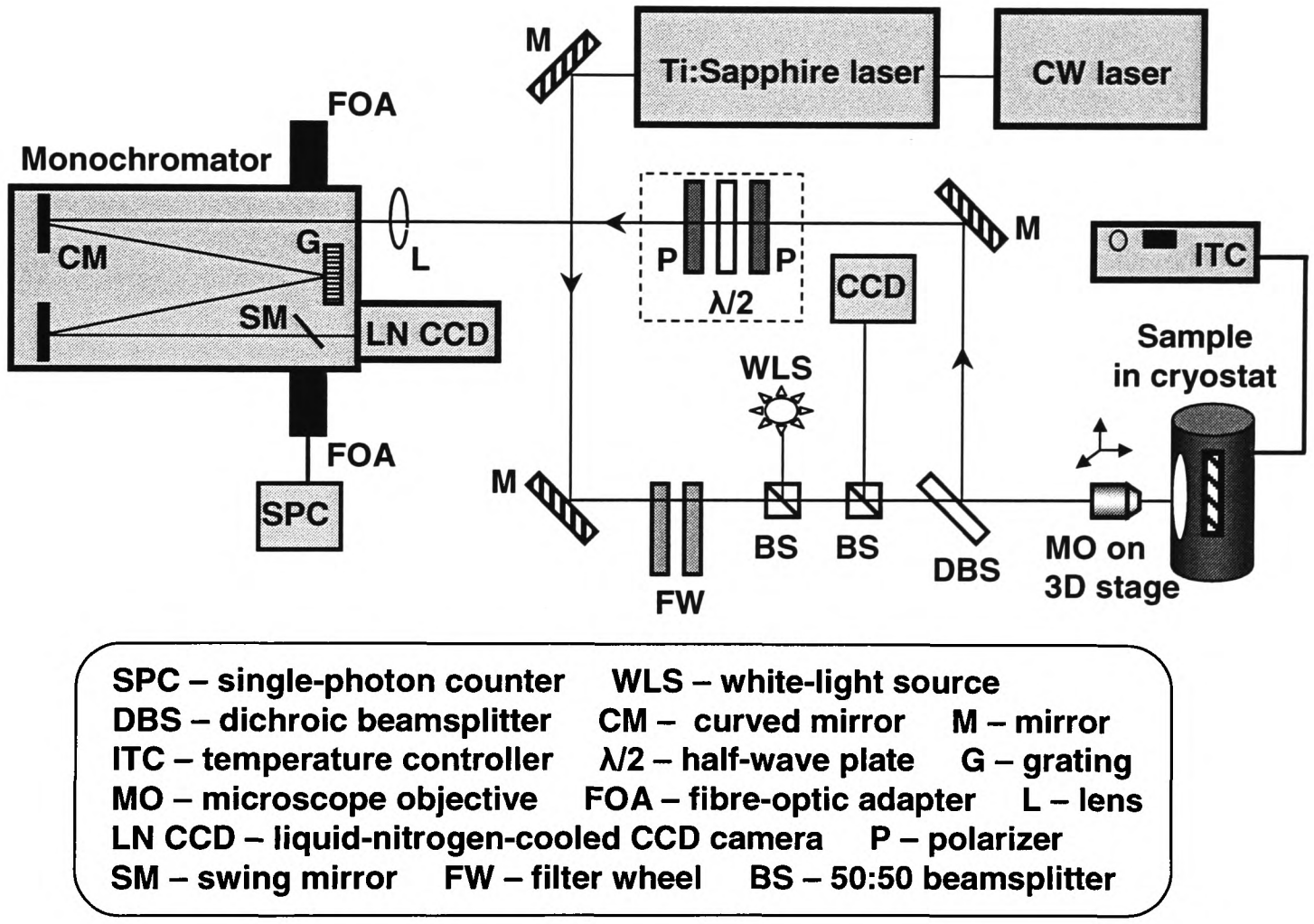


Figure 5.1: *Schematic of the micro-PL setup discussed in the text. The polarization analysis block is outlined by the dashed line.*

single-photon counter (SPC). A polarization analysis can be performed by inserting two linear polarizers with a half-wave plate (block depicted by the dashed line). To align the excitation spot, the white-light source (WLS) is used to illuminate the sample through the MO, and the reflected image is acquired by the CCD camera connected to a screen.

Resonant excitation

By slightly defocussing the MO, we can take an *ensemble-PL* spectrum of the sample, whereby the excitation spot size is much larger than the diffraction limit and a macroscopic number of QDs is excited at the same time. A typical spectrum of InAs SAQDs in the GaAs matrix is shown in Figure 5.2.

Ultimately, we need to be able to excite a QD on resonance, i.e. the laser source should operate in the region from 870 nm to 980 nm where the QD PL is observed. However, for the first optical studies of samples and for installing and testing new equipment, it is sufficient to excite the samples above the GaAs bandgap or better still, *quasi-resonantly* in the WL at 855 nm or in the p-shell to avoid generation of charged excitons due to diffusion of carriers from the GaAs matrix into the QDs [110].

Our laser system supplied by Spectra-Physics consists of a 10 W cw diode-pumped solid-state laser (Millenia), which pumps a mode-locked Ti:Sapphire laser (Tsunami), which generates 60-ps pulses (convertible to 5 ps and 100 fs) at the repetition rate of 82 MHz. The coherence time of the pulses was chosen to optimize the time-resolved photon-correlation experiment described in Section 4.5. The actual tests on the system showed the mode-locking operation in the region from 710 nm to 860 nm (which is appropriate for the wetting-layer excitation) with the output power $P_{out} \approx 2$ W. To work in the strictly resonant regime, a new set of mirrors should be installed for operating at longer wavelengths.

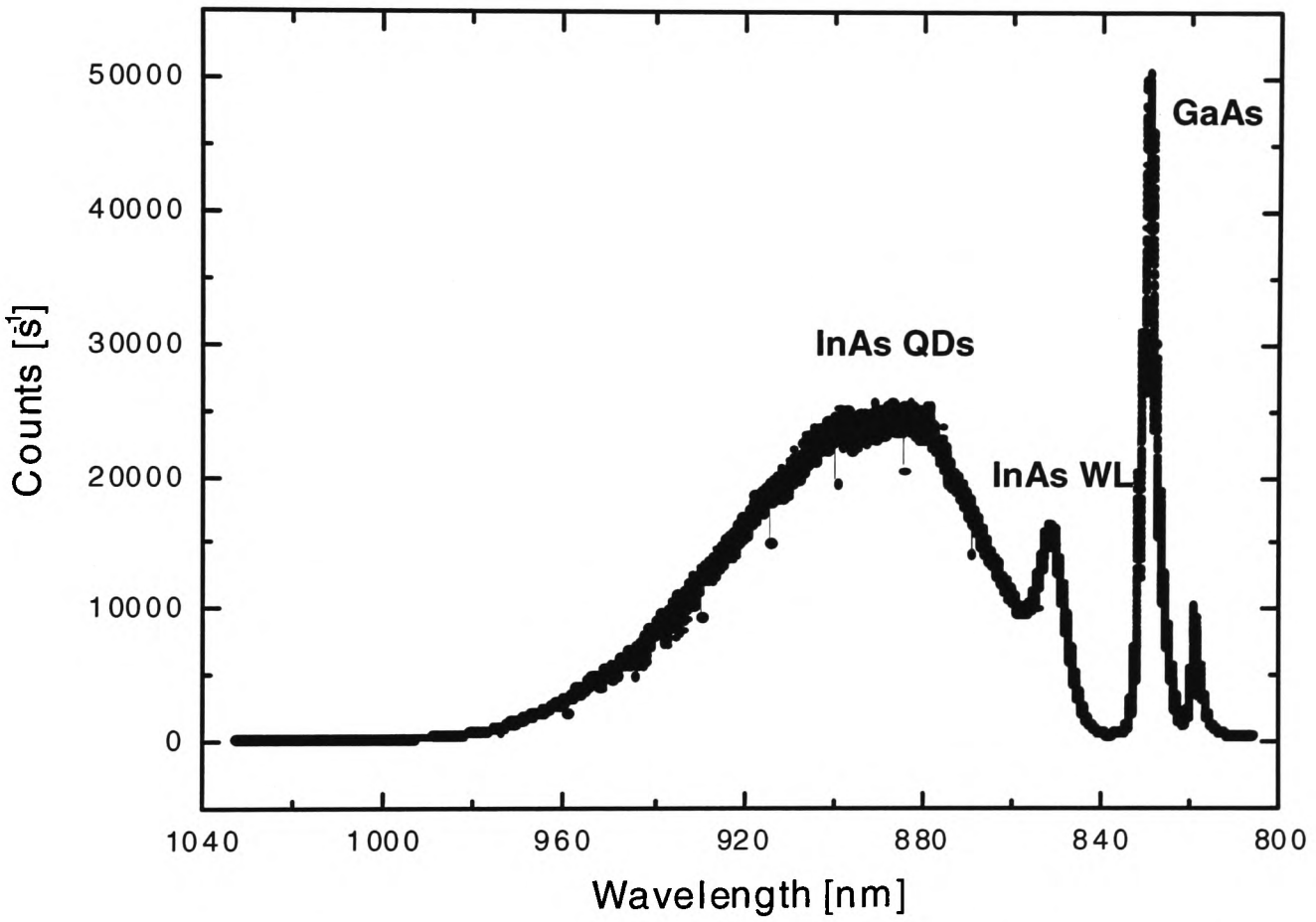


Figure 5.2: *Ensemble-PL spectrum of the typical QD sample. One can see the peaks for GaAs matrix, InAs wetting layer, and an inhomogeneously broadened distribution of InAs self-assembled QDs. Narrow vertical dips seen in the QD spectrum are an artefact of the LN CCD camera.*

Spatial resolution

To excite a single QD, the laser spot size should be on the order of the average distance between the adjacent QDs. While it imposes a condition on the maximum density of QDs, it also requires to minimize the spot size, which is limited by Eq. (4.18).

In our setup, light is focussed with a 50× microscope objective with a numerical aperture NA = 0.55 (Nikon). It has a long working distance WD = 10.1 mm, which allows for the focus to reach the sample mounted in the cryostat. For comparison, submersion-lens objectives have higher NA, which provides a better collection efficiency, but are limited to insufficiently short working distances.

To ensure accurate and repeatable positioning, our microscope objective is mounted on an x-y computer-controlled piezo-translator (Physics Instruments) with nanometer resolution, which is installed on an x-y-z manual translation stage to increase the travel range during coarse alignment.

Spectral resolution

The spectral resolution of our setup should be sufficient to detect the fine splitting of the lowest exciton transition due to the QD anisotropy, as will be mentioned in Section 6.3. To see whether the splitting is suppressed, the two levels need to overlap within the linewidth of a single peak. Thus the optimum resolution should be as high as ~ 0.002 nm at the wavelength of 950 nm.

Our monochromator (Jobin-Yvon 1250M) with a 1.25-meter focal length is a trade-off between performance and cost. It is equipped with a 1200 groove/mm grating optimized for the 500–1500 nm range providing a resolution of 0.04 nm with a LN CCD (limited by the 20 μm CCD pixel size) or 0.006 nm with an external detector

limited by the exit-slit width (≥ 3 μm). A customary fiber-optic adapter (FOA) is installed at one of the exit ports, which allows to connect a single-photon counter (SPC) via a fibre, in order to combine the highest resolution with single-photon sensitivity. In this way, the CCD camera at the axial port is used to take a wide spectrum of the sample (with a spectral window of 16 nm) and define the region of interest, whereas the SPC at the lateral port is used for high-resolution measurements. Switching between the ports is done automatically with a swing mirror (SM).

Collection and detection efficiency

The experiments proposed in Sections 4.5 and 4.7 require working at the single-photon level and acquiring very low-intensity signals. The main challenge of the experiment is the measurement time. To minimize this time, special attention has been paid to improving the collection and detection efficiency of the setup. Optimization included the following steps:

1. High-NA microscope objective.

As mentioned in Section 4.3.5, high NA is needed for collecting the emitted photons. The NA of our microscope objective is among the highest available for the given magnification and working distance.

2. Dichroic beamsplitter.

In our setup we use the same microscope objective for excitation and collection. This presents a technical difficulty, since one has to maximize collection of the 'good' signal photons while allowing sufficient pump intensity to the sample. For the non-resonant excitation, the separation of the excitation and collection paths can be achieved with a dichroic beamsplitter (DBS), see Figure 5.1. The transmissivity of the custom-coated DBS that we have ordered from CVI [163] is shown in Figure 5.3. It reflects about 99.5% of light for wavelengths between 900 nm and 990 nm, which covers most of the

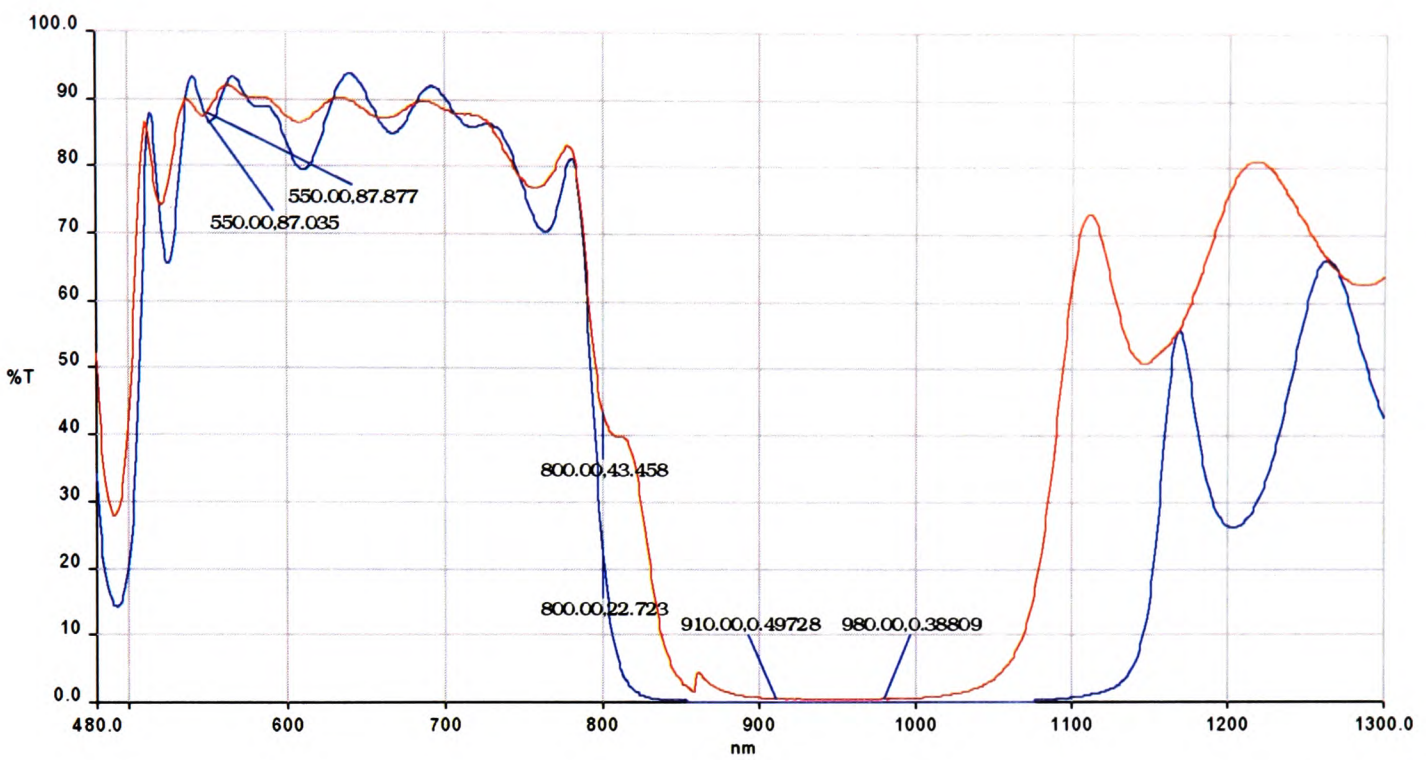


Figure 5.3: *Transmission spectrum of the custom-made CVI dichroic beamsplitter used in the μ-PL setup to separate QD signal from excitation pump. Curves for two orthogonal light polarizations are given. Pairs of numbers denote wavelengths with corresponding transmissivities.*

QD emission spectrum. At the same time, the pump light at shorter wavelengths is transmitted.

3. Aperture matching.

The light from the sample to be coupled through the entrance slit of the monochromator. To avoid underfilling or overfilling, when the light image is larger than the CM and part of it is lost to scatter inside the monochromator, or underfilling a lens with a matching NA should be used to focus the beam on the entrance slit.

Our monochromator has NA = 0.11, and a lens with a focal distance of 5 cm was placed to match for the signal beam size of about 5 mm. Alternatively the signal can be coupled in through a fibre and the FOA installed at the lateral entrance port. The aperture matching is done by means of the two lenses of the FOA.

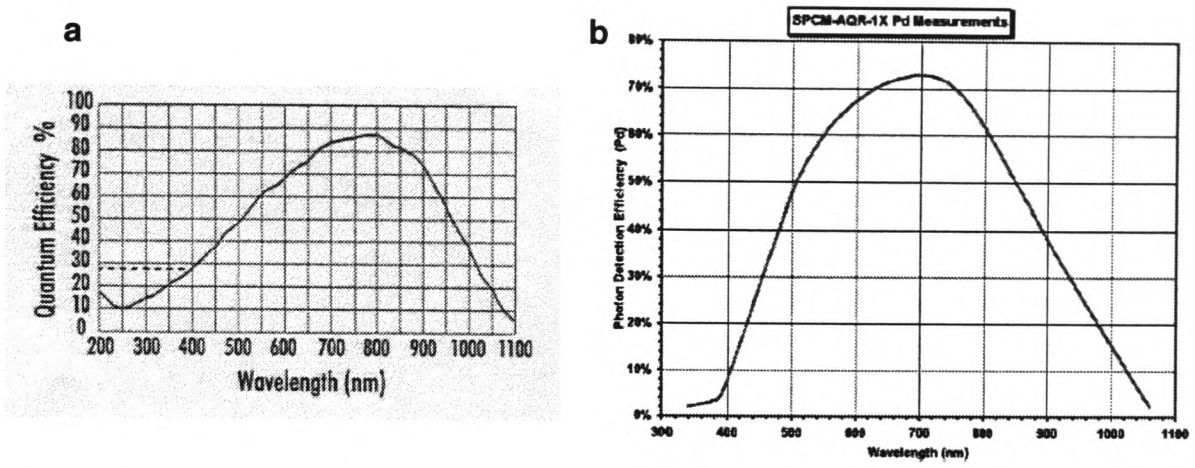


Figure 5.4: *Quantum efficiency of the (a) Princeton Instruments Spec-10:100BR LN CCD camera, and (b) Perkin-Elmer single-photon counter.*

4. Monochromator optics.

The monochromator grating (G) is blazed at 900 nm (the closest available to 950 nm) for an improved performance at that wavelength. The mirrors inside and lenses of the FOA were coated to improve transmission in the NIR.

5. Detection.

The Princeton Instruments Spec-10:100BR LN CCD camera was chosen because of its low-noise operation and high quantum efficiency (QE) in the NIR. The deep-depletion back-illuminated chip architecture provides a dark current as low as 11 electrons/pixel/hour at $-120°$C while suppressing the etaloning effect (appearance of Fabry-Perot peaks on top of the signal), which is a common problem in the NIR. The QE curve is shown in Figure 5.4a, giving as much as 55% at 950 nm. The camera also has the 1340×100 imaging array of 20×20 μm pixels, which make it suitable for spectral data acquisition.

The other type of detectors we are using is the Perkin-Elmer single-photon counter (SPC) based on the avalanche photo-diode. Its quantum efficiency (see Figure 5.4b) is not as good as for the LN CCD, QE $\sim$ 25% at 950 nm. However, its low dark

count of about 100 s^{-1} and fiber-optic access makes the SPCs very useful for our experiment.

Low-temperature operation

The experiment should be carried out at low temperatures to minimize the phonon-induced effects and thermal occupation of higher states. Since the energy separation between QD confined states is on the order of a few meV, helium temperatures ($T \sim 4$ K) are required. Our sample is placed in a continuous-flow liquid helium cryostat (Oxford Instruments MichrostatHe) that has optical access. The sample can be placed as close as 3 mm of the window, which makes it suitable for the μ-PL studies.

The QD transition and the cavity mode are tuned in and out of resonance by varying the temperature. A temperature controller is used to actively stabilize the temperature to 0.1 K.

Stability

Despite the improved collection and detection efficiency, the low signal intensity requires long-time data acquisition, and thus the stability of the experimental setup is important. Our cryostat has a sample holder drift of 1 μm per hour at 4.2 K, and vibration of 0.1 μm. The main sources of vibrations are the vacuum pump, which can be switched off, and the helium-flow pump, whose action can be replaced for a limited amount of time by creating an overpressure in the helium dewar. The hand contact with the optical table during the measurement is minimized by an automatised control of the equipment. Furthermore, the cryostat is fixed on the air-cushioned optical table, with the temperature, humidity, and air cleanliness maintained with an air-conditioning system and flow boxes.

As a result, we achieved a high-resolution, high-sensitivity setup capable of measureing the emission from a single QD (see e.g. Figure 5.16 below). Exciton transitions from individual QDs are easily observed with the LN CCD, and the count-rate of an individual transition typically reaches 2000 s^{-1} at the saturated value for high pump powers. The intensity of the signal does not change over a time of 1 hour. The achieved performance is better than what has been reported for the other setups at UCSB.

Having built the setup, we completed a major step in the development of our project, which enabled us to start experiments on the samples provided by our collaborators at UCSB. The results of these experiments are presented in the following sections.

5.2 QDs in square-lattice single-defect photonic crystal slab

Our two proposals benefit enormously if individual QDs can be coupled to high-Q, low-V_{eff} microcavities. Photonic crystals, developed to control the spontaneous emission of light [155] are very promising both in terms of efficient light confinement and ultra-small mode volumes.

By definition, a *photonic crystal* (PC) is a low-loss medium with a periodic modulation of the dielectric constant. The propagation of electromagnetic waves in PCs turns out to have properties similar to the propagation of electron waves in a periodic crystal, namely, there exist gaps of forbidden energies leading to a band structure. This analogy arises from the fact that both the Maxwell equations (photons) and the Schrödinger equation (electrons) are wave equations, as outlined in the next section.

5.2.1 Maxwell *vs* Schrödinger

The Maxwell equations for a linear isotropic medium without free charges or currents are given by

$$\begin{aligned} \nabla \cdot \mathbf{H}(\mathbf{r},t) = 0 \qquad & \nabla \times \mathbf{E}(\mathbf{r},t) + \frac{1}{c}\frac{\partial \mathbf{H}(\mathbf{r},t)}{\partial t} = 0 \\ \nabla \cdot \varepsilon(\mathbf{r})\mathbf{E}(\mathbf{r},t) = 0 \qquad & \nabla \times \mathbf{H}(\mathbf{r},t) - \frac{\varepsilon(\mathbf{r})}{c}\frac{\partial \mathbf{E}(\mathbf{r},t)}{\partial t} = 0, \end{aligned} \tag{5.1}$$

where $\mathbf{E}$ and $\mathbf{H}$ are the macroscopic electric and magnetic fields, and $\mathbf{D} = \varepsilon(\mathbf{r})\mathbf{E}$, $\mathbf{B} = \mathbf{H}$ the related displacement and magnetic induction fields [67]. The position-dependent dielectric constant $\varepsilon(\mathbf{r})$ can be treated as purely real in a low-loss medium.

Expanding the fields in a set of harmonic modes $\mathbf{H}(\mathbf{r},t) = \mathbf{H}(\mathbf{r})e^{i\omega t}$, $\mathbf{E}(\mathbf{r},t) = \mathbf{E}(\mathbf{r})e^{i\omega t}$, substituting them in the two curl equations in (5.1), and eliminating $\mathbf{E}(\mathbf{r})$, we obtain the *master equation*

$$\nabla \times \left[\frac{1}{\varepsilon(\mathbf{r})}\nabla \times \mathbf{H}(\mathbf{r})\right] = \left(\frac{\omega}{c}\right)^2 \mathbf{H}(\mathbf{r}). \tag{5.2}$$

The master equation is similar in form to the stationary Schrödinger equation

$$\left[-\frac{\hbar^2}{2m^*}\nabla^2 + V(\mathbf{r})\right]\psi(\mathbf{r}) = E\psi(\mathbf{r}).$$

Indeed, both equations are eigenvalue problems of the second-derivative operators, the Hamiltonian and the Maxwellian, acting on the electron wavefunction $\psi(\mathbf{r})$ and magnetic field $\mathbf{H}(\mathbf{r})$, respectively. Periodicity is inserted in the Schrödinger equation through the potential of the crystal $V(\mathbf{r}) = V(\mathbf{r}+\mathbf{R})$ and in the master equation by the dielectric constant $\varepsilon(\mathbf{r}) = \varepsilon(\mathbf{r}+\mathbf{R})$ of the PC.

Despite the similarity, there are two important distinctions between the two equations. First, the Schrödinger equation includes interactions between electrons occupying different eigenstates, which were the main subject of Chapter 2. On the

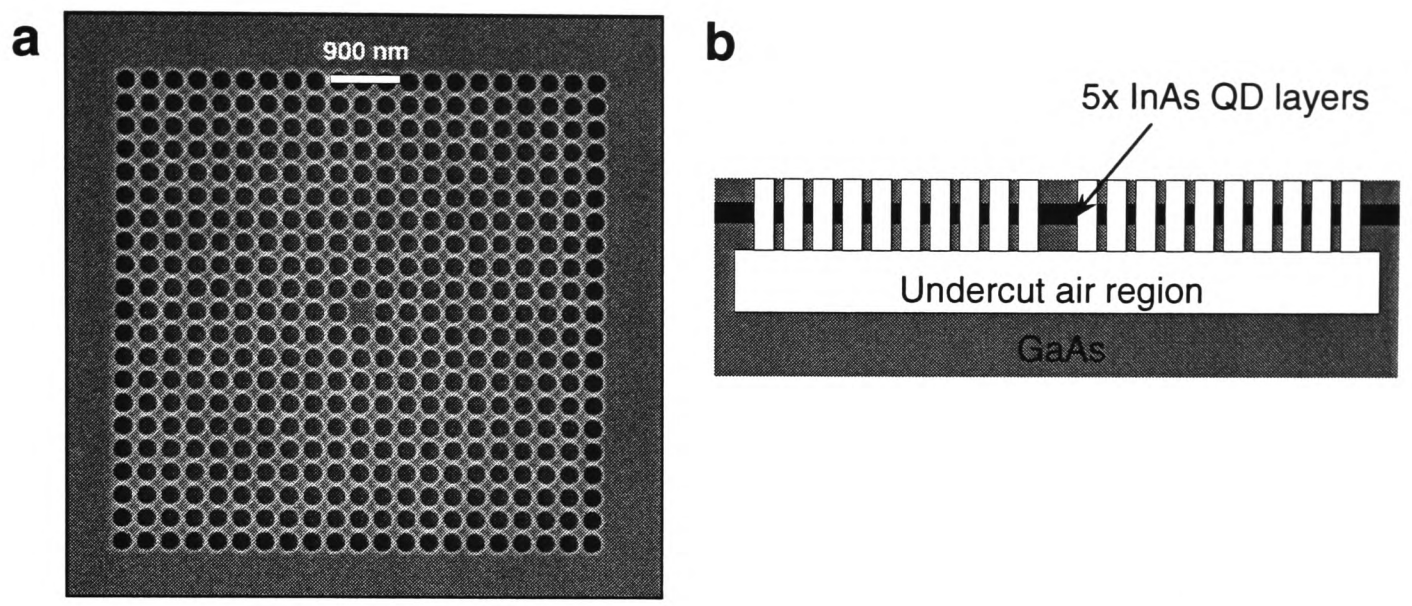


Figure 5.5: *(a) SEM image of a GaAs free-standing square-lattice single-defect PC slab (top view). (b) Schematic of the device in the vertical cross-section showing the embedded layers of InAs self-assembled QDs.*

other hand, electromagnetic modes of the master equation do not interact in the linear regime and hence can be solved for independently, which greatly facilitates the computational schemes. Second, the Schrödinger equation has a fundamental length scale, which is determined by the Bohr radius of the electron. On the contrary, the Maxwell equations are scalable, which is very useful, as it allows to test PC structures on model systems of suitable size, as well as to tune their properties as needed.

5.2.2 Sample

A typical PC that we have studied is shown in Figure 5.5. The sample was grown by Antonio Badolato (group of Prof. Pierre Petroff) and processed by Kevin Hennessy (group of Prof. Evelyn Hu). A 500 nm sacrificial layer of $Al_{0.7}Ga_{0.3}As$, is grown on the (100) GaAs substrate by molecular-beam epitaxy. It is followed by a layer of GaAs which contains five layers of InAs SAQDs, spaced by 20 nm, with an average area density of 2×10^{10} cm^{-2}.

A periodic lattice of air-holes is patterned into the wafer by the electron-beam lithography using a ZEP-520A resist, followed by reactive ion etching (RIE). The square-lattice pattern contains a single-hole defect in the center (so called *S1*) surrounded by 10 rows of holes on each of the four sides. At the final processing step, the sample is selectively etched in HF to remove the sacrificial layer underneath and form a free-standing GaAs slab of thickness $d = 180$ nm.

The sample contains several hundred devices separated by 50 μm with a varied lattice constant $a = 270$ to 360 nm, air-hole ratio $r/a = 0.36$ to 0.42, and four different e-beam doses (resist exposures). To reduce the effect of fabrication faults, there are 5 copies of each device with the same lithographic parameters.

Each device is a PC, which efficiently confines light in the x-y plane due to the modulation of refractive index, and vertically due to the waveguiding effect (since $\varepsilon_{GaAs}/\varepsilon_{air} \approx 12$). In our case, the light to be confined is the PL emission of the SAQDs embedded in the middle of the slab around the defect.

5.2.3 Electromagnetic modes

Generally, the solutions of the master equation (5.2) represent the electromagnetic modes that exist in the PC. However, many mode properties can be predicted without solving the master equation, by looking at the structural symmetries of the system only. This analysis greatly reduces the computational overhead of the band structure calculations by limiting the number of points in the **k**-space. To make use of it for our sample, we first consider a 2D square lattice of holes (periodic in the x-y plane and uniform along z), then introduce the finite thickness d of the slab, and then discuss the significance of the single-hole defect in the middle.

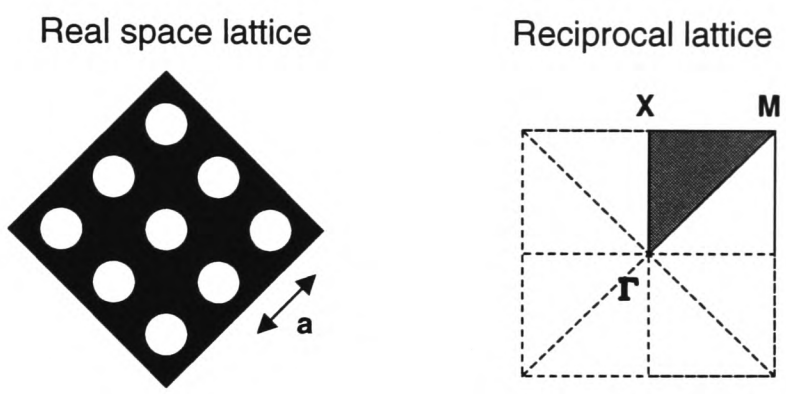


Figure 5.6: *(a) Square lattice of air holes in a high-refractive-index material (GaAs) forms a 2D photonic crystal in real space. Lattice constant a is shown. (b) Brillouin zone in the reciprocal space showing the symmetry points* Γ, X, *and* M. *The irreducible Brillouin zone is the shaded triangle. The figures are rotated 45 degrees relative to each other in order to match the coordinate axes.*

Figure 5.6a shows a 2D square lattice of air holes in GaAs. Here we will summarize without proof (which can be found in Ref. [67] or derived from the analogy with solid-state) the symmetries of the square lattice and their effects on the band structure.

1. *Discrete translational symmetry.*

The in-plane periodicity of the dielectric constant $\varepsilon(\mathbf{r}) = \varepsilon(\mathbf{r}+\mathbf{R})$, where $\mathbf{R} = \sum_{i=x,y} c_i \mathbf{a_i}$ is a lattice vector expanded in the primitive basis $\{\mathbf{a_x}, \mathbf{a_y}\}$, leads to the *Bloch form* of the modes $\mathbf{H_k}(\mathbf{r}) = e^{i\mathbf{kr}} u_\mathbf{k}(\mathbf{r})$ where $u_\mathbf{k}(\mathbf{r}) = u_\mathbf{k}(\mathbf{r}+\mathbf{R})$.

In addition, the frequency eigenvalues $\omega_n(\mathbf{k})$ of the master equation (5.2), which form the *band structure* of the PC, are periodic in the reciprocal space $\omega_n(\mathbf{k}) = \omega_n(\mathbf{k}+\mathbf{G})$. Thus, the allowable values for the in-plane wavevector $\mathbf{k}$ lie in the *Brillouin zone* $-\frac{\pi}{a_i} < k_i \leq \frac{\pi}{a_i}$, as shown in Figure 5.6b.

2. *Symmetry under rotation and inversion.*

If the PC is invariant under specific rotations and inversions, so are the solutions of the master equation. The square-lattice structure is invariant under $\pi/2$ rotations, as well as under inversions about the x, y, and diagonal axes. As a result, the Brillouin zone shrinks to its significant part called the *irreducible Brillouin zone*, shown in Figure 5.6b. Furthermore, the maxima and minima of the band structure mostly occur at the boundaries of the irreducible Brillouin zone [19]. Practically, it means that it is sufficient to consider only the path $\Gamma \rightarrow \mathrm{X} \rightarrow \mathrm{M} \rightarrow \Gamma$ in the band structure calculations.

3. *Mirror symmetry.*

The 2D square lattice uniform along z is also invariant under mirror reflections around the x-y plane. It can be shown that in this case the master equation separates into two independent equations for two different classes of polarization modes. In *transverse-electric* (TE) modes, the magnetic field is oriented perpendicular to the mirror plane and the electric field is confined to the plane, or (E_x, E_y, H_z). In *transverse-magnetic* (TM) modes, or (H_x, H_y, E_z), the situation is the opposite.

3. *Effect of slab thickness.*

Introducing the slab of finite thickness d reduces the symmetry in the vertical direction, and the modes are not purely TE or TM polarized. Instead, there is residual mirror symmetry about the x-y plane bisecting the slab, and the modes can now be classified as *TE-like (even)* or *TM-like (odd)* [69]. These even and odd states have strong similarities with TE and TM states, respectively, and in the following we will maintain referring to the modes as TE and TM.

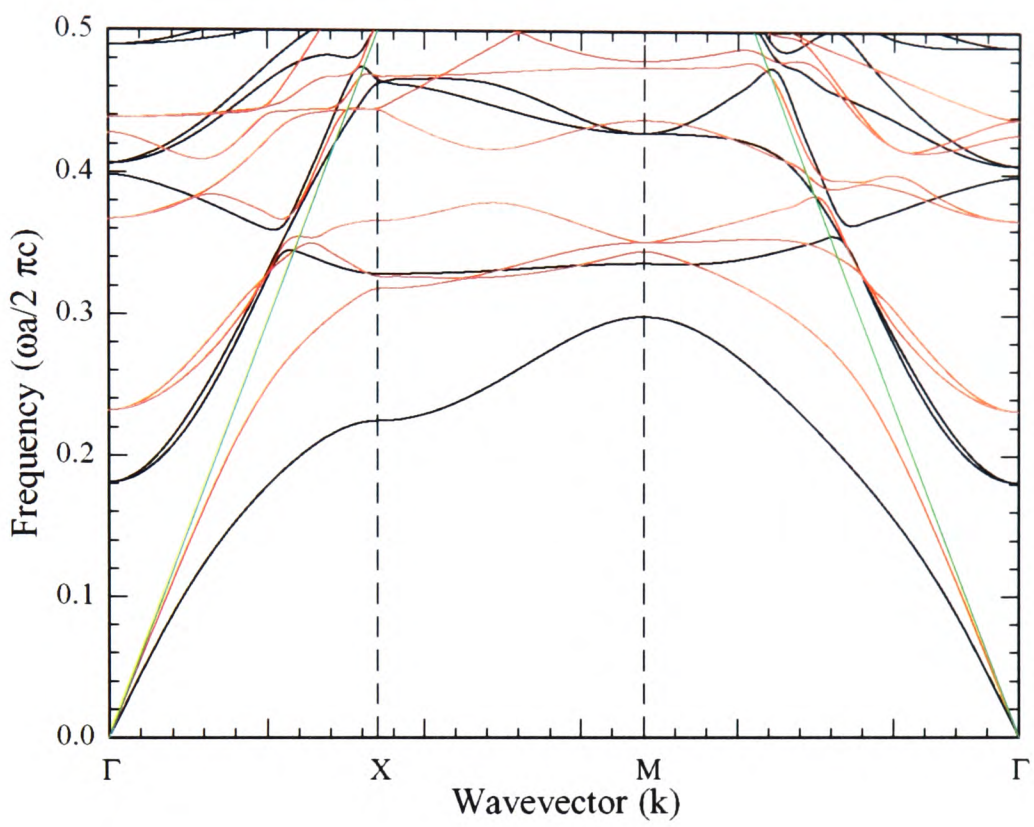


Figure 5.7: *Band structure of a square-lattice slab with no defect, calculated for the irreducible Brillouin zone of the 2D square lattice. The slab parameters are:* $d = 180$ *nm,* $a = 300$ *nm,* $r/a = 0.38$, $\varepsilon = 12$. *Black and red curves correspond to the TE and TM bands, respectively. Light lines (shown in green) separate the guided modes localised in the PC plane from the radiation modes extending outside the slab, as discussed in the text.*

5.2.4 Band structure calculations

Figure 5.7 shows the band diagram calculated for a square-lattice slab without a defect. Calculations were done in a plane-wave basis using a freely available MIT photonic-bands software package [68]. The slab parameters were taken to correspond to our typical fabricated device: lattice constant $a = 300$ nm, air-hole ratio $r/a = 0.38$, and the dielectric constant of GaAs $\varepsilon = 12$.

The lowest-energy TE (black curves) and TM (red curves) bands in the figure are calculated for the 2D irreducible Brillouin zone shown in Figure 5.6b. The band

diagram shows a photonic bandgap formed for the guided TE modes around the normalised frequency of $0.3\omega a/2\pi c$. The *light cone* is depicted by the two green lines. The bands below the light cone correspond to the *guided modes*, i.e. the states that propagate within the PC slab but decay exponentially outside of it. The bands above the light cone correspond to the *radiation modes* that are infinitely extended outside the slab region [68].

5.2.5 Photonic bandgap

The *photonic bandgap* (PBG) is defined as the range of frequencies for which light cannot propagate through the PC as a result of the coherent scattering between different dielectric regions. If light is prohibited from propagation for any $\mathbf{k}$ (i.e. in any direction) and any polarization, then the PC has a *complete* PBG. In the case of our PC-slab, the bandgap is two-dimensional, since there is no periodicity in refractive index along z.

The formation of the PBG can be understood by looking at the distribution of the electromagnetic field in the two lowest bands, the *dielectric band* below the bandgap, and the *air band* above the bandgap [67].

The $\mathbf{D}$-field of the dielectric TE band tends to occupy the regions of high ε, in order to minimize the physical energy of the system

$$E = \frac{1}{8\pi}\int d\mathbf{r}\left(\frac{1}{\varepsilon}|\mathbf{D}|^2 + |\mathbf{H}|^2\right). \tag{5.3}$$

Being polarized in the x-y plane, the $\mathbf{D}$-field has to be continuous, which is facilitated by the fact that our PC structure is *connected*, i.e. the high-ε regions form a continuous path.

As to the $\mathbf{D}$-field of the air band, it is distributed in the mode orthogonal to that of the dielectric band. Together with the continuity condition, this forces the

D-field of the air band to occupy the high-ε regions of the PC. Hence, its energy (5.3) increases, which is the origin of the bandgap. For the TM modes, the **D**-fields are polarized along z, which relaxes the continuity condition and closes the bandgap.

5.2.6 Defect modes

Introducing a defect into the PC structure breaks the translational symmetry of the dielectric constant. As a result, it may create an allowed state in the PBG, which is localised around the defect, in a similar way as impurity defects form localised states in the semiconductor bandgap.

E.g. if a defect is formed in the square-lattice slab by making the radius of one of its holes smaller, then it is more favourable for a state to be localised in the defect, since it will be localised in a region with a higher content of the high-refractive-index material. Thus the defect mode pulls out a state from the air band, as its energy is lower than the air band (c.f. acceptor states in a semiconductor). The opposite is true, if the radius of the hole is increased: the defect state goes from the dielectric band into the photonic bandgap (c.f. donor states).

Thus, by changing the size of the defect it is possible to tune the defect modes across the bandgap. On the other hand, the defect should not be smaller than the minimum cavity size of $\left(\frac{\lambda}{2n}\right)^3$, in order to be able to confine light.

The defect in our S1 PC-slab is made by removing one air-hole in the centre of the square lattice. 3D finite-difference time-domain calculations of the structures of this type including the defect show the existence of two types of defect-cavity modes in the TE bandgap [118].

One is a non-degenerate quadrupole mode, also called the *whispering-gallery mode* (WGM). It has frequency near the middle of the bandgap where the light confinement

is the strongest. As a result, it has an ultra-small calculated mode volume of $\sim 0.5(\lambda/n)^3$ and a high theoretical Q-factor ~ 18000 [119].

The second type is a doubly degenerate dipole mode, which is leaky, i.e. it partially extends into the dielectric band for wavevector directions around the M-point, leading to a low Q/V_{eff} ratio. For that reason, the dipole modes are not of interest for efficient light coupling to QDs. Note that both types of modes are described by a $\pi/2$ rotational symmetry imposed by the PC structure.

5.2.7 Observed mode properties

Our sample is a first-generation S1 PC, which has been made for testing its mode properties. For that reason, five layers of high-density QD layers were embedded to provide a broad-band light source (see Figure 5.2) whose emission decorates the cavity mode. A high-resolution PL spectrum of the observed S1 PC cavity mode is shown in Figure 5.8. The mode at $\lambda = 926.5$ nm is fully decorated by the high-intensity QD emission and has a FWHM of 0.4 nm, which corresponds to a

$$Q = \frac{\lambda}{\text{FWHM}} \approx 2400.$$

Together with the small mode volume $V_{eff} \sim 0.5(\lambda/n)^3$ this provides a much higher Q/V_{eff} ratio than that reported for a hexagonal single-defect PC (H1) in Ref. [159] (see Table 4.1). Resonant modes with Q as high as 4000 have been observed experimentally in the H2 PC slabs [114], but their Q/V_{eff} ratio is compromised by the big mode volume $V_{eff} > 2(\lambda/n)^3$ to be almost as low as the H1 value. In this respect, the S1 cavity is an obvious improvement.

Furthermore, the value of $Q = 2400$ that we have obtained is definitely not the limit for the S1 structures. The Q values as high as 4000 have been observed using a cw excitation source at 780 nm [57], and an improvement of the fabrication procedure

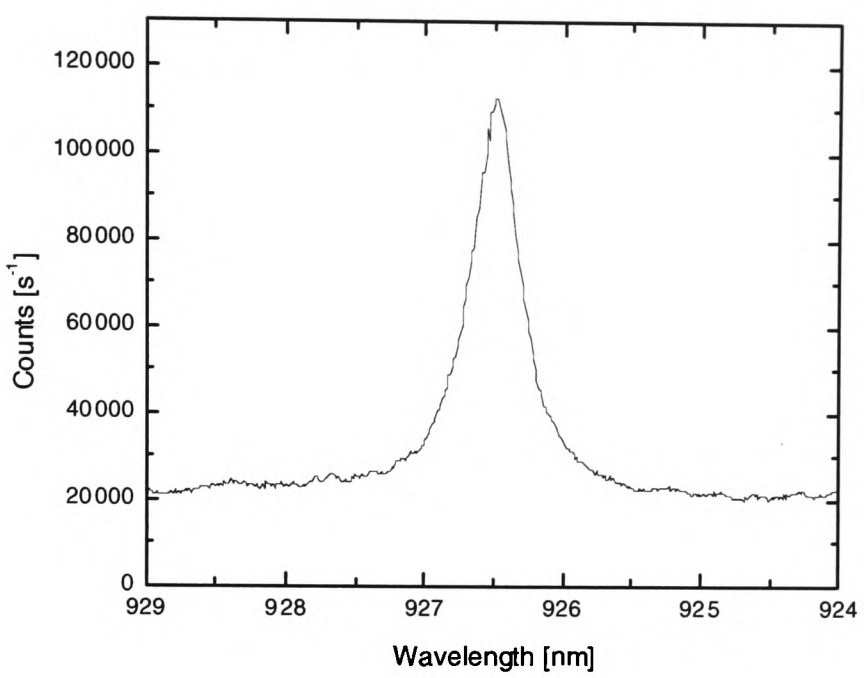


Figure 5.8: *Photoluminescence spectrum of the cavity mode of the S1 PC device with parameters* $a = 300$ *nm,* $r/a = 0.35$. *The PL was excited with a 60-ps Ti:sapphire laser @ 793 nm, pump power 252* μW, *at* $T = 4.2$ *K.*

to achieve straight and smooth sidewalls of the air-holes in order to minimize the undesired light scattering is currently underway. In addition, the S1 cavity mode, unlike the hexagonal cavities, has the maximum electric field in the semiconductor region [57] providing good spatial overlap with the QD emitters. All of the above suggests that S1 PC microcavities containing SAQDs are well on the way towards achieving the strong-coupling regime, outlined in Section 6.4.

We have also performed a polarization study of the cavity mode, shown in Figure 5.9. One can see that the same mode as in Figure 5.8 shows a pronounced linear polarization, which agrees with the experimental findings of Ref. [118] for a dipole mode. On the other hand, the resonant wavelength at 926.5 nm and high Q suggest that this is a WGM mode. A possible explanation may be that at the $r/a = 0.35$, the WGM mode starts coupling to the radiation modes outside the PC bandgap, which have a preferential linear polarization. Further study is needed to verify this idea.

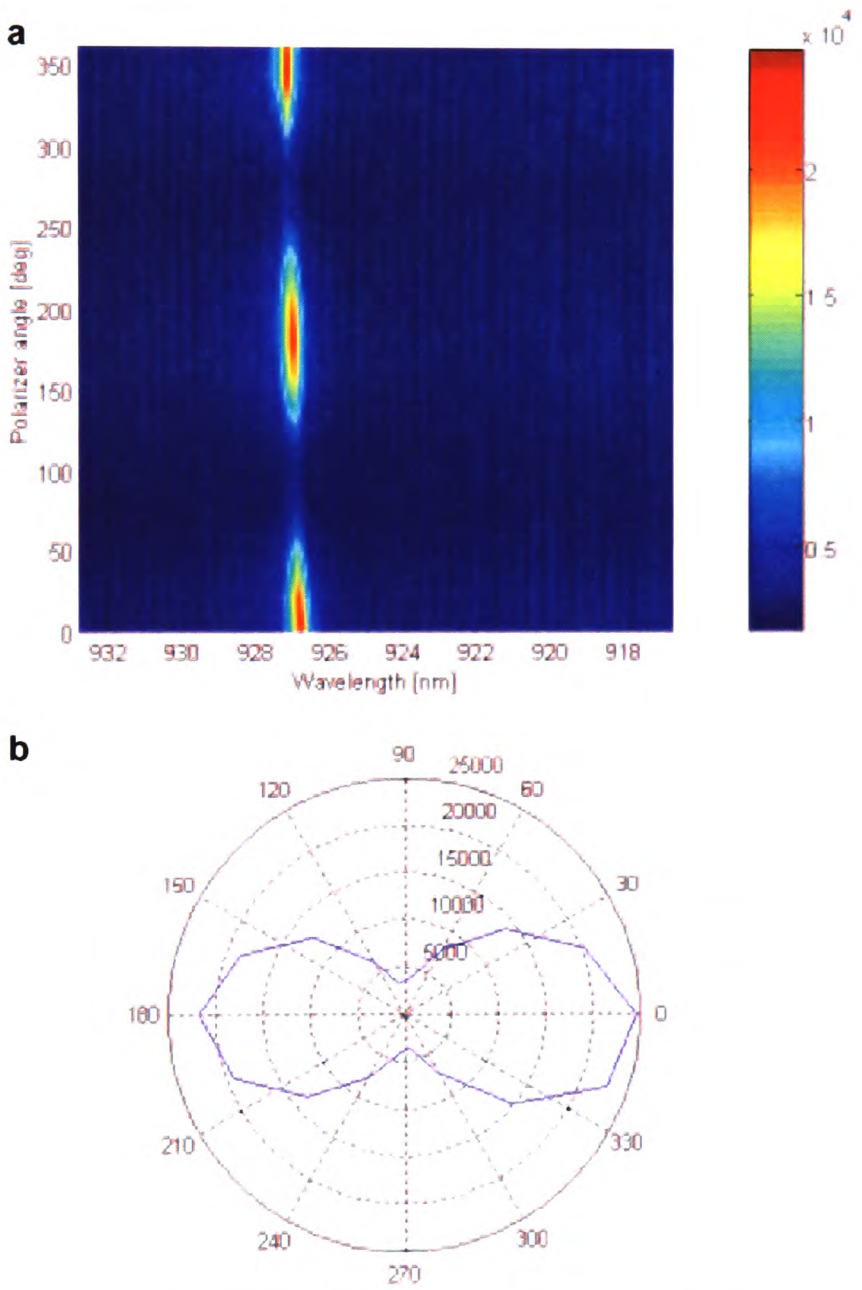


Figure 5.9: *(a) PL intensity of the S1 PC cavity mode as a function of the polarizer angle and wavelength. Vertical fringes in the background are an artefact of the polarizer. (b) Polarization diagram of the mode peak.*



Figure 5.10: *Resonant-mode map of the S1 PC microcavity showing the wavelength of the cavity mode as a function of the device lattice constant a and air-hole ratio r/a. Shaded area corresponds to the high-Q mode region. Solid lines are linear fits to the data. Figure from Ref. [57].*

5.2.8 Mode tuning

To confine the photons emitted by QDs, the resonant mode of the PC-microcavity should overlap with the QD PL spectrum. It is important to have control over the mode tuning. Fortunately, the scalability of the Maxwell's equations allows one to do that in a predictable way by changing the lattice parameters of the PC. The frequency on the vertical axis in Figure 5.7 is normalized by the lattice constant a. Therefore it should change linearly with a to provide the same band structure, if the slab thickness d is scaled accordingly. Although a and r/a can be changed by making different devices on the same substrate, the slab thickness d is fixed.

An extensive optical study of different devices in the same sample, performed by our collaborators [57], is summarized in the resonant-mode map of the S1 cavity in



Figure 5.11: *Courtesy of Kevin Hennessy, group of Prof. E. Hu, UCSB. Temperature dependance of the resonant mode of the S1 PC microcavity*

Figure 5.10. Here, the experimental WGM mode wavelength shows a linear dependance on the r/a at a fixed value of the lattice constant. Devices in the region of r/a from 0.37 to 0.39 have the highest Q observed. Varying the radius r of the holes at a fixed a leads to a change in the size of the defect, which drags the defect cavity mode across the bandgap [67], that exists for r/a ratios between 0.37 and 0.39 only.

The optical study [57] has shown that the WGMs can be tuned in three ways: large shifts of 25–40 nm are achieved by changing the lattice constant by ± 10 nm, moderate shifts of about 10 nm by changing the r/a, and the small shifts of 1–2 nm can be obtained by varying the e-beam dose, which induces tiny changes in the r/a due to under- or overexposure. However, it is important to be able to tune the cavity modes e.g. in and out of resonance with a QD transition in a reversible way, which is not possible with a fixed lithographical setting.

This degree of flexibility is provided by the fine-tuning of the mode with temperature, as shown in Figure 5.11. The WGM mode can be red-shifted by $\Delta\lambda \approx 3$ nm

as the temperature increases from 4 to 100 K due to the change in the refractive index (as a consequence of the thermal renormalization of the bandgap). On the other hand, the InAs SAQD exciton transition is expected to vary to a greater extent with temperature because the bandgap renormalization affects directly the transition wavelength [144], which will provide a net relative change between the cavity and QD peaks. This effect was used to tune InAs QDs into resonance with the WGM modes of GaAs microdisks [75].

5.2.9 Outlook

In the given sample, we estimate to have a few hundred QDs around the defect. The cavity mode shown in Figure 5.8 is decorated by the QD emission at high pump power. Even at strongly reduced excitation power, there are still to many QD transitions coupled to the cavity mode, which make a single QD peak indistinguishable from the others.

Obviously, the next step is to couple a cavity mode to a single QD emitter. To achieve this, a single low-density layer of QDs should be embedded in the structure. A sample with a gradient density is currently being fabricated, which contains on average from 1 to 100 QDs per 1 μm^2 in its low- and high-density parts, respectively. Patterning a PC microcavity around such a sparse array of QDs will raise issues such as achieving a spatial and spectral overlap between the cavity mode and the emitter. While at the beginning we are going to get around this problem by collecting enough statistics on many devices, obviously a better approach is needed. For future experiments, we are developing methods in collaboration with the groups of Professors Pierre Petroff and Evelyn Hu to spatially align a microcavity around an individual SAQD of known resonant wavelength.

In terms of measurements, the next step is to perform a photon-correlated study using a Hanbury-Brown and Twiss (HBT) setup [122], aiming to observe the Purcell effect and photon anti-bunching from a single QD. The HBT setup is currently being built in the lab.

5.3 QDs in micropillars

In parallel to the project on QDs in a PC, we have studied new ways of fabricating semiconductor micropillars, which should be suitable for the interference experiment proposed in Section 4.7.

5.3.1 Planar cavity

Our initial sample[i] is a planar cavity made of two distributed Bragg reflectors (DBR) epitaxially grown on a GaAs substrate, and an active region of GaAs in between. The top and bottom DBRs consist of 11 and 25 pairs of GaAs and AlAs layers with a thickness equal to $\lambda_0/4n_i$, where $\lambda_0 = 966$ nm is the designed resonant wavelength and n_i is the refractive index of GaAs and AlAs, respectively. The active region has a thickness of λ_0/n_{GaAs} (forming a λ-cavity) and contains a layer of InAs SAQDs in the middle. The QDs are MBE grown *in situ* with a gradient area density varying from 10^8 to 5×10^9 cm^{-2}.

An ensemble PL spectrum from the cavity obtained by removing the microscope objective (MO) is plotted in Figure 5.12a. The resonant cavity mode decorated by the QD emission occurs at $\lambda = 968$ nm, which is in good agreement with the designed value. The observed FWHM = 1.2 nm of the cavity mode is larger than the the calculated value of 0.6 nm, see Figure 5.12b, and gives $Q \approx 800$. The inconsistency

[i]The sample was designed and grown by Brian Gerardot and Dan Lofgren, UCSB.

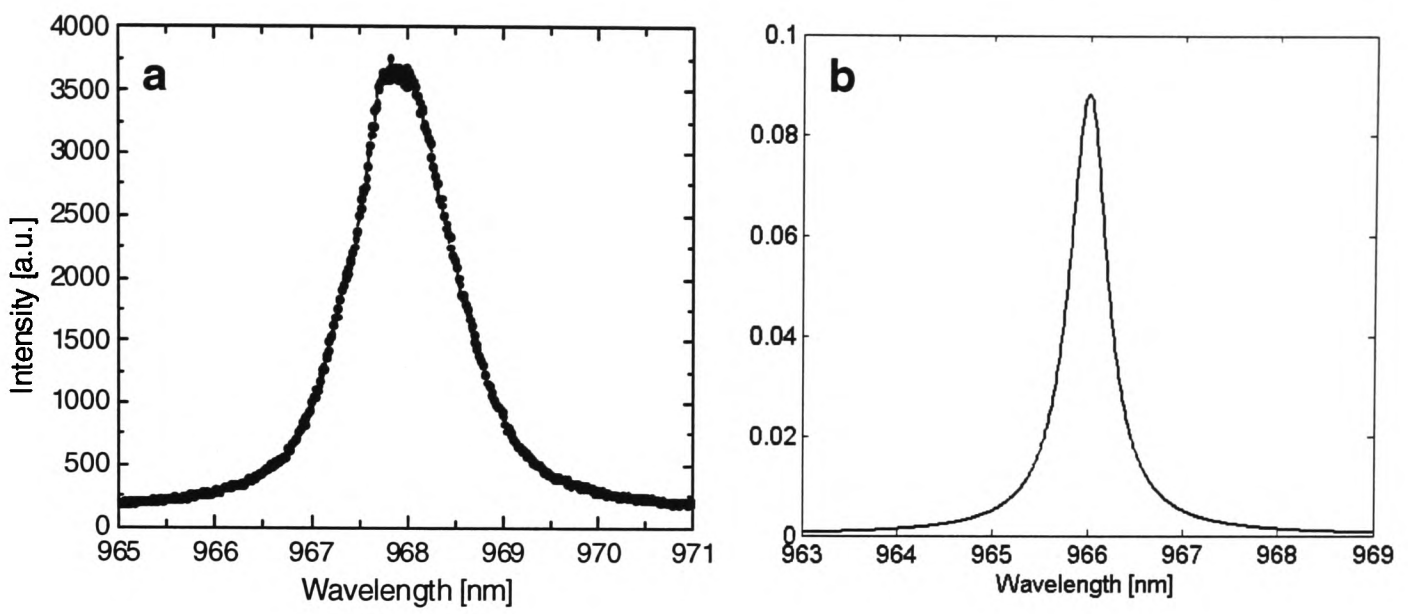


Figure 5.12: *(a) Ensemble-PL spectrum of the InAs QDs in a planar GaAs/AlAs cavity. The sample is pumped by a 30 mW diode laser at 780 nm. (b) Transmissivity of the designed structure, calculated using a MATLAB code provided by Dan Lofgren, group of Larry Coldren, UCSB.*

between the calculated and observed Q may be due to a slight variation of the layer thicknesses in the DBR mirrors, or surface roughness.

When the MO is put back in place and focussed on the sample, the PL signal from the cavity mode spreads out in spectrum to FWHM $\approx$ 11 nm. This is a result of the angular distribution of the emitted light collected by the MO. In the same way as in Figure 4.9, the maximum angle at which light can be collected by the MO is given by $\varphi_0 = \arcsin(\mathrm{NA}/n_{GaAs})$. However, at any angle other than normal, the cavity has a different effective thickness of the layers that transmit a different wavelength. This will give rise to the spectral broadening of collected light:

$$\Delta\lambda = \lambda_0(1 - \frac{1}{\cos\varphi_0}) \approx \frac{\lambda_0}{2}\Big(\frac{\mathrm{NA}}{n_{GaAs}}\Big)^2, \tag{5.4}$$

which for the observed resonant wavelength $\lambda = 968$ nm corresponds to $\Delta\lambda \approx 12$ nm, in good agreement with the observed FWHM.

5.3.2 Micropillars fabricated with FIB

A planar cavity by itself is not suitable for performing single-QD spectroscopy, since a high-NA objective needed for the spatial selection collects a large angular distribution of emitted light. The solution is to introduce the directionality of emission from the sample itself! Experimentally, it has been done by etching the planar cavity into small pillars, which act as micro-waveguides to provide a lateral confinement of light and direct it into the vertical mode.

We have explored a new way of producing micropillars with the *focussed ion-beam* (FIB) technique. This technique employs a focussed beam of 30 keV Ga^+ ions that locally sputters away the material at which it is aimed. Compared with commonly used reactive ion etching (RIE) techniques, the FIB is much simpler, since it does not require a mask and pattern transfer stage. In addition, the spatial resolution of the FIB is mainly determined by the diameter of the beam and can be typically on the order of 5 nm, whereas the resolution of the e-beam mask writing is usually limited by the molecular size of the resist, which is limited to e.g. 20–30 nm in the case of the PMMA resist.

Since we need two very similar micropillars for the second proposed experiment, we decided to invest time in producing and characterising micropillars produced by the FIB technique. We made two series of micropillars, two examples of which are shown in Figure 5.13. Pillars with diameters from 0.5 to 20 μm were cut through either the top DBR or the whole structure using different FIB currents. A lower current gives rise to the cleaner surfaces (a major source of optical losses in the micropillars) but also to a longer fabrication time.

Although the FIB technique produced clean and reproducible pillars, unfortunately, the optical study showed no PL signal from the QDs even for the largest

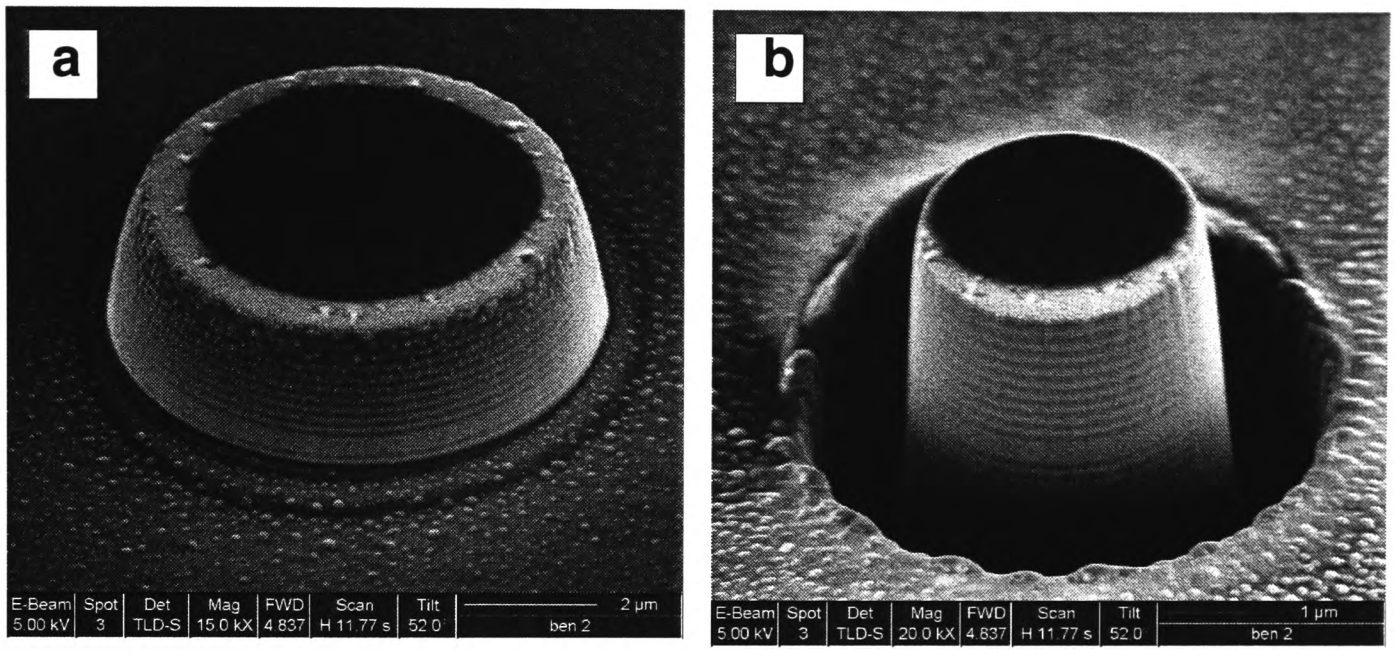


Figure 5.13: *SEM images of the micropillars etched in a planar cavity with a FIB: (a) 4-µm pillar etched through the top DBR with the 20 nA current, the active region is seen at the bottom; (b) 2-µm pillar etched through both DBRs with the 20 nA current and further patterned with the 3 nA current.*

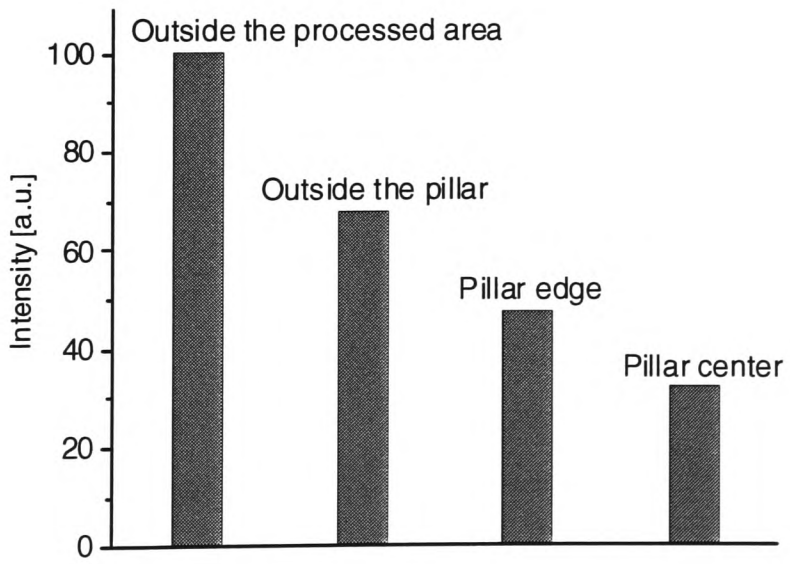


Figure 5.14: *Suppression of the photoluminescence from bulk GaAs at* $\lambda = 815$ *nm in the micropillars, suggesting the radiation damage caused by the FIB.*

20-μm micropillar. This cannot be explained only by the formation of the depletion layer or non-radiative carrier recombination on the surface. A more likely reason is radiation damage of the sample caused by the ion beam [110]. The distribution of the implanted Ga^+ ions has a long-depth tail due to the ion channelling into the crystal lattice of GaAs causing non-radiative recombination of excitons on the introduced defects. This is supported by the suppression of the bulk GaAs PL in the micropillar region, see Figure 5.14.

The PL signal could not be recovered by a rapid thermal annealing (RTA) of the sample for 2 min at 400°C. RTA temperatures higher than 650°C are not desired as they will lead to the redistribution of the material in the QDs with the corresponding shift of the PL signal [154, 8], which may drive it out of resonance with the cavity mode. The conclusion is that, unfortunately, the FIB patterning of micropillars turns out to be detrimental for the PL of SAQDs. We decided to switch to another novel technique for producing QDs embedded in micropillars, as will be discussed in the next section.

5.3.3 Micropillars with tapered oxide apertures

In collaboration with the group of Professor Larry Coldren at UCSB, we are working to improve the fabrication procedure for high-quality micropillars. The Q/V_{eff} ratio of the existing micropillars made by etching is limited by the optical losses due to the diffraction in the bottom DBR and scattering by the roughness of the sidewalls [127, 47]. Because of these two factors, the diameter of the micropillar, and hence its cavity mode volume V_{eff} cannot be decreased below a few μm without compromising its Q.

A way round this problem has become possible mainly through the fifteen-year research by the group of L.C. on vertical-cavity surface-emitting lasers (VCSELs)



Figure 5.15: *(a) Active region of the proposed micropillar with a tapered oxide aperture containing InAs SAQDs. The dashed line shows the distribution of the field intensity in the cavity mode. (b) SEM image of a laterally oxidized tapered aperture (black region). Figure from Ref. [56].*

employing the micropillar architecture. The basic idea is to reduce the cavity mode volume by 'focussing' the optical field inside the etched pillar with an internal lensing element.

Figure 5.15 illustrates this idea in more detail. Here, the optical microlens is implemented by placing a *tapered oxide aperture* near the node of the optical field distribution (standing wave) of the cavity. To make the aperture, a thin layer of AlAs surrounded by a thicker layer of AlGaAs are grown in the GaAs active region at the position of the field node. During the following thermal oxidation, the AlAs layer oxidizes laterally quicker than the AlGaAs and causes the latter to oxidize vertically. Thus, the AlGaAs oxide is linearly tapered in thickness from the tip of the AlAs oxide.

Although simple abrupt oxide apertures have been used in VCSELs for lateral optical confinement, it is the tapered form of the aperture that focuses, rather than scatters, the optical field. As a result, the cavity mode is confined within the pillar far away from its sidewalls vastly reducing the scattering and diffraction losses. Quality

factors as high as $Q \approx 40000$ have been estimated indirectly from the laser efficiency of these devices [29].

The group of L.C. have been primarily using InGaAs quantum wells as an active medium for the population inversion in these VCSELs. For our project, we are now designing a sample that would integrate the InAs SAQD emitters into a tapered-oxide-aperture micropillar with a resonant cavity mode. This is the most promising route for realising the two experiments proposed in this thesis. Moreover, this project has generated a five-year research grant.

5.4 Artificial molecules

The recent interaction with other groups at UCSB has triggered several related research directions, for which our experimental setup has been and is being used. One project of particular interest has started very recently in collaboration with the group of Prof. Pierre Petroff, who has put a considerable effort into fabricating the samples. The experiment is currently at the stage of on-going measurements on our μ-PL setup.

The project focuses on the implementation of the simplest *artificial molecule*, i.e. a system of two coupled QDs, which is the first step towards scalability of the artificial atoms. If the quantum-mechanical coupling between the constituent dots can be achieved and controlled, such an artificial molecule will be a very suitable system to study the conditional dynamics of the optically generated excitons. More precisely, creating two excitons in the electronic states of two QDs that allow quantum tunnelling between the dots will be very promising for an implementation of the two-qubit optical gate, which will open a way towards the realisation of a fully fledged solid-state quantum computer [87, 35]. Furthermore, quantum-mechanical

coupling between the QDs can give rise to quantum correlations between the optical recombination paths of the two excitons, which can be employed as a source of polarization-entangled photons.

Previous experiments on coupled QDs were mainly done in the 2DEG-based systems [43, 16] and cleaved-edge overgrowth QDs [124], whose energy splitting of the molecular states did not exceed ~ 1 meV, partly because of the relatively weak confinement, resulting in a large sensitivity to thermal perturbations. Our samples, on the contrary, make use of the self-assembled QDs with strong confinement and a precise control over the inter-dot distance.

The samples made by Brian Gerardot (P.P. group) consist of two vertically separated layers of InAs SAQDs grown by MBE in GaAs (see inset of Figure 5.16). In the Stranski-Krastanow epitaxial growth, the positions of the SAQDs are random. However, the strain field of a dot in the first layer facilitates the growth of another dot in the second layer just above it. Thus, pairs of vertically correlated double-dots are formed in the two layers with a probability close to unity [49]. We have two series of samples with a vertical separation of $d = 45$ Å and 120 Å between the layers, which is expected to correspond to the coupled and uncoupled double-dots, respectively. The average distance between the adjacent pairs of QDs in the low-density part is ~ 10 μm, which allows to isolate a single double-dot molecule for a μ-PL study.

A similar system of vertically aligned pairs of SAQD has been recently studied in experiments by Bayer *et al.* [11, 105] whereby they reported to have observed the quantum-mechanical coupling and entanglement between the molecular states of the double-dot. However, their data show very complicated behaviour and are far from being conclusive.

Figure 5.16 shows our first experimental spectrum of an individual artificial double-dot molecule. Here, the μ-PL spectrum is taken by exciting the sample above the



Figure 5.16: *Courtesy of Brian Gerardot and Stefan Strauf, group of Prof. Pierre Petroff, UCSB. μ-PL spectrum of an InAs strain-assisted self-assembled double-dot molecule with the 4.5-nm inter-dot distance. The observed peaks are identified to correspond to the one-exciton transitions X_1 and X_2 of the two QDs, and the bi-exciton transition (XX) of one of the QDs. The X^- peak around 924 nm is possibly due to a trion transition, while the broad signal around 922 nm is assigned to multi-exciton transitions. The spectrum is taken at 4 K, excited by a 60-ps Ti:sapphire laser @ 793 nm, pump power 1.8 μW, monochromator slit width 60 μm. Inset: schematic of the double-dot system.*

GaAs bandgap. Two peaks around 919 nm and 920 nm appear at the lowest excitation powers of 0.18 nm and exhibit a linear increase as a function of the pump power. This allows us to attribute the peaks to the two lowest exciton transitions X_1 and X_2 of the two QDs. The observed splitting between the two states is $\Delta\lambda \approx 0.9$ nm, or $\Delta E \approx 13$ meV, which is larger than 1 meV reported for the other QD systems. The peak at 921.5 nm appears at higher excitation intensities than the X_1 and X_2, and shows a super-linear dependance on the pump power. We thus attribute it to a bi-exciton transition, although the power dependance is not quadratic as it is supposed to be in this case. The origin of the peak around 924 nm is unknown. Since it appears at the same pump powers as the X_1 and X_2, we tentatively ascribe it to a trion transition formed because of the Coulomb interaction of excitons with electrons optically generated, e.g., in the GaAs matrix. Our on-going studies should clarify this issue.

More power and temperature dependent data are currently being taken and compared for $d = 45$ Å and 120 Å. The next step is to study the quantum statistics of the emission peaks X_1 and X_2 with the Hanbury-Brown and Twiss setup that is currently under construction.

Chapter 6

Future experiments

6.1 Bell-inequality test

As an ultimate proof of the coherent quantum information transfer between photons and excitons, it would be interesting to know whether excitons in QDs can store entanglement. Imagine that a pair of photons is created by the PDC in the singlet state $|\Psi^-\rangle = \frac{1}{\sqrt{2}}\big(|H\rangle|V\rangle - |V\rangle|H\rangle\big)$. One of the photons is then sent to a delay line, while the other is absorbed by a QD. The question is: will the two photons be still entangled after the absorption and re-emission of one of them by the QD? To find that out, one can perform a standard Bell-inequality test [20], which is essentially measuring the photon coincidences in two different polarization bases and comparing them with the classical case. The violation of the Bell inequality will be a clear sign of entanglement and thus its successful transfer from photons to excitons and back to photons.

A related experiment has recently been carried out with surface acoustic plasmons (SAP) [2]. In the experiment of Ref. [2], one of the entangled photons was sent through a sub-wavelength aperture in a thin silver screen, creating SAP, and then recollected on the other side of the screen for the Bell analysis, which showed that entanglement

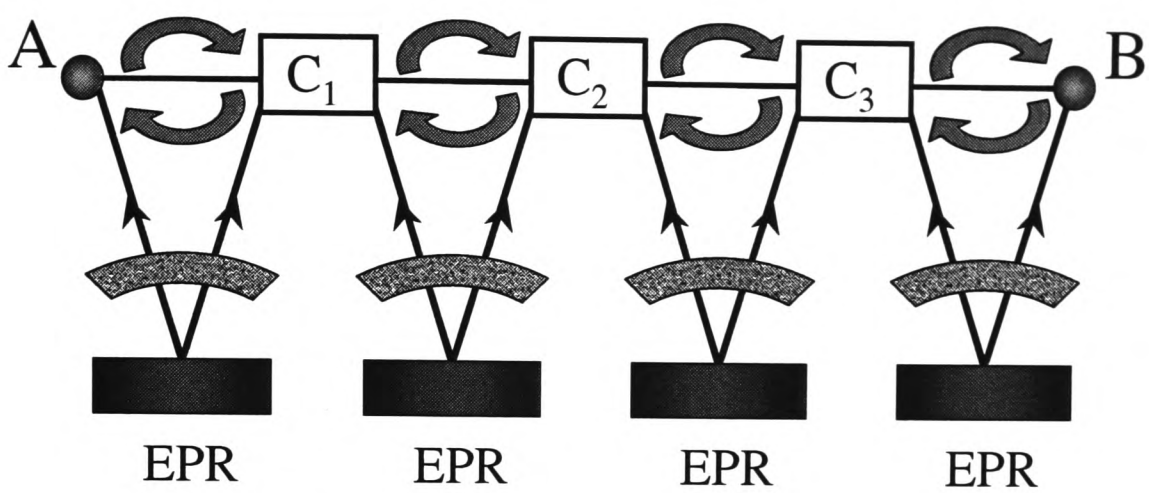


Figure 6.1: *A schematic of the quantum communication protocol between Alice (A) and Bob (B) using quantum repeaters (C_1, C_2, C_3) and sources of entangled photons (EPR), for a channel decomposed into $N = 4$ segments.*

had been preserved during the transfer between photons and SAP.

6.2 Quantum repeaters

The concept of quantum repeaters has been proposed[i] as a way of performing a long-distance quantum communication where the photon absorption and noise become major issues.

Here is a typical situation. Alice needs to send an (unknown) photon quantum state to Bob over a dissipative channel, which has a probability for a successful transmission of the qubit equal to $p(l) = e^{-l/l_0}$, where l is the channel length and l_0 is determined by an optical absorption rate in the channel. However, Alice cannot just repeatedly copy and send the initial quantum state on to Bob because of the *no-cloning theorem* [153, 157].

The proposed solution is to use entanglement as a resource, see Figure 6.1. One first cuts the channel into N segments, such that the transmission over each segment

[i]The details of the original proposal can be found in section 8.7 of Ref. [20].

is fairly high, and puts $N-1$ quantum repeaters between the segments. The further strategy consists of the following steps:

1. *Generation and delivery of entangled pairs.*

Pairs of entangled photons are generated by the external EPR-sources to be shared between the adjacent repeaters, Alice, and Bob, as shown in Figure 6.1. Since the channel is dissipative, one or both photons of an entangled pair may be lost on the way from each source to the given two recipients, e.g., repeaters C_1 and C_2. For that reason, C_1 and C_2 communicate with each other over a classical channel (shown by round arrows), and photon pairs are repetitively generated and sent to them until a successful receipt of both photons of a pair has been confirmed by the two repeaters.

2. *Storage of entangled photon states.*

Since all N pairs are received independently at different times, each recipient needs to be able to store a photon of the pair that has arrived early while awaiting the remaining photon to perform a two-photon Bell-state measurement. More precisely, it is the quantum states of the photons that need be stored, rather than the photons themselves.

3. *Establishing entanglement over the channel.*

Once the entangled photons pairs have been shared, a well-known quantum protocol of entanglement swapping [12, 107] is to be done at each repeater. Namely, it consists of a Bell-state measurement on the two stored photons that belong to the two pairs shared with the adjacent nodes on the left and right, followed by the classical communication of the measurement results to the neighbours.

The two measured photons are then discarded, but their two counterparts at the neighbouring nodes become entangled. After the same procedure is carried out at each repeater, only two photons are left, one at Alice's and one at Bob's side, that are entangled despite the fact there has been a long-distance lossy fibre between them.

4. *Teleportation of quantum information from Alice to Bob.*

Finally, the remaining pair of entangled photons is used to teleport a desired quantum state from Alice to Bob [12, 20].

Technically, entanglement purification is also needed to accomplish the quantum data transmission in the presence of imperfect generation and transmission of entangled photons from an EPR-source, as well as errors in the local operations of quantum repeaters. Section 8.7 of Ref. [20] provides an accurate mathematical treatment of this issue. The question that we are interested in, though, is the following: what is needed to implement a quantum repeater? According to the above protocol a quantum repeater is required to

- store quantum states of photons;

- perform local two-qubit operations on request (e.g. Bell-state measurements for the entanglement swapping, Controlled-NOT gates for the entanglement purification);

- send and receive classical information.

In a way, a quantum repeater carries out all the functions of an elementary unit of a quantum computer. This is an example of the use of quantum logic with only a few qubits, as opposed to the multi-qubit quantum computer suitable e.g. for the Shor's quantum factoring. A quantum repeater will also be important for creating a *quantum network* [20], where qubits are locally stored and manipulated at the spatially separated nodes connected by optical quantum communication channels.

So far conceived physical implementations of the quantum repeater include atoms in the cavities (see sections 6.2 and 8.6 in Ref. [20]) and atomic ensembles recently proposed by Duan *et al.* [37]. Photon quantum states are stored as collective spin-wave excitations of an ensemble of atoms, and the entanglement purification turns out to be superfluous due to the smart way of generating effective maximally entangled states. In support of the latter proposal, Julsgaard *et al.* have experimentally demonstrated

an atomic quantum memory device and entangled two ensembles of caesium atoms for half a millisecond [70, 111].

Our idea of Section 4.4, published in Ref. [25], proposes to implement the storage of the photon quantum states in the exciton degrees of freedom of semiconductor QDs. As described, it corresponds to a rudimentary quantum memory device with a fixed storage time determined by the QD exciton recombination. Placing the QD in a microcavity and tuning the cavity mode on- and off-resonance with the QD transition, it should be possible in principle to vary the storage time thanks to the Purcell effect. The remaining question is to realise a subnanosecond mode tuning, either mechanically or electro-optically, for which a relevant cavity design should be considered.

6.3 Source of entangled photons

First proposed by the Yamamoto group [13], the idea is to produce pairs of polarization-entangled photons on demand, i.e. at well-defined time intervals, using the recombination of a biexciton in a QD. In a symmetric QD, the biexciton generated by an excitation laser pulse has two possible recombination paths: either by emitting first a σ^+ photon to the one-exciton spin-up state and then a σ^- photon to the ground state, or by emitting a σ^- photon to the one-exciton spin-down state followed by a σ^+ photon to the ground state. Since the spin-up and spin-down states are degenerate, the "which-path" information is erased, and the emitted two-photon cascade will be in a maximally entangled state $|\psi\rangle = \frac{1}{\sqrt{2}}\left(|\sigma^+\rangle_1|\sigma^-\rangle_2 + |\sigma^-\rangle_1|\sigma^+\rangle_2\right)$. Such a source is expected to have a better statistics than the PDC, since the probability of creation of two and more pairs per pulse is suppressed, and possibly higher generation rates due to the Purcell effect, if put in a microcavity.

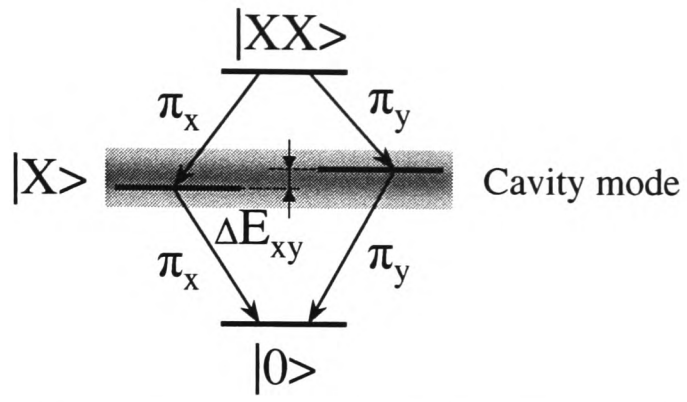


Figure 6.2: *Spectrum of a realistic asymmetric SAQD, showing the biexciton $|XX\rangle$, doubly split one-exciton $|X\rangle$, and ground $|0\rangle$ states. Optical transitions π_x and π_y are excited by linearly polarized photons. Also shown is a cavity mode resonant with the non-degenerate one-exciton state.*

An essential condition for that as well as for the resonant coupling scheme of Section 4.4 is the degeneracy of the two exciton spin states. However, InAs SAQDs specifically grown by the MBE techniques have an elongated shape as a consequence of the large in-plane anisotropy. This anisotropy causes the lowest exciton state to split by the electron-hole exchange interaction into two levels with dipole moments oriented along the two orthogonal QD axes [45]. As a result, each of the levels is excited by a linearly polarized photon π_x or π_y instead of σ^+ and σ^-, see Figure 6.2. For the InAs QDs, the reported energy splitting ΔE_{xy} exceeds the 1.3 μeV linewidth of the exciton state, but is less than the experimental resolution limit of 50 μeV [122].

Because of the lifted degeneracy of the one-exciton state, the two recombination paths are now distinguished in energy, and the two-photon emission is a statistical mixture of the linear-polarization states $|\pi_x\rangle_1|\pi_x\rangle_2$ and $|\pi_y\rangle_1|\pi_y\rangle_2$ [132]. This is supported by the observed polarization correlation of the two photons in the linear basis, which is strongly basis-dependent. That is a major obstacle to the implementation of an entangled-photon device [122, 132].

A proposed way around this problem is to couple the one-exciton transition on

resonance with a 'bad' cavity mode whose linewidth exceeds the splitting ΔE_{xy},[ii] as shown in Figure 6.2. In this case, both spin states of the one-exciton transition will be coupled to the optical field via the same cavity mode, and a resonant photon whose coherence time equals the cavity lifetime will be absorbed by either of the spin states depending on its polarization. In addition, the Purcell effect will give rise to the broadening of the exciton states which may as well overlap for the splittings smaller than 50 μeV. Both factors contribute to an erasure of the "which-path" information.

Specifically for the entangled-pair source, the biexciton transition should be resonantly coupled to another cavity mode, so that both emitted photons of the pair would be able to leave the cavity efficiently [130]. As described in Section 4.3.3, the biexciton transition is shifted due to the binding energy from the one-exciton transition by a few meV for InAs SAQDs. To have such a small FSR, it follows from Eq. 4.7 that the cavity length has to be on the order of a few tens of μm in GaAs, which is not desired for keeping the cavity mode volume small. On the other hand, our photonic crystal samples allow for the existence of two cavity modes with the separation of the same order.

6.4 QED effects in the strong-coupling regime

We mentioned in Section 4.6.1, that the Purcell effect is observed in the weak-coupling regime, which is characteristic of most modern experiments on QDs in microcavities and has been used e.g. for the implementation of a single-photon source.

On the other hand, it is very interesting to consider the *strong-coupling regime*, where spontaneous emission becomes a reversible process (i.e. an emitted photon is

[ii] In fact, most existing semiconductor microcavities that have been coupled with QDs act as 'bad' cavities, as outlined in Section 4.6.

reabsorbed before leaking from the cavity), and the system has to be described in terms of emitter-cavity dressed states. In the strong-coupling regime, the effects of quantum electrodynamics (QED) become more pronounced and give access to many atomic physics experiments in solid-state. E.g. it should be possible to observe the exciton Rabi oscillations in an individual QD already at a single-photon level. This is qualitatively different from the recent experiments [72, 61, 133] where Rabi oscillations were driven by a strong applied electromagnetic field. Ultimately, the schemes for quantum information processing, where single-QD-based qubits interact with each other via a common cavity mode (used as a *quantum bus*) [63], may only be implemented in the strong-coupling regime.

How difficult is it to achieve the strong-coupling regime with SAQDs in semiconductor microcavities? Ref. [48] gives a simple criterion to observe the *vacuum Rabi splitting* between the two eigenstates of the emitter-cavity system, which is

$$2\hbar\Omega > \delta E_e + \delta E_c, \tag{6.1}$$

where δE_e and δE_c are the emitter and cavity linewidths, respectively, and $\hbar\Omega$ is the Rabi energy

$$2\hbar\Omega = |\mathbf{d} \cdot \mathbf{E}(\mathbf{r})|. \tag{6.2}$$

Here the amplitude of the one-photon field in the cavity mode is given by

$$E_{max} = \sqrt{\frac{\pi\hbar}{\varepsilon_0 \lambda n^2 V_{eff}}},$$

and is about 10^5 V/m for $V_{eff} \approx 3(\lambda/n)^3$). The electric dipole of the emitter $\mathbf{d}$ has been estimated for InAs SAQDs in [48] to be on the order of 10^{-28} C m. Putting these values in Eq. (6.2), we obtain $\hbar\Omega \approx 60$ μeV.

We know from Ref. [18] that undisturbed InAs SAQD have linewidths as narrow as several μeV, which is negligible compared with the other terms in Eq. (6.1). Hence, to

satisfy the criterion (6.1), it is desirable to fabricate high-Q cavities with the linewidth $\delta E_c \leq 100$ μeV (i.e. $Q \approx 13000$ for $\lambda = 950$ nm) and mode volumes $V_{eff} \leq 3(\lambda/n)^3$, or alternatively, with the same or better ratio of $Q/\sqrt{V_{eff}}$.[iii]

High-Q photonic-crystal microcavities that combine a three-dimensional light confinement with small mode volumes are very promising in reaching the strong-coupling regime. We estimate that a value of $Q \approx 5300$ is needed in order that the S1 PC cavity described in Section 5.2 satisfy the vacuum Rabi splitting criterion (6.1).

[iii]The $Q/\sqrt{V_{eff}}$ ratio follows from the definitions of $E_{max} \propto 1/\sqrt{V_{eff}}$ and $\delta E_c \propto 1/Q$.

Chapter 7

Conclusion

My D.Phil. course has been rather unique since a significant part of my work has been to set up a completely new line of research. This implied that I had to accumulate the required background knowledge, get to know active research groups in the field, design and build a state-of-the-art setup, establish collaborations with the world-leading experts in sample fabrication, acquire clean-room experience, propose new experiments and secure long-term funding. As a result, there was a large period of study and labour before reaching the level of conducting experiments and obtaining novel experimental results.

It has been very rewarding too, since the project that was not clear three years ago, not only survived the test of time but is now a strong collaboration going full steam ahead. Personally, I have acquired the versatile skills of an experimentalist and project manager. Combined with my theoretical background that I continued to improve in parallel with the experiment, they enable me to pursue independent research in the field of solid-state nanostructures.

The scientific conclusions of this thesis can be divided in two groups, corresponding to two types of artificial atoms that we have studied: (a) Numerical simulations of GaAs/AlGaAs modulation-doped quantum dots (QDs) formed by electrostatic

squeezing of the two-dimensional electron gas. (b) Experimental study of InAs/GaAs self-assembled QDs formed by the bandgap difference of the two materials.

For the first type of artificial atoms, we have investigated the effect of spontaneous spin polarization. We have developed a theoretical model, which is based on the Kohn-Sham density-functional formalism and takes into account contributions from a patterned gate, doping, surface states, and mirror charges. Separate computer codes were written to calculate a realistic confinement potential and obtain the ground-state density distributions for up and down-spin electrons self-consistently using the Thomas-Fermi and local spin-density approximations. We have found the following:

1) Spontaneous spin polarization occurs in single QDs as a result of symmetric electrostatic confinement (giving rise to an atomic-like shell structure) and exchange-correlation interactions between electrons (leading to the splitting of sub-shells for spin up and down). The total magnetic moment of the modelled QDs containing from 0 to 50 electrons can be controlled by an applied gate voltage.

2) Spin polarization disappears due to introduced asymmetry of the confinement in single QDs, or as a result of quantum-mechanical coupling in double-dot artificial molecules. The origin of the suppression of spin polarization is reduced degeneracy of the energy states.

3) In quantum point contacts, spontaneous spin polarization occurs at low electron densities, as controlled by an applied gate voltage, as a result of an increased contribution of the exchange-correlation interactions. This leads to the spin-dependent splitting of the electronic potentials and their deviation from the saddle-point form, which may explain the experimentally observed 0.7 anomaly in conductance of quantum point contacts.

4) In our systems, electron exchange is the dominant mechanism that drives spontaneous magnetization, while electron correlation plays a minor role. The developed

theoretical model can therefore be considerably simplified and calculation time reduced by considering an exchange-only approximation.

These results demonstrate the intrinsic magnetic properties of realistic GaAs/AlGaAs modulation-doped QDs suggesting their high potential for all-semiconductor implementations of spin manipulation and spin injection mechanisms. Moreover, these devices avoid complicated fabrication issues, such as position-controlled implantation of magnetic impurities or interfacing of ferromagnetic and semiconductor materials, which would facilitate their integration in consistent electronic or spintronic circuits.

For the second type of artificial atoms, we have investigated the experimental implementation of the photon-exciton coupling in InAs/GaAs self-assembled QDs:

1) We propose two experiments for *resonant* single-photon excitation of the QD. The technical challenge of separation of QD emission from resonant excitation is solved in the first experiment by detecting time-correlated two-photon coincidences resulting after photon bunching of signal and reference beams at a beamsplitter. In the second experiment, scattered pump light is suppressed as a result of destructive quantum interference in two nearly identical optical paths, only one of which contains a resonant QD.

2) We have evaluated the feasibility of the proposed experiments and showed that the main limitation for their implementation with available technology is the small coupling efficiency between the optical mode and the QD. To make the proposed experiments feasible, the QD has to be inserted in a microcavity with a high ratio of Q/V_{eff}, where Q is the quality factor and V_{eff} the effective volume of the resonant cavity mode.

3) We have explored novel ways of developing high-(Q/V_{eff}) semiconductor microcavities with embedded self-assembled QDs. The first type of fabricated microcavity samples is based on a GaAs single-defect square-lattice photonic crystal slab, where

the lateral optical confinement is achieved by the two-dimensional photonic bandgap, and the vertical confinement is due to the total internal reflection. We have performed an optical study of QD emission in this structures, which in addition to estimated $V_{eff} \sim 0.5(\lambda/n)^3$ (where λ is the resonant wavelength) shows $Q \sim 2400$, linear polarization, and controlled tunability of the resonant cavity modes as a function of lithographic parameters and temperature. New samples containing low-density arrays of QDs with controlled positioning of the cavity-defect modes are currently being fabricated.

4) The second type of microcavities that we have studied is based on GaAs/AlAs micropillars where light is confined vertically by two distributed Bragg reflectors and laterally by the waveguiding effect. The novel focussed ion-beam technique that we have used for fabrication provided high spatial resolution and clean surfaces of the sidewalls. Unfortunately, it has also resulted in suppression of the QD emission due to radiation damage caused by the ion beam. We are currently developing a new generation of micropillars with QDs, where the cavity mode is confined without diffraction and scattering losses by means of internal focussing with oxidized tapered apertures.

5) We have performed the first optical studies of artificial molecules composed of pairs of vertically coupled strain-assisted self-assembled quantum dots. The results to date clearly show bright exciton transitions from individual molecules. More data are currently being acquired on the photoluminescence and quantum statistics of the coupled QD emitters.

These first results indicate the high potential of the QDs embedded in microcavites for the implementation of resonant transfer of quantum information, entangled-photon source, and QED effects in the 'strong-coupling' regime, all of which are conceived directions of further experimental study.

In addition to performing research, I had the opportunity to extensively discuss and communicate scientific ideas and results at several international conferences (see Appendix B). Furthermore, in June 2001 I took an interview with Professor Zhores Alferov for the Europhysics News magazine. Later that year Prof. Alferov received a Nobel Prize in Physics for "developing semiconductor heterostructures used in high-speed- and opto-electronics". In November to December 2001 during my visit to Fujistu Laboratories, I made a series of presentations on the optical schemes for quantum information processing at research institutions in Japan. I also gave a graduate lecture on quantum computing at St. John's College, Oxford, to a general audience.

Appendix A

Derivation of Thomas-Fermi kinetic energy functional

We divide the space into many small cells, each of volume $\Delta V = l^2$ and containing some fixed number of electrons ΔN (which may have different values for different cells), and we assume that the electrons in each cell behave like independent fermions at the temperature 0 K, with the cells independent of one another.

The energy levels of a particle in each cell can be given by the formula for a 2D infinite well:

$$\varepsilon(n_x, n_y) = \frac{h^2}{8ml^2}(n_x^2 + n_y^2) = \frac{h^2}{8ml^2}R^2,$$

where n_x, n_y =1,2,3,... Since $n_x, n_y > 0$, the number of levels below given energy ε can be approximated by one quadrant of a circle with radius R in the space (n_x, n_y). This number is

$$\Phi(\varepsilon) = \frac{1}{4}\pi R^2 = \frac{ml^2}{2\pi\hbar^2}\varepsilon.$$

Accordingly, the density of states at energy ε is given by

$$g(\varepsilon) = \frac{\Phi(\varepsilon + \delta\varepsilon) - \Phi(\varepsilon)}{\delta\varepsilon} = \frac{ml^2}{2\pi\hbar^2} = \text{const.}$$

We can now find the total energy of the particles in each cell by integrating with the probability for the state with energy ε to be occupied. For electrons, the latter is

the Fermi-Dirac distribution function

$$f(\varepsilon) = \frac{1}{1 + e^{\frac{\varepsilon - \mu}{k_B T}}},$$

which at 0 K reduces to a step function:

$$f(\varepsilon) = \begin{cases} 1, & \varepsilon < \varepsilon_F \\ 0, & \varepsilon > \varepsilon_F \end{cases}$$

where ε_F is the Fermi energy. The total energy of the electrons in a cell is

$$\Delta E = 2 \int \varepsilon f(\varepsilon) g(\varepsilon) d\varepsilon = \frac{ml^2}{\pi\hbar^2} \int_0^{\varepsilon_F} \varepsilon d\varepsilon = \frac{ml^2}{2\pi\hbar^2} \varepsilon_F^2, \tag{A.1}$$

where the factor 2 enters because of the spin degeneracy. The total number of electrons in a cell is derived in a similar way as

$$\Delta N = 2 \int f(\varepsilon) g(\varepsilon) d\varepsilon = \frac{ml^2}{\pi\hbar^2} \varepsilon_F. \tag{A.2}$$

Excluding ε_F from (A.1) and (A.2), we obtain

$$\Delta E = \frac{1}{2} \Delta N \varepsilon_F = \frac{\pi\hbar^2 l^2}{2m} \rho_i^2, \tag{A.3}$$

where $\rho_i = \lim_{l \to 0} \frac{\Delta N}{l^2}$ is the 2D electron density in the i-th cell. Note that every cell has its own number of electrons ΔN and thus its local value of ρ_i. Adding the contributions from all cells, we find the total kinetic energy, or the *Thomas-Fermi kinetic energy functional*

$$T_{TF}[\rho] = \sum_i \frac{\pi\hbar^2}{2m} \rho_i^2 l^2 = \frac{\pi\hbar^2}{2m} \int \rho^2(\mathbf{r}) d\mathbf{r}. \tag{A.4}$$

Appendix B

Papers and presentations by the author

Scientific publications

1) K.-F. Berggren, I. I. Yakimenko, and A. M. Bychkov, *On the role of electron exchange and correlation in semiconductor quantum dots*, Nanotechnology **12**, 529 (2001).

2) I. I. Yakimenko, A. M. Bychkov, and K.-F. Berggren, *Symmetry and spin polarization in single and coupled quantum dots*, Phys. Rev. B **63**, 165309 (2001).

3) A. M. Bychkov, I. I. Yakimenko, and K.-F. Berggren, *Spin-dependent electron behaviour in quantum point contacts*, Nanotechnology **11**, 318 (2000).

General interest publications

1) A. M. Bychkov, *NANO–2002: 10th anniversary*, Europhysics News, Sep/Oct 2002, p. 174.

2) A. M. Bychkov, *NANO–2001*, Europhysics News, Sep/Oct 2001, p. 186.

3) A. M. Bychkov, *NANO–2000: conference report and interview with Professor Zhores Alferov*, Europhysics News, Sep/Oct 2000, p. 28-29; *ibid* Jan/Feb 2001, p. 26.

Conference contributions

1) A. M. Bychkov, S. Strauf, K. Hennessy, M. J. A. de Dood, A. Badolato, D. Bouwmeester, P. M. Petroff, and E. Hu, *Quantum dots in 2D photonic crystals for quantum information science*, Proceedings of the 4th QIPC Workshop, Oxford, UK (Jul 2003).

2) A. M. Bychkov and D. Bouwmeester, *Single-photon storage in a single quantum dot for the implementation of a solid-state quantum repeater*, Proceedings of IQEC/LAT 2002, Moscow, Russia, p. 367 (Jun 2002).

3) A. M. Bychkov and D. Bouwmeester, *Single-photon storage in a single quantum dot for the implementation of a solid-state quantum repeater*, Proceedings of the 10th International Symposium on Nanostructures: Physics and Technology, St Petersburg, Russia, p. 495-496 (Jun 2002).

4) I. I. Yakimenko, A. M. Bychkov, and K.-F. Berggren, *Spontaneous magnetization in single*

and coupled quantum dots, Proceedings of the 9th International Symposium on Nanostructures: Physics and Technology, St Petersburg, Russia, p. 339-341 (Jun 2001).

5) A. M. Bychkov, I. I. Yakimenko, and K.-F. Berggren, *Spin-dependent electron behavior in quantum point contacts and dots*, Proceedings of the 8th International Symposium on Nanostructures: Physics and Technology, St Petersburg, Russia, p. 391-394 (Jun 2000).

6) K.-F. Berggren, I. I. Yakimenko, A. M. Bychkov, *Spin-polarization effects in quantum point contacts and dots*, Abstracts of the 5th MEL-ARI / NID Workshop and COST meeting, Pisa, Italy, p. 18, 51 (Feb 2000).

Presentations

1) *Single-photon storage in a single quantum dot for the implementation of a solid-state quantum repeater*, Prize in poster competition, NTT Basic Research Labs summer camp on quantum information and nanotechnology, Hakone, Japan (Aug 2002).

2) *Optical schemes for quantum information processing*, Series of talks at universities and research centers of Japan (Nov–Dec 2001).

3) *Solid-state approach to quantum computing*, Clarendon Lab, Oxford University, UK (Sep 2001).

4) *Förster energy transfer: applications in nature and high technology*, First-year talk, Clarendon Lab, Oxford University, UK (May 2001).

5) *How to build a quantum computer?* Graduate lecture, St. John's College, Oxford University, UK (Feb 2001).

6) *Spin-dependent electron behavior in quantum dots and point contacts*, Young Physicists Conference lecture competition, Chester, UK (Nov 2000).

7) *Quantum dots for quantum computing*, Clarendon Lab, Oxford University, UK (Oct 2000).

Bibliography

[1] A. P. Alivisatos, Science **271**, 933 (1996).

[2] E. Altewischer, M. P. van Exter and J. P. Woerdman, Nature **418**, 304 (2002).

[3] D. K. Armani, T. J. Klippenberg, S. M. Spillane, and K. J. Vahala, Nature **421**, 925 (2003).

[4] N. W. Ashcroft and N. D. Mermin, *Solid-state physics* (Holt, Rinehart and Winston, New York, 1976).

[5] M. Aspelmeyer, T. Jennewein, M. Pfennigbauer, W. Leeb, and A. Zeilinger, *Long-distance quantum communication with entangled photons using satellites*, `quant-ph/0305105`.

[6] D. G. Austing, S. Sasaki, S. Tarucha, S. M. Reimann, M. Koskinen, and M. Manninen, Phys. Rev. B **60**, 11 514 (1999).

[7] D. Awschalom, J. Kikkawa, Phys. Today **52**, 33 (1999).

[8] A. Babinski, J. Jasinski, R. Bozek, A. Szepelow, and J. M. Baranowski, Appl. Phys. Lett. **79**, 2576 (2001).

[9] H. U. Baranger, D. Ullmo, L. I. Glazman, Phys. Rev. B **61**, R2425 (2000).

[10] P. K. Basu, *Theory of optical processes in semiconductors: bulk and microstructures*, Series on semiconductor science and technology (Clarendon Press, Oxford, 1997).

[11] M. Bayer, O. Stern, P. Hawrylak, S. Fafard, and A. Forchel, Nature **405**, 923 (2000).

[12] C. H. Bennett, G. Brassard, C. Crépeau, R. Jozsa, A. Peres, and W. K. Wooters, Phys. Rev. Lett. **70**, 1895 (1993).

[13] O. Benson, C. Santori, M. Pelton, and Y. Yamamoto, Phys. Rev. Lett. **84**, 2513 (2000).

[14] J. Bernholc, Phys. Today **52**(9), 30 (1999).

[15] D. Bimberg, M. Grundmann, N. N. Ledentsov, *Quantum dot heterostructures* (Wiley, New York, 1999).

[16] R. H. Blick, D. Pfannkuche, R. J. Haug, K. von Klitzing, K. Eberl, Phys. Rev. Lett. **80**, 4032 (1998).

[17] N. H. Bonadeo, J. Erland, D. Gammon, D. Park, D. S. Katzer, D.G. Steel, Science **282**, 1473 (1998).

[18] P. Borri, W. Langbein, S. Schneider, U. Woggon, R. L. Sellin, D. Ouyang, and D. Bimberg, Phys. Rev. Lett. **87**, 157401 (2001).

[19] L. P. Bouckaert, R. Smoluchowski, and E. Wigner, Phys. Rev. **50**, 58 (1936).

[20] D. Bouwmeester, A. Ekert, A. Zeilinger (Eds.), *The physics of quantum information* (Springer, Berlin, 2000).

[21] D. Bouwmeester, J-W. Pan, K. Mattle, M. Eible, H. Weinfurter, and A. Zeilinger, Nature **390**, 575 (1997).

[22] N. A. Bruce and P. A. Maksym, Phys. Rev. B **61**, 4718 (2000).

[23] H. Bruus, V. V. Cheianov, K. Flensberg, *From mesoscopic magnetism to the anomalous 0.7 conductance plateau*, `cond-mat/0002338`.

[24] M. Büttiker, Phys. Rev. B **41**, 7906 (1990).

[25] A. M. Bychkov and D. Bouwmeester, *Single-photon storage in a single quantum dot for the implementation of a solid-state quantum repeater.* Proc. 10th Int. Symp. on Nanostructures: Physics and Technology, St Petersburg, Russia, p. 495-496 (June 2002).

[26] A. M. Bychkov, I. I. Yakimenko, and K.-F. Berggren, Nanotechnology **11**, 318 (2000).

[27] R. L. Cappelletti, J. R. D. Copley, W. A. Kamitakahara, F. Li, J. S. Lannin, and D. Ramage , Phys. Rev. Lett. **66**, 3261 (1991).

[28] J. R. Chelikowski and M. L. Cohen, Phys. Rev. B **14**, 556 (1976).

[29] L. Coldren, private communications.

[30] J. H. Davies, *The physics of low-dimensional semiconductors* (Cambridge University Press, Cambridge, 1998).

[31] J. H. Davies, Semicond. Sci. Technol. **3**, 995 (1988).

[32] J. H. Davies, I. A. Larkin, and E. V. Sukhorukov, J. Appl. Phys. **77**, 4504 (1995).

[33] P. A. M. Dirac, Proc. Cambridge Phil. Soc. **26**, 376 (1930).

[34] D. P. DiVincenzo, Fortschr. Phys. **48**, 771 (2000).

[35] D.P. DiVincenzo, G. Burkard, D. Loss, E. V. Sukhorukov, *Quantum computation and spin electronics*, `cond-mat/9911245`.

[36] V. G. Dmitriev, G. G. Gurzadyan, D. N. Nikogosyan, *Handbook of nonlinear optical crystals*, 3rd Edition (Springer Verlag, Berlin, 1999).

[37] L.-M. Duan, M. D. Lukin, J. I. Cirac, P. Zoller, Nature **414**, 413 (2001).

[38] C. S. Dürr, R. J. Warburton, K. Karrai, J. P. Kotthaus, G. Medeiros-Ribeiro, P. M. Petroff, Physica E **2**, 23 (1998).

[39] R. P. Feynman, *There's plenty of room at the bottom*, talk at the 1959 Annual Meeting of the American Physical Society. Published in Caltech's Engineering and Science, Feb. 1960. Also available at `http://www.zyvex.com/nanotech/feynman.html`.

[40] R. Fiederling, M. Kelm, G. Reuscher, W. Ossau, G. Schmidt, A. Waag, L. W. Molenkamp, Nature **402**, 787 (1999).

[41] J. J. Finley, P. W. Fry, A. D. Ashmore, A. Lemaitre, A. I. Tartakovskii, R. Oulton, D. J. Mowbray, M. S. Skolnick, M. Hopkinson, P. D. Buckle, and P. A. Maksym, Phys. Rev. B **63**, 161305 (2001).

[42] V. V. Flambaum and M. Y. Kuchiev, Phys. Rev. B **61**, R7869 (2000).

[43] T. Fujisawa, T. H. Oosterkamp, W. G. van der Wiel, B. W. Broer, R. Aguado, S. Tarucha, and L. P. Kouwenhoven, Science **282**, 932 (1998).

[44] D. Gammon and D. Steel, Physics Today **55**(10), 36 (2002).

[45] D. Gammon, E. S. Snow, B. V. Shanabrook, D. S. Katzer, and D. Park, Phys. Rev. Lett. **76**, 3005 (1996).

[46] B. Gayral, J. M. Gérard, B. Sermage, A. Lemaitre, and C. Dupuis, Appl. Phys. Lett. **78**, 2828 (2001).

[47] J. M. Gérard, B. Sermage, B. Gayral, B. Legrand, E. Costard, and V. Thierry-Mieg, Phys. Rev. Lett. **81**, 1110 (1998).

[48] J. M. Gérard, B. Gayral, Physica E **9**, 131 (2001).

[49] B. Gerardot, private communications.

[50] A. Gold and L. Calmels, Philos. Mag. Lett. **74**, 33 (1996).

[51] P. Grangier, Nature **419**, 577 (2002).

[52] P. Grangier and I. Abram, Physics World **16**(2), 31 (2003).

[53] S. Grosse, J. H. H. Sandmann, G. von Plessen, J. Feldmann, H. Lipsanen, M. Sopanen, J. Tulkki, J. Ahopelto, Phys. Rev. B **55**, 4473 (1997).

[54] E. Hecht, *Optics*, 4th Edition (Addison Wesley, San Francisco, 2002).

[55] E. R. Hegblom, D. I. Babic, B. J. Thibeault, and L. A. Coldren, IEEE J. Select. Topics Quantum Electron. **3**, 379 (1997).

[56] E. R. Hegblom, N. M. Margalit, A. Fiore, and L. A. Coldren, IEEE J. Select. Topics Quantum Electron. **5**, 553 (1999).

[57] K. Hennessy, C. Reese, A. Badolato, C. F. Wang, G. Jin, S. Shi, D. W. Prather, A. Imamoglu, P. M. Petroff, and E. Hu, *Square-lattice photonic crystal microcavities for coupling to single InAs quantum dots*, accepted to Appl. Phys. Lett. (2003).

[58] K. Hirose and N. S. Wingreen, Phys. Rev. B **59**, 4604 (1999).

[59] P. Hohenberg and W. Kohn, Phys. Rev. **136**, B864 (1964).

[60] C. K. Hong, Z. Y. Ou, L. Mandel, Phys. Rev. Lett. **59**, 2044 (1987).

[61] H. Htoon, T. Takagahara, D. Kulik, O. Baklenov, A. L. Holmes, and C. K. Shih, Phys. Rev. Lett. **88**, 087401 (2002).

[62] A. Imamoğlu, Fortschr. Phys. **48**, 987 (2000).

[63] A. Imamoğlu, D. D. Awschalom, G. Burkard, D. P. DiVincenzo, D. Loss, M. Sherwin, and A. Small, Phys. Rev. Lett. **83**, 4204 (1999).

[64] L. Jacak, private communications.

[65] L. Jacak, P. Hawrylak, and A. Wojs, *Quantum dots* (Springer, Berlin, 1998).

[66] L. Jacak, J. Krasnyj, and A. Wojs, Physica B **229**, 279 (1997).

[67] J. D. Joannopoulos, R. D. Meade, J. N. Winn, *Photonic crystals: molding the flow of light* (Princeton University Press, Princeton, 1995).

[68] S. G. Johnson and J. D. Joannopoulos, Optics Express **8**, 173 (2001).

[69] S. G. Johnson, S. Fan, P. R. Villeneuve, J. D. Joannopoulos, and L. A. Kolodziejski, Phys. Rev. B **60**, 5751 (1999).

[70] B. Julsgaard, A. Kozhekin, and E. S. Polzik, Nature **413**, 400 (2001).

[71] H. Kalt, *Optical Properties of III-V Semiconductors: The Influence of Multi-Valley Band Structures*, Springer Series in Solid-State Sciences (Springer, Berlin, 1996).

[72] H. Kamada, H. Gotoh, J. Temmyo, T. Takagahara, and H. Ando, Phys. Rev. Lett. **87**, 246401 (2001).

[73] T. E. Keller and M. H. Rubin, Phys. Rev. A **56**, 1534 (1997).

[74] J. M. Kikkawa, J. A. Gupta, I. Malajovich and D. D. Awschalom, Physica E **9**, 194 (2001).

[75] A. Kiraz, P. Michler, C. Becher, B. Gayral, A. Imamoğlu, L. Zhang, E. Hu, W. V. Schoenfeld, and P. M. Petroff, Appl. Phys. Lett. **78**, 3932 (2001).

[76] C. Kittel, *Introduction to Solid-State Physics* (Wiley, New York, 1996).

[77] E. Klarreich, Nature **418**, 270 (2002).

[78] M. V. Klein and T. E. Furtak, *Optics*, 2nd Edition (John Wiley & Sons, New York, 1986).

[79] M. Koskinen, M. Manninen, and S. M. Reimann, Phys. Rev. Lett. **79**, 1389 (1997).

[80] A. Kristensen, J. B. Jensen, M. Zaffalon, C. B. Sorensen, S. M. Reimann, P. E. Lindelof, M. Michel, and A. Forchel, J. Appl. Phys. **83**, 607 (1998).

[81] A. Lamas-Linares, J. C. Howell, D. Bouwmeester, Nature **412**, 887 (2001).

[82] A. Lamas-Linares, C. Simon, J. C. Howell, D. Bouwmeester, Science **296**, 712, (2002).

[83] I.-H. Lee, V. Rao, R. M. Martin, and J.-P. Leburton, Phys. Rev. B **57**, 9035 (1998).

[84] X. Li, Y. Wu, D. G. Steel, D. Gammon, T. H. Stievater, D. S. Katzer, D. Park, C. Piermarocchi, and L. J. Sham, Science **301**, 809 (2003).

[85] C.-T. Liang, M. Pepper, M. Y. Simmons, C. G. Smith, and D. A. Ritchie, Phys. Rev. B **61**, 9952 (2000).

[86] H. Lipsanen, M. Sopanen, J. Ahopelto, Phys. Rev. B **51**, 13 868 (1995).

[87] D. Loss, D. P. DiVincenzo, Phys. Rev. A **57**, 120 (1998).

[88] M. I. Lubin, O. Heinonen, and M. D. Johnson, Phys. Rev. B **56**, 10 373 (1997).

[89] O. Madelung, *Introduction to solid-state theory* (Springer, New York, 1978).

[90] L. Mandel, E. Wolf, *Optical Coherence and Quantum Optics* (Cambridge Univ. Press, Cambridge, 1995).

[91] R. G. Mani, J. H. Smet, K. von Klitzing, V. Narayanamurti, W. B. Johnson, and V. Umansky, Nature **420**, 646 (2002).

[92] J. Martorell, H. Wu, and D. W. L. Sprung, Phys. Rev. B **50**, 17 298 (1994).

[93] P. Matagne, J.-P. Leburton, D. G. Austing, and S. Tarucha, Phys. Rev. B **65**, 085325 (2002).

[94] A. E. Mattsson, Science **298**, 759 (2002).

[95] P. Michler, A. Kiraz, C. Becher, W. V. Schoenfeld, P. M. Petroff, L. Zhang, E. Hu, and A. Imamoğlu, Science **290**, 2282 (2000).

[96] E. Moreau, private communications.

[97] E. Moreau, I. Robert, J. M. Gérard, I.Abram, L. Manin, and V. Thierry-Mieg, Appl. Phys. Lett. **79**, 2865 (2001).

[98] S. Nagaraja, P. Matagne, V.-Y. Thean, J.-P. Leburton, Y.-H. Kim, and R. M. Martin, Phys. Rev. B **56**, 15 752 (1997).

[99] S. Nagaraja, J.-P. Leburton, and R. M. Martin, Phys. Rev. B **60**, 8759 (1999).

[100] H. S. Nalwa (Ed.), *Handbook of nanostructured materials and nanotechnology*, vol. 3 (Academic Press, San Diego, 2000).

[101] M. Oestreich, Nature **402**, 735 (1999).

[102] A. M. van Oijen, J. Köhler, J. Schmidt, M. Müller, and G. J. Brakenhoff, J. Opt. Soc. Am. A **16**, 909 (1999).

[103] T. H. Oosterkamp, *Artificial atoms and molecules,* PhD Thesis (Technical University Delft, The Netherlands, 1999).

[104] T. H. Oosterkamp, S. F. Godijn, M. J. Uilenreef, Y. V. Nazarov, N. C. van der Vaart, and L. P. Kouwenhoven, Phys. Rev. Lett. **80**, 4951 (1998).

[105] G. Ortner, M. Bayer, A. Larionov, V. B. Timofeev, A. Forchel, Y. B. Lyanda-Geller, T. L. Reinecke, P. Hawrylak, S. Fafard, and Z. Wasilewski, Phys. Rev. Lett. **90**, 086404 (2003).

[106] M. Paillard, X. Marie, P. Renucci, T. Amand, A. Jbeli, J. M. Gérard, Phys. Rev. Lett. **86**, 1634 (2001).

[107] J.-W. Pan, D. Bouwmeester, H. Weinfurter, and A. Zeilinger, Phys. Rev. Lett. **80**, 3891 (1998).

[108] R. G. Parr and W. Yang, *Density-functional theory of atoms and molecules* (Oxford University Press, New York, 1989).

[109] T. P. Pearsall (Ed.), *Quantum Semiconductor Devices and Technologies*, Electronic Materials Series (Kluwer, Boston, 2000).

[110] P. Petroff, private communications.

[111] E. S. Polzik, Physics World **15**, 33 (2002).

[112] E. M. Purcell, Phys. Rev. **69**, 681 (1946).

[113] K. S. Pyshkin, C. J. B Ford, R. H. Harrel, M. Pepper, E. H Linfeld, and D. A. Ritchie, Phys. Rev. B **62**, 15 842 (2000).

[114] C. Reese, B. Gayral, B. D. Gerardot, A. Imamoğlu, P. M. Petroff, and E. Hu, J. Vac. Sci. Technol. B **19**, 2749 (2001).

[115] S. M. Reimann, M. Koskinen, and M. Manninen, Phys. Rev. B **62**, 8108 (2000).

[116] H.-W. Ren, S. V. Nair, J.-S. Lee, S. Sogou, Y. Matsumoto, J. Electron. Mat. **29**, 520 (2000).

[117] M. Rontani, F. Rossi, F. Manghi, and E. Molinari, Phys. Rev. B **59**, 10 165 (1999).

[118] H.-Y. Ryu, S.-H. Kim, H.-G. Park, and Y.-H. Lee, J. Appl. Phys. **93**, 831 (2003).

[119] H.-Y. Ryu, J.-K. Hwang, and Y.-H. Lee, IEEE J. Quantum Electron. **39**, 314 (2003).

[120] C. Santori, M. Pelton, G. Solomon, Y. Dale, and Y. Yamamoto, Phys. Rev. Lett. **86**, 1502 (2001).

[121] C. Santori, D. Fattal, J. Vučković, G. S. Solomon, and Y. Yamamoto, Nature **419**, 594 (2002).

[122] C. Santori, D. Fattal, M. Pelton, G. S. Solomon, and Y. Yamamoto , Phys. Rev. B **66**, 045308 (2002).

[123] S. Sauvage, P. Boucaud, T. Brunhes, V. Immer, E. Finkman, and J.-M. Gérard, Appl. Phys. Lett. **78**, 2327 (2001).

[124] G. Schedelbeck, W. Wegscheider, M. Bichler, G. Abstreiter, Science **278**, 1792 (1997).

[125] A. Shields, private communications.

[126] J. Singh, *Excitation energy transfer process in condensed matter: theory and applications* (Plenum Press, London, 1994).

[127] G. S. Solomon, M. Pelton, and Y. Yamamoto, Phys. Rev. Lett. **86**, 3903 (2001).

[128] S. M. Spillane, T. J. Klippenberg, and K. J. Vahala, Nature **415**, 621 (2002).

[129] B. Spivak and F. Zhou, Phys. Rev. B **61**, 16 730 (2000).

[130] T. M. Stace, G. J. Milburn, and C. H. W. Barnes, Phys. Rev. B **67**, 085317 (2003).

[131] A. A. Starikov, I. I. Yakimenko, and K.-F. Berggren, Phys. Rev. B **67**, 235319 (2003).

[132] R. M. Stevenson, R. M. Thompson, A. J. Shields, I. Farrer, B. E. Kardynal, D. A. Ritchie, and M. Pepper, Phys. Rev. B **66**, 081302 (2002).

[133] T. H. Stievater, X. Li, D. G. Steel, D. Gammon, D. S. Katzer, D. Park, C. Piermarocchi, and L. J. Sham, Phys. Rev. Lett. **87**, 133603 (2001).

[134] S. Strauf, private communications.

[135] B. Tanatar and D. M. Ceperley, Phys. Rev. B **39**, 5005 (1989).

[136] S. Tarucha, D. G. Austing, T. Honda, R. J. van der Hage, and L. P. Kouwenhoven, Phys. Rev. Lett. **77**, 3613 (1996).

[137] S. Tarucha, D. G. Austing, Y. Tokura, W. G. van der Wiel, and L. P. Kouwenhoven, Phys. Rev. Lett. **84**, 2485 (2000).

[138] B. M. Terhal, M. W. Wolf, and A. C. Doherty, Physics Today **56**(4), 46 (2003).

[139] B. J. Thibeault, E. R. Hegblom, P. D. Floyd, R. Naone, Y. Akulova, and L. A. Coldren, IEEE Photon. Technol. Lett. **8**, 593 (1996).

[140] K. J. Thomas, J. T. Nicholls, M. Y. Simmons, M. Pepper, D. R. Mace, and D. A. Ritchie, Phys. Rev. Lett. **77**, 135 (1996).

[141] K. J. Thomas, J. T. Nicholls, N. J. Appleyard, M. Y. Simmons, M. Pepper, D. R. Mace, W. R. Tribe, and D. A. Ritchie, Phys. Rev. B **58**, 4846 (1998);

[142] K. J. Thomas, J. T. Nicholls, M. Pepper, W. R. Tribe, M. Y. Simmons, and D. A. Ritchie, Phys. Rev. B **61**, R13 365 (2000).

[143] J. Tulkki, A. Heinamaki, Phys. Rev. B **52**, 8239 (1995).

[144] Y. P. Varshni, Physica **34**, 149 (1967).

[145] C.-K. Wang, *Electronic structure and transport in nanofabricated low-dimensional semiconductor systems: a theoretical study*, Ph.D. thesis (Linköping University, Sweden, 1997).

[146] C.-K. Wang and K.-F. Berggren, Phys. Rev. B **54**, R14 257 (1996).

[147] C.-K. Wang and K.-F. Berggren, Phys. Rev. B **57**, 4552 (1998).

[148] R. J. Warburton, C. Schäflein, D. Haft, F. Bickel, A. Lorke, K. Karrai, J. M. Garcia, W. Schoenfeld, and P. M. Petroff, Nature **405**, 926 (2000).

[149] B. J. van Wees, H. van Houten, C. W. J. Beenakker, J. G. Williamson, L. P. Kouwenhoven, D. van der Marel, and C. T. Foxon, Phys. Rev. Lett. **60**, 848 (1988).

[150] D. A. Wharam, T. J. Thornton, R. Newbury, M. Pepper, H. Ahmed, J. E. F. Frost, D. G. Hasko, D. C. Peacock, D. A. Ritchie, and G. A. C. Jones, J. Phys. C **21**, L209 (1988).

[151] U. Woggon, *Optical properties of semiconductor quantum dots* (Springer, Berlin, 1997).

[152] S. A. Wolf, D. D. Awschalom, R. A. Buhrman, J. M. Daughton, S. von Molnar, M. L. Roukes, A. Y. Chtchelkanova, D. M. Treger, Science **294**, 1488 (2001), and references therein.

[153] W. K. Wooters and W. H. Zurek, Nature **299**, 802 (1982).

[154] S. J. Xu, X. C. Wang, S. J. Chua, C. H. Wang, W. J. Fan, J. Jiang, and X. G. Xie, Appl. Phys. Lett. **72**, 3335 (1998).

[155] E. Yablonovitch, Phys. Rev. Lett. **58**, 2059 (1987).

[156] I. I. Yakimenko, I. V. Zozoulenko, and K.-F. Berggren, Semicond. Sci. Technol. **14**, 949 (1999).

[157] Y. Yamamoto, *Lecture notes on physics of quantum information*, course AP/EE226 at Stanford University, USA. Available at `http://feynman.stanford.edu/APEE226.html`

[158] C. Yannouleas and U. Landman, Phys. Rev. Lett. **82**, 5325 (1999).

[159] T. Yoshie, A. Scherer, H. Chen, D. Huffaker, and D. Deppe, Appl. Phys. Lett. **79**, 114 (2001).

[160] Z. Yuan, B. E. Kardynal, R. M. Stevenson, A. J. Shields, C. J. Lobo, K. Cooper, N. S. Beattie, D. A. Ritchie, and M. Pepper, Science **295**, 102 (2002).

[161] Q.-M. Zhang, J.-Y. Yi, J. Bernholc, Phys. Rev. Lett. **66**, 2633 (1991).

[162] V. Zwiller, H. Blom, P. Jonsson, N. Panev, S. Jeppesen, T. Tsegaye, E. Goobar, M.-E. Pistol, L. Samuelson, and G. Björk, Appl. Phys. Lett. **78**, 2476 (2001).

[163] CVI Laser Corp. *Laser Optics and Coatings Catalog* (`www.cvilaser.com`).

[164] Product of the MathWorks, Inc. (`www.mathworks.com`)

[165] `http://www.ioffe.rssi.ru/SVA/NSM/Semicond/GaAs/Figs/421.gif`

[166] `http://www.ee.leeds.ac.uk/nanomsc/presentations/module2presentation.htm`

[167] `http://www.nottingham.ac.uk/ ppzqt/qtqdots.html`